

**Mesozoic-Cenozoic Tectonic Controls On Basin Formation And
Hydrocarbon Potential Of The Deep-water, Mexican Sector Of The Gulf Of
Mexico Basin**

by
Jack Joseph Kenning

A dissertation submitted to the faculty of the Department of Earth and Atmospheric Sciences,
College of Natural Sciences and Mathematics
in partial fulfillment of the requirements for the degree of

DOCTOR OF PHILOSOPHY

in Geology

Chair of Committee: Paul Mann

Committee Member: John Suppe

Committee Member: Jonny Wu

Committee Member: Jeff Corrigan

University of Houston
May 2020

DEDICATION

To the big bang,

To the dinosaurs,

To my wife, Courtney,

To my family

ACKNOWLEDGMENTS

I thank Dr. Paul Mann for his guidance and support on my doctoral dissertation and his supervision throughout my graduate career at the University of Houston. I appreciate the industry sponsors of the Conjugate Basins, Tectonics, and Hydrocarbons (CBTH) for funding my employment as a graduate research assistant that allowed me to undertake and complete my doctoral studies. Special thanks go to Dr. John Suppe, Dr. Jonny Wu, and Dr. Jeff Corrigan for their service on my thesis committee, and their willingness to provide guidance and contributions to my research.

I would like to especially thank Mike Saunders from Spectrum Geo (now TGS), for providing the seismic data used in Chapters 2 and 3 of this study. Similarly, I give many thanks to James Keay of TGS for providing the seismic data used in Chapter 4 of this study. I would also like to thank Dr. Zhiyong He of Zetaware Inc. for granting the Genesis and Trinity software packages for use in my research. Additionally, I would like to thank Dr. Alan Nunns of StructureSolver for providing their software for academic use at the University of Houston.

I would like to thank the numerous people, including academic researchers, industry professionals, and other students who have provided their support and insights regarding my project. Finally, I would like to thank my friends and family members for their support.

ABSTRACT

The deep-water, Mexican sector of the Gulf of Mexico covers an area of >500,000 km² and includes some of the least studied regions of the entire basin. Five main tectonic events affected the Mexican Gulf of Mexico from the Triassic to recent. 1) Triassic-Jurassic rifting, 2) Late Jurassic oceanic spreading, 3) Cretaceous passive margin development, 4) Late Cretaceous-Eocene Laramide orogeny; and 5) Eocene to recent passive margin fold-belt formation. The purpose of this dissertation is to improve understanding of the Mesozoic to recent, tectonic, structural, and stratigraphic history of the deep-water margins of the region to aid future hydrocarbon exploration. This study utilizes a database of >60,000 line-km of modern, industry 2D depth-converted seismic data.

In *Chapter 2*, I conducted thermal modeling along the deep-water Yucatan margin that used a range of estimates of lithospheric thickness and heat-flow. These models demonstrate that deeply buried, salt-related minibasins along the marginal rift are low-risk for source rock maturity and that the uppermost slope is much higher-risk. Large, salt-related traps are located directly adjacent to oil kitchens within deep minibasins, where accompanying vertical faulting allows for effective migration pathways.

In *Chapter 3*, twelve, regional-scale mass transport deposits (MTDs) of Paleogene age were mapped across the Mexican Ridges and Salina del Bravo salt province. MTD deposition is related to south-to-north, post-Laramide deformation, and exhumation of orogenic belts along the coastal area of eastern Mexico. Folds overlying a thicker MTD detachment zone in the northern Mexican Ridges possess shorter wavelengths and higher amplitudes compared to the southern Mexican Ridges.

In *Chapter 4*, area-depth strain measurements were performed for ten folds across two regional seismic profiles through the Lamprea fold-belt and Mexican Ridges that are adjacent to the southeastern Salina del Bravo salt province. Miocene-age deformation across the Lamprea coincides with a phase of renewed salt canopy extrusion that is driven by ongoing up-dip sediment loading and extensional deformation west of the Salina del Bravo salt province. These results are consistent with early Miocene fold growth onset that was controlled primarily by the advancing salt canopy and with minimal control of the underlying autochthonous salt body.

TABLE OF CONTENTS

DEDICATION.....	ii
ACKNOWLEDGMENTS	iii
ABSTRACT.....	iv
TABLE OF CONTENTS	vi
LIST OF TABLES	x
List of Figures.....	xi
CHAPTER 1: INTRODUCTION TO THIS DISSERTATION.....	1
1.1 History and development of this dissertation.....	1
1.2 Rationale, topics, and organization of this dissertation	6
1.2.1 Summary of Chapter 2	8
1.2.2 Summary of Chapter 3	9
1.2.3 Summary of Chapter 4	10
CHAPTER 2: REGIONAL THERMAL MATURITY MODELING OF HYDROCARBONS ALONG THE DEEP-WATER YUCATAN MARGIN, SOUTHERN GULF OF MEXICO	13
2.1 Introduction.....	13
2.1.1 Rationale for thermal maturity modeling.....	13
2.1.2 Evolution and tectonic history of the Gulf of Mexico	20
2.1.3 Geological setting of the Yucatan margin.....	21
2.2 Dataset and methodology	25
2.2.1 Seismic dataset and regional mapping	25
2.2.2 Model setup and parameters.....	27
2.2.3 Thermal conductivity of salt and timing of extrusion.....	36
2.2.4 Source-rock types.....	37
2.3 Structural and stratigraphic trends along the deep-water Yucatan margin	38
2.3.1 Characterization of the deep-water salt diapir structural province	38

2.3.2	Characterization of the up-dip salt-roller structural province	40
2.3.3	Regional depositional trends along the western deep-water Yucatan margin	51
2.4	Burial history and thermal modeling of the deep-water Yucatan margin	52
2.4.1	Constraint of 1D model thermal maturities using lithospheric properties	52
2.4.2	Regional maturity trends predicted by lithospheric thermal modeling	58
2.4.3	Application of alternate thermal scenarios to characterize uncertainty	63
2.5	Implications for play prospectivity and evaluation of future exploration risk	68
2.5.1	Predicted source rock thermal maturity and model uncertainty	68
2.5.2	Evaluation of source rock maturity risk across the deep-water Yucatan	72
2.5.3	Impact of regional depositional patterns on hydrocarbon generation	73
2.5.4	Analysis of trapping styles, hydrocarbon migration, and timing	75
2.6	Conclusions	82
CHAPTER 3: CONTROL OF STRUCTURAL STYLE BY LARGE, PALEOGENE, MASS TRANSPORT DEPOSITS IN THE MEXICAN RIDGES FOLD-BELT AND SALINA DEL BRAVO, WESTERN GULF OF MEXICO		
84		
3.1	Introduction	84
3.2	Regional geologic setting	91
3.2.1	Tectonic evolution of the western Gulf of Mexico	91
3.2.2	Characterization of MTDs in the Mexican Ridges	93
3.3	Data	94
3.4	Structural and stratigraphic interpretation	99
3.4.1	Seismic facies classification of MTDs in the southwestern Gulf of Mexico	99
3.4.2	Seismic interpretation of MTDs as detachment units	102
3.4.3	Distribution, size, and thickness of Paleogene MTDs	112
3.4.4	Structural analysis of MTDs and the overlying Mexican Ridges	118
3.4.5	Characterization of DHIs and amplitude anomalies in the Mexican Ridges	122
3.5	Discussion	127
3.5.1	Characterization of western Gulf of Mexico detachment shales as MTDs	127

3.5.2 Mechanisms for controlling MTD deposits in the period following the Laramide orogeny.....	129
3.5.3 Control on the structural development of the Mexican Ridges by MTDs	135
3.5.4 Implications for hydrocarbon prospectivity	138
3.6 Conclusions.....	141
CHAPTER 4: CONTROL OF STRUCTURAL DEFORMATION AND SEDIMENTATION BY THE INTERACTION OF SALT AND SHALE TECTONICS ACROSS THE DEEP-WATER LAMPREA FOLD-BELT AND SALINA DEL BRAVO SALT PROVINCE, WESTERN GULF OF MEXICO.....	144
4.1 Introduction.....	144
4.2 Geological background.....	149
4.3 Data and seismic interpretation.....	152
4.3.1 Chronostratigraphic interpretation framework	152
4.3.2 Regional correlation using seismic facies relationships.....	159
4.4 Style of folding across the Lamprea fold-belt and deep-water region..	160
4.4.1 Detachment folds	160
4.4.2 Faulted detachment folds	160
4.4.3 Imbricate thrust faults and pop-up structures.....	162
4.5 Area-depth strain methodology	163
4.6 Results from Area-depth strain analysis and structural geometric measurements.....	168
4.6.1 Structural analysis of pre-growth strata	168
4.6.2 Timing of fold growth onset and associated erosion of pre-growth strata.....	181
4.6.3 Structural analysis of syn- to post-growth strata.....	183
4.6.4 Sediment thickness trends of the principal mapped growth successions.....	187
4.6.5 Characterization of fold-belt structural geometries.....	187
4.7 Discussion.....	193
4.7.1 Analysis of the growth model and controls on structural deformation.....	193
4.7.2 Interaction between salt and shale tectonics and their impact on the development of the Lamprea fold-belt.....	195

4.7.3 Mechanisms for mass transport deposit development across the deep-water syn- to post-growth succession	201
4.7.4 Oligocene play concept and hydrocarbon potential of the southeastern Lamprea fold-belt trend.....	202
4.8 Conclusions.....	208
CHAPTER 5: SUMMARY AND CONCLUSIONS OF THIS DISSERTATION	211
5.1 Tectonic controls on the geological development of the Mexican Gulf of Mexico	211
5.2 Regional impacts on petroleum system risk and hydrocarbon prospectivity	213
BIBLIOGRAPHY.....	218
Appendix.....	243

LIST OF TABLES

Table 2.1	Table displaying values of thickness, heat production, thermal conductivity, density, and heat capacity for continental and oceanic lithosphere. Estimates correspond to upper and lower crust, and lithospheric mantle. Estimates of thickness are based on the seismic observations and gravity modeling of the conjugate Florida margin by Christeson <i>et al.</i> , (2014). Lithospheric properties were taken from Davison and Cunha (2017), after Turcotte and Schubert (2002) and Vilà <i>et al.</i> , (2010), and Priestley <i>et al.</i> , (2018).....35
Table A1.1	Area-depth strain measurements for folds along Profile 1 (Figure 4.9).....243
Table A1.2	Area-depth strain measurements for folds along Profile 2 (Figure 4.10).....245

LIST OF FIGURES

- Figure 1.1** Summary chart illustrating the principal tectonic and structural characteristics of the three project areas in this study. The main differences between the areas are an absence of significant Laramide and post-Laramide tectonic influences on the distal Yucatan margin, resulting in a lack of thick, Paleogene shales that act as detachment surfaces in southwestern Gulf of Mexico. Unlike the salt-cored fold-belts in the other areas, the Mexican Ridges fold-belt detaches solely on Paleogene shales as it overlies a substrate of late Jurassic oceanic that formed after middle Jurassic salt deposition rather than rifted continental crust. This study aims to illustrate that these factors play a crucial role in the hydrocarbon prospectivity of each of these highly-frontier structural provinces.....7
- Figure 2.1** Map showing the main structural and basinal provinces of the Gulf of Mexico and its onshore areas in eastern Mexico. The deep-water Yucatan margin is located along the northern continental margin of the Yucatan Peninsula and is bounded by the Yucatan Shelf to the south, the deep-water Campeche salt basin to the southwest, and the abyssal Gulf of Mexico to the north. Map information from Mexico compiled from Gray *et al.*, (2001); Garcia-Palomo *et al.*, (2004); Andreani *et al.*, (2008); Ferrari *et al.*, (2012); Yarbuh and Contreras (2017); Nguyen and Mann (2016); Sanford *et al.*, (2016).....17
- Figure 2.2** Map showing the extent of the 2D seismic dataset available in the area. The boxed study area represents the area of the dataset that was primarily interpreted for the results of this paper. The area the grid east of the boxed, study area was interpreted by Steier and Mann (2019). Most of the study area is located in water depths of > 3,000 m below sea-level, and significant parts of the study area lie above ocean crust. The pseudo well profile and limited well locations in the area are also highlighted in addition to locations of representative interpreted seismic sections. The local continent-ocean boundary has been defined based on gravity data from Sandwell *et al.*, (2014).....19
- Figure 2.3** Chronostratigraphic chart summarizing the assumed lithology for the deep-water Yucatan margin. The main tectonic events are shown in addition to potential source rock and reservoir intervals. Ages for mapped seismic units are defined. Additional information used to create the chart was compiled from CNH (2015); Hudec and Norton (2019); Steier and Mann (2019).....24
- Figure 2.4** **a)** Interpreted seismic section illustrating the primary mapped stratigraphic horizons across the study area that highlights the main structural trends and tectonic domains. Modeled pseudo well locations are also shown with the pseudo wells located to capture representative stratigraphic and crustal differences across the dip-length of the margin. **b)** Simplified stratigraphic

sections and representative formation lithologies constructed for each pseudo well location and used to create 1D burial history models are shown.....32

Figure 2.5 a) Annotated burial history restoration profile for the Oxfordian. b) Annotated burial history restoration profile for the Late Cretaceous. c) Annotated burial history profile for the Late Eocene. d) Annotated burial history profile for the Late Miocene. Location of the model profile is displayed in Figure 2.2.....34

Figure 2.6 Interpreted seismic profile showing an example of the salt diapiric and minibasin structural province located in the marginal rift domain adjacent to the continent-ocean boundary in the deep-water western part of the study area. Salt diapirs and pillow structures form a variety of large trapping structures in the Mesozoic and additional associated structures in the overlying Cenozoic section.....43

Figure 2.7 Interpreted seismic profile showing an example of the minibasin development and salt pillows along the flanks of the marginal rift domain adjacent to the continent-ocean boundary in the deep-water eastern part of the study area. Thicknesses of Cenozoic minibasins can exceed 6 km in burial depth.....44

Figure 2.8 Interpreted seismic profile showing an example of salt-roller structures located along the Mesozoic slope. Basinward gravitational movement of salt along a basal detachment during the late Jurassic and Cretaceous resulted in the formation of an extensive listric fault system and associated rafted growth sediments. Extensive underlying Triassic-Middle Jurassic normal faulting in the pre-salt section and associated sedimentary sequences are a result of rifting associated with the early opening of the Gulf of Mexico.....46

Figure 2.9 Interpreted seismic profile showing an example of normal faulting within the Cenozoic sequence and associated with the up-dip pinch-out of salt and thin-out of the overlying Mesozoic strata against the shelf margin. Faulting is likely the result of continued salt tectonics in the distal basinward domain or continued minor movement along the sloping salt detachment.....48

Figure 2.10 a) Isopach thickness map from the uppermost Cretaceous unconformity to uppermost Jurassic salt. b) Isopach thickness map from the near uppermost Paleocene to the uppermost Cretaceous unconformity. c) Isopach thickness map from near the uppermost Eocene to near the upmost Paleocene. d) Isopach thickness map from near the uppermost Oligocene to near the uppermost Eocene. e) Isopach thickness map from the uppermost Miocene to near the uppermost Oligocene. f) Isopach thickness map from the seafloor (recent) to uppermost Miocene.....50

Figure 2.11 Example of a pseudo well (PW-4) showing the burial and thermal history modeling that was carried out on each pseudo well. a) Burial history and

predicted maturity of late Cretaceous, Tithonian, and Oxfordian potential source horizons. Blue annotations state the predicted transformation ratio as a percentage of transformed kerogen at various stages of burial. The model predicts an oil window maturity for the principal Tithonian source rock from the Oligocene to recent. **b)** Modeled vitrinite reflectivity curve versus depth, highlighting the present-day maturity of the three potential Mesozoic source intervals. **c)** Predicted oil and gas generation rates through time for the principal Tithonian source rock. Oil generation began in the Eocene and peaked in the Oligo-Miocene. **d)** Cumulative oil and gas expulsion curves for the principal Tithonian source rock. Oil and gas expulsion is predicted to continue to the present-day.....55

Figure 2.12 Temperature-depth graph showing modeled geothermal gradients from all six pseudo well 1D models plotted with measured formation temperature data from wells located in Cantarell area in the southeastern part of the Campeche salt basin >300 km to the south of the study area. Modeled pseudo well geotherms based on the lithospheric heat-flow model fit within the range of Campeche basin temperature data and fall within the low end of the data range. If the Yucatan margin is, in fact, cooler than this part of the Campeche basin as suggested, this could be explained by the presence of thinner stretched continental crust and oceanic crust in the Yucatan margin study area. Thinner crust would generate less radiogenic heat, especially beneath the deeper, cold, overlying water column, and because of differences in burial timing and thickness in the two areas. Measured temperature data from Magoon *et al.*, (2001); Waples *et al.*, (2004); Ortuño *et al.*, (2009). The continent-ocean boundary is inferred from Sandwell *et al.*, (2014) satellite gravity data.....57

Figure 2.13 Generated maps of predicted thermal maturity based on regional burial and thermal histories modeled using an estimated lithospheric heat-flow model. **a)** Map of modeled vitrinite reflectivity (%) for the Oxfordian source interval (approximated with uppermost salt structure map). **b)** Map of modeled vitrinite reflectivity (%) for the Tithonian source interval (approximated with the near uppermost Jurassic structure map). **c)** Map of modeled vitrinite reflectivity for the Cretaceous source intervals (approximated with uppermost Cretaceous structure map). The continent-ocean boundary is inferred from Sandwell *et al.*, (2014) satellite gravity data.....60

Figure 2.14 Model cross-sectional profiles showing modeled thermal maturities in terms of vitrinite reflectivity (%) across the deep-water Yucatan margin from the lithospheric heat-flow model. **a)** Profile through the eastern part of the study area. **b)** Profile through the central part of the study area, with pseudo well locations that were used for 3D model calibration. **c)** Profile through the western part of the study area near the boundary with the Campeche salt basin.....62

- Figure 2.15** Generated maps of predicted Oxfordian source rock thermal maturity based on regional burial and thermal histories modeled using for three different heat flow scenarios. **a)** Map of Oxfordian source rock modeled vitrinite reflectivity (%) for the low-case thermal scenario. **b)** Map of Oxfordian source rock modeled vitrinite reflectivity (%) for the mid-case thermal scenario. **c)** Map of Oxfordian source rock modeled vitrinite reflectivity (%) for the high-case thermal scenario.....65
- Figure 2.16** Generated maps of predicted Tithonian source rock thermal maturity based on regional burial and thermal histories modeled using for three different heat flow scenarios. **a)** Map of Tithonian source rock modeled vitrinite reflectivity (%) for the low-case thermal scenario. **b)** Map of Tithonian source rock modeled vitrinite reflectivity (%) for the mid-case thermal scenario. **c)** Map of Tithonian source rock modeled vitrinite reflectivity (%) for the high-case thermal scenario.....66
- Figure 2.17** Generated maps of predicted Cretaceous source rock thermal maturity based on regional burial and thermal histories modeled using for three different heat flow scenarios. **a)** Map of Cretaceous source rock modeled vitrinite reflectivity (%) for the low-case thermal scenario. **b)** Map of Cretaceous source rock modeled vitrinite reflectivity (%) for the mid-case thermal scenario. **c)** Map of Cretaceous source rock modeled vitrinite reflectivity (%) for the high-case thermal scenario.....67
- Figure 2.18** Map of near Late Jurassic structure map with Tithonian maturity contours from the preferred lithospheric heat-flow superimposed. Black triangles mark cataloged oil slicks observed at sea-surface and modified from Saunders *et al.*, (2016). Recovered oil and gas samples from shallow cores samples are also summarized based on information from Watkins and Buffler (1996) and Naehr *et al.*, (2007). Numerous oil slicks are clustered around salt diapirs and Mesozoic structural features adjacent to primary oil kitchen areas within salt minibasins in the marginal rift. Less numerous oil slicks up-dip and on the Yucatan shelf and slope provide evidence of possible long-distance migration from the primary marginal rift kitchen area.....71
- Figure 2.19** Risk index maps of thermal maturation for each Mesozoic source rock interval based on the sum of predicted thermal maturity (>0.6% Ro) from each high, mid, and low-case thermal maturity map. **a)** Maturity risk for the Oxfordian source rock. **b)** Maturity risk for the Tithonian source rock. **c)** Maturity risk for the Cretaceous source rocks. Continent-ocean boundary inferred from Sandwell *et al.*, (2014) gravity data.....80
- Figure 2.20** Play schematic summary profile across the deep-water Yucatan margin illustrating a variety of potential structural and stratigraphic trapping

configurations identified across the margin from the seismic data. Potential routes for hydrocarbon migration from deep, thermally mature kitchen areas, via both vertical fault conduits, and through long-distance lateral migration are characterized.....81

- Figure 3.1** Map showing the main structural and basinal provinces of the Gulf of Mexico and eastern Mexico, highlighting the location of the Mexican Ridges. Onshore map information from Mexico compiled from Gray *et al.*, (2001); Garcia-Palomo *et al.*, (2004); Andreani *et al.*, (2008); Ferrari *et al.*, (2012); Offshore, map information compiled from Nguyen and Mann (2016) and Yarbuh and Contreras (2017). The inset map shows the location of the study area in a more regional view.....88
- Figure 3.2** **a)** The 2D seismic dataset used in this study is shown in grey, and select seismic profiles highlighted in yellow. Fold axes of the deep-water Mexican Ridges are compiled from Pew (1982); Yarbuh and Contreras (2017). Normal faults of the up-dip Quetzalcoatl Extensional System from Le Roy *et al.*, (2007). **b)** Schematic cross-section of a passive-margin, gravitationally-driven fold-belt, showing up-dip extension corresponding to the Quetzalcoatl Extensional System and down-dip contraction corresponding to the Mexican Ridges. The figure is modified from Rowan *et al.*, (2004).....90
- Figure 3.3** **a)** Stratigraphic column showing the late Eocene to early Miocene interval of interest for this study, with the late Eocene and Oligocene detachments indicated by the thrust symbols. The eustatic sea-level curve is from Haq *et al.*, (1987), the stratigraphic column is modified from Alzaga-Ruiz *et al.*, (2009). **b)** Partial logs from the Puskon-1 well from O’Reilly *et al.*, (2017) show the dominantly, fine-grain lithology of the up-dip section of the Oligocene detachment interval as shown in **a)**.....95
- Figure 3.4** **a)** Uninterpreted, northeast-trending, seismic dip profile intersecting the Puskon-1 well drilled ~55 km from the coast of eastern Mexico to a total depth of 7200 m (locations of this seismic line and Puskon-1 are shown on the map in Figure 2a). The inset schematic illustrates the polarity of the seismic data displayed in **a)**. **b)** Interpreted seismic profile showing age horizons extrapolated from Puskon-1 well. Units located along the basal detachment were interpreted as Eocene, with the up-dip part of the MTD 7 as Oligocene based on the well biostratigraphic ages. TVDSS = total vertical depth subsea.....98
- Figure 3.5** Classification of gravity-induced, mass transport deposits compiled from previous authors: Dott (1963); Nardin *et al.*, (1979); Moscardelli *et al.*, (2006); and Moscardelli and Wood (2008); Ogata *et al.*, (2012). All types of slide, slump, and debris flow end-members are present in the Mexican Ridges;

however, the majority of Paleogene-age deposits mapped as part of this study are debris flows.....100

Figure 3.6 Seismic facies classification of gravity-induced depositional sequences within the Mexican Ridges deep-water fold-belt. Three principal seismic facies were identified associated with gravity-induced deposits: 1) Seismic facies 1 (**SF-1**) consists of chaotic, low-amplitude reflectors typical of the shale-rich debris flows; 2) **SF-2** displays imbricated, moderate-amplitude reflectors commonly observed in areas of slumps or debris flows with syn-depositional, compressional deformation; and 3) **SF-3** consists of high amplitude, planar, and continuous reflectors representing sand-rich turbidite fan deposits that provide potential Oligo-Miocene hydrocarbon reservoirs within the Mexican Ridges.....101

Figure 3.7 a) Uninterpreted, north-trending, 2D seismic strike profile showing the distribution of regionally-extensive Eocene - Oligocene MTDs that provided the stratigraphic control for the basal detachment level. b) Interpreted seismic strike profile showing the northern Mexican Ridges area overlies the thickest (>1400 m) area of the structurally-deformed MTD 7. MTD 7 thins southwards (<400km) where thicker parallel-bedded strata separate the individual MTD units. Structural deformation is more intense above the thicker MTD units in the northern Mexican Ridges.....106

Figure 3.8 a) Uninterpreted, northeast-trending seismic dip profile showing the distribution of regionally extensive late Eocene-Oligocene MTDs that form a stacked, 2.5-km-thick package above the basal detachment level. b) Interpreted seismic dip profile displaying six stacked MTDs within the late Eocene-Oligocene sequence with minor faults terminating at various intervals within the package. MTDs extend laterally at least 100 km to the west from this area and continue beneath the Salina del Bravo salt canopy.....108

Figure 3.9 a) Uninterpreted, east-trending, seismic dip profile showing the distribution of regionally-extensive Eocene-Oligocene MTDs that are deformed by their proximity above the primary detachment level. b) Interpreted seismic profile showing Eocene (MTD 2, 3) and Oligocene (MTD 7) detachment units in the eastern deep-water area of the Mexican Ridges. Major, thrust faults penetrate most of the section and have propagated to the basal detachment. Smaller thrusts are less laterally extensive and less penetrative. Thrust faults are present in the fold cores overlying MTD 7, with many of these thrusts terminating along the top of this unit and within the underlying, parallel-bedded strata.....110

Figure 3.10 a) Uninterpreted, southeast-oriented, seismic dip profile through the thickest (>3000 m) and most intensively structurally-deformed area of MTDs in the

northern Mexican Ridges. **b)** Interpreted seismic dip profile illustrating structural thickening of the MTD package and overlying strata. A stacked package of numerous MTDs thins laterally to form fine-grained inter-beds within the strata overlying MTD 7. Thrust faults are imbricated and utilize MTDs as secondary detachments.....111

Figure 3.11 Summary of isochore maps of selected MTD units mapped in this study. **a)** MTD 1, **b)** MTD 2, **c)** MTD 3, **d)** MTD 4, **e)** MTD 5, **f)** MTD 6. MTDs deposited during the late Eocene are regionally-present over the entire Mexican Ridges, with greater average thicknesses in the northern Mexican Ridges overall.....114

Figure 3.12 Summary of isochore maps of selected MTD units mapped in this study. **a)** MTD 7, **b)** MTD 8, **c)** MTD 9, **d)** MTD 10, **e)** MTD 11, **f)** MTD 12. MTDs deposited during the Oligocene are present predominantly over the northern Mexican Ridges, where thicknesses are greatest, in addition to the areas adjacent to the Salina del Bravo salt province.....116

Figure 3.13 **a)** Composite thickness isochore of fine-grained mapped units located near the level of the basal detachment level (MTDs 1-12). Thicknesses range from > 3200 m in the northern Mexican Ridges to < 2500 m in the southern Mexican Ridges. Locations of seismic profiles 1-4 used for thickness and fold geometric measurements are shown on the map. **b)** Measurements of total MTD package thickness compared to fold wavelength. **c)** Measurements of overburden thickness compared to fold wavelength. **d)** Measurements of total MTD package thickness compared to fold amplitude. **e)** Measurements of overburden thickness compared to fold amplitude.....121

Figure 3.14 **a)** Hydrocarbon prospectivity summary map showing mapped amplitude anomalies, hydrocarbon seep data, hydrocarbon fields and select well shows, Jurassic source rock maturity, and locations of seismic examples shown in **b)**, **c)**, **d)** and **e)**. Additional geologic and hydrocarbon data were compiled from previous authors, including Ambrose *et al.*, (2005), Holguin-Quinones *et al.*, (2005); Salomon-Mora (2013); CNH (2015); and Nguyen and Mann (2016). **b)** Seismic example of a tilted amplitude anomaly associated with the crest of a major faulted fold-structure. **c)** Seismic example of a shallow amplitude anomaly disrupted by a shale inter-bed. **d)** Seismic example displaying multiple BSRs and associated amplitude anomalies focused along the crests of anticlines. **e)** Seismic example showing a shallow amplitude anomaly that may be associated with shallow gas hydrates.....126

Figure 3.15 Area versus length, log-log plot that compares the sizes of MTDs measured in this study for the Mexican Ridges with MTD measurements from other areas that were compiled by Moscardelli and Wood (2016). The very large sizes of the MTD deposits in the Mexican Ridges indicates an origin resulting from

extra-basinal, tectonic events related to the post-Laramide, regional deformation of eastern Mexico.....130

Figure 3.16 Schematic cross-sections and depositional events maps for key periods in the tectonic evolution of the Mexican Ridges. **a)** Laramide orogenic phase from the late Cretaceous and Middle Eocene. **b)** Post-Laramide late Eocene inversion and erosion of the southern Sierra Madre Oriental and coinciding with deposition of MTDs offshore. **c)** Post-Laramide Oligocene inversion and erosion of the northern Sierra Madre Oriental coinciding with deposition of MTDs offshore. **d)** Late Miocene to recent passive-margin gravitational failure and formation of the Mexican Ridges that was closely controlled by deformation of fine-grained Paleogene MTDs. Additional tectonic, structural, and depositional elements compiled from Galloway *et al.*, (2000); Gray *et al.*, (2001); Galloway *et al.*, (2011); Cossey *et al.*, (2016); Yarbuh and Contreras, (2017); Snedden *et al.*, (2018).....134

Figure 4.1 Regional map of the western and central Gulf of Mexico, showing the offshore location of the Salina del Bravo salt province and its adjacent and distal Lamprea fold-belt. The transform-dominated, continental margin of western Gulf of Mexico exhibits a steep and narrow continental slope with part of the Salina del Bravo salt canopy and Lamprea fold-belt extruding over Jurassic oceanic crust in the deep-water area. Structural and tectonic elements are modified from Garcia-Palomo *et al.*, (2004); Andreani *et al.*, (2008); Ferrari *et al.*, (2012); CNH (2015); Nguyen and Mann (2016); and Yarbuh and Contreras (2017).....148

Figure 4.2 **a)** Map of structural elements, seismic figure orientations, shallow salt, and key well locations across the Lamprea fold-belt, Salina del Bravo province, and Kama fold-belt. Up-dip gravitational failure and sediment loading across the Burgos Basin produced an extensive, deep-rooted extensional fault system. Deformation is translated down-dip along Jurassic and Eocene detachment surfaces into a compressional area that extrudes Jurassic salt to form shallow-detached salt canopies and the shale-detached Lamprea fold-belt. Figures 4.5a and 4.5b represent locations of the two seismic profiles that cross a series of anticlines in the deep-water Lamprea fold-belt and used for area-depth strain analysis in this study. **b)** Map of structural elements, seismic figure orientations, and key well locations superimposed on the EMAG2 regional magnetic anomaly map. The position of the BAHA high from Hudec *et al.* (2019) is highlighted. Regional structural elements for a) and b) are modified from Le Roy *et al.*, (2007); CNH (2015); Nguyen and Mann (2015); Yarbuh and Contreras (2017); Vazquez-Garcia (2018); Hudec *et al.* (2019). **c)** Conceptual schematic dip profile across the study area from northwest to southeast. The Lamprea fold-belt, forming the primary focus of this study, represents the contractional deformation front of a margin-wide linked gravitational system. The style of deformation along the margin is controlled by a steep angle of dip combined

with the BAHA high acting as a buttress. Schematic based on interpreted sections from CNH (2015).....155

Figure 4.3 Seismic to stratigraphic age correlation for the area of the deep-water Gulf of Mexico that is located directly east of the southern Lamprea and northern Mexican Ridges fold-belts. The white numerals on the left-hand side of the seismic image indicate interpreted horizons used for area-depth strain analysis shown in Figures 4.5a and 4.5b. The basal detachment for the Lamprea fold-belt is inferred from seismic interpretation to be located within layer 3. Age constraints for this undrilled deep-water area were estimated based on up-dip well control and previously interpreted seismic data from Le Roy *et al.*, (2007) and Kenning and Mann (2020).....156

Figure 4.4 Seismic well-tie with the Vespa-1 well that provides age constraints on the Oligocene-Recent strata in the up-dip Salina del Bravo salt province and adjacent Kama fold-belt. Numerous shallow debris flows form correlation markers across parts of the salt canopy and extend across the deep-water Lamprea fold-belt. Age control from the Vespa-1 well was modified from O'Reilly *et al.*, (2017).....157

Figure 4.5 **a)** Seismic profile across the deep-water western Gulf of Mexico in the northern part of the study area. The seismic line is ~40-km long, has a depth penetration of 9 km, and is orientated NW-SE, perpendicular to the strike of the fold structures of the labeled fold belts. The profile covers a narrow section of the Lamprea fold-belt characterized by highly-imbricate folds proximal to the salt canopy front, before transitioning into isolated thrust-detachment folds that are typical of the Mexican Ridges fold-belt to the south. **b)** Seismic profile across the deep-water western Gulf of Mexico in the southern part of the study area. The line is ~80-km long, has a depth penetration of 9 km, and is orientated NW-SE and perpendicular to the strike of the fold structures. The Lamprea fold-belt is significantly wider at this location and is influenced by salt-tectonics in the proximal part of the imbricated fold zone. The structural style of the Lamprea fold-belt transitions into Mexican Ridges detachment folds towards the south-east.....158

Figure 4.6 Interpreted growth-strata geometries observed from seismic data crossing the Lamprea fold-belt and the Mexican Ridges fold-belt transition. The stratigraphy consists of four primary successions; 1) pre-growth strata of Eocene-Oligocene age deposited before the onset of folding (partially shown in figures), 2) early syn-growth strata of early Miocene age that is often truncated along the crests of folds by an angular unconformity, 3) variably syn-growth to post-growth strata of Miocene-Pliocene age deposited either synchronously with or in-between phases folding, which often display as either thinning or overlapping sets of reflections across the fold crests, and 4) variably syn-growth to post-growth

strata of Pleistocene to recent age consisting predominantly of stacked debris flow sequences and unconformable with the previously deposited growth section. **a)** Patterns of onlap and truncation located between the stratigraphic successions in the proximal, imbricate Lamprea fold-belt. **b)** Patterns of onlap and truncation in the central and distal Lamprea fold-belt are broadly similar to the proximal area; however, the episodic timing of fold growth and the end of fold growth can vary across the fold-belt **c)** Similar patterns of onlap and truncation are noted in the distal Mexican Ridges fold-belt transition to the east, and often exhibit growth strata close to the seafloor.166

Figure 4.7 Schematic, structural parameters of detachment folds in the framework of an area-depth strain analysis using the depth-to-detachment method. Measurements of the excess area (a) beneath each interpreted horizon of a fold structure are plotted graphically versus depth (h) from a reference horizon, that in this case, is sea-level. Pre-growth strata typically exhibit a linear trend of decreasing area with increasing depth, which allows for an estimation of the basal detachment depth (at a=0). Syn- to post-growth strata are expected to exhibit the opposite trend, with progressively decreasing excess area as depth decreases. Overlying units that exhibit zero area either may indicate either post-growth deposition or that the rate of uplift is less than the rate of sedimentation during fold growth.....167

Figure 4.8 Area-depth strain analysis of fold structures across Profile 1 located in the map in Figure 4.5a. Estimated detachment depths were consistently estimated within layer 3 with high correlation coefficients (RSq). The values in the format -D (-N, -S%) beside each fold complex represent the calculated area-depth displacement (D), nominal displacement (N), and layer-parallel strain (S), respectively. Profile 1 was divided into four sections: **a)** a grouped series of imbricate fold-thrusts, constrained by the regional base level, located ahead of the salt canopy, **b)** a grouped series of pop-ups and imbricate thrust-folds, **c)** an individual detachment fold, and **d)** an individual detachment fold representing the main deformation front.171

Figure 4.9 Area-depth strain analysis of fold structures across Profile 2 located in the map in Figure 4.5b. Estimated detachment depths were consistently estimated within layer 3 with high correlation coefficients (RSq). The values in the format -D (-N, -S%) beside each fold complex represent the calculated area-depth displacement (D), nominal displacement (N), and layer-parallel strain (S), respectively. Profile 1 was divided into six sections: **a)** a grouped series of imbricate fold-thrusts and pop-ups constrained by the regional base level, **b)** a salt and shale cored fold with numerous faults, **c)** a series of highly-uplifted pop-up structures, **d)** a complex fold structure at the Lamprea to Mexican Ridges transition, **e)** a large fold with multiple associated imbricate thrusts, **f)** a grouping of two detachment folds with limits constrained to the regional base level.....173

- Figure 4.10** Plots of the area of structural relief (a) as a function of depth (h) for folds 1-4 along Profile 1. The slope is obtained by a best-fit line and the break-down of the linear relation marks the onset of folding. For folds 1-4 (**a**), **b**), **c**), and **d**)), the onset of growth is observed around layer 9 (Late Oligocene). **e**) Schematic interpretation of Profile 1. It is important to note that both horizon 9 and 10 (Late Oligocene/Early Miocene) exhibit a degree of variable erosion along the crests of the folds, which would reduce the measured area.....174
- Figure 4.11** Plots of the area of structural relief (a) as a function of depth (h) for folds 1-6 along Profile 2. The slope is obtained by a best-fit line, and the break-down of the linear relation marks the onset of folding. For folds 1 and 2 (**a**) and **b**)) the onset of growth is observed around layer 7 (Oligocene), for folds 3 and 4 (**c**) and **d**)) around layer 8, and for folds 5 and 6 (**e**) and **f**)) around layer 9 (Late Oligocene). **g**) Schematic interpretation of Profile 2 that is similar to interpretations of layers 9-10 in Profile 1. Layers 8-10 are interpreted to represent the erosion of fold-crests and may not necessarily represent an earlier onset of fold-growth.176
- Figure 4.12** Plots of **a**) total calculated area depth displacement and **b**) calculated layer-parallel strain across Profile 1 of the Lamprea fold-belt. Displacement is similar for each fold-complex across this part of the fold belt. Higher layer-parallel strain is associated with fold 2, which represents the front of the Lamprea imbricate-fold zone. **c**) Schematic section based on Profile 1 seismic that displays the measured fold complexes and primary growth packages.....178
- Figure 4.13** Plots of **a**) total calculated area depth displacement and **b**) calculated layer-parallel strain across Profile 2 of the Lamprea fold-belt. Displacement is fairly consistent and increases slightly towards the front of the adjacent Lamprea fold-belt, decreases with a change in detachment angle, then increases across the sizeable outer Mexican Ridges structures in this area that exhibits larger area-depth displacements. The layer-parallel strain of the structures is also consistently high across the profile with the exception of fold 4, which represents a change in detachment angle between the proximal Lamprea fold-belt and the more isolated distal fold structures **c**) Schematic section based on Profile 2 seismic that shows the measured fold complexes and their primary growth packages.....180
- Figure 4.14** **a**) Interpreted schematic depiction of Profile 1 growth sequences and a graph of area-depth calculated thicknesses for each primary sequence along the profile. Pre-growth strata thins slightly towards the front of the fold-belt with a thickening of the total present-day syn-growth sequences. **b**) Interpreted schematic depiction of Profile 2 growth sequences and a graph of area-depth calculated thicknesses for each primary sequence along the profile. Pre-growth

strata are thicker more proximally to the west with a thinner overlying present-day syn-growth sequence. Compared to Profile 1, the total sediment thickness is greater despite a slightly thinner pre-growth sequence across the equivalent distal area.186

Figure 4.15 a) Graph of individual fold wavelength measurements across the length of Profile 1 that reveals the differences in structural style between the proximal imbricate zone of the Lamprea fold-belt and the more distal and isolated detachment folds, which are typically spaced more widely. b) Graph of individual fold amplitude measurements across the length of Profile 1, showing more numerous smaller fold-thrusts in the proximal Lamprea fold-belt and higher-amplitude folds in the distal section. c) Interpreted schematic section of Profile 1 showing the primary structural domains with numbering to indicate the folds that were measured..... 190

Figure 4.16 a) Graph of individual fold wavelength measurements across the length of Profile 2. The proximal area of Lamprea fold-belt in this area consists of both wide and closely spaced thrust-folds. There are more numerous, closely-spaced folds before a transition into the wider-spaced isolated detachment folds of the more distal area. b) Graph of individual fold amplitude measurements across the length of Profile 2 that shows higher-amplitude folds in the distal section compared to lower amplitude folds across the proximal Lamprea fold-belt. c) Interpreted schematic section of Profile 2 showing the primary structural domains and numbering to indicate the folds that were measured..... 192

Figure 4.17 Interpreted seismic section oriented NW-SE through an isolated salt diapir in the Lamprea fold-belt. The salt diapir is emplaced within the Eocene shale-layers and has been extruded either along the Eocene shale detachment from the main proximal salt canopy or alternatively and more likely from a deep and underlying salt feeder structure. Erosion along the crest of folds is consistent with that observed across the Lamprea fold-belt (layer 10 – Early Miocene), and is interpreted as the regional onset of fold-belt growth. Onlap patterns within the Oligocene strata not observed across exclusively shale-cored folds and support the interpretation for earlier development of the salt-controlled structures across the Lamprea fold-belt (and Salina del Bravo salt province) in post-early Oligocene time.....199

Figure 4.18 Map displaying the interpreted ages for the prime onset of deformation for each of the structural sub-provinces within the immediate study area of the western Gulf of Mexico. In the extensional domain, major growth deposition began in the offshore Burgos basin by the Oligocene coinciding with formation of the Perdido fold-belt down-dip. Formation of the Paleogene shale-detached Lamprea fold-belt occurred as a result of a phase a salt canopy extrusion related to continued basinward sedimentation and formation of the shallow shale-

detached Kama fold-belt, behind the salt canopy to the west. Most of the Paleogene shale-detached Mexican Ridges fold-belt formed later and is unrelated to salt tectonics, driven primarily by up-dip, gravity-driven loading and extensional collapse along the Quetzalcoatl shelf-edge. Regional structural elements are modified from Le Roy *et al.*, (2007); CNH (2015); Nguyen and Mann (2015); Yarbuh and Contreras (2017); Vazquez-Garcia (2018); Hudec *et al.* (2019).....200

Figure 4.19 a) Seismic age interpretation of the up-dip Kama fold-belt and Salina del Bravo salt province. Numerous shallow debris flows form correlation markers across parts of the salt canopy and into the deep-water area. Numerous large debris flows of mostly Pleistocene age originate from the up-dip extensional fault zone, blanket parts of the salt canopy, and correlate with interpreted marker horizons within the stacked shallow debris flow package present across the shale-core minibasins and distal Lamprea fold-belt. b) Detailed interpretation of the Kama fold-belt faulted section. Many of the debris flow units can be traced up-dip into zones of erosion, collapse, and slumping that are associated with extensive normal faulting in the thick growth strata.....205

Figure 4.20 a) Map summarizing the SE Lamprea fold-belt trend, which was the focus of this study, in relation to compiled well results and hydrocarbon seep data. Wells that encountered hydrocarbons in the Oligocene section are highlighted along the length of the Perdido and Lamprea fold-belts to the north and are associated with numerous oil slicks that extend into the underexplored SE Lamprea trend. b) Schematic summary section integrating the results of this study with information on petroleum systems. Oligocene reservoirs above the thick shale detachment of the Lamprea fold-belt would require complex migration routes that are charged by underlying Mesozoic source rocks. The most obvious potential migration routes follow deep salt-related structures. The influence of these inferred migration routes decrease to the east across the fold-belt and increases migration risk - despite the presence of numerous oil seeps in the distal area. Regional structural elements for a) are modified from Le Roy *et al.*, (2007); CNH (2015); Nguyen and Mann (2015); Yarbuh and Contreras (2017); Vazquez-Garcia (2018); Hudec *et al.* (2019). Well data is modified from CNH (2019) and seep locations from CNH (2015).....207

Figure 5.1 Regional map of the Mexican sector of the Gulf of Mexico showing assessed petroleum system risk. Characterized risk is purely qualitative and based on evaluations made during the course of this study. Risk is relative between the areas within the study as currently all three provinces are significantly underexplored, and therefore remain high-risk regions for hydrocarbon exploration overall. Continent-ocean boundary and spreading ridges from Nguyen and Mann (2015).....214

CHAPTER 1: INTRODUCTION TO THIS DISSERTATION

1.1 History and development of this dissertation

I grew up in Devonshire, a county in southwestern England. I went on to obtain a BSc degree in Geology from the University of Manchester in 2011, and an MSc degree in Petroleum Geoscience from Royal Holloway, University of London in 2012. Following my graduation, I was a summer intern with Anadarko Petroleum in London during 2011 and was hired as an explorationist for North Africa by Anadarko, USA, who transferred me from their UK office to their Woodlands, Texas, office in 2014. In the Woodlands office, I worked on asset development for the Eagle Ford shale play and exploration within the north Louisiana salt basin.

In 2016, my fledgling career in oil and gas was cut short as a result of the oil price downturn. I decided to take to use this hiatus to return to obtain a PhD in geosciences with a plan to return to the petroleum industry. I wanted to return to being able to expand my experience in areas of personal interest that includes tectonics, basin analysis, and thermal modeling for petroleum systems.

I reached out to Dr. Paul Mann, a professor and principal investigator of the Conjugate Basins, Tectonics, and Hydrocarbons (CBTH) research consortium at the University of Houston. I applied and was accepted into the PhD program at the University of Houston, starting in fall 2017, and I was granted a UH presidential fellowship award based on my previous academic record.

While awaiting the start of my PhD program at the University of Houston in late August of 2017, I worked as an operations geosteering geologist in Oklahoma in April-May, 2017, and

in June, 2017, I began with the CBTH project by working on the project GIS database. As part of this effort, I created materials for the September, 2017, release of the consortium's Phase IV atlas and database for their industry sponsors.

Working with the CBTH project during that period allowed me an earlier start on requesting seismic data using Dr. Mann's contacts at various seismic companies. One possible project involved data from the Namibian passive margin from the Namibian national oil company and regulator (NAMCOR). By the time I had started my PhD program officially in the 2017 fall semester, it had become apparent that this Namibia study would not be possible as a result of the financial cost of licensing data for academic use from the Namibian national oil company.

Following the opening of Mexico to bidding for international exploration companies in 2014, several phases of offshore licensing rounds planned for the southern Gulf of Mexico over the following five years had significantly increased interest in the region by major oil companies. Several seismic acquisition companies had also acquired modern, high-quality, 2D multi-client surveys over large parts of the Mexican sector of the Gulf of Mexico around this time. Dr. Mann and I realized that several of the deep-water regions in the southern Gulf of Mexico were understudied as a result of this relatively recent access to pervasive, high-quality data now available for workers outside of Mexico.

Dr. Mann's contact, Mike Saunders from Spectrum, allowed me to use their 2015 regional Mexico 2D survey for my project, after he obtained the necessary permissions from their partners at PGS and Schlumberger. I began my study focusing on the largely under-

explored area of the Mexican Ridges fold-belt, where there was significant seismic data coverage.

Andrew Steier, an MS student, working at CBTH with Dr. Mann, completed a mapping study on the northern Yucatan margin of the southern Gulf of Mexico using the same 2015 Yucatan Spectrum dataset that had previously been provided to CBTH. After becoming interested in Andrew's previous work that was completed as an MS thesis and published in 2019, I felt that I could both build on his study and expand the mapping to the southwest in the direction of the Campeche Basin. This project used the Spectrum seismic grid for the basin modeling study described in Chapter 3.

I was also interested in the salt-cored fold-belts north of the Mexican Ridges in the western Gulf of Mexico. For these data, we contacted James Keay at TGS, who agreed to provide CBTH data access for this area as part of their Gigante survey, which was received in 2019. The tighter line spacing of the Gigante survey allowed for a more detailed mapping of the salt-shale transition between the northern Mexican Ridges and the Salina del Bravo salt province and was developed into Chapter 4 of this study. Collectively, the overall project goals evolved into three chapters that characterize three under-explored areas with hydrocarbon potential in the southern Gulf of Mexico.

During the summer of 2018, I interned at ConocoPhillips in Houston, where I mapped Wolfcamp and Bone Spring play boundaries along the edge of the Delaware Basin and analyzed acreage production and valuation. I was offered a return internship in the summer of 2019, where I conducted play characterization and risk analysis for the offshore Sirt basin in Libya. I was offered a full-time position in the following my internship in the fall of 2019 and will begin

working full-time for the ConocoPhillips New Ventures exploration group following my graduation from the University of Houston in spring 2020. Other activities during my PhD studies include serving as AAPG student chapter president for the 2018-2019 year.

During the course of my PhD program, I presented my research at many national and international conferences. Feedback gained from these meetings were important milestones and interactions for continuously improving the quality of my research. The presentations and meetings attended are summarized below:

Event	Title	Award	Year
HGS Sheriff Lecture Houston and AAPG Leadership day	Tectonic control on along-strike variations in wedge geometry of the Mexican Ridges deepwater fold-thrust belt, western Gulf of Mexico		2017
AGU Fall Meeting New Orleans	Cretaceous to Recent Asymmetrical Subsidence of South American and West African Conjugate Margins		2017
UH EAS student research day	Role of Eocene-Oligocene mass transport deposits for controlling along-strike variations in thickness, structural geometry, and hydrocarbon sealing, Mexican Ridges fold-thrust belt, western Gulf of Mexico	1 st place oral presentation, MS/first-year PhD category	2018
AAPG ACE Annual Convention and Exhibition	Tectonic Controls on Along-Strike Variations in the Bathymetry, Width, and Structural Style of the Mexican Ridges Deepwater, Fold-thrust Belt, Western Gulf of Mexico	4 th place student poster presentation competition	2018
Gulf Coast Association of	Seismic characterization of Eocene-Oligocene mass transport deposits and their	2 nd place student poster	2018

Geological Societies conference	influence on the structural development of the Mexican Ridges fold-thrust belt, Western Gulf of Mexico	presentation competition	
HGS Sheriff Lecture Houston (and AAPG Leadership day)	Seismic characterization and quantitative structural analysis of detachment shales in the Mexican Ridges Fold Belt, Western Gulf of Mexico	1 st place poster presentation PhD category	2018
AAPG ACE Annual Convention and Exhibition	Controls on variability in size, geometry, and depositional character between Neogene and Paleogene aged mass transport deposits in the Mexican Ridges fold-belt: implications for hydrocarbon prospectivity	1 st place student poster presentation competition	2019
GeoGulf conference	Structural and stratigraphic controls on Mesozoic source rock maturity and hydrocarbon play prospectivity of the deep-water Yucatan and Campeche margins, southern Gulf of Mexico	1 st place student oral presentation	2019
Geological Society of London: Petroleum Potential of the Gulf of Mexico and the northern Caribbean	Tectonic, structural, and stratigraphic controls on hydrocarbon prospectivity in the Mexican Ridges deep-water fold-belt, western Gulf of Mexico		2019
AAPG Hedburg: Geology and Hydrocarbon Potential of the Circum Gulf of Mexico Pre-salt Section	Tectonic, structural, and stratigraphic controls on the burial and thermal maturity of Mesozoic source rocks of the deep-water Yucatan margin, Gulf of Mexico		2020

1.2 Rationale, topics, and organization of this dissertation

The purpose of this dissertation is to improve understanding of how regional tectonic events have controlled or influenced the structural and stratigraphic history of the Mexican, deep-water sector of the Gulf of Mexico. This dissertation includes three integrated chapters which cover ~280,000 km² - or 52% of the Mexican deep-water sector of the GOM.

Each of the three chapters focusses on a different tectonic sub-domain of the southern and western GOM and the tectonic controls on its deposition and structural development. Each chapter focus on a specific section of the regional stratigraphy that ranges from the Mesozoic (Chapter 2), Paleogene (Chapter 3), and the Paleogene-Neogene (Chapter 4) (Figure 1.1).

This dissertation addresses these main topics:

Chapter 2: Defining the burial history, present-day thermal maturity, and maturation risk of Mesozoic source rocks across the deep-water Yucatan margin;

Chapter 3: Mapping large-scale, Paleogene, mass transport deposits acting as detachment shales across the deep-water Mexican Ridges fold-belt and determining their source of origin;

Chapter 4: Characterizing the interaction of salt and shale tectonics, and timing of Miocene to recent growth sedimentation across the deep-water Lamprea fold-belt.

As of the time of submission of this dissertation Chapter 3 has been published as: Kenning, J. J., Mann, P., 2020. Control of structural style by large, Paleogene, mass transport deposits in the Mexican Ridges fold-belt and Salina del Bravo, Western Gulf of Mexico. *Marine and Petroleum Geology*, 115, 104254. Chapter 2 and Chapter 4 are both currently in review with the Geological Society of London and *Journal of Structural Geology*, respectively.

Region	Yucatan margin	Salina del Bravo / Lamprea fold-belt	Mexican Ridges fold-belt
Tectonic evolution	Triassic-middle Jurassic rifted margin		Absent
	Late Jurassic-early Cretaceous oceanic spreading		
	Absent	Late Cretaceous – middle Eocene Laramide orogeny	
	Cenozoic passive margin with gravity-driven tectonics		
Detachment	Middle Jurassic salt detachment		Absent
	Absent	Late Paleogene shale detachments	
	Late Jr. - present	Eocene - present	Late Miocene - present

Figure 1.1 Summary chart illustrating the principal tectonic and structural characteristics of the three project areas in this study. The main differences between the areas are an absence of significant Laramide and post-Laramide tectonic influences on the distal Yucatan margin, resulting in a lack of thick, Paleogene shales that act as detachment surfaces in southwestern Gulf of Mexico. Unlike the salt-cored fold-belts in the other areas, the Mexican Ridges fold-belt detaches solely on Paleogene shales as it overlies a substrate of late Jurassic oceanic that formed after middle Jurassic salt deposition rather than rifted continental crust. This study aims to illustrate that these factors play a crucial role in the hydrocarbon prospectivity of each of these highly-frontier structural provinces.

1.2.1 Summary of Chapter 2

The deep-water Yucatan-Campeche rifted-passive margin along the northern edge of the Campeche salt province covers an area of >130,000 km² and includes an area of rifted continental crust overlain by salt in the south, and an adjacent area of younger oceanic crust that lacks salt in the north (Lin *et al.*, 2019). Both the rifted continental area and the adjacent, oceanic crust are overlain by potential Oxfordian, Tithonian, and Cretaceous source intervals (CNH, 2015). Numerous documented, seafloor, oil seeps over extensive parts of the southern Gulf of Mexico support the idea that an active, petroleum system is present within the Mesozoic section (Saunders *et al.*, 2016).

One important play that has been recently proposed is Oxfordian-age, Norphlet-equivalent aeolian sandstone reservoirs above salt rollers along the continental slope (Steier, 2018; Steier and Mann, 2019). Large, structural traps are associated with extensive salt features at the base of the Yucatan slope adjacent to the late Jurassic, oceanic crust (Hudec and Norton, 2019). As a result, the Mexican, deep-water Yucatan remains one of the least explored and understood areas of the Gulf of Mexico, yet holds much future potential (Gomez *et al.*, 2018).

The only well penetrations along the deep-water part of the Yucatan margin are shallow DSDP wells that do not penetrate lower than the Neogene (Steier and Mann, 2019). As a result, there are few, well-based, geochemical data available for basin modeling. To de-risk future exploration activities and will also improve the understanding of the tectonic history and geological development of the area, I assessed regional source rock maturity trends along the southern Gulf of Mexico margin as the main focus of Chapter 2.

Because of a lack of well calibration data, Chapter 2 relies on informed assumptions of lithospheric thickness, radiogenic heat-flow, and lithology. Combining results from high, medium, and low heat-flow scenarios also allow the definition of index maps that characterize source rock maturity risk across the study area for each of the potential Oxfordian, Tithonian, and Cretaceous source rock intervals. My results indicate low maturity risk for minibasins in the diapiric province and that these are likely mature for oil and gas through the post-salt Mesozoic sequence. I also identify multiple hydrocarbon trap concepts that could be exploited during future exploration of this frontier margin.

1.2.2 Summary of Chapter 3

The Mexican Ridges is a 550-km-long, shale-detached, passive margin fold-belt located along the western margin of the Gulf of Mexico. The Mexican Ridges is bordered by the Salina del Bravo salt province and Perdido fold-belt to the north; to the south, the Mexican Ridges transitions into the Catemaco fold-belt. Deformation of the contractional toe of the Mexican Ridges fold-belt is driven by up-dip, gravitational collapse of shelf sediments along the Quetzalcoatl extensional system. The basinward motion of the shelf sediments is accommodated by normal faults that sole into basal detachments of Paleogene age that overlie a substrate of Paleocene foreland deposits, Mesozoic carbonate rocks, and late Jurassic, oceanic crust formed during the opening of the GOM (Alzaga-Ruiz *et al.*, 2009; Salomon-Mora *et al.*, 2009).

Twelve of the largest, most laterally extensive Paleogene-age MTDs were mapped across the length of the Mexican Ridges and adjacent areas of the western Gulf of Mexico.

Regional mapping of this stacked sequence of MTDs assists with better defining the nature of its basal detachment zone and how the deformation of the Mexican Ridges fold-belt varies along-strike and across-strike. Observations from seismic reflection data suggest that the thickness and distribution of detachment shales exhibit a significant control on the structural development of the overlying Mexican Ridges folds. Data from one well penetration indicate that stratigraphic units at the level of the detachment fault are mud-rich; seismic facies analysis suggests the units may have been initially deposited a series of debris flows. The Oligocene timing of MTD deposition correlates with the timing of post-Laramide tectonic activity that affected this part of the eastern margin of Mexico.

The chapter also included mapping of seismic amplitude anomalies in the Mexican Ridges fold-belt that overlies the mud-rich mass transport deposit sequence at the detachment level. Defining the thickness and distribution of the detachment shales has important implications for hydrocarbon prospectivity in the Mexican Ridges fold-belt as deformed shale units along the detachment horizon form a thick, over-pressured, impermeable layer which may inhibit upward migration of hydrocarbons from deep Mesozoic source rocks beneath this area. The presence of amplitude anomalies and thermogenic hydrocarbon seep data in thrust faulted fold-structures supports the existence of hydrocarbon migration routes through the stacked detachment shale sequence.

1.2.3 Summary of Chapter 4

The salt-cored Salina del Bravo province and the shale-cored Perdido fold-belt of the western Gulf of Mexico form a productive hydrocarbon province that formed on the western,

passive margin of the Gulf of Mexico following its late Jurassic-earliest Cretaceous opening (Hudec *et al.*, 2013; Eddy *et al.*, 2014). Most previous exploration has occurred in the northern Perdido fold-belt, which forms a linear, southward extension into Mexican waters of the Paleocene-lower Eocene Wilcox and Oligocene deep-water fan plays (Snedden *et al.*, 2018; Smith *et al.*, 2019). Towards the southern part of the Salina del Bravo salt province, the Perdido fold-belt plunges beneath the salt canopy and is replaced in the southeastern area by a shallow, Paleogene detached thrust system known as the Lamprea fold-belt. Unlike the northern region close to the US border, the southern part of the Salina del Bravo salt province and adjacent Lamprea fold-belt is very under-explored and less well understood as a result.

A more detailed characterization of the area is essential for understanding the salt vs. shale mechanical controls for both the Lamprea fold-belt and the entire gravitational system, along with providing a structural framework for hydrocarbon prospectivity in the area. The southern Lamprea fold-belt and Salina del Bravo salt province represent the southeasternmost edge of the northern Gulf of Mexico salt basin, and better defining this transitional area was a goal of the study. Excess area measurements of fold structures across two seismic dip profiles through the Lamprea provide insight into the timing of deformation, depth to detachment surface, and characterization of pre-growth and syn-growth units within the fold-belt.

The timing of trap formation, tectonic interaction of salt with shale structures, and the mechanisms for fold-belt formation all control hydrocarbon migration and charge of potential Oligocene reservoirs in overlying structures of the Lamprea fold-belt. This chapter identifies the presence of folds involving both salt and shale tectonics in the Lamprea transition zone between the salt-cored Salina del Bravo province and the shale-cored Mexican Ridges fold-

belt. Excess-area measurements demonstrate that salt-involved structures of the Salina del Bravo developed earlier in the Eocene-Oligocene relative to a younger Miocene phase of the salt canopy and linked Lamprea fold-belt deformation, as concluded from previous studies (Billotti *et al.*, 2019; Smith *et al.*, 2019).

CHAPTER 2: REGIONAL THERMAL MATURITY MODELING OF HYDROCARBONS ALONG THE DEEP-WATER YUCATAN MARGIN, SOUTHERN GULF OF MEXICO

The following chapter has been reviewed as part of inclusion in a Geological Society of London Special Publication on The Geology and Hydrocarbon Potential of Mexico and the Northern Caribbean.

2.1 Introduction

2.1.1 Rationale for thermal maturity modeling

The Gulf of Mexico (GOM) has been surrounded by passive margins since the rifting and seafloor spreading ceased in the earliest Cretaceous (Pindell 1985; Marton and Buffler 1999; Pindell and Kennan 2009; Nguyen and Mann 2016) (Figure 2.1). The regional distribution of prolific, Tithonian-age source rocks is a crucial element for the GOM becoming one of the most productive hydrocarbon basins in the world (Weimer *et al.*, 2017).

Previous hydrocarbon exploration in the southern Gulf of Mexico has been focused mainly on the Salina del Bravo and Campeche salt basin, and along the frontier Yucatan margin, there have been no deep exploration wells drilled to date (CNH 2015) (Figs. 2.1, 2.2). As a result, the stratigraphy, structure, and hydrocarbon prospectivity of the margin remains less well-understood in comparison to other margins of the GOM, especially in the United States. Numerous oil slicks have been observed at the sea-surface along the length of the Yucatan margin and oil recovered from core samples, indicating the presence of at least one active

petroleum system in the area (Holguin-Quinones *et al.*, 2005; Saunders *et al.*, 2016). Despite the presence of these oil slicks, the maturity of potential source rock intervals, distribution of hydrocarbon kitchen areas, and the degree of uncertainty regarding maturation risk are not well characterized.

Three principal Mesozoic source rock intervals of varying quality can be defined in the southeast Gulf of Mexico from well penetrations located in the offshore Campeche salt basin and adjacent onshore areas (Guzman-Vega and Mello 1999; Santamaria-Orozco 2000; CNH 2015). Tithonian-age source rock is predicted to be regionally-present across the Campeche salt basin and is expected to extend northwards into the unexplored deep-water Yucatan margin (Watkins and Buffler 1996; Jacques and Clegg 2002; CNH 2015). Localized areas of Oxfordian and Cretaceous source facies found in the Campeche basin (Guzman-Vega and Mello 1999; CNH 2015) and the eastern GOM (Katz *et al.*, 1984; CNH 2015) could also be present at some locations along the Yucatan margin between these two areas.

In this paper, I evaluate possible thermal maturities for these three proposed Mesozoic source intervals in the western area of the deep-water Yucatan margin. Primary modelling was constrained based on the closest estimates of the structure and thermal properties of the underlying lithosphere and used to produce a best-estimate maturity model for the area. There is an absence of deep temperature and geochemical data available for model calibration in the deep-water Yucatan region; however, lithospheric thermal models have been shown to be useful for providing plausible tectonic and thermal models based on these constraints (Cunha *et al.*, 2018; Davison and Cunha, 2018). Due to the lack of data in the area, additional conceptual models were created by applying a range of reasonable geothermal gradients to the mapped

section, allowing the evaluation of alternate thermal maturity scenarios without incorporating the lithospheric thermal assumptions. From these model iterations, the degree of the sensitivity of thermal maturity to heat-flow can be determined, and source rock maturity risk across the area characterized.

Figure 2.1 Map showing the main structural and basinal provinces of the Gulf of Mexico and its onshore areas in eastern Mexico. The deep-water Yucatan margin is located along the northern continental margin of the Yucatan Peninsula and is bounded by the Yucatan Shelf to the south, the deep-water Campeche salt basin to the southwest, and the abyssal Gulf of Mexico to the north. Map information from Mexico compiled from Gray *et al.*, (2001); Garcia-Palomo *et al.*, (2004); Andreani *et al.*, (2008); Ferrari *et al.*, (2012); Yarbuh and Contreras (2017); Nguyen and Mann (2016); Sanford *et al.*, (2016).

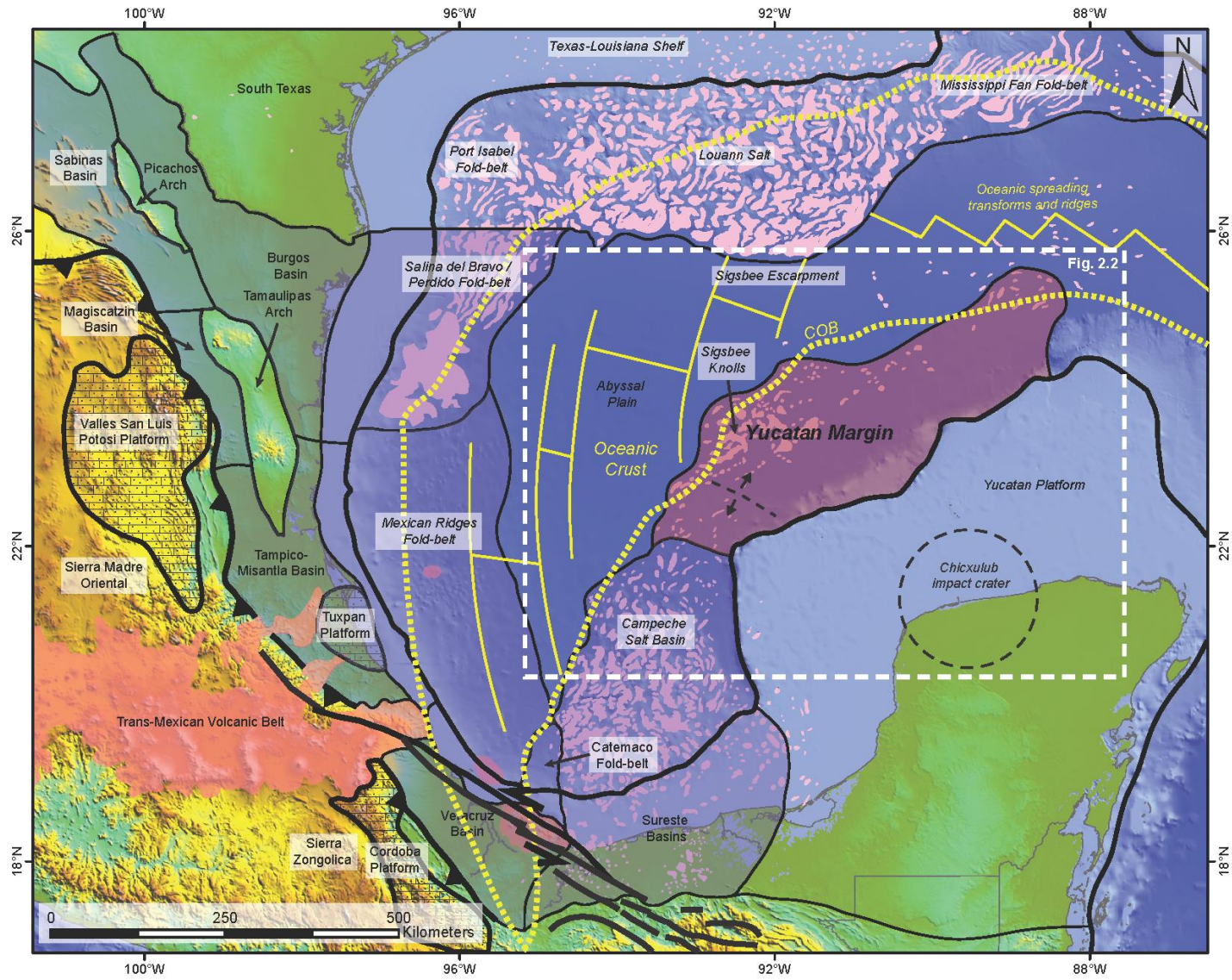
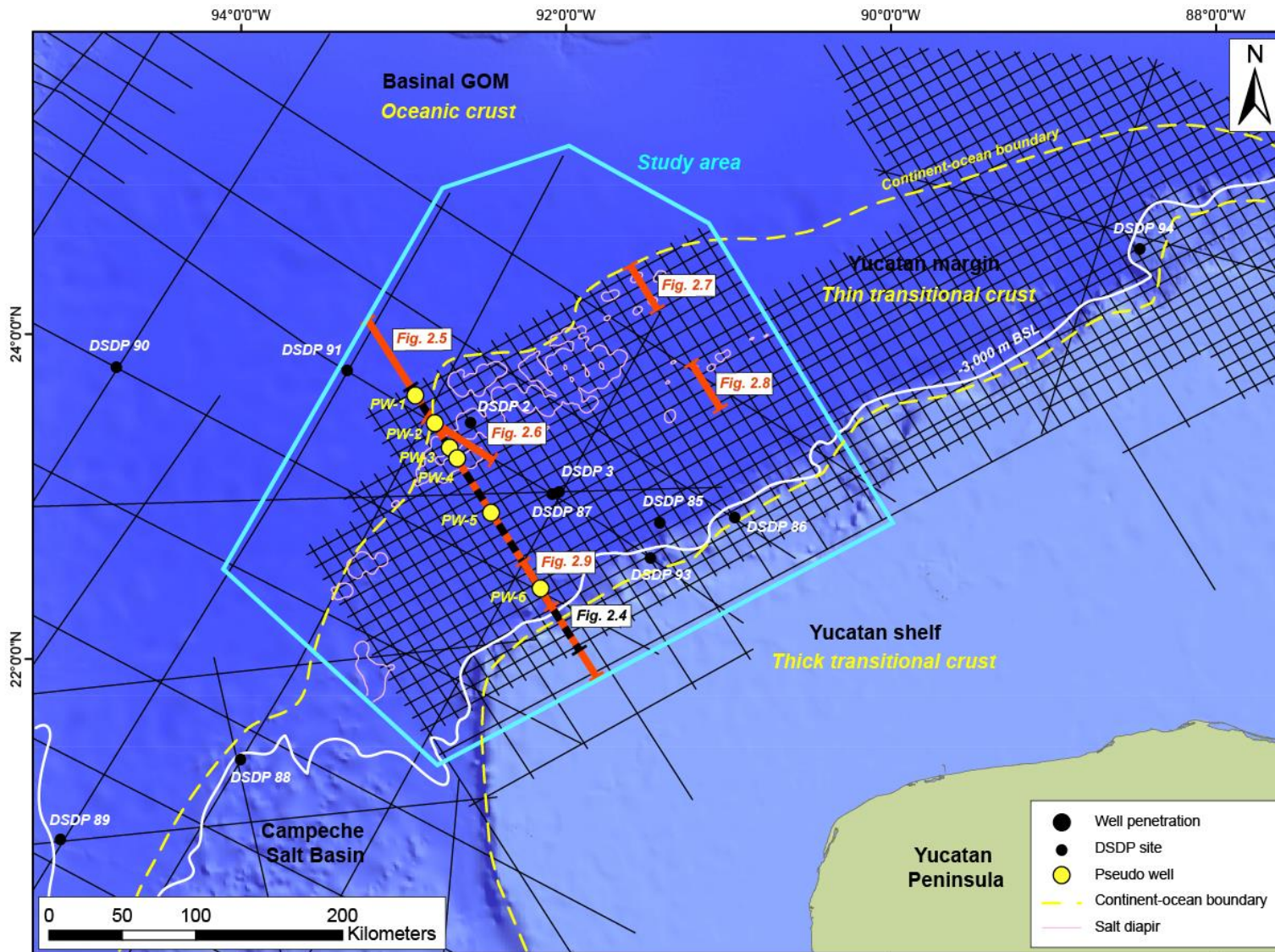


Figure 2.2 Map showing the extent of the 2D seismic dataset available in the area. The boxed study area represents the area of the dataset that was primarily interpreted for the results of this paper. The area the grid east of the boxed, study area was interpreted by Steier and Mann (2019). Most of the study area is located in water depths of $> 3,000$ m below sea-level, and significant parts of the study area lie above ocean crust. The pseudo well profile and limited well locations in the area are also highlighted in addition to locations of representative interpreted seismic sections. The local continent-ocean boundary has been defined based on gravity data from Sandwell *et al.*, (2014).



2.1.2 Evolution and tectonic history of the Gulf of Mexico

The deep-water margin area of the Yucatan peninsula is located in the southern Gulf of Mexico, situated outboard of the northern shelf-edge of the Yucatan carbonate platform and to the northeast of the offshore Campeche salt basin; forming the northern extension of the Isthmian salt basin (Hudec *et al.*, 2013) (Figure 2.1). The GOM basin began to form in the Triassic as a result of Phase 1, northwest-to-southeast orientated rifting between the North American, Yucatan, and South American continental terranes (Salvador 1987; Pindell 2010; Nguyen and Mann 2016; Lin *et al.*, 2019). Beginning in the Bajocian to earliest Oxfordian, widespread evaporites were deposited in a restricted basinal setting extending from eastern Mexico (Campeche salt) to southern Florida during the subsequent post-rift, thermal-sag phase (Pindell *et al.*, 2011; Pindell *et al.*, 2018; Pindell *et al.*, 2020). Infilling of the restricted, topographic sag basin with seawater likely occurred via the Balsas portal in central Mexico, allowing transmission from the Pacific Ocean (Salvador 1987, Rueda-Gaxiola 2009; Mann *et al.*, 2016). Ammonite assemblages in the Early Jurassic of onshore Mexico also suggest the possibility of an additional Tethyan seaway connection to the GOM (Cantu-Chapa *et al.*, 2001).

From the Late Jurassic, counter-clockwise rotation of the Yucatan continental block away from North America led to Phase 2 rifting and the onset of oceanic spreading, which separated the previously deposited salt basin into two parts (Pindell and Dewey 1982; Pindell *et al.*, 2016; Nguyen and Mann 2016; Lin *et al.*, 2019). By the end of the Early Cretaceous, seafloor spreading had ceased, and the Yucatan block reached its present-day position (Pindell 1985; Marton and Buffler 1999; Nguyen and Mann 2016). Following this time, the majority of

the GOM basin, including the Yucatan margin area, entered a passive margin phase, which has mostly continued to the present-day (Galloway 2008).

2.1.3 Geological setting of the Yucatan margin

Triassic to Middle Jurassic Phase 1 rifting of the GOM resulted in the development of an extensive system of steeply-dipping basement-involved normal faults underlying the deep-water Yucatan margin area, accompanied by deposition of a syn-rift to early post-rift, pre-salt, basinward-thickening sedimentary sequence (Rowan 2018). The lithology of this syn-rift section formed during Phase 1 rifting remains speculative, although some of the syn-rift units are expected to comprise continental red beds and localized volcanics deposited during continental break-up (Salvador 1987; Gomez *et al.*, 2018) (Figure 2.3).

Large-scale, northward, gravitational sliding occurred along the continental slope of the Yucatan margin following salt deposition in the Bajocian. Sediment loading and basinward tilting in the direction of newly-formed oceanic crust resulted in the down-dip translation of salt and rafted blocks of overlying late Mesozoic strata (Steier and Mann 2019; Hudec and Norton 2019) (Figure 2.3). Down-dip sliding continued until the end of the Cretaceous, forming a series of salt rollers and thick growth-wedges composed of Late Jurassic-Cretaceous sediments that thicken into the down-thrown side of listric, normal faults, which are present along the length of the Yucatan slope (Steier and Mann 2019). This unconfined seaward flow of salt and the overlying sedimentary cover is closely analogous to structures observed on the conjugate deep-water Florida margin in the north-eastern GOM; where overlying Norphlet

sandstones form productive hydrocarbon reservoirs (Pilcher *et al.*, 2014; Steier and Mann 2019; Hudec and Norton 2019).

An outer marginal trough, or “outer trough” (Hudec and Norton 2019), formed along the edge of the continental boundary as a result of necking of the underlying lithosphere during the latest stages of continental rifting, and immediately prior to the onset of adjacent seafloor spreading and oceanic crust formation (Pindell *et al.*, 2014; Pindell *et al.*, 2018; Rowan 2018). Greater thicknesses of salt were deposited within the outer marginal trough, and basinward tilting caused movement of salt from the slope into the depression from up-dip. Sediment loading of these thicker salt deposits resulted in large diapirs and pillow structures developing along the outer marginal trough, with salt movement continuing to the present-day (Steier and Mann 2019; Hudec and Norton 2019) (Figure 2.3).

Significant periods of the Late Jurassic and Cretaceous were characterized by marine carbonate deposition around the margins of the GOM, however lateral facies variability and phases of clastic dominated input did occur at various times throughout the basin (Salvador 1987; Galloway 2008; CNH 2015). The three principal Mesozoic source intervals in the GOM occur within the Upper Jurassic (Oxfordian), Uppermost Jurassic (Tithonian), and Cretaceous (Cenomanian-Turonian) and represent organic-rich mudstone intervals coinciding with episodes of marine transgression (Salvador 1987; Hood *et al.*, 2002) (Figure 2.3). The Cretaceous-Tertiary boundary represented a transition from predominantly carbonate to clastic deposition in the GOM and the onset of successive episodes of terrigenous clastic influx into the basin during the Cenozoic, mainly derived from the present-day areas of the western and central USA and Mexico (Galloway 2008). During this tectonically-quiet period, the deep-

water Yucatan Mesozoic strata were progressively buried by gradual deposition and onlap of the overlying Cenozoic clastic sequences (Steier and Mann 2019).

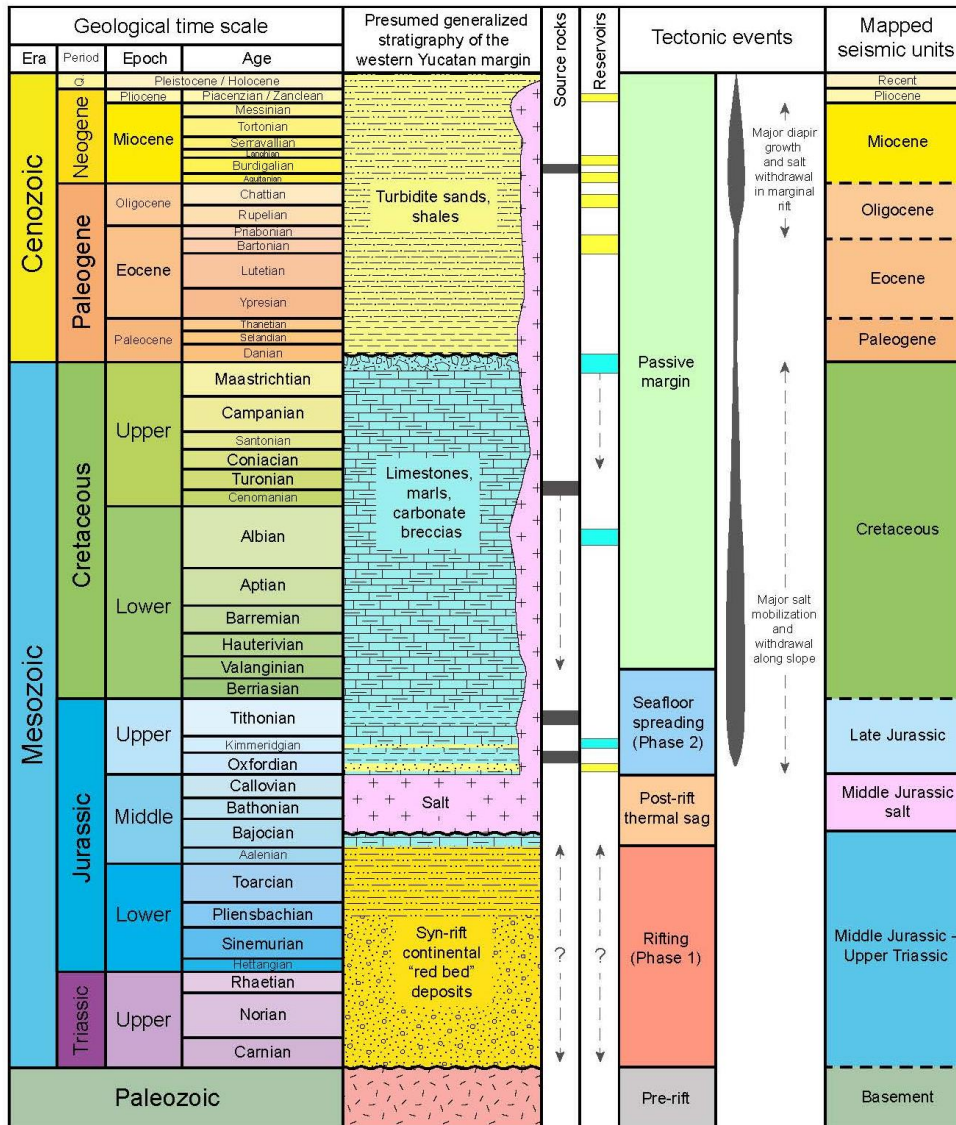


Figure 2.3 Chronostratigraphic chart summarizing the assumed lithology for the deep-water Yucatan margin. The main tectonic events are shown in addition to potential source rock and reservoir intervals. Ages for mapped seismic units are defined. Additional information used to create the chart was compiled from CNH (2015); Hudec and Norton (2019); Steier and Mann (2019).

2.2 Dataset and methodology

2.2.1 Seismic dataset and regional mapping

This study uses a grid of 2D, post-stack depth migration (PSDM), seismic reflection data covering an area of approximately 120,000 km² along the northern Yucatan margin, with an average line-spacing of 10 km (Figure 2.2). The seismic dataset spans the shelf, slope, and basinal areas of that range in water depth between -500 m to -3,800 m across the deep-water study area. Additional seismic profiles not part of the primary grid cross the abyssal GOM and allowed regional correlation with better-studied regions in the GOM. Unlike the US GOM, the Yucatan margin has no deep-water exploration wells of significant depth.

Seven publically-available DSDP wells are located within the study area. Of these DSDP wells, only four are located within the deep-water area, of which the deepest penetration terminates within Miocene strata. Stratigraphically older sequences penetrated by a number of DSDP wells on the Yucatan shelf cannot be easily correlated across the shelf-break into the deep-water area.

Due to the paucity of wells, this study relies upon interpreted seismic lines from previously published literature to approximate age horizons deeper than the Miocene. The regional seismic data were used to correlate approximate age horizons from other areas of the GOM across the structurally-undeformed abyssal plain. For the Paleogene section, approximate ages were correlated from the Perdido fold-belt of the northwestern Gulf of Mexico (Figure 2.1), based on the interpretation of Trudgill *et al.*, (1999) and regional mapping of Wilcox sequences by Snedden *et al.*, (2018). Regional correlation of approximate age horizons was also obtained from previous studies of the Mexican Ridges (Figure 2.1), where the passive margin fold-belt is known to detach above Middle Eocene shales (Salomon-Mora *et al.*, 2009).

Although age-constraints for the Paleogene sequence are approximate, any relatively minor uncertainties of age horizons would have fairly negligible effects on the modelled present-day thermal maturities of the underlying Mesozoic section; as maximum burial depth and maturity is at the present-day, and peak hydrocarbon generation and expulsion is predicted to have occurred relatively recently. The uppermost Cretaceous can be regionally correlated across the GOM and is straightforwardly characterized by its high-amplitude reflection character in a peak-trough-peak configuration (Sanford *et al.*, 2016). Additionally, the base of salt can also be readily identified where its basal detachment is defined by a high-amplitude peak, overlain by chaotic reflections representing salt and slumped sediments (Steier and Mann 2019). These seismic indicators allow confident depth constraint of the post-salt Mesozoic section underlying the Paleogene sequence.

Recent publications have proposed that salt was deposited in the GOM basin as early as Bajocian and as late as the Oxfordian in some areas (Pulham *et al.*, 2019, Pindell *et al.*, 2020). These age constraints can be applied to the top and base of the post-salt Mesozoic sequence within which the primary hydrocarbon source rock intervals are located. Other previous published seismic profiles across the Yucatan margin and nearby Campeche salt basin were also used as a general guide for age interpretations, such as Hudec *et al.*, (2013), Rodriguez (2011); CNH (2015), Gomez *et al.*, (2018), Hudec and Norton (2019).

2.2.2 Model setup and parameters

The ZetaWare Inc. 1D Genesis modelling package was used to model six pseudo-wells across a regional seismic transect of the deep-water Yucatan margin (Figure 2.4). An initial 1D modelling approach allowed the thermal history to be estimated using a range of parameters including the nature and thickness of continental crust and lithosphere, lithology and thermal properties of sediments, and source rock type.

The 1D model stratigraphy is based on the estimated ages of horizons interpreted along the seismic transect (Figure 2.4a). Lithologies from the deep-water Yucatan DSDP wells were used for the Miocene to Recent strata, and primary formation lithologies for the Paleogene and older section based on known gross stratigraphy from the nearby Campeche salt basin to the southwest (e.g. Ricoy-Paramo 2005, Cantu-Chapa 2009, CNH 2015) (Figure 2.4b). Average lithological proportions used for the Miocene to Recent section were 20% sand, 20% silt, and 60% shale, decreasing to 10% sand, 10% silt and 80% shale by the Paleocene (Figure 2.4b). The Cretaceous was assumed to be limestone (60%) and carbonate shale (40%) dominated, with a mixture of these and other lithologies in the Jurassic, including a small percentage of clastics (<20%). The Genesis default values were used for thermal conductivity and compaction parameters of formation lithologies used in the modelling. A normal hydrostatic pressure was assumed for the 1D models along the 2D transect (Figure 2.4). The models also take into account the timing of salt withdrawal and diapir growth where required.

A fixed temperature of 1330°C was assumed at the base lithosphere as a boundary condition for the modelling (Turcotte and Schubert 2002). Transient heat flow effects associated with rifting during the Triassic and Middle Jurassic do not appear to have a

significant impact on thermal maturities. The associated, rift-related thermal anomaly dissipated during the late Mesozoic period and Mesozoic sediments were not thick enough to generate hydrocarbons during this period - even at higher heat flows.

Surface temperatures were also varied through time and were seen to be primarily controlled by the water depths and the presence of shallow salt bodies. Present-day seafloor temperature in the western Gulf of Mexico was determined by Nagihara *et al.*, (1996) to average about 4°C in areas where no significant salt bodies are present in the subsurface. Water depths were assumed to have generally increased since the Middle Jurassic when massive salt deposition likely occurred in relatively shallow water depths (Hudec *et al.*, 2013; Steier and Mann 2019).

The modelled seismic section extends from oceanic crust in the northwest to thinned continental crust in the southeast (Figure 2.4a). At each pseudo-well location, the 1D model was set up for the corresponding basement type and accounted for the position of the continent-ocean boundary mapping from the marine gravity data of Sandwell *et al.*, (2014) (Figure 2.4a).

A deep, high-amplitude reflection on the Yucatan margin seismic data, inferred to be the Moho, provides an estimate for crustal thickness used for our maturity modelling (Figure 2.4a). Seismic refraction modelling of the conjugate Florida margin by Christeson *et al.*, (2014) suggests some similarity with our seismic observations and provides a good analogue for the Yucatan margin. We assume a thickness of about 8 km for the oceanic crust, and a thinned continental crust increasing from 8 km at the continent-ocean boundary to about 14 km at the Yucatan shelf-break (Table 2.1).

Total lithospheric thicknesses from Priestley *et al.*, (2018) were combined with our estimated crustal thicknesses to determine lithospheric mantle (mantle lid) thicknesses which were estimated to range between approximately 100 to 120 km (Table 2.1). Continental crust also has higher conductivity and higher radiogenic heat production compared to oceanic crust (Table 2.1) (Turcotte and Schubert 2002; Vilà *et al.*, 2010; Davison and Cunha, 2017). Crustal heat-flow differences are relevant for the modelled study area, which straddles the continent-ocean boundary and where significant areas of the basin floor overly oceanic crust (Figure 2.2).

1D pseudo-well models created in Genesis were imported into ZetaWare Inc.'s 3D Trinity modelling package where their formation tops were tied to regionally mapped structural isopachs. An average temperature curve was then fit to the imported Genesis pseudo-well modelled temperature curves. Temperature scalar maps were used to calculate the temperature at a surface through time and ensure the Trinity model honors the Genesis models. The average temperature curve was modified spatially using the scalars to match temperature curves at specific pseudo-well locations. Pseudo-well temperature curves were extrapolated along-strike for each tectonic domain based on predicted crustal properties.

In the models, the depth to uppermost salt and depth to uppermost Cretaceous mapped surfaces were used as approximations for the depths to Oxfordian and Cretaceous source rock intervals, respectively. Publicly-available formation temperature data from the Campeche salt basin were compared to simulated temperature profiles from the pseudo-well models (Magoon *et al.*, 2001; Waples *et al.*, 2004; and Ortuño *et al.*, 2009). Although this data is as far as 300-350 km away in an area with different burial history and crustal thickness, it represents some

of the closest available well data and is used as a broad guide to ensure our model results are reasonable.

A range of additional model scenarios was also performed by applying 'high-', 'mid-', and 'low-case', geothermal scenarios across the entire study area and without incorporating any lithospheric thermal assumptions from the 1D pseudo-well models. The model's temperature curves were fit to the average, and upper and lower ranges of formation temperature data from the Campeche salt province, and are close to 35°C/km, 30°C/km, and 25°C/km, respectively, through the shallower section. Risk index maps were created by combining the results of these three different model scenarios to assess maturity risk across the study area. Areas of the maturity map equal or above 0.6% vitrinite reflectivity and predicted to be oil mature were assigned a value of 'one,' and areas falling below this cut-off value as 'zero' were assumed to be thermally immature. Areas of the maturity map above 2.0% vitrinite reflectivity and predicted to be post-mature were also assigned a value of 'zero'. The maturity outcomes from the three possible thermal scenarios were summed for each source rock to provide a separate overall risk value for each interval.

Figure 2.4 a) Interpreted seismic section illustrating the primary mapped stratigraphic horizons across the study area that highlights the main structural trends and tectonic domains. Modeled pseudo well locations are also shown with the pseudo wells located to capture representative stratigraphic and crustal differences across the dip-length of the margin. **b)** Simplified stratigraphic sections and representative formation lithologies constructed for each pseudo well location and used to create 1D burial history models are shown.

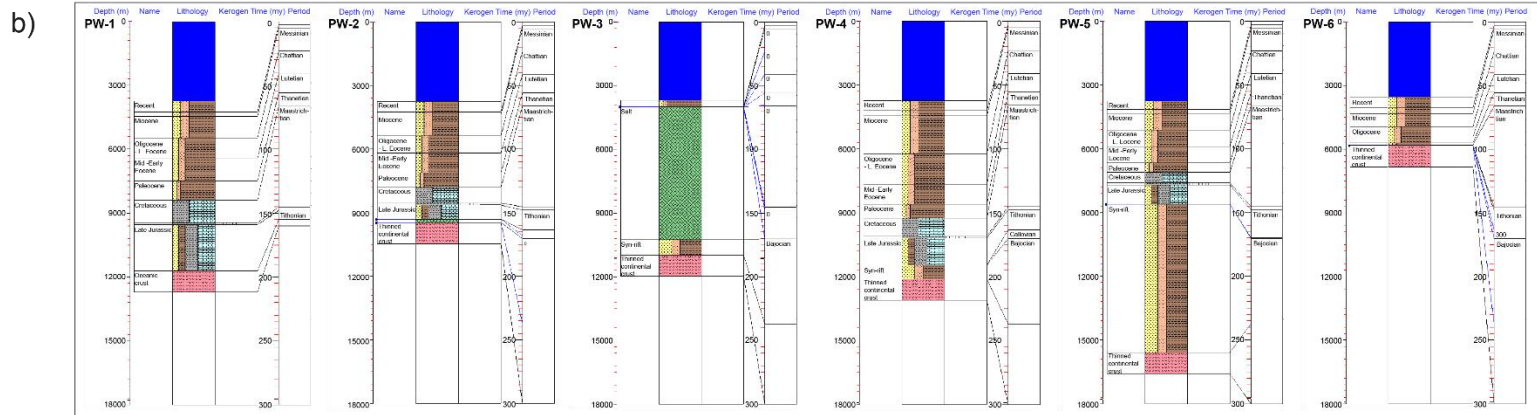
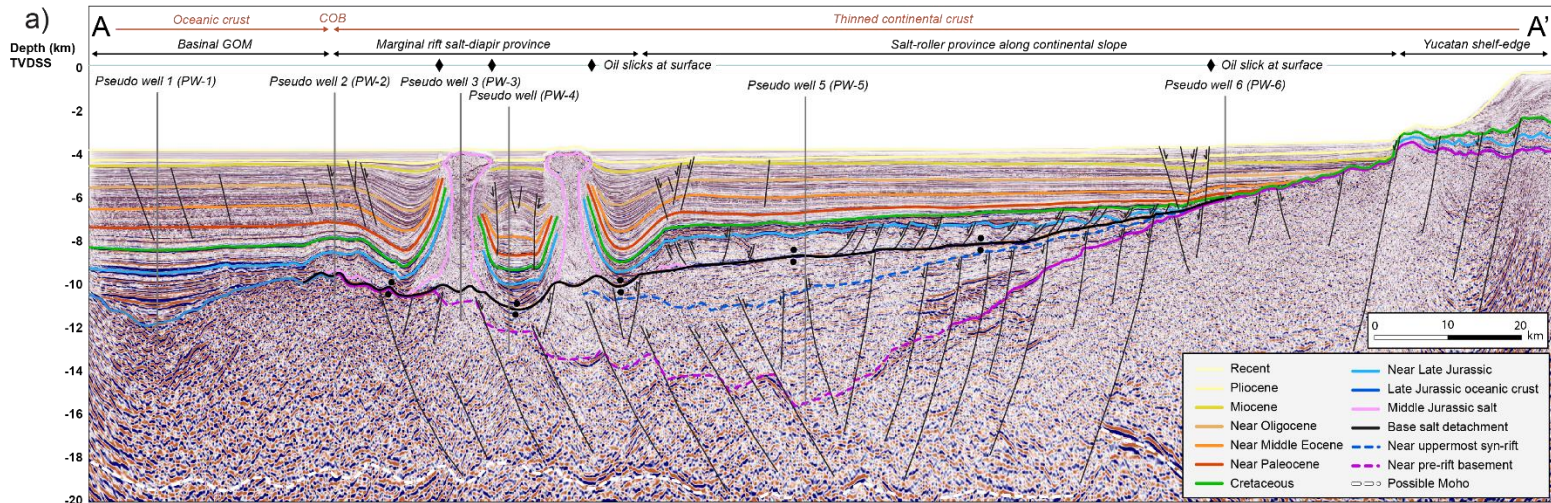


Figure 2.5 **a)** Annotated burial history restoration profile for the Oxfordian. **b)** Annotated burial history restoration profile for the Late Cretaceous. **c)** Annotated burial history profile for the Late Eocene. **d)** Annotated burial history profile for the Late Miocene. Location of the model profile is displayed in Figure 2.2.

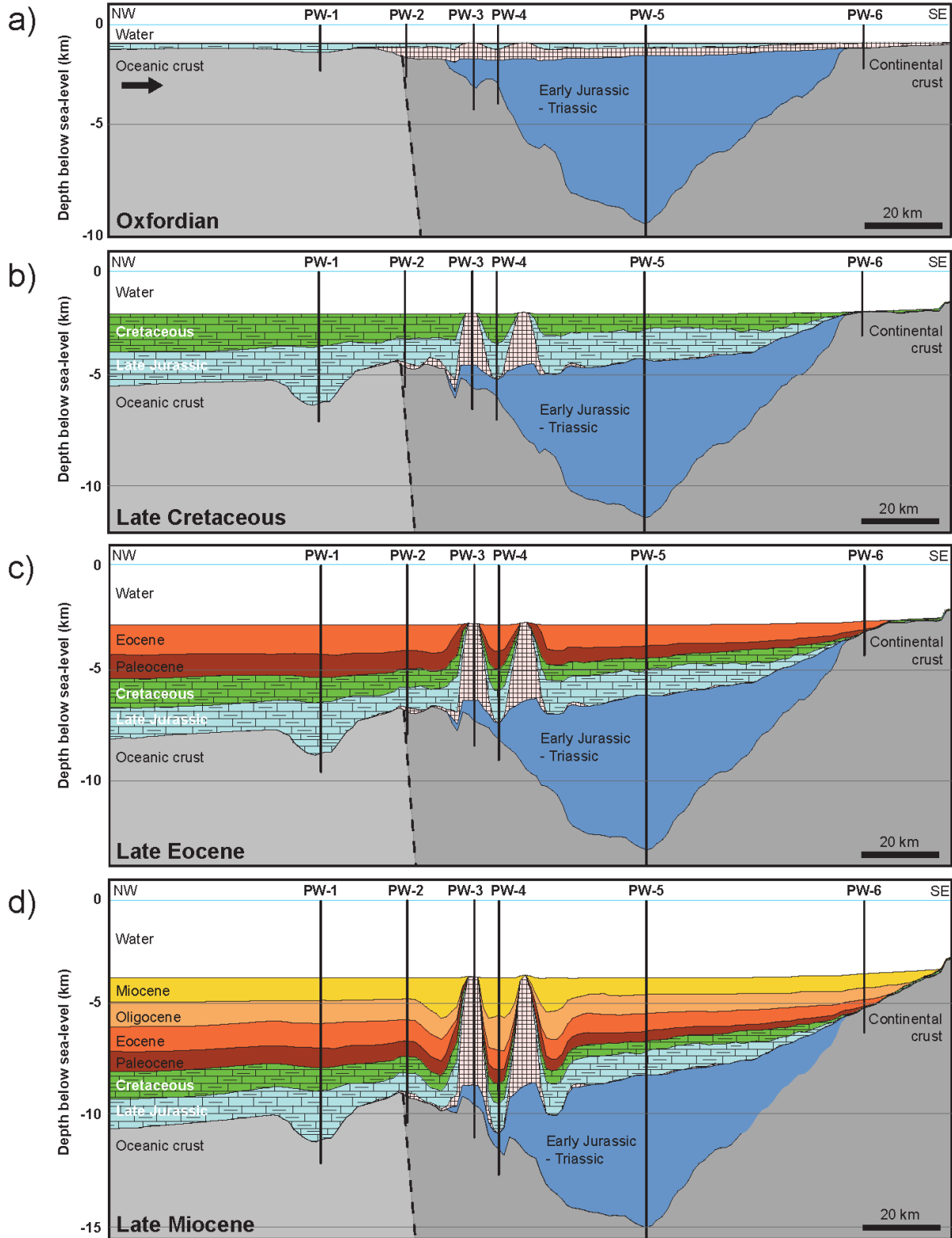


Table 2.1 *Lithospheric properties*

	Thickness (km)	Heat production (microW /m ³)	Thermal conductivity (W /m.K)	Density (kg/m ³)	Heat capacity (J /kg/K)
Thinned continental crust					
Upper crust	4-7	3	2.8	2700	900
Lower crust	4-7	0.5	2.5	2900	1050
Mantle lid	100-120	0.01	3	3400	1200
Mid-Jurassic oceanic crust					
Upper crust	4	0.3	2	2700	900
Lower crust	4	0.5	2.5	2900	1050
Mantle lid	100	0.01	3	3400	1200

Table 2.1 Table displaying values of thickness, heat production, thermal conductivity, density, and heat capacity for continental and oceanic lithosphere. Estimates correspond to upper and lower crust, and lithospheric mantle. Estimates of thickness are based on the seismic observations and gravity modeling of the conjugate Florida margin by Christeson *et al.*, (2014). Lithospheric properties were taken from Davison and Cunha (2017), after Turcotte and Schubert (2002) and Vilà *et al.*, (2010), and Priestley *et al.*, (2018).

2.2.3 Thermal conductivity of salt and timing of extrusion

Thermal conductivity of sediments differ by lithology and vary by depth as a result of temperature and compaction effects (Hantschel and Kauerauf 2009; Davison and Cunha 2017). Finite-element modelling of salt bodies by Mello *et al.*, (1995) illustrates that the salt presence can strongly influence the maturation of source rocks in the vicinity of a salt body. Although there is a lack of a thick salt layer across the present-day Yucatan margin, salt diapirs - especially the largest diapirs concentrated in the outer marginal trough - are capable of disrupting the isotherms around the localized salt bodies.

Salt thermal conductivity and movement is taken into account by both Genesis and Trinity modelling packages. For the 3D models, the salt movement was defined using Trinity's automated salt movement tool. Present-day salt volume was estimated based on regional mapping of present-day salt bodies and used to calculate an average initial salt thickness for the study area. Initial salt thickness was assumed to be zero at the up-dip limit of salt and increase in thickness slightly towards the continent-ocean boundary (Figure 2.5a). The salt movement tool attempts to conserve salt volume in 3D and relate the timing of salt movement to burial trends through time using our mapped structural isopachs.

Restoration and timing of salt withdrawal were made to match the timing of inflation in our 1D pseudo-well models, and are consistent with the timing of events from the structural restorations of Steier and Mann (2019). Salt withdrawal on the slope ended by the Late Cretaceous, whereas diapirs in the outer marginal trough would continue to develop until the present-day and deform the surrounding sediments as onlapping Cenozoic sequences progressively bury the margin (Figure 2.5) (Steier and Mann 2019).

Mudstone is generally less thermally conductive than both sandstone and limestones, but also produce more radiogenic heat, so the relative proportions of input lithology are likely to be a primary control for model sensitivity (Mello *et al.*, 1995; Hantschel and Kauerauf 2009). Our reliance on generalized analogue data below the Miocene, therefore, adds some uncertainty to our results.

2.2.4 Source-rock types

Oxfordian and Tithonian source rocks consist of calcareous shale intervals deposited in relatively deep-water anoxic environments (Ortuño *et al.*, 2009). These source rocks are probably deposited over much of the nearby Campeche salt basin and represent the most prolific source rocks in the region (Ortuño *et al.*, 2009; CNH 2015). Tithonian source rocks in the Campeche salt basin are of variable quality and can range from between 0.5 - 5% total organic carbon (TOC), and Oxfordian-Kimmeridgian source intervals between 0.5 - 3% TOC (Ortuño *et al.*, 2009).

Additional source potential is also found nearby in the Cretaceous, including both the Cenomanian-Turonian and Albian-Barremian intervals, reported from onshore southern Mexico and also the southeastern GOM (CNH, 2015). On the eastern margin of the deep-water Yucatan, DSDP Site 535 penetrated a thick section of Lower Cretaceous limestones and marls with oil-prone TOCs averaging 2-3%, but reaching as high as 11% (Katz 1984; Watkins and Buffler 1996). Nearby DSDP Site 540 also penetrated Cenomanian carbonate rocks with average TOCs of between 2-3% (Patton *et al.*, 1984).

Based on geochemistry data from the Campeche salt basin published by the Comisión Nacional de Hidrocarburos (2015), a mixture of type-II and type-IIS kerogens are expected for the Tithonian, with the Oxfordian and Cretaceous predominantly type-II kerogen. An initial TOC value of 4% was input for the Tithonian, with 3% for the Oxfordian and 2.5% for the Cretaceous. Hydrogen index (HI) values of 600 mg/g were applied for the Tithonian and Oxfordian and 550 mg/g for the Cretaceous intervals, respectively. An average thickness of 100 m was assumed for each Mesozoic source rock interval, based on ranges from CNH (2015).

Triassic-Early Jurassic lacustrine source intervals of limited potential have been encountered in analogous syn-rift deposits across the northern edge of the GOM basin (Watkins and Buffler 1996; Hood *et al.*, 2002; CNH 2015; Yallup 2019). Potential pre-salt source intervals have also been documented in the Tampico-Misantla basin of onshore Mexico (Rueda-Gaxiola 2009; Stabler and Gonzalez 2020); however, their presence in the offshore Yucatan margin pre-salt sequence remains unproven.

2.3 Structural and stratigraphic trends along the deep-water Yucatan margin

2.3.1 Characterization of the deep-water salt diapir structural province

Some of the largest salt-involved structures are present along the outer marginal trough and are located close to the continent-ocean boundary (Figure 2.4a). Locations of significant salt bodies are shown in Figure 2.2. The outer marginal trough feature is characterized by numerous normal faults that accommodate structural collapse in the pre-salt section (Figs. 2.6, 2.7). Based on seismic facies analysis, salt in the outer marginal trough appears to be directly underlain by basement consisting of either oceanic or thinned continental igneous crust,

characterized by chaotic, higher amplitude reflections. Parallel, semi-continuous reflections present immediately below the detachment may be clastic sediments (Figs. 2.4, 2.6, 2.7). Salt pillows are often present along the flanks of the outer marginal trough, along the base of the basinward-sloping salt detachment, and are extruded along the approximate continental-ocean boundary. Salt pillows usually accommodate significant thrust faulting and folding of the overlying Mesozoic carbonate strata. Numerous faults are also observed within the Cenozoic section, particularly above the underlying Mesozoic structures and minor salt bodies (Figs. 2.4, 2.6, 7).

Large salt diapirs up to approximately 7-8 km across are common and deform the surrounding sediments, forming adjacent salt minibasins (Figs. 2.4, 2.6). Sedimentary layers from the uppermost Jurassic through to the Pliocene are truncated and upturned along the flanks of the salt diapirs with both shallow and deep faulting observed along the diapir edges. There is also significant structural deformation and later inversion of the minibasins themselves (Figs. 2.6, 2.7). A degree of wedging of the minibasin strata is observed throughout the entire post-salt sequence; however, growth-strata is particularly prominent within the approximate Oligocene-Miocene sequences. Salt welds are present below most minibasins that flank the major salt bodies (Figs. 2.6, 2.7).

Towards the eastern end of the study area, there are fewer large diapirs present in the outer marginal trough; however, salt pillow structures continue to flank deeply buried minibasins along the edges of the outer marginal trough (Figure 2.7). Cenozoic sediment accumulations are shown to reach over 6 km thick in some of the deepest minibasins, in comparison to thicknesses of less than 3 or 4 km on the adjacent minibasin flanks (Figure 2.7).

Large-scale faulting can often penetrate the entire stratigraphic section to the seafloor, linking with primary underlying Mesozoic salt-related structures and mirroring pre-salt, rift-related structural trends (Figure 2.7).

2.3.2 Characterization of the up-dip salt-roller structural province

Up-dip from the outer marginal trough, the Yucatan slope is characterized primarily by an interval of salt-detached gravity sliding within the Mesozoic section (Figs. 2.4, 2.8). Salt rollers and accompanying listric extensional faulting are separated by thick, growth wedges of rafted Mesozoic sediments transported down-slope along a basal detachment. As a result of the variable thicknesses of growth strata, the near Late Jurassic horizon can only be inferred to be somewhere within this package in the thicker southeastern part of the study area up-dip (Figure 2.8).

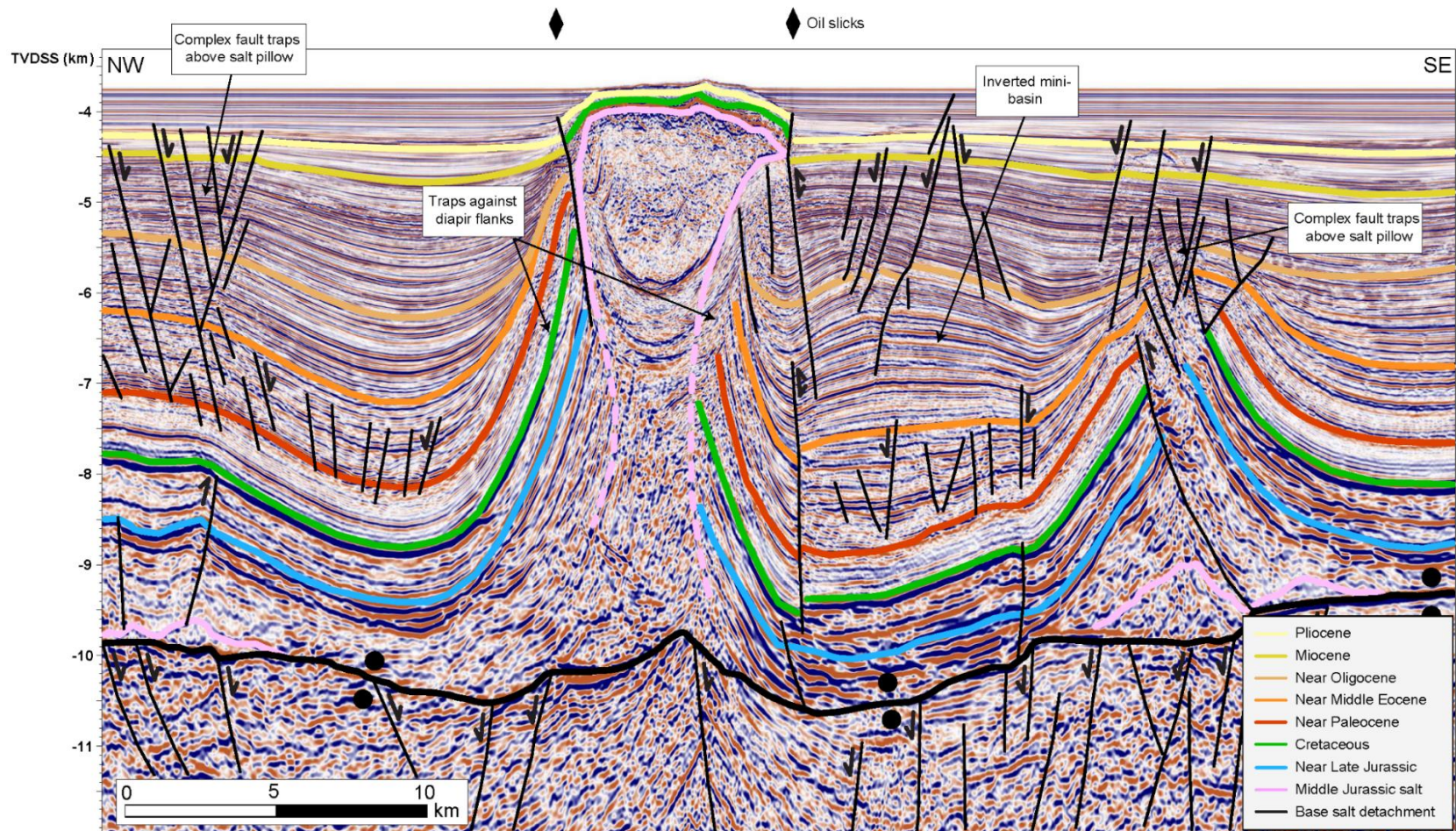
There is little salt remaining on the late Mesozoic slope where large parts of the detachment are welded and overlain by slumped, low-to-moderate amplitude reflector packages of uppermost Jurassic sediments. The late Mesozoic extensional system is capped by a regional unconformity marking the Cretaceous-Paleogene boundary and overlapped by younger Cenozoic sediments above (Figs. 2.3, 2.4). Major listric growth faults extend all the way up to the Cretaceous-Paleogene unconformity; however, the majority of extensional faulting terminates by the approximate top Jurassic (Figs. 2.4, 2.8). Numerous minor antithetic faults are observed to accommodate deformation within the late Mesozoic sediment growth wedges. Although salt rollers are more common, occasional salt pillows or small diapirs are present along the slope and often display progressive onlap of strata along their flanks through the Late Jurassic (Figure

2.8). Lenses of chaotic, high-amplitude seismic facies are occasionally observed along the uppermost Cretaceous unconformity of the Mesozoic-age slope (Figure 2.8).

Numerous basement-rooted normal faults are present in the syn-rift section below the sloping salt detachment. These faults characterize a series of horst and graben geometries that offset basinward thickening sequences of sub-parallel, continuous and semi-continuous reflections of variable amplitude (Figs. 2.4, 2.8). The majority of these deep faults terminate before reaching the base of salt detachment; however, some major faults do extend through the entire pre-salt sedimentary sequence (Figure 2.8).

Towards the western part of the study area, the Mesozoic sequence thins and pinches out against the underlying shelfal margin (Figure 2.9). A zone of normal faulting penetrates the entire Cenozoic section up to the seafloor and coincides with the up-dip limit of salt and its overlying Mesozoic strata. Cenozoic clastic sequences can be observed progressively onlapping the unconformity along the underlying Cretaceous-Paleogene boundary along the length of the slope. The Cenozoic faulting offsets mostly parallel, continuous reflections and occasional packages of low-amplitude chaotic facies assemblages representing debris flow units (Figure 2.9).

Figure 2.6 Interpreted seismic profile showing an example of the salt diapiric and minibasin structural province located in the marginal rift domain adjacent to the continent-ocean boundary in the deep-water western part of the study area. Salt diapirs and pillow structures form a variety of large trapping structures in the Mesozoic and additional associated structures in the overlying Cenozoic section.



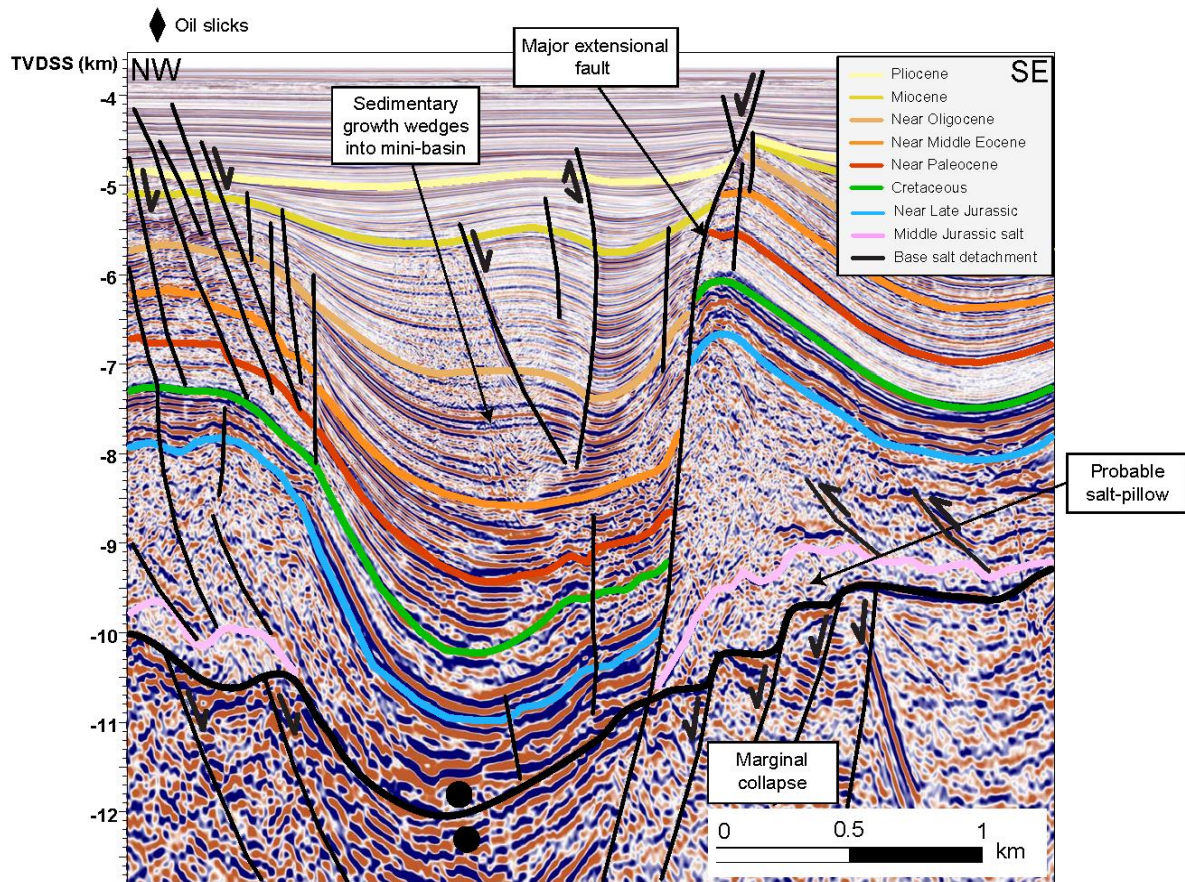


Figure 2.7 Interpreted seismic profile showing an example of the minibasin development and salt pillows along the flanks of the marginal rift domain adjacent to the continent-ocean boundary in the deep-water eastern part of the study area. Thicknesses of Cenozoic minibasins can exceed 6 km in burial depth.

Figure 2.8 Interpreted seismic profile showing an example of salt-roller structures located along the Mesozoic slope. Basinward gravitational movement of salt along a basal detachment during the late Jurassic and Cretaceous resulted in the formation of an extensive listric fault system and associated rafted growth sediments. Extensive underlying Triassic-Middle Jurassic normal faulting in the pre-salt section and associated sedimentary sequences are a result of rifting associated with the early opening of the Gulf of Mexico.

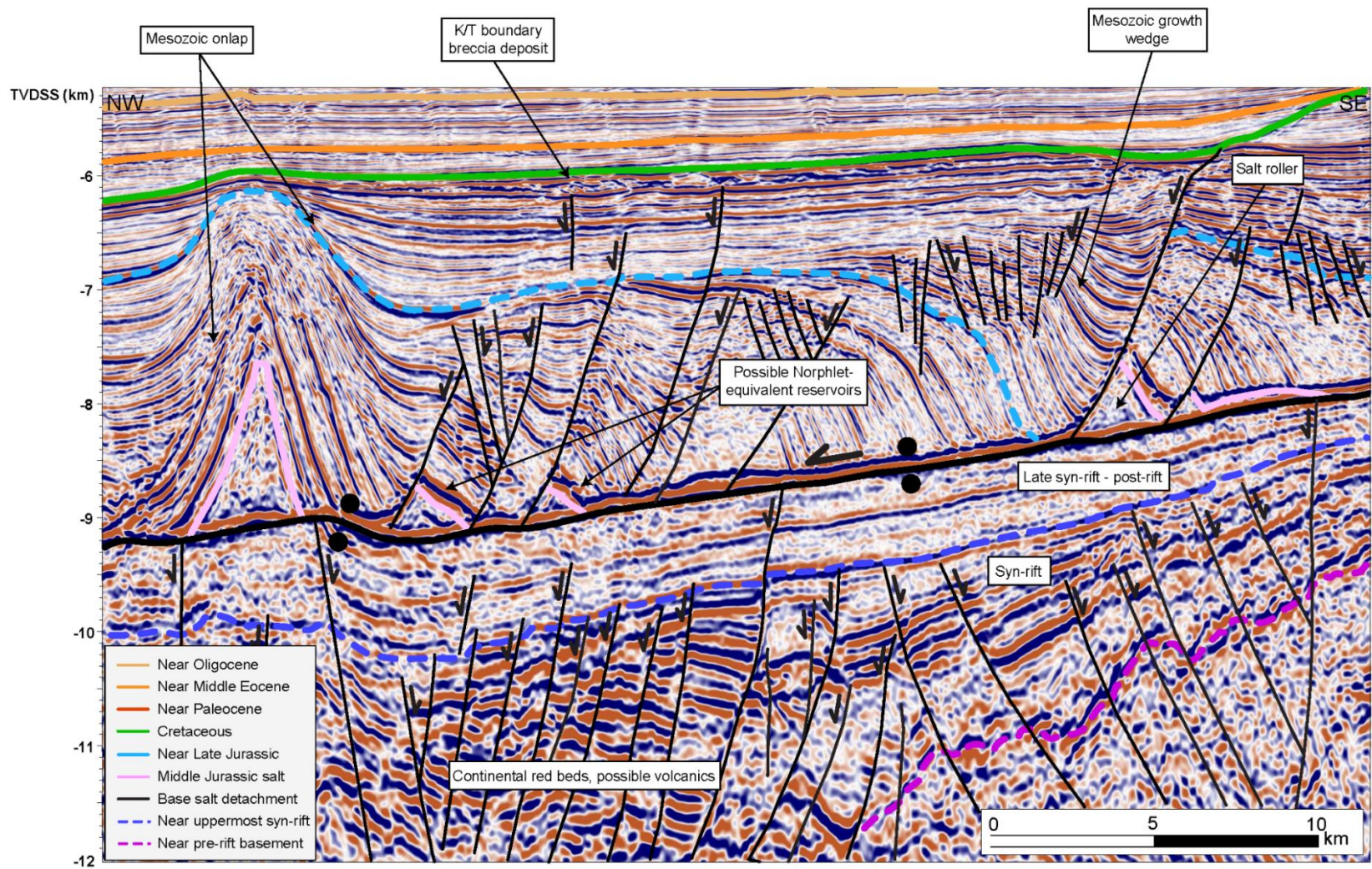


Figure 2.9 Interpreted seismic profile showing an example of normal faulting within the Cenozoic sequence and associated with the up-dip pinch-out of salt and thin-out of the overlying Mesozoic strata against the shelf margin. Faulting is likely the result of continued salt tectonics in the distal basinward domain or continued minor movement along the sloping salt detachment.

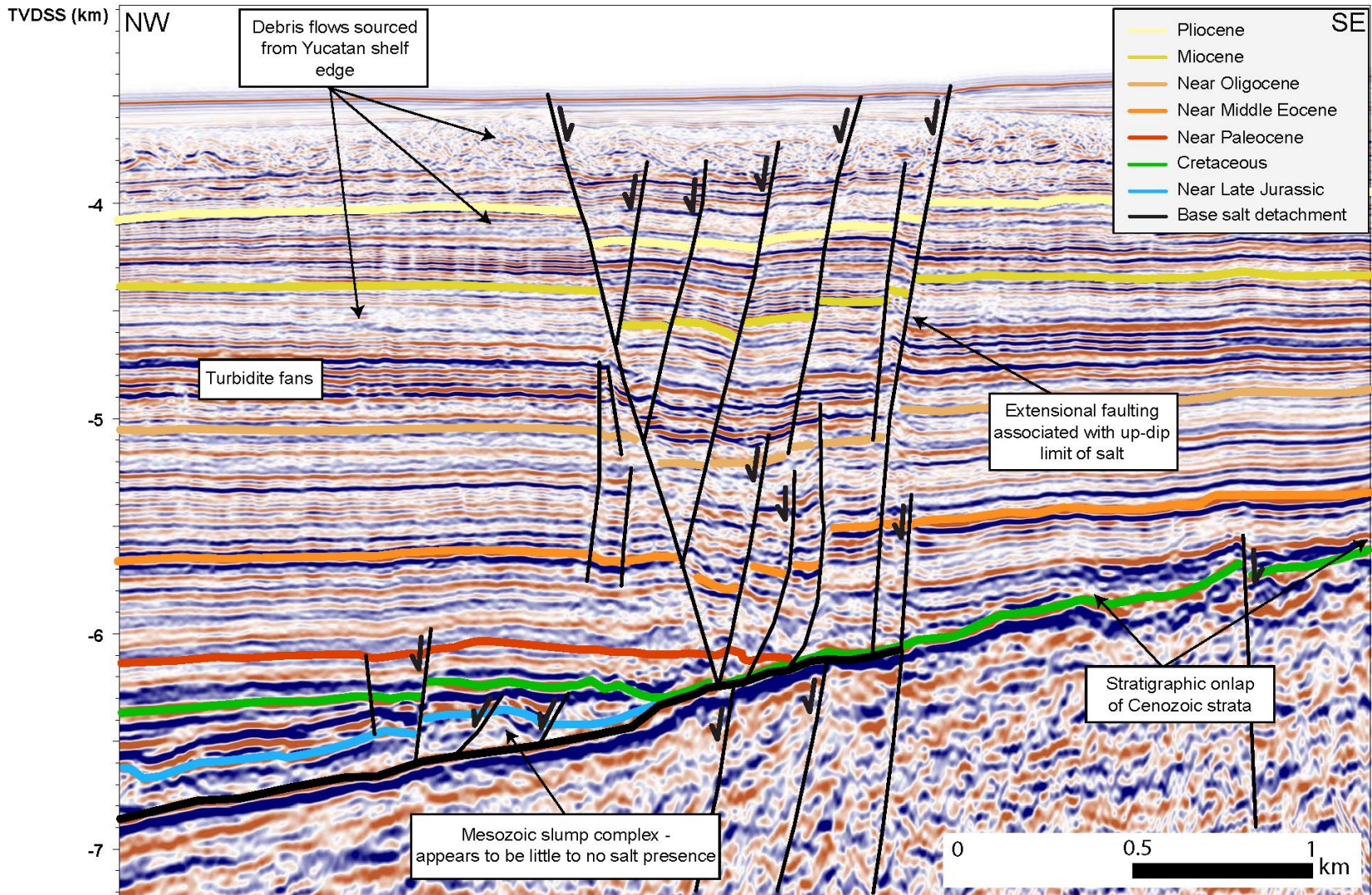
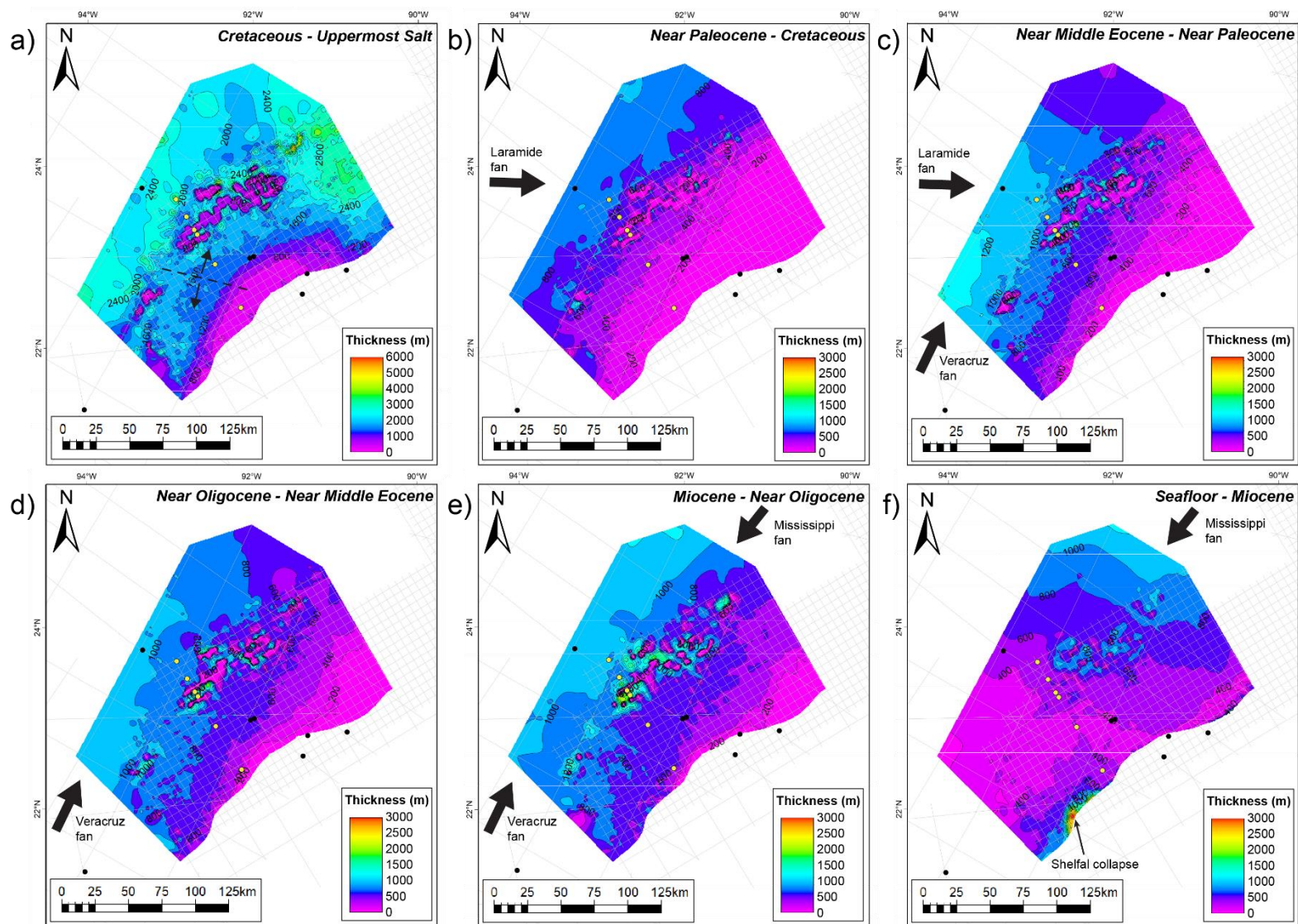


Figure 2.10 a) Isopach thickness map from the uppermost Cretaceous unconformity to uppermost Jurassic salt. b) Isopach thickness map from the near uppermost Paleocene to the uppermost Cretaceous unconformity. c) Isopach thickness map from near the uppermost Eocene to near the upmost Paleocene. d) Isopach thickness map from near the uppermost Oligocene to near the uppermost Eocene. e) Isopach thickness map from the uppermost Miocene to near the uppermost Oligocene. f) Isopach thickness map from the seafloor (recent) to uppermost Miocene.



2.3.3 Regional depositional trends along the western deep-water Yucatan margin

Regional-scale mapping of post-salt Mesozoic and Cenozoic sequences allow us to characterize the up-dip salt roller, diapiric, and basin floor structural provinces along the deep-water margin (Figure 2.10). The post-salt Mesozoic thins towards the southeast where it pinches out against the base of the Yucatan shelf-edge (Figure 2.10a). Approaching the northern edge of the Campeche salt basin in the southwestern part of the study area, the post-salt Mesozoic thins across a structural nose that separates the two subbasins. The Mesozoic sequence ranges from approximately 0 – 2000 m thickness along the slope at this location; however, it gradually thickens towards the east where a more substantial Mesozoic growth package of up to approximately 3000 m thickness characterizes the up-dip salt-roller domain (Figure 2.10a).

Regionally, Paleogene sequences can be observed thinning from the west to east across the study area until they thin out and onlap the margin and produce deeper burial of the underlying Mesozoic section in the westernmost part of the margin. In this area, the Paleocene, Eocene, and Oligocene intervals can each reach over 1000 m in thickness (Figs. 2.10b, 2.10c, 2.10d). In the Miocene, regional thickness trends become more evenly distributed from northeast-to-southwest; however, somewhat thicker deposition still occurs towards the west where sediment thicknesses of over 800 m characterize the slope of the northern edge of the Campeche salt basin (Figure 2.10e).

A significant shift in the depositional axis becomes apparent within the Miocene to Recent sequence, with the most abundant sedimentation occurring in the deep-water area to the northeast and thinning onto the margin towards the southwest (Figure 2.10f). An area of thick

sediments near the Yucatan shelf margin to the southwest represents a relatively recent collapse of the shelf-edge.

Locally, sediments are very thin above the large, active, salt diapirs, and thicken substantially in the adjacent minibasins in a common pattern that is observed throughout the post-salt sequence (Figure 2.10). As indicated on the seismic profiles, minibasin growth and sedimentation are most significant during the Oligocene and Miocene and locally, maximum sediment thicknesses can reach over 2000 m for both intervals (Figs. 2.10d, 2.10e).

2.4 Burial history and thermal modeling of the deep-water Yucatan margin

2.4.1 Constraint of 1D model thermal maturities using lithospheric properties

At each pseudo-well location (PW-1 – PW-6), a 1D model was set up for the corresponding basement type (oceanic versus thinned continental crust) (Figure 2.4). Appropriate crustal thicknesses and heat-flow values were assigned before burial, and thermal histories were modelled. An example of one of the pseudo-well burial history results (PW-4) is illustrated in Figure 2.11.

The location of PW-4 corresponds to a thick section of Cenozoic overburden (approximately 5.5 km) and is positioned in one of the deepest minibasins along the margin (Figure 2.4a). At the PW-4 location, the Cretaceous and Tithonian intervals are projected to be in the main oil window and the Oxfordian in the condensate window at present-day (Figs. 2.11a, 2.11b). All three source intervals are not yet fully exhausted based on their modelled transformation ratios (Figure 2.11a). However, for the principal Tithonian source interval, peak generation is predicted to have occurred during the Oligocene-Miocene, with initial generation

as early as the Eocene (Figure 11c). Oil and gas expulsion is predicted to have occurred from the Oligocene onwards at this location, with a little predicted gas generation relative to oil (Figure 2.11d).

All six calculated pseudo-well geotherms lie in the cooler part of the Campeche temperature measurements (Figure 2.12). The deep-water Yucatan pseudo-wells are located above oceanic crust or very thin continental crust. In contrast, the Campeche temperature data is from wells more proximally located above thicker continental crust (Figure 2.12). Oceanic crust typically generates much lower radiogenic heat compared to continental crust, with greater thicknesses of continental crust usually generating higher heat-flows (Table 2.1) (Nagihara *et al.*, 2005).

Figure 2.11 Example of a pseudo well (PW-4) showing the burial and thermal history modeling that was carried out on each pseudo well. **a)** Burial history and predicted maturity of late Cretaceous, Tithonian, and Oxfordian potential source horizons. Blue annotations state the predicted transformation ratio as a percentage of transformed kerogen at various stages of burial. The model predicts an oil window maturity for the principal Tithonian source rock from the Oligocene to recent. **b)** Modeled vitrinite reflectivity curve versus depth, highlighting the present-day maturity of the three potential Mesozoic source intervals. **c)** Predicted oil and gas generation rates through time for the principal Tithonian source rock. Oil generation began in the Eocene and peaked in the Oligo-Miocene. **d)** Cumulative oil and gas expulsion curves for the principal Tithonian source rock. Oil and gas expulsion is predicted to continue to the present-day.

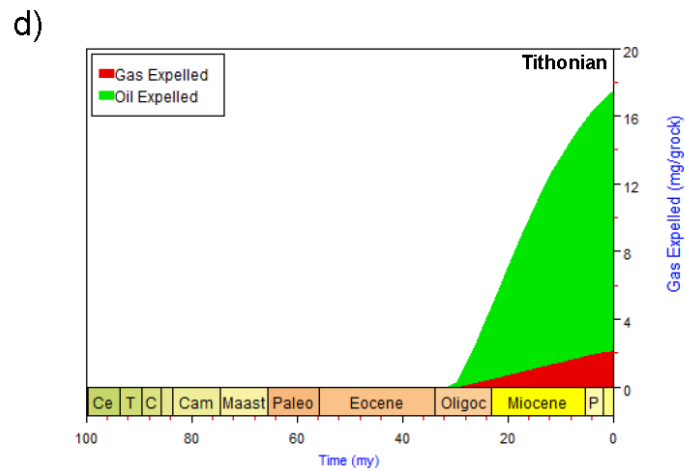
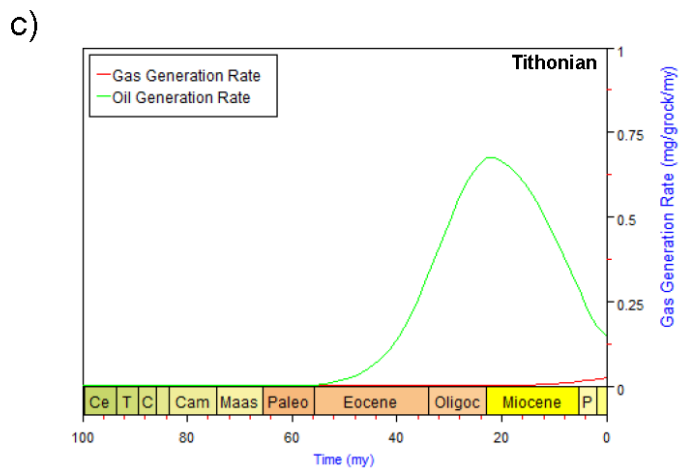
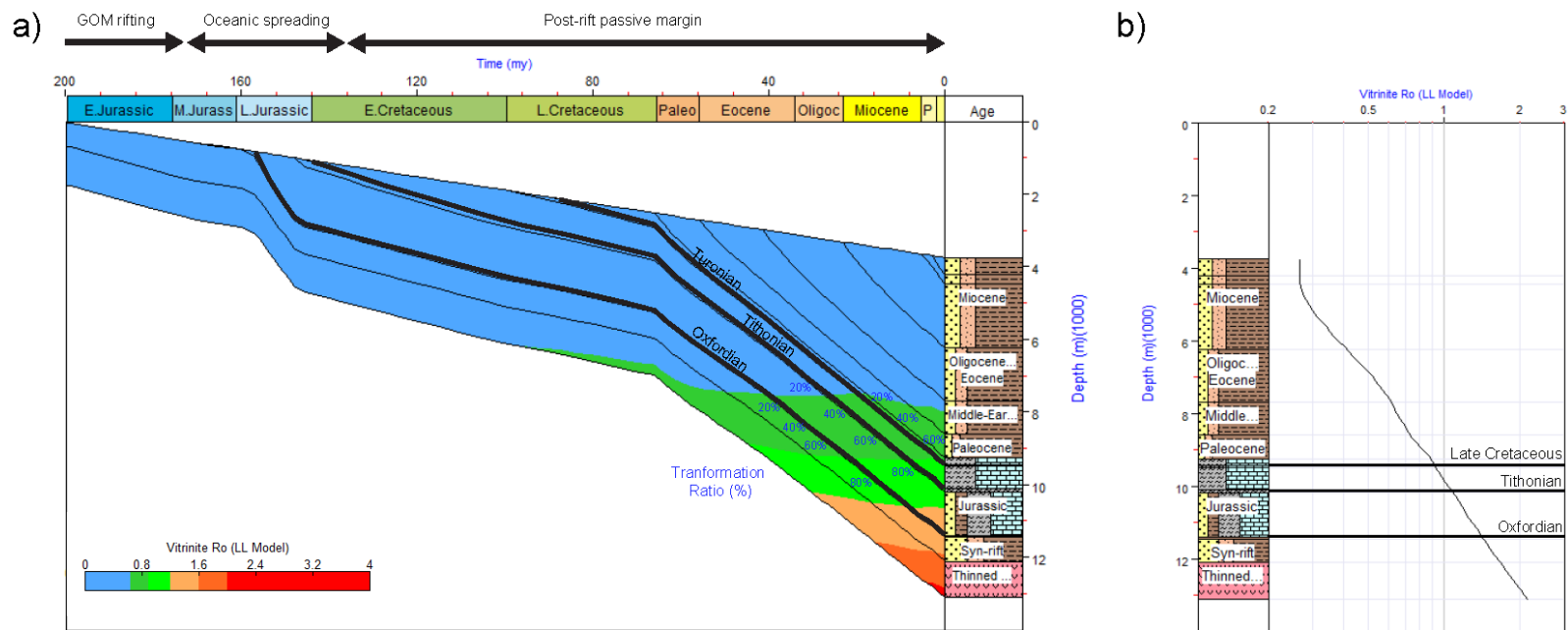
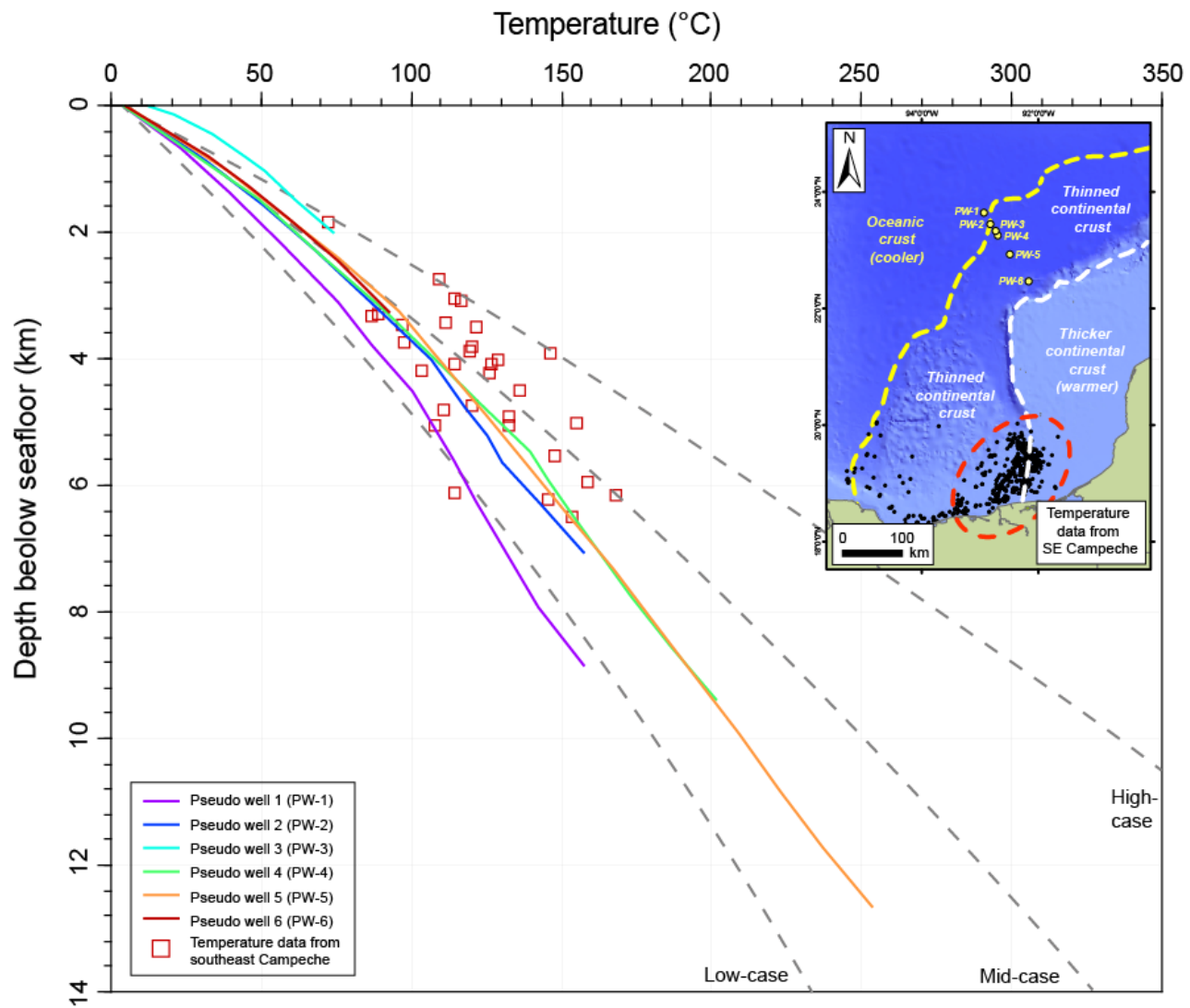


Figure 2.12 Temperature-depth graph showing modeled geothermal gradients from all six pseudo well 1D models plotted with measured formation temperature data from wells located in Cantarell area in the southeastern part of the Campeche salt basin >300 km to the south of the study area. Modeled pseudo well geotherms based on the lithospheric heat-flow model fit within the range of Campeche basin temperature data and fall within the low end of the data range. If the Yucatan margin is, in fact, cooler than this part of the Campeche basin as suggested, this could be explained by the presence of thinner stretched continental crust and oceanic crust in the Yucatan margin study area. Thinner crust would generate less radiogenic heat, especially beneath the deeper, cold, overlying water column, and because of differences in burial timing and thickness in the two areas. Measured temperature data from Magoon *et al.*, (2001); Waples *et al.*, (2004); Ortuño *et al.*, (2009). The continent-ocean boundary is inferred from Sandwell *et al.*, (2014) satellite gravity data.



2.4.2 Regional maturity trends predicted by lithospheric thermal modeling

Integrating the 1D pseudo-well models with regional structure grids allows their modelled geothermal gradients to be matched at model locations and extrapolated laterally in two dimensions. Maps of modelled vitrinite reflectivity tied to the pseudo-well results were created for the Oxfordian, Tithonian, and Cretaceous intervals (Figure 2.13). LLNL (Lawrence Livermore National Laboratory) vitrinite kinetics were used for maturity modelling.

The Oxfordian is today predicted to be mature for oil over the basin floor, outer marginal trough, and lower to middle Mesozoic slope areas, even reaching the gas-condensate window in most of the deeply-buried salt minibasins (Figure 2.13a). For the approximate Tithonian interval, the minibasins are predicted to be mostly oil mature but approach the condensate window at some locations where burial depth is sufficient (Figure 2.13b). Towards the western part of the study area into the Campeche subbasin, the entire slope is predicted to be oil mature for the Tithonian. However, more extensive areas of the Mesozoic slope are likely immature towards the east where only the outer marginal trough and lower slope are estimated to enter the oil window. Along the continent-ocean boundary, areas overlying colder, oceanic crust less deeply buried by basin-floor sediments are anticipated to be less thermally mature as a result (Figure 2.13b). The preferred lithospheric thermal model also predicts the Cretaceous to be within the oil window, although these areas are restricted primarily to the minibasins and southwestern slope (Figure 2.13c).

Schematic model sections with estimated maturity contours characterize the variability of stratigraphy, structure, and thermal maturity from east-to-west (Figure 2.14). To the east, a substantially thicker Mesozoic salt-roller growth section and thinner overlying Cenozoic cover

result in large areas of the upper Mesozoic slope being immature (Figure 2.14a). A lack of significant salt bodies in the outer marginal trough domain results in salt having a negligible impact on maturity in the east of the study area. In the western part of the study area where many salt diapirs are present, the effects of salt thermal conductivity can be observed where maturity contours are displaced either positively or negatively by the salt bodies (Figure 2.14b, 2.14c). Speculative deep source intervals that could exist in the syn-rift section are predicted to be of marginally lower maturity immediately below the base of a salt diapir compared to the surrounding sediments. However, any pre-salt sedimentary deposits are either very thin or absent below the outer marginal trough.

Overall, the syn-rift clastic sequence underlying the salt detachment is anticipated to range from the late oil window to overmature along-strike, with the majority of the section positioned within the gas and post-gas windows (Figure 2.14). Model results suggest the syn-rift section may have begun generating hydrocarbons between the middle-Cretaceous to Paleocene depending on burial depth, before the formation of overlying Cenozoic, and some late Mesozoic-age salt-controlled structures.

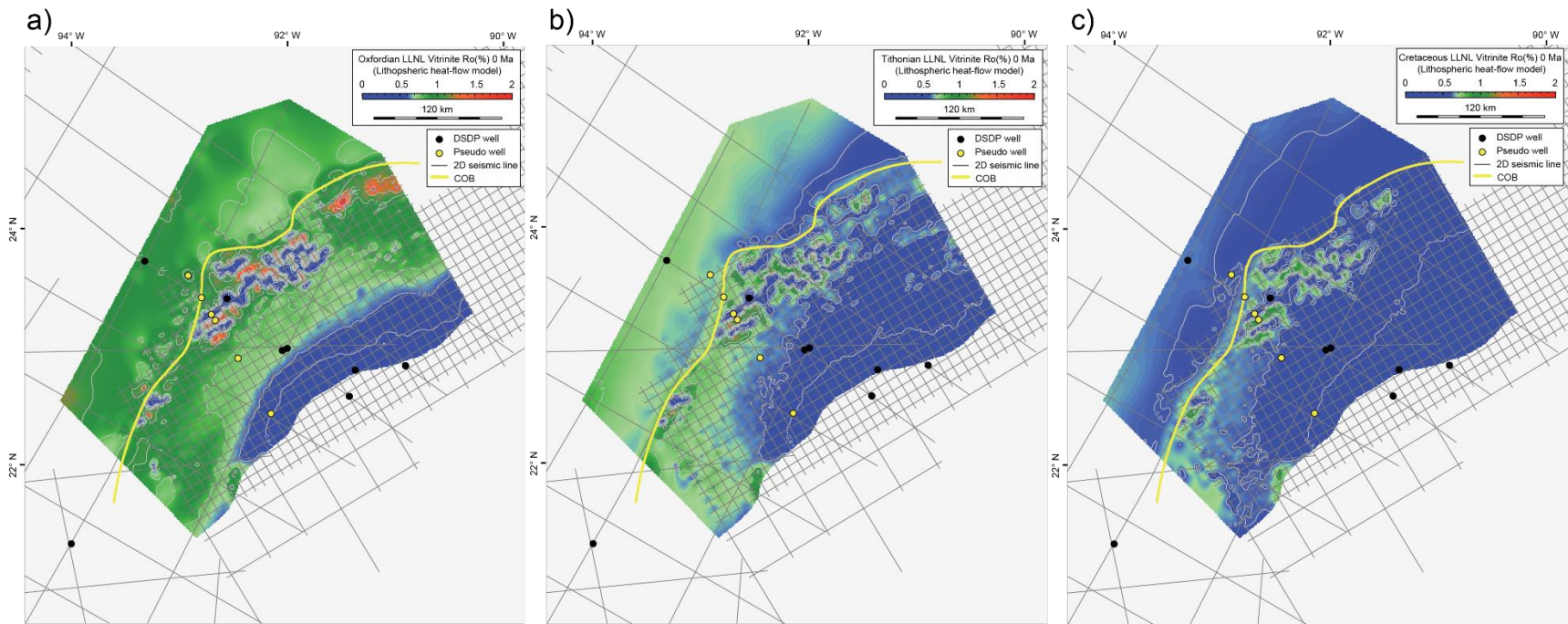
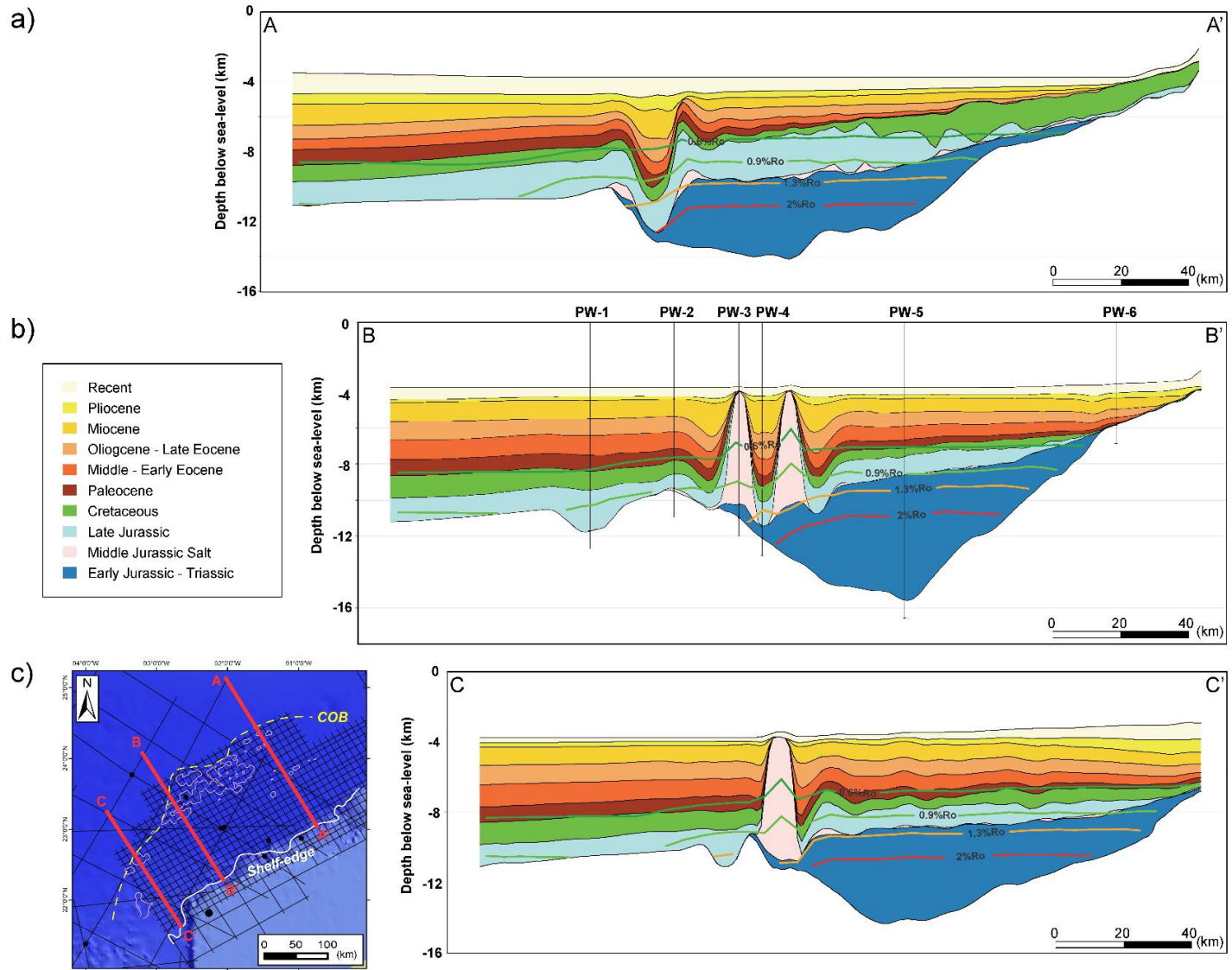


Figure 2.13 Generated maps of predicted thermal maturity based on regional burial and thermal histories modeled using an estimated lithospheric heat-flow model. **a)** Map of modeled vitrinite reflectivity (%) for the Oxfordian source interval (approximated with uppermost salt structure map). **b)** Map of modeled vitrinite reflectivity (%) for the Tithonian source interval (approximated with the near uppermost Jurassic structure map). **c)** Map of modeled vitrinite reflectivity for the Cretaceous source intervals (approximated with uppermost Cretaceous structure map). The continent-ocean boundary is inferred from Sandwell *et al.*, (2014) satellite gravity data.

Figure 2.14 Model cross-sectional profiles showing modeled thermal maturities in terms of vitrinite reflectivity (%) across the deep-water Yucatan margin from the lithospheric heat-flow model. **a)** Profile through the eastern part of the study area. **b)** Profile through the central part of the study area, with pseudo well locations that were used for 3D model calibration. **c)** Profile through the western part of the study area near the boundary with the Campeche salt basin.



2.4.3 Application of alternate thermal scenarios to characterize uncertainty

Additional thermal maturity scenarios were modelled without assumptions regarding lithospheric thermal properties and therefore unconstrained by the 1D pseudo-well models. Given the lack of data, these scenarios offer a simple alternative approach to help define the degree of variability of thermal maturities that could exist under a reasonable range of thermal regimes and present a way to characterize maturity risk across the study area resulting from uncertainty (Figure 2.11).

In the ‘low-case’ thermal model, the Oxfordian is still predicted to occupy the oil window over significant areas of the outer marginal trough and lower part of the Mesozoic slope. Deep minibasins and parts of the basin floor could also reach the gas window in this scenario (Figure 2.15a). If a ‘mid-case’ geothermal gradient exists across the area, the Oxfordian is predicted to be in the gas and condensate windows over most of the basin floor and outer marginal trough (Figure 2.15b). Increasing the thermal gradient to the ‘high-case’ would result in the entire deep-water basin floor and outer marginal trough occupying the gas window and a smaller area along the middle Mesozoic slope being oil mature (Figure 2.15c). All three model scenarios predict oil and gas maturity within the outer marginal trough domain and minibasins and suggest that the upper slope along the southeastern part of the study area is consistently immature for hydrocarbon generation (Figure 2.15).

When the ‘low-case’ thermal gradient is applied across the area, the Tithonian is anticipated to reach the main oil window. However, thermal maturation would occur only in the deeper areas of the minibasins and the outer marginal trough (Figure 2.16a). The ‘mid-case’ scenario suggests more significant areas of the outer marginal trough would be oil mature for

the Tithonian with deeper areas of the abyssal plain and some minibasins entering the gas-condensate phase (Figure 2.16b). The 'high-case' scenario predicts gas maturity in the minibasins and across the basin floor and oil maturity over most of the salt-roller province along the slope (Figure 16c). Similar to the Oxfordian interval, the Tithonian along the upper part of the slope in the southeastern part of the study area is anticipated to remain immature under both high- and low-temperature scenarios (Figure 2.16).

Regarding thermal maturity for the Cretaceous interval, the early oil window is still attained under a 'low-case' thermal scenario; however, this is restricted to the deeply buried minibasins, and most of the deep-water margin is likely immature (Figure 2.17a). With higher temperature gradients in the modelled 'mid-case' and 'high-case', most minibasins, and moderate-size areas of the outer marginal trough are predicted to be either oil-mature or oil-mature with localized areas of gas-condensate maturity (Figs. 2.17b, 2.17c). Substantial areas of the upper and middle slope are predicted to remain thermally immature for the Cretaceous interval under all three model scenarios (Figure 2.17).

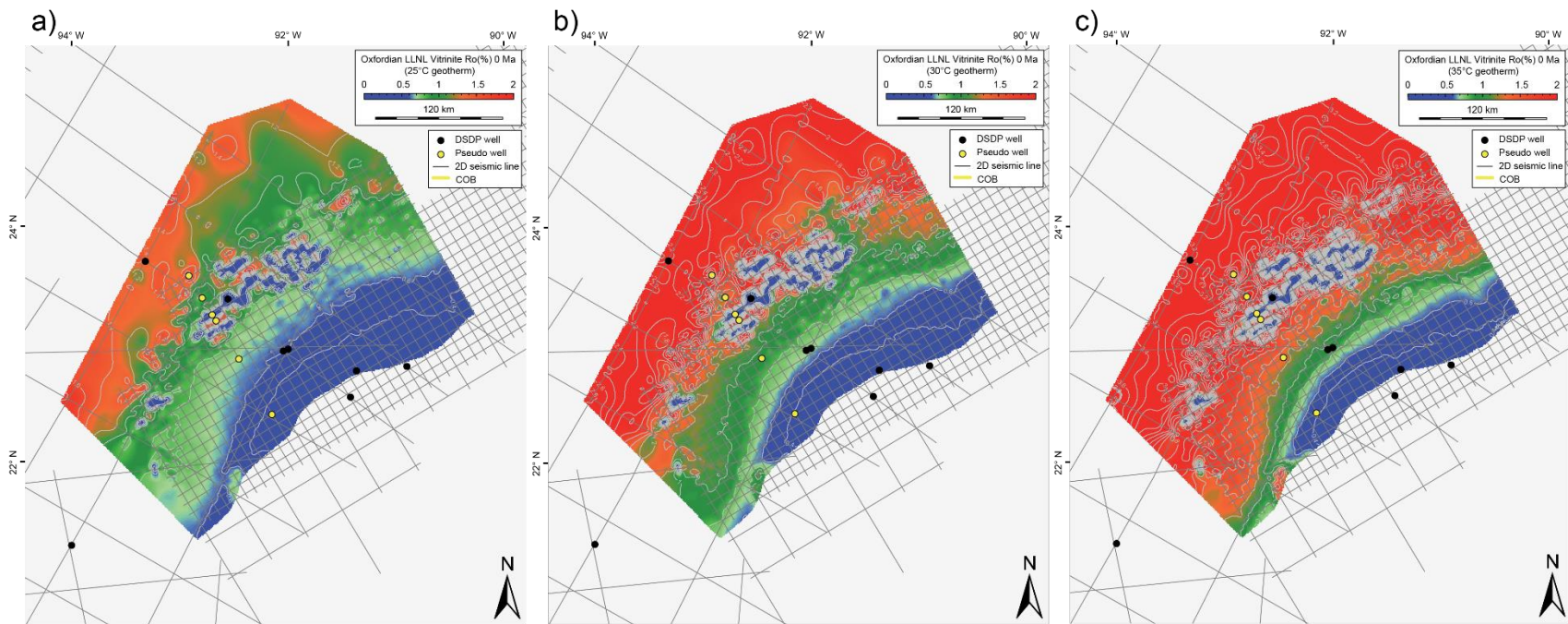


Figure 2.15 Generated maps of predicted Oxfordian source rock thermal maturity based on regional burial and thermal histories modeled using for three different heat flow scenarios. **a)** Map of Oxfordian source rock modeled vitrinite reflectivity (%) for the low-case thermal scenario. **b)** Map of Oxfordian source rock modeled vitrinite reflectivity (%) for the mid-case thermal scenario. **c)** Map of Oxfordian source rock modeled vitrinite reflectivity (%) for the high-case thermal scenario.

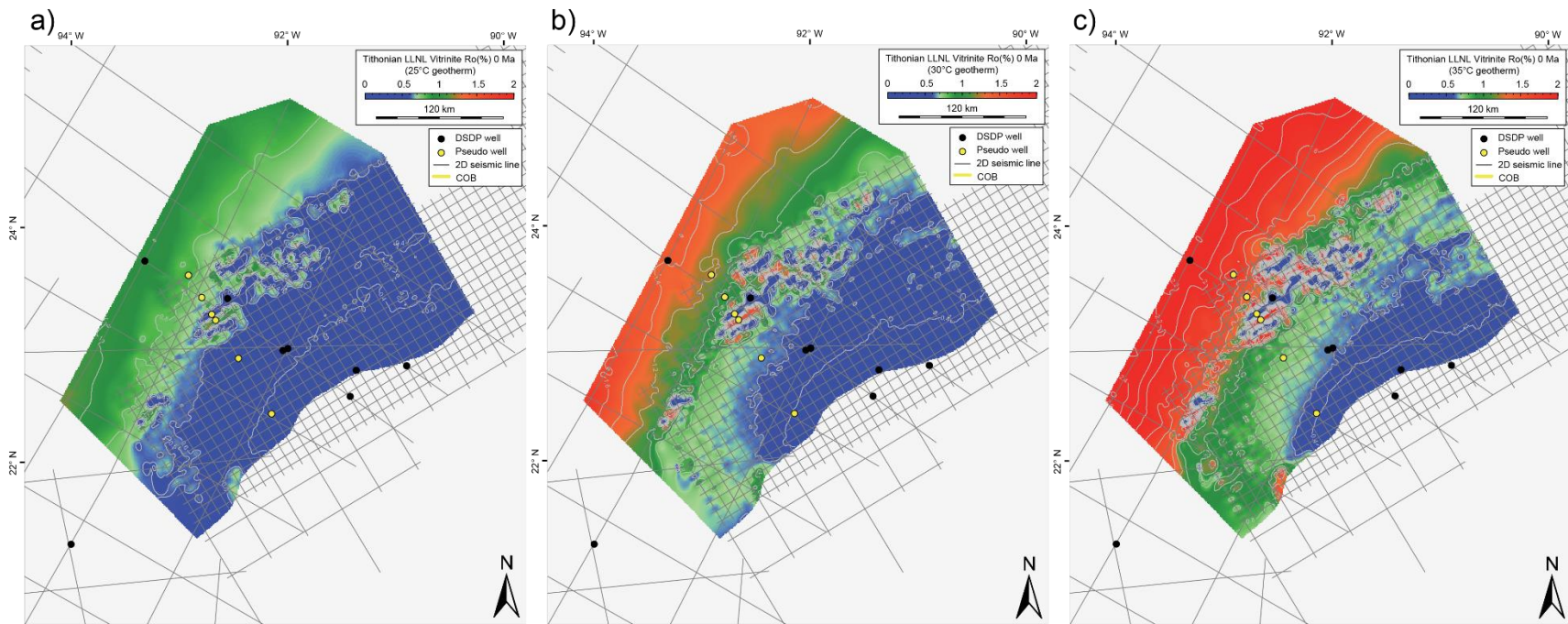


Figure 2.16 Generated maps of predicted Tithonian source rock thermal maturity based on regional burial and thermal histories modeled using for three different heat flow scenarios. **a)** Map of Tithonian source rock modeled vitrinite reflectivity (%) for the low-case thermal scenario. **b)** Map of Tithonian source rock modeled vitrinite reflectivity (%) for the mid-case thermal scenario. **c)** Map of Tithonian source rock modeled vitrinite reflectivity (%) for the high-case thermal scenario.

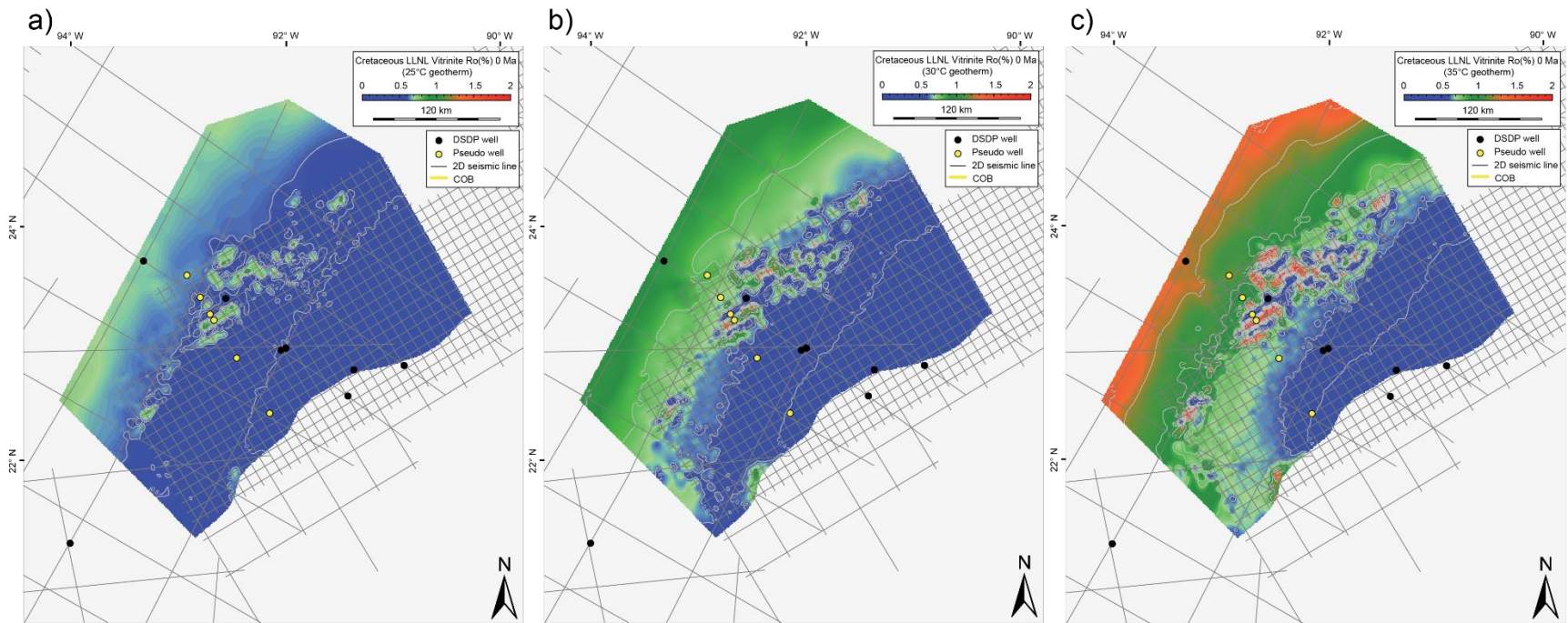


Figure 2.17 Generated maps of predicted Cretaceous source rock thermal maturity based on regional burial and thermal histories modeled using for three different heat flow scenarios. **a)** Map of Cretaceous source rock modeled vitrinite reflectivity (%) for the low-case thermal scenario. **b)** Map of Cretaceous source rock modeled vitrinite reflectivity (%) for the mid-case thermal scenario. **c)** Map of Cretaceous source rock modeled vitrinite reflectivity (%) for the high-case thermal scenario.

2.5 Implications for play prospectivity and evaluation of future exploration risk

2.5.1 Predicted source rock thermal maturity and model uncertainty

The present-day thermal maturity of the principal Tithonian source interval is predicted to have reached the oil window based on our thermal modelling from estimates of lithospheric thermal properties and thickness (Figure 2.18). Areas of oil mature source rock predicted by the model are within the distribution suggested by this limited available hydrocarbon occurrence data. A large number of surface oil slicks are present along the length of the Yucatan margin, with the majority focused along the outer marginal trough where minibasins are predicted to be mostly in the main-to-late oil window for the late Jurassic. Far fewer slicks are located up-dip, where thermal maturities are anticipated to be lower or immature (Figure 2.18).

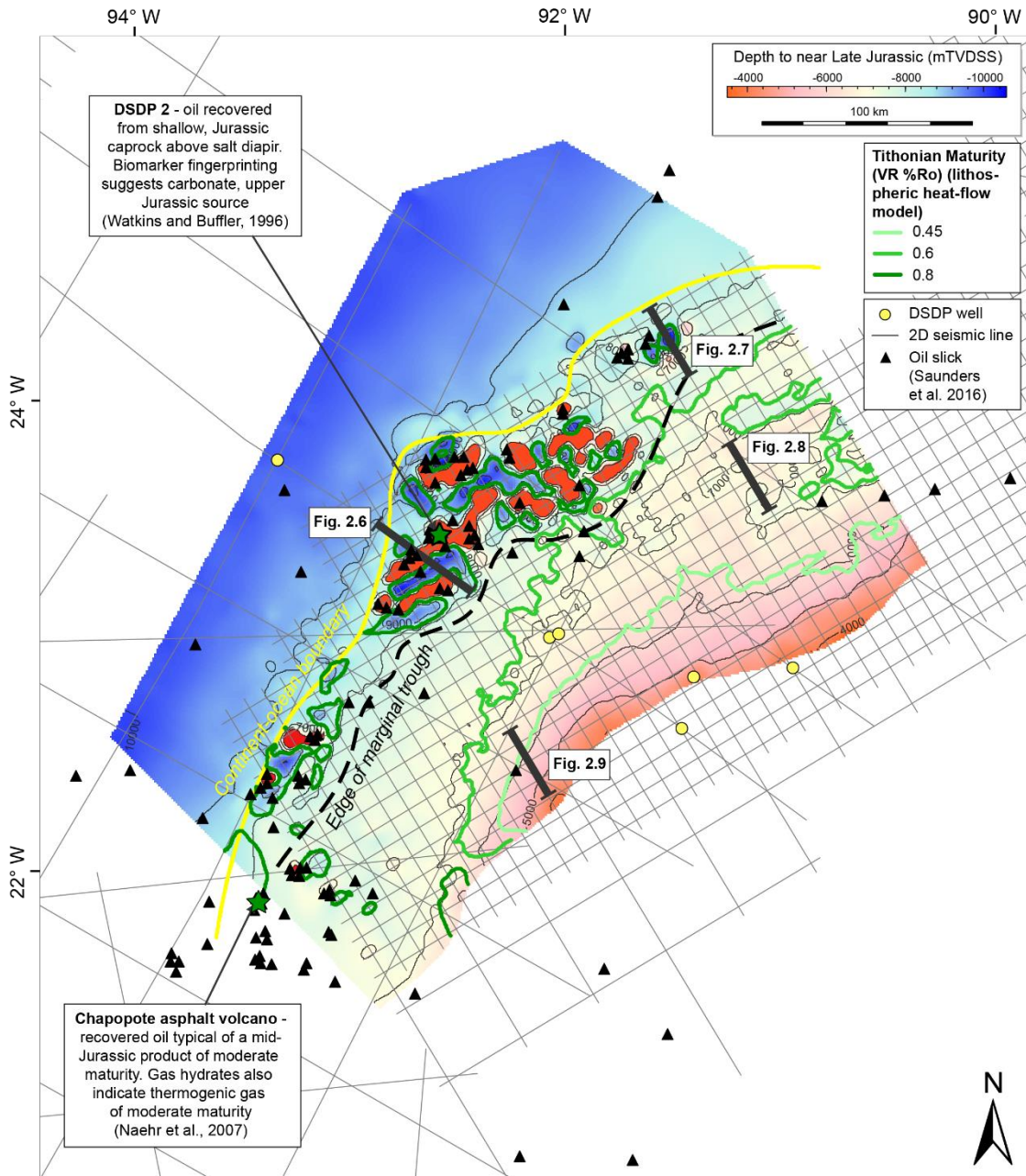
Drilling at DSDP Site 2 in 1968 recovered oil-stained caprock from above one of the salt diapirs. Biomarker fingerprinting of samples indicate oil sourced from an upper Jurassic, carbonate source rock (Figure 2.18) (Watkins and Buffler 1996). Further south, along the predicted oil-mature southern edge of the study area and near the border of the deep-water Campeche salt basin, oil was recovered from an asphalt volcano at the seafloor that was reportedly typical of a mid-Jurassic product of moderate maturity (Figure 2.18) (Naehr *et al.*, 2009). Gas hydrates tested in the subsurface from this location were thermogenic and resembled associated gas produced along with oil generation at moderate maturity (Naehr *et al.*, 2009).

Our results indicate that predicted thermal maturities by the lithospheric model are relatively robust for a model without data calibration and appear to fall within a reasonable range of the thermal maturity inferred from recorded sea-surface oil slicks from Saunders *et al.*, (2016), and the few recovered oil and gas samples in the area (Watkins and Buffler 1996; Naehr

et al., 2009). The deep-water Yucatan margin has a relatively straightforward burial history through most of its development, which helps to improve general confidence in the model. Lithospheric properties and formation lithology (i.e. thermal conductivity) are the primary controlling factors on predicted maturities. As a result, our assumptions regarding these factors provide the most uncertainty. Future thermal models will be able to improve on these results if data is acquired in the area, especially deep-penetration well data.

Source rock kerogen types and kinetic parameters are also likely to impact both the maturity and timing of generation. Type-IIS kerogen in Tithonian carbonate source facies could lead to generation at lower maturities (~0.45% vitrinite Ro) than regular type II source facies (Santamaria-Orozco 2000). Earlier type-IIS onset of hydrocarbon generation would result in larger areas of the Mesozoic slope being oil mature for the Tithonian (Figure 2.19).

Figure 2.18 Map of near Late Jurassic structure map with Tithonian maturity contours from the preferred lithospheric heat-flow superimposed. Black triangles mark cataloged oil slicks observed at sea-surface and modified from Saunders *et al.*, (2016). Recovered oil and gas samples from shallow cores samples are also summarized based on information from Watkins and Buffler (1996) and Naehr *et al.*, (2007). Numerous oil slicks are clustered around salt diapirs and Mesozoic structural features adjacent to primary oil kitchen areas within salt minibasins in the marginal rift. Less numerous oil slicks up-dip and on the Yucatan shelf and slope provide evidence of possible long-distance migration from the primary marginal rift kitchen area.



2.5.2 Evaluation of source rock maturity risk across the deep-water Yucatan

Thermal maturity risk for Mesozoic source rock intervals can be inferred based on burial history model results that include the range of ‘high-’, ‘mid-’, and ‘low-case’ geotherms across the study area (Figs 2.15, 2.16, 2.17). The Oxfordian interval exhibits low risk across significant parts of the study area with multiple models predicting maturity in high, mid, and low thermal scenarios (Figure 2.19a). Thermal maturity at this level is only likely to become high-risk towards the southeast of the study area close to the base of the Yucatan shelf-edge, and where overmaturity may become an issue towards the northwest. For the Tithonian, more significant areas of the Mesozoic slope to the southeast are likely to be higher-risk for maturity. However, the likelihood of encountering mature hydrocarbons increases towards the outer marginal trough and the Campeche salt basin (Figure 2.19b).

Based on these combined results, we interpret a low maturity risk for the salt minibasins, which are predicted to be thermally mature under all modelled thermal scenarios. Cretaceous source intervals are probably high-risk in terms of maturity across substantial areas of the Mesozoic salt-roller province along the slope (Figure 2.19c). Despite this, some Cretaceous source horizons may have reached thermal maturity in the salt minibasins and outer marginal trough area.

As no assumptions were made regarding crustal type for these model scenarios, the risk may be misrepresented over some regions of the oceanic crust where the heat-flow (and thermal gradient) could be significantly lower than the thinned, continental crust. However, the presence of oil slicks in the outboard area of the deep-water GOM basin floor suggests that areas of the oceanic crustal domain are likely oil mature for the Tithonian and matches our model (Figure

2.18). When comparing the lithospheric thermal model to the simple geothermal gradient models, thermal maturity trends are generally comparable to levels between the ‘low-case’ and ‘mid-case’ geotherm scenarios. The actual average geothermal gradient could, therefore, lie somewhere within a range of about 25°C/km to 30°C/km for the deep-water Yucatan margin.

2.5.3 Impact of regional depositional patterns on hydrocarbon generation

Gradual Cenozoic burial, heating, and maturation culminate at the present day. There have been no significant thermal or tectonic events since the Mesozoic that could result in complex burial histories (Figure 2.11a). As a result, predicted regional maturity trends and risk profiles are largely explained by the thickness and timing differences of deposited sediments, and their ultimate burial depth along the length of the Yucatan margin.

The Late Cretaceous to Middle Eocene Laramide orogeny affecting onshore Mexico is interpreted to have deposited significant thicknesses of foreland sediments across the western basin-floor of the GOM (Snedden *et al.*, 2018). Increasingly during the Oligocene and Miocene, high volumes of sediment were delivered northwards into the northern part of the deep-water Campeche salt basin and Yucatan margin areas along the Veracruz trough to the southeast (Clark *et al.*, 2019). These patterns of sedimentation have resulted in the earlier, deeper burial of the western edge of the deep-water Yucatan and Campeche margins compared to further eastwards along the Yucatan margin where thin Paleogene sediments onlap against a thickening Mesozoic sequence (Figs. 2.10a, 2.10b, 2.10c, 2.10d). The deeper, earlier burial of the Mesozoic explains the higher levels of thermal maturity predicted in the western part of the study area and along the western edge of the deep-water Campeche salt basin (Figs. 2.13-2.17).

From the Miocene onwards, the deposition of the Mississippi delta in the northeastern GOM was caused by a west-to-east shift in the dominant sediment supply into the GOM as a result of regional subsidence of the Rocky Mountains and epeirogenic uplift of the Appalachian mountains (Bentley *et al.*, 2015). Additionally, beginning in the Early Miocene, strong eastward oceanographic currents and accelerated current flow from the south have been attributed to a general deep-water fan shift towards the Mississippi Canyon area in the GOM during this period (Snedden *et al.*, 2012). The change in the axis of sedimentation can be observed across the Yucatan margin and is interpreted to correspond to a combination of these factors (Figs. 2.10e, 2.10f). These depositional trends mean that the eastern part of the margin was only buried by thicker sequences of sediment from the Miocene onwards, resulting in shallower burial depths and lower thermal maturities of more substantial areas of the underlying Mesozoic slope deposits at this location.

Although thermal maturity has been predicted for the Mesozoic age sequences containing major known source rocks, source rock facies of sufficient organic richness may not necessarily be present in these intervals across the entire margin. The Tithonian is generally interpreted to be widespread across large areas of the US GOM (Weimer *et al.*, 2017) and is also likely to be regionally present across large parts of the deep-water Yucatan (Watkins and Buffler 1996; Jacques and Clegg 2002; CNH 2015). In the deep-water Campeche, however, organic richness is found to vary significantly with lateral facies changes for both Tithonian and Oxfordian intervals (Ortuño *et al.*, 2009). Cretaceous source interval quality is also likely to be variable across the southern GOM as indicated by their pattern of known occurrences (Patton *et al.*, 1984, Katz *et al.*, 1984, CNH 2015) Even if the formations are thermally mature,

the presence of sufficient quality source rock is not guaranteed regionally, and facies prediction remains a risk without any data from deep well penetrations in the area.

Pre-salt strata are interpreted to represent a basinward-thickening, prograding sedimentary sequence related to GOM rifting with some high-amplitude seismic reflections representing localized, Triassic-Jurassic, rift-related volcanics (Rowan 2018) (Figure 2.8). There is the possibility for oil-prone, marine source rocks in the pre-salt section as evidenced by oils generated in the Early Jurassic Huayacocotla formation located in the onshore Tampico-Misantla basin to the west (Stabler and Gonzalez 2020). However, pre-salt hydrocarbons were not found in the recent Yaaxtaab-1 exploration well in the nearby Campeche salt basin, suggesting the deposition of pre-salt lacustrine or marine source rocks are not necessarily widespread if they exist offshore (Yallup 2019).

Any pockets of non-marine, lacustrine source rocks are more likely to develop in locations of deepest rift accommodation (Hood *et al.*, 2002; Yallup 2019). Pre-salt deposits offshore northern Yucatan are expected to be younger than the those of the northern Gulf Coast, as a sufficient increase in accommodation space for sediments in the GOM only developed from 200-180 Ma onwards (Frederick *et al.*, 2020). These younger rift sediments could potentially be more prospective for hydrocarbons - with better quality reservoirs, and a more favorable thermal history as demonstrated by our thermal model. Deeper, mature rift grabens could also facilitate deposition of lacustrine or marine source rocks in these developing structural lows.

2.5.4 Analysis of trapping styles, hydrocarbon migration, and timing

In the diapiric province, localized thickening of the sedimentary sequence can be observed within all post-salt units, suggesting salt movement has been occurring since the

Mesozoic and began not long after the salt deposition occurred (Figs. 2.6, 2.7). Significant thickening of the Oligocene-Miocene suggests the main phase of diapiric growth occurred during this period, and this burial would have initiated the primary phase of oil generation and expulsion in the minibasin areas (Figs. 2.3, 2.6, 2.7). Deformation of the overlying seafloor suggests the largest diapirs are feeding salt upwards and probably not yet welded (Figs. 2.3, 2.6). Shallow faulting along the edges of the diapirs or associated with underlying salt pillows is often associated with the locations of oil slicks at the sea-surface (Figs. 2.6, 2.7). The majority of oil slicks are clustered around the edges of large salt bodies and correlate well with underlying primary late Jurassic fault-fold structures and related overlying Cenozoic faults from which they are most likely sourced (Figure 2.18). Timing of trap formation versus hydrocarbon expulsion is assumed not to be a significant issue, with peak expulsion occurring relatively late; however, it is not clear if continued, recent salt movement could provide a risk of breaching some trapping structures. Numerous hydrocarbon slicks while indicating an active petroleum system also raise the issue of trap integrity, particularly along the uplifted flanks of shallow salt diapirs (Figure 2.4, 2.5).

Outer marginal trough collapse during the final stages of rifting in the Late Jurassic appears to control the overlying salt thickness and the subsequent structural development, with major Cenozoic faults often mirroring primary underlying rift structural trends (Figure 2.7) (Pindell *et al.*, 2014). Salt pillows are commonly present along both the inner and outer flanks of the outer marginal trough; however, salt no longer appears to be present below the majority of minibasins suggesting these are now welded (Hudec *et al.*, 2013) (Figs. 2.6, 2.7).

The thickest area of salt in the outer marginal trough domain results in the development of large (km-scale) salt-related structures that are directly adjacent to the oil mature, lowest-risk kitchen areas located in the neighboring minibasin depocenters (Figs. 2.18, 2.19). Potential trapping structures in this area include thrust-faulted Mesozoic strata above salt pillows in addition to associated faulting and folding of the overlying Cenozoic section (Figure 2.20). Combined structural and stratigraphic traps likely occur in the upturned strata against the flanks of major diapirs and in fault traps along the edges of salt diapirs or inverted minibasins. Intense fracturing of carbonates rocks can occur as a result of stresses from the growth of adjacent salt diapirs, providing good reservoir quality at these locations (Davison *et al.*, 2000). The deposition of turbidite basin-floor fans occur throughout the Cenozoic, and medium-coarse sands of potential reservoir quality are confirmed in the Miocene by DSDP wells in the area, transported from the south via the Veracruz trough (Clark *et al.*, 2019). Potential reservoirs could exist in multiple intervals throughout the section; however, facies changes across the stratigraphy may mean that not every well location necessarily has stacked pay potential (Figure 2.20).

Significant normal faulting throughout the stratigraphic section and permeable carrier beds likely provide efficient vertical migration pathways from local kitchen areas, and minimal lateral, long-distance is required to provide hydrocarbon charge in the outer marginal trough domain (Figure 20). Substantial variation in burial depth either side of some structural features could also result in individual traps being charged by a mixture of different fluid types produced from source rocks at variable levels of thermal maturity (Figure 2.7).

Up-dip salt rollers and Mesozoic growth faulting provide potential traps above the sloping salt detachment (Figure 2.20). High-amplitude reflections above the salt could represent possible Norphlet-equivalent sandstones, sourced by overlying Oxfordian source intervals (Figs. 2.8, 2.20) (Godo 2017; Steier and Mann 2019). Lenses of chaotic, high amplitude reflections along the uppermost Cretaceous unconformity are interpreted as carbonate breccia deposits related to the Chixculub impact (Grajales-Nishimura *et al.*, 2003; Paull *et al.*, 2014; Sanford *et al.*, 2016), located at the base of the platform edge and further downdip along the Mesozoic slope (Figure 2.8). Brecciated Mesozoic carbonates form some of the primary reservoir rocks in the Campeche basin to the south (CNH 2015) and could have similar reservoir and trapping possibilities in the Yucatan margin area. Large, listric faults penetrating the full Mesozoic growth section could also provide effective migration pathways into overlying reservoir units along the uppermost Cretaceous unconformity or within the Mesozoic growth-strata wedges (Figure 2.20).

Hydrocarbon migration could occur up-dip along the primary salt detachment, unconformities, and other permeable carrier beds (Figure 2.20). The presence of seeps associated with shallow structures along the thermally immature, up-dip parts of the Mesozoic slope and even above the Yucatan shelf itself provide possible evidence of long-distance migration from the deeper-water kitchen (Figs. 2.9, 2.18). As the majority of salt movement along the slope had ended by the Cenozoic, trap integrity risk is interpreted to be relatively low and the timing of hydrocarbon generation favorable. Shallow faulting is associated with the up-dip limit of more thinly deposited Mesozoic strata in the western part of the deep-water margin.

These structures indicate more recent, minor movement along the salt detachment – or as a result of ongoing distal salt tectonics in the outer marginal trough down-dip (Figure 2.9).

Turbidite fans in the Cenozoic may form stratigraphic traps where they onlap against the margin and could be charged by long-distance lateral migration along the detachment from thermally matures source rocks down-dip (Figure 2.21). Low-amplitude chaotic seismic facies are interpreted to represent mud-rich debris flows sourced from the shelf-edge and are likely to form good sealing horizons (Figure 2.9).

The presence of Triassic or Early Jurassic lacustrine source rocks would likely be required for favorable hydrocarbon prospectivity in the pre-salt section as the relative structural and stratigraphic positions make it unlikely that post-salt source rocks could have charged the pre-salt system (Figure 2.20) (Yallup 2019). If pre-salt, Triassic-Middle Jurassic source rocks are present along the deep-water Yucatan margin; they are likely to be thermally mature gas or overmature across significant areas (Figure 2.15). Numerous, thick-skinned rift-related normal faults would provide excellent migration routes and trapping structures in the form of tilted fault blocks, particularly in the deeper syn-rift section if effective source and reservoir rocks are present at this depth (Figs. 2.8, 2.20). Pre-salt source intervals may have begun generating hydrocarbons as early as the Late Cretaceous to Paleocene, which is prior to the formation of the majority of post-salt structures (Figure 2.3). Pre-salt source intervals encountered along the US Gulf Coast have indicated low potential yields (Yallup 2019), and it is unlikely they would be overly important for the post-salt petroleum system compared to the late Jurassic.

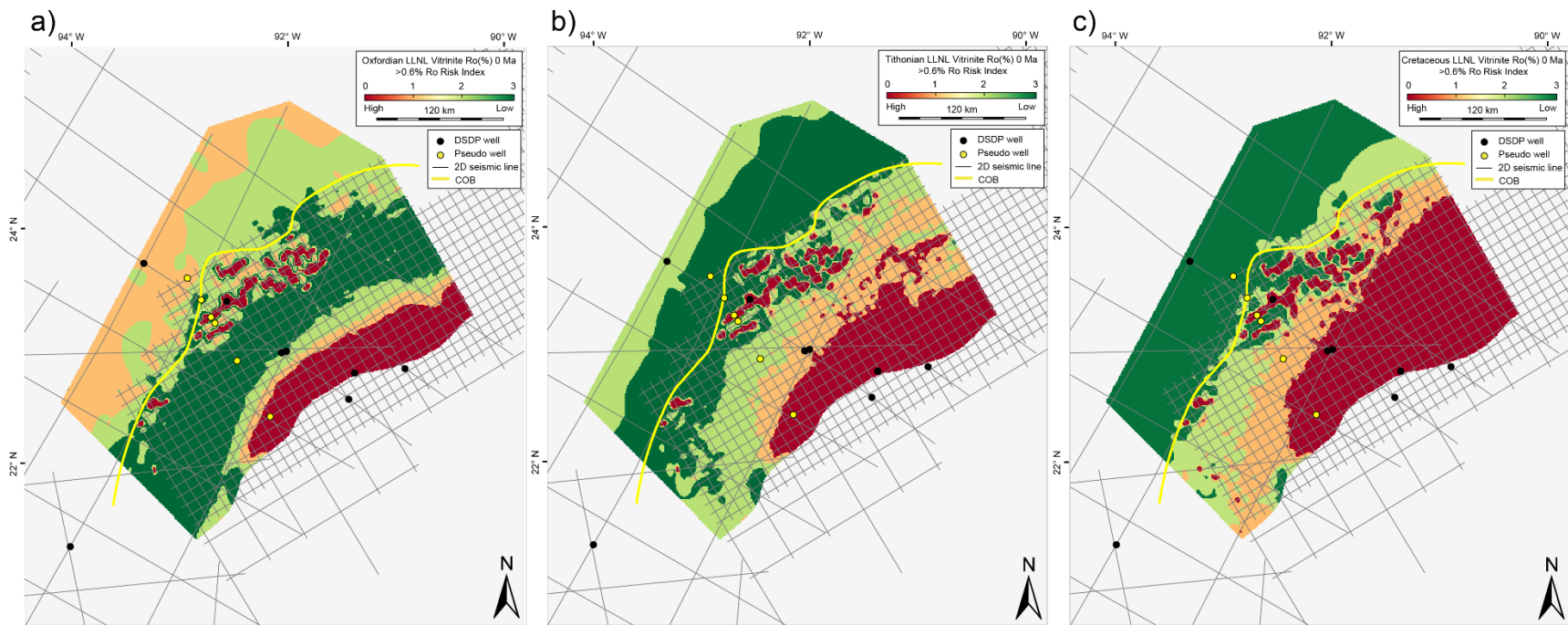


Figure 2.19 Risk index maps of thermal maturation for each Mesozoic source rock interval based on the sum of predicted thermal maturity ($>0.6\%$ Ro) from each high, mid, and low-case thermal maturity map. **a)** Maturity risk for the Oxfordian source rock. **b)** Maturity risk for the Tithonian source rock. **c)** Maturity risk for the Cretaceous source rocks. Continent-ocean boundary inferred from Sandwell *et al.*, (2014) gravity data.

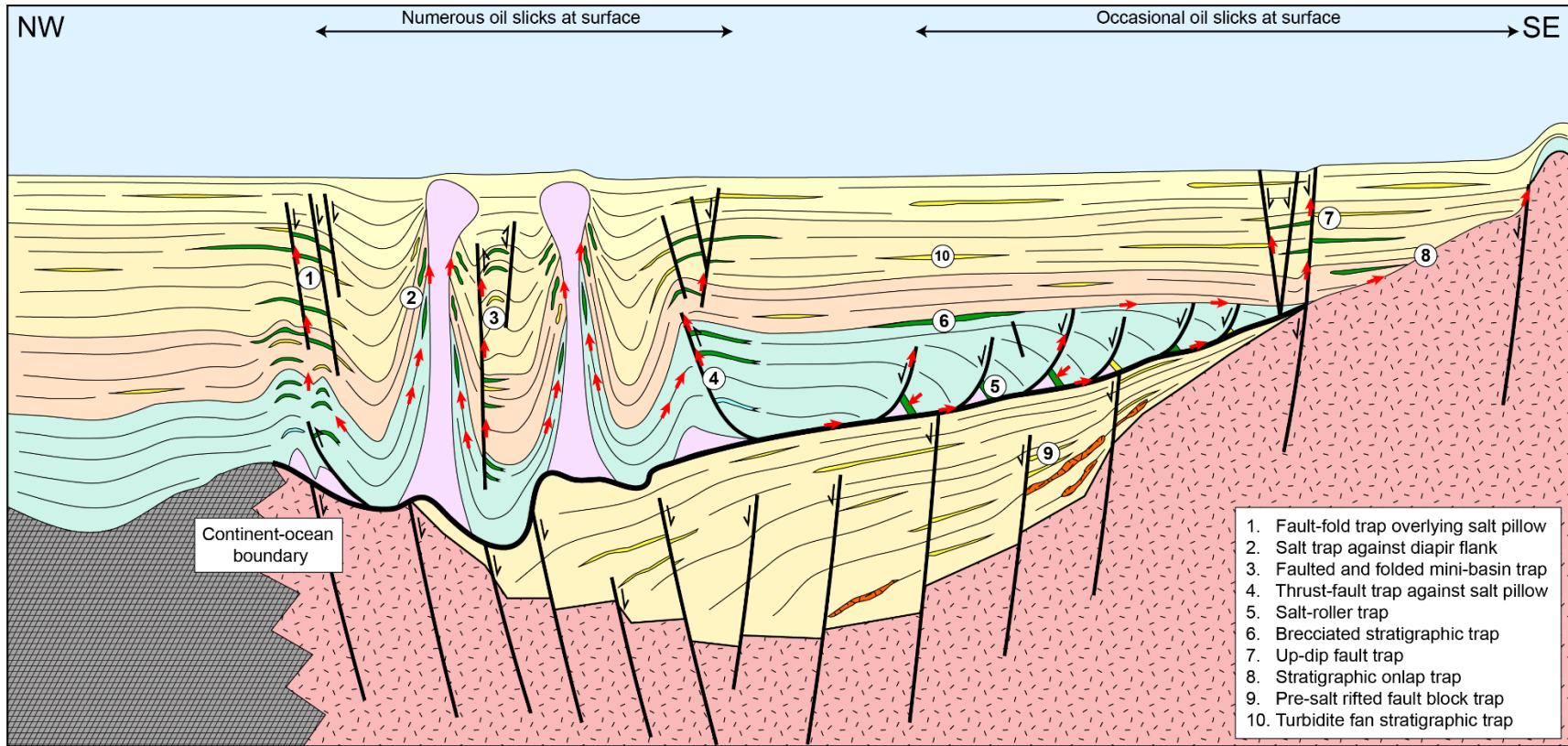


Figure 2.20 Play schematic summary profile across the deep-water Yucatan margin illustrating a variety of potential structural and stratigraphic trapping configurations identified across the margin from the seismic data. Potential routes for hydrocarbon migration from deep, thermally mature kitchen areas, via both vertical fault conduits, and through long-distance lateral migration are characterized.

2.6 Conclusions

1. Thermal modeling of lithospheric heat-flow was carried out using a series of vertical pseudo wells along a 3D cross-section of the deep-water Yucatan margin (Figure 2.4). Thermal modeling was able to predict burial closely, and thermal histories of three principal Mesozoic source rocks that are consistent with observed hydrocarbon seeps in this area that lacks deep-water wells in the Mesozoic section (Figure 2.18).

2. Thermal modeling indicates that the primary Tithonian marine source rocks of the Yucatan margin entered the oil window during the Paleogene, with peak generation occurring in the Oligo-Miocene. Hydrocarbon generation and expulsion continue to the present-day time of maximum burial and thermal maturity that accompanied gradual Cenozoic subsidence and burial under a thick, passive margin sedimentary sequence (Figure 2.11).

3. Regional 3D modeling using estimates of lithospheric thickness and heat-flow properties for the Yucatan margin predicts; 1) the Oxfordian source interval to reach gas-condensate maturity in the most deeply-buried salt minibasins and to be oil-mature over significant areas of the Mesozoic slope, 2) Tithonian source rocks as oil and condensate mature over most of the outboard marginal rift/salt diapir domain, 3) Late Cretaceous intervals reach the oil window only in salt minibasins and localized parts of the Mesozoic slope.

4. Alternate models were created by applying a range of geothermal gradients representing high, medium, and low heat-flow scenarios. This range of models characterize the risk indexes for thermal maturity of Mesozoic source rocks and indicate that localized salt minibasin depocenters along the deep-water marginal rift provide the lowest maturity risk. These minibasin depocenters are predicted to be thermally mature in all three modeled cases

for each source rock interval. The highest risk area for thermal maturity is anticipated to be the up-dip, southeastern part of the Mesozoic slope close to the base of the Yucatan shelf-edge, where thinner Cenozoic overburden deposition results in the Mesozoic consistently predicted as thermally immature in each heat-flow scenario.

5. Hydrocarbons generated from the Paleogene to present-day in the deep minibasin kitchen areas are predicted to migrate vertically along deeply-penetrating normal faults or tilted carrier beds to charge large-scale, salt-formed structural traps in the deep-water diapir province and are often directly associated with numerous clustered oil slicks at the surface. The presence of oil slicks overlying thermally immature areas of the proximal Yucatan slope and shelf provides possible evidence of long-distance migration from thermally mature areas further basinward and suggests the potential to charge widespread, structural and stratigraphic traps within the up-dip zone of Mesozoic gravitational extension and overlying Cenozoic clastic sequence.

CHAPTER 3: CONTROL OF STRUCTURAL STYLE BY LARGE, PALEOGENE, MASS TRANSPORT DEPOSITS IN THE MEXICAN RIDGES FOLD-BELT AND SALINA DEL BRAVO, WESTERN GULF OF MEXICO

The following chapter is based on: Kenning, J. J., Mann, P., 2020. Control of structural style by large, Paleogene, mass transport deposits in the Mexican Ridges fold-belt and Salina del Bravo, Western Gulf of Mexico. Marine and Petroleum Geology, 115, 104254.

3.1 Introduction

The Mexican Ridges fold-belt is a deep-water, passive margin fold-belt located in the western Gulf of Mexico and extends >400 km along the length of the eastern continental margin of Mexico (Pew, 1982; Yarbuh *et al.*, 2018) (Figure 3.1). Previous, deep-water hydrocarbon exploration has been much more extensive in the US sector compared to the Mexican sector of the Gulf of Mexico. There are very few deep-water wells located in the deep-water Mexican Gulf of Mexico, and other than Puskon-1 (used in this study), many wells do not penetrate below the Oligo-Miocene (Salomon-Mora *et al.*, 2011; Comisión Nacional de Hidrocarburos, 2015; Snedden *et al.*, 2018). Consequently, the along-strike stratigraphy and structural evolution of the Mexican Ridges remains poorly understood. The recent acquisition of modern, high-quality, 2D seismic surveys, including the 2015 grid used for this study (Figure 3.2a), allows for a more detailed interpretation of the structure and stratigraphy of the Mexican Ridges than was previously possible. International operators secured acreage in the Mexican Ridges

for the first time following the 2017 deep-water bid rounds for the Mexican Gulf of Mexico (Comisión Nacional de Hidrocarburos, 2017). Despite ongoing and planned hydrocarbon exploration activity and drilling, the deep-water hydrocarbon system remains unproven, with large parts of the fold-belt overlying oceanic crust (Figure 3.1).

The Mexican Ridges possesses significantly different structural style compared to the Jurassic salt-cored provinces in the northern US Gulf of Mexico, the Salina del Bravo salt province to the south of the US border, and the Campeche salt basin of the southern Gulf of Mexico (Comisión Nacional de Hidrocarburos, 2015, Snedden *et al.*, 2018) (Figure 3.1). In the Mexican Ridges, there is an absence of middle Jurassic salt because most of the crust underlying the Mexican Ridges consists of oceanic crust formed during the late Jurassic rather than rifted, continental crust overlain by salt (Nguyen and Mann, 2016). The Mexican Ridges fold and thrust belt detach instead along Eocene and Oligocene clay-rich horizons (Salomón-Mora *et al.*, 2009; Comisión Nacional de Hidrocarburos, 2015).

These variations in basement type and detachment level in the Mexican Ridges have crucial implications for hydrocarbon generation, migration, and accumulation. Based on seismic observations, Paleogene detachment shales within the Mexican Ridges vary significantly in both distribution and thickness along the length of the fold-belt. Paleogene shales are also present across the salt-cored Salina del Bravo salt province and form the primary detachment for its adjacent, shale-cored area, known as the Lamprea fold-belt (Vazquez-Garcia, 2018) (alternatively called the "Peripheral fold belt," Comisión Nacional de Hidrocarburos, 2015). The Lamprea fold-belt is located ahead of the advancing salt canopy and transitions into the Mexican Ridges towards the southeast (Vazquez-Garcia, 2018) (Figure 3.1). Structural

deformation within the shale detachment zone is complex, with the proposed presence of multiple detachments in the Mexican Ridges (Salomón-Mora *et al.*, 2009).

Figure 3.1 Map showing the main structural and basinal provinces of the Gulf of Mexico and eastern Mexico, highlighting the location of the Mexican Ridges. Onshore map information from Mexico compiled from Gray *et al.*, (2001); Garcia-Palomo *et al.*, (2004); Andreani *et al.*, (2008); Ferrari *et al.*, (2012); Offshore, map information compiled from Nguyen and Mann (2016) and Yarbuh and Contreras (2017). The inset map shows the location of the study area in a more regional view.

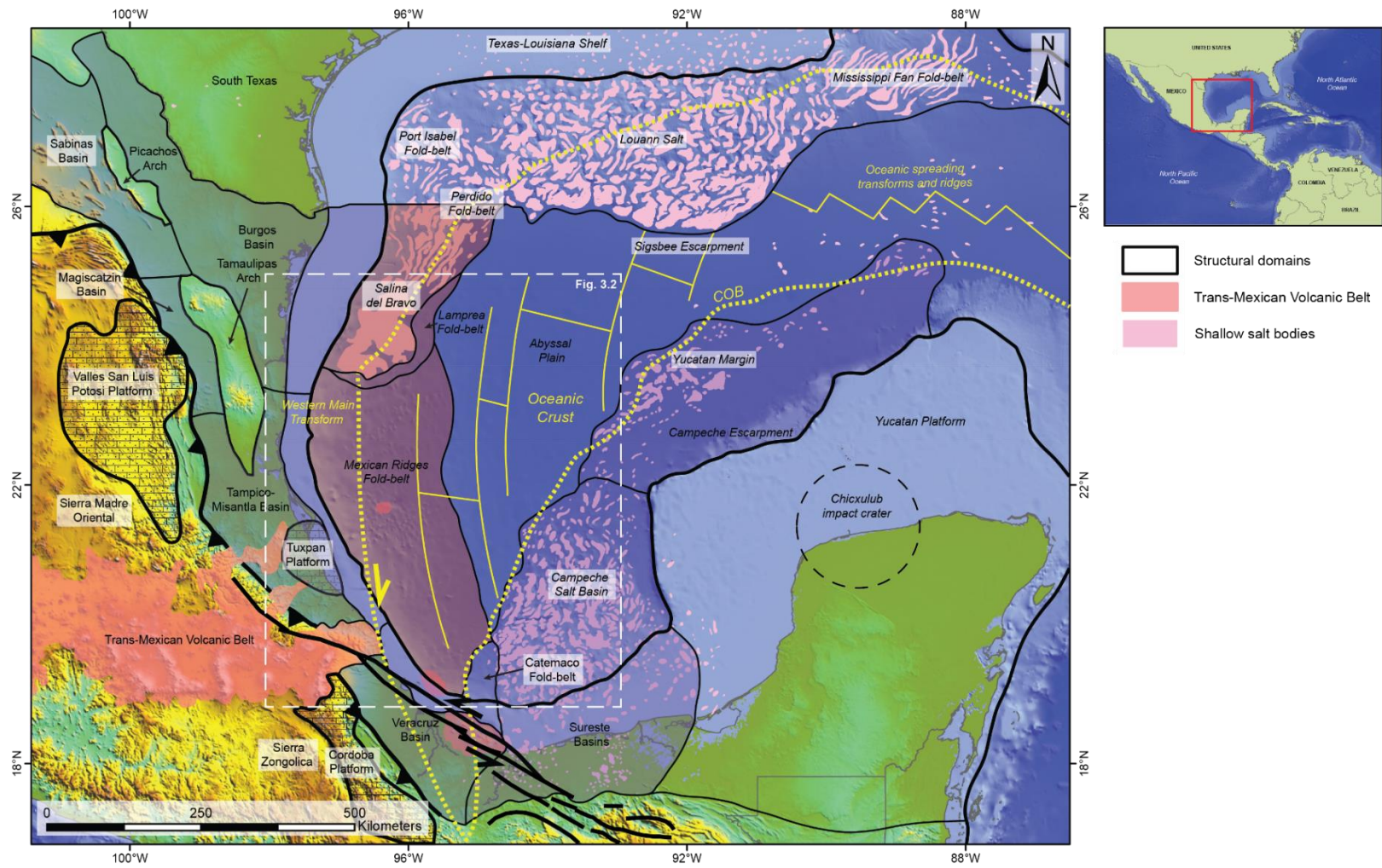
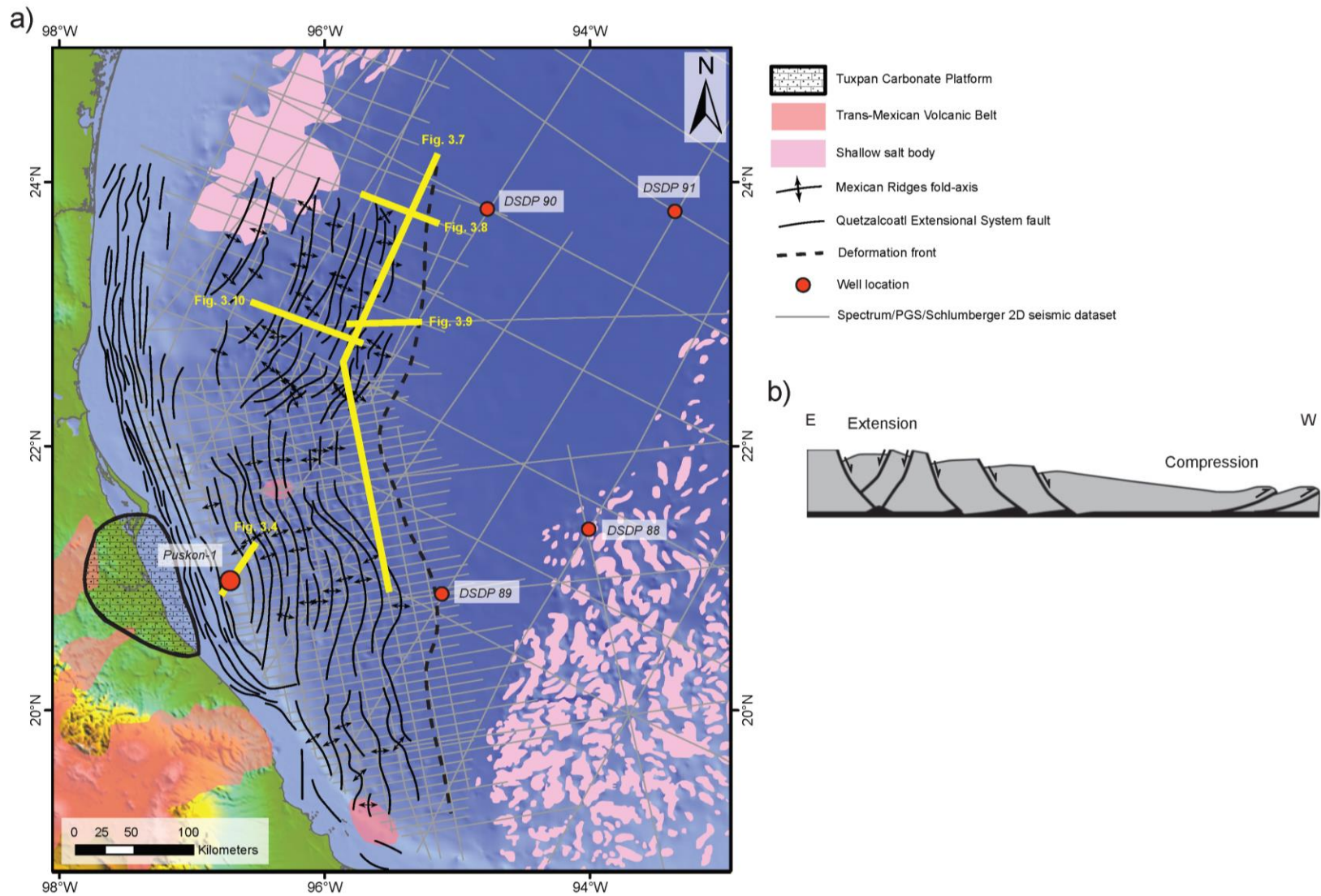


Figure 3.2 a) The 2D seismic dataset used in this study is shown in grey, and select seismic profiles highlighted in yellow. Fold axes of the deep-water Mexican Ridges are compiled from Pew (1982); Yarbuh and Contreras (2017). Normal faults of the up-dip Quetzalcoatl Extensional System from Le Roy *et al.*, (2007). **b)** Schematic cross-section of a passive-margin, gravitationally-driven fold-belt, showing up-dip extension corresponding to the Quetzalcoatl Extensional System and down-dip contraction corresponding to the Mexican Ridges. The figure is modified from Rowan *et al.*, (2004).



3.2 Regional geologic setting

3.2.1 Tectonic evolution of the western Gulf of Mexico

Formation of the Gulf of Mexico began with northwest to southeast rifting between North America, the Yucatan block, and South America during the Triassic and early Jurassic (Pindell and Kennan, 2009; Hudec *et al.*, 2013). Salt deposited in a single sag basin following rifting was subsequently separated into the southern (Mexican) and northern (US) salt provinces during the latest Jurassic as a result of the onset of oceanic spreading (Pindell and Kennan, 2009; Nguyen and Mann, 2016). The widening area of oceanic crust and continental rocks in eastern Mexico along the right-lateral, Western Main Transform fault, accommodated late Jurassic to earliest Cretaceous counter-clockwise rotation of the Yucatan block away from North America (Nguyen and Mann, 2016) (Figure 3.1). Oceanic spreading resulted in the formation of a width of >400 km of oceanic crust along part of the western Gulf of Mexico margin underlying the Mexican Ridges (Figure 3.1). The margin remained passive for much of the remainder of the Mesozoic as the result of post-rift thermal subsidence (Goldhammer and Johnson, 2001).

The late Cretaceous to middle Eocene Laramide orogeny uplifted and shortened significant areas of onshore eastern Mexico adjacent to the Mexican Ridges and Salina del Bravo salt province as a result of the shallow subduction of the Farallon plate beneath North America in the Pacific (Feng *et al.*, 1994; Gray and Lawton, 2011). Both the Sierra Madre Oriental and the Sierra Zongolica formed during this period, along with proximal foreland basins that underlie the present-day areas of the Burgos, Tampico-Misantla, and Veracruz basins (Gray *et al.*, 2001; Lawton, 2008; Snedden *et al.*, 2018) (Figure 3.1).

From the late Eocene to early Miocene, uplift and denudation continued along the Laramide fold-belt in eastern Mexico and contributed large amounts of clastic sediments to the deep-water, western Gulf of Mexico (Gray *et al.*, 2001) that contained thick, mass transport deposits (MTDs) (Galloway *et al.*, 2000). In the Neogene, flat-slab subduction of the Cocos Plate beneath southern Mexico resulted in the propagation of the Trans-Mexican Volcanic Belt that accompanied the eastward motion of the Chortis Block. This early Miocene to recent Trans-Mexican magmatic activity extended into the western Gulf of Mexico and the Mexican Ridges (Ferrari *et al.*, 2012) (Figure 3.1).

Sediment loading and related down-dip compression during the Oligo-Miocene formed the salt-cored Perdido fold-belt, the overlying salt canopies of the Salina del Bravo salt province, and the linked development of its easternmost, Paleogene shale-detached Lamprea fold-belt (Vazquez-Garcia, 2018) (Comisión Nacional de Hidrocarburos, 2015). To the south of the Salina del Bravo salt province, gravitational failure along the Mexican continental shelf from the middle-late Miocene onwards produced a 50 km-wide zone of listric, normal faults called the Quetzalcoatl Extensional System (Alzaga-Ruiz *et al.*, 2009, Salomón-Mora *et al.*, 2009). Accommodation of extensional deformation translated down-dip along a Paleogene-age detachment that formed a linked Mexican Ridges contractional domain in the deep-water western Gulf of Mexico (Pew, 1982; Salomón-Mora *et al.*, 2009; Yarbuh and Contreras, 2017) (Figure 3.2).

3.2.2 Characterization of MTDs in the Mexican Ridges

Fick (2016) used a combination of well and seismic data to describe the thickest and most laterally extensive of the Paleogene detachment units underlying the Mexican Ridges (MTD 7 in this study) and interpreted it as an Oligocene-age mass transport deposit that controlled the structural expression in the overlying Mexican Ridges. Galloway *et al.*, (2000) also mapped a large Oligocene-age MTD in the offshore Tampico-Misantla area.

In the study, MTD 7 partially mapped by Fick (2016), plus eleven additional previously undescribed MTDs were interpreted from a grid of seismic reflection profiles across the length of the fold-belt (Figure 3.2a). I describe the seismic facies, location, lateral extent, and thickness measurements from twelve of the largest MTD units underlying the Mexican Ridges, the largest of which covers an area of over 100,000 km² (Figure 3.12a).

Submarine MTDs are broadly defined as solid or plastically deforming sediments moving under the force of gravity. The descriptive classification of MTDs employed in this study follows the classification proposed by Nardin *et al.*, (1979) that was modified by Moscardelli and Wood (2008). In the classification of Moscardelli and Wood (2008), MTDs are sub-divided into three categories: slides, slumps, and debris flows. These end-members in their MTD classification are based on their sedimentary facies, their inferred transport mechanism, and their mechanical behaviors (Moscardelli and Wood, 2008; Ogata *et al.*, 2012) (Figure 3.5). Large-scale MTDs can result from multiple semi-continuous events originating from a continually replenishing shelf-edge sediment source, or destabilization of large areas as a result of regional tectonic events (Moscardelli and Wood, 2016).

3.3 Data

Four, industry 2D seismic surveys (Mexico WR North RR, Mexico WR South RR, Mexico WR South RR Infill, and Mexico Well Tie MC2D) were acquired in 2015 by a partnership of Spectrum, PGS, and Schlumberger and were used for interpretation in this study (Figure 3.2a). Each survey consists of a grid of 2D PSDM seismic profiles that were processed using automatic gain control (AGC). All seismic sections are displayed with SEG standard polarity, where an increase in acoustic impedance is represented by a peak (black) and a decrease in acoustic impedance represented by a trough (white) (Figure 2.4a – inset schematic).

The main well used for seismic correlation in this study is Puskon-1, drilled by PEMEX in 2011 (E&P Magazine, 2012) (Figure 3.2a). Available partial well data consists of age information, a lithological column, and logs (GR, DT, RHOB, NPHI) from the late Eocene to middle Miocene, modified from O'Reilly *et al.*, (2017) (Figure 2.3). Regional seismic correlation focused on the Eocene and Oligocene intervals of the Mexican Ridges and was extrapolated more than >500 km from the Puskon-1 well location.

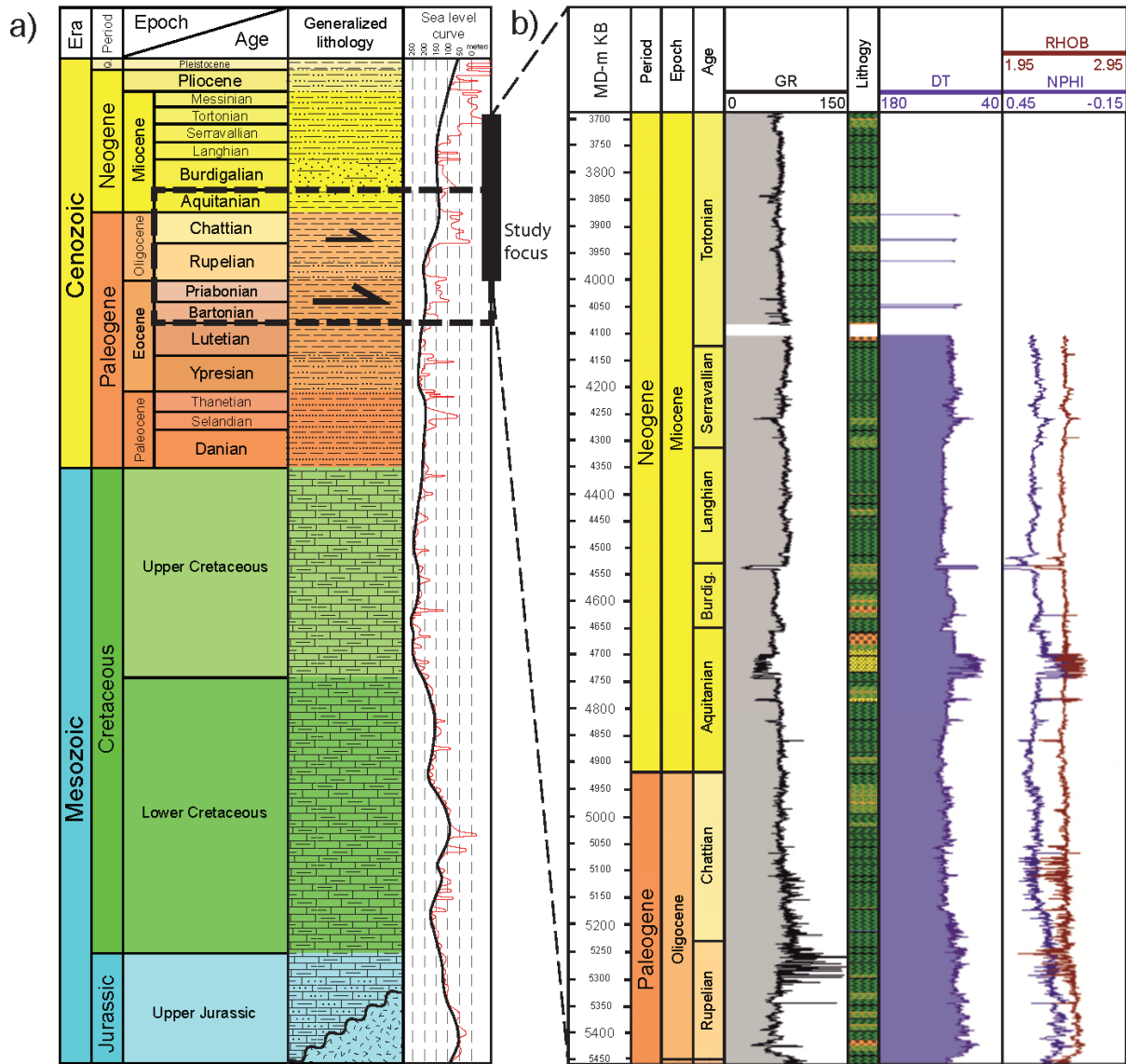
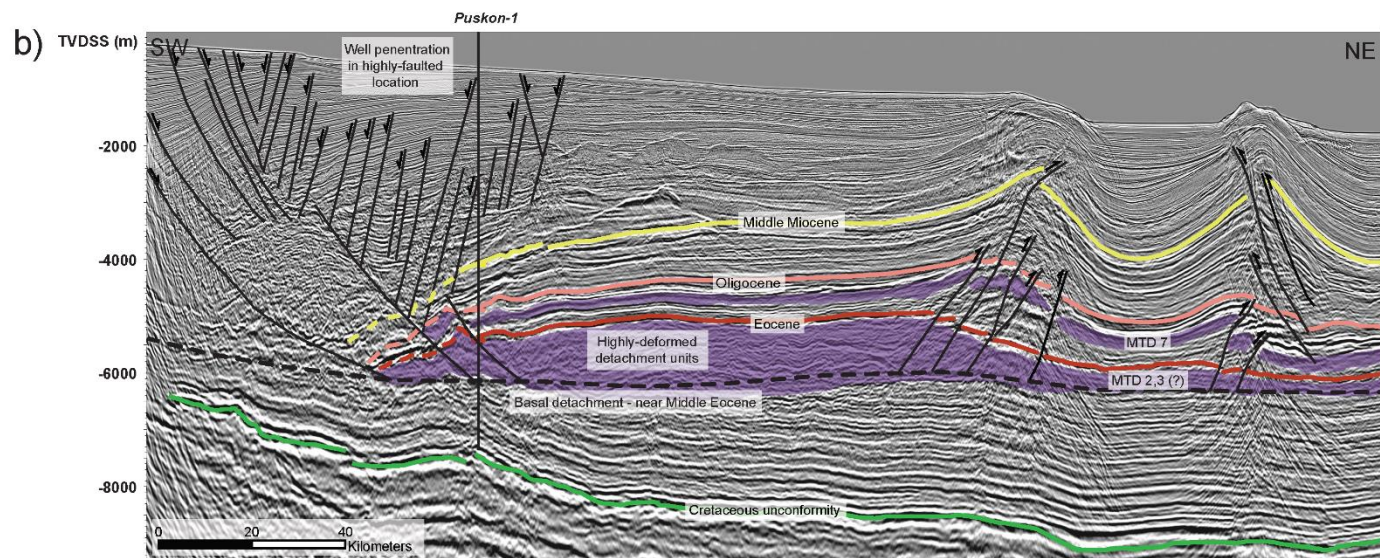
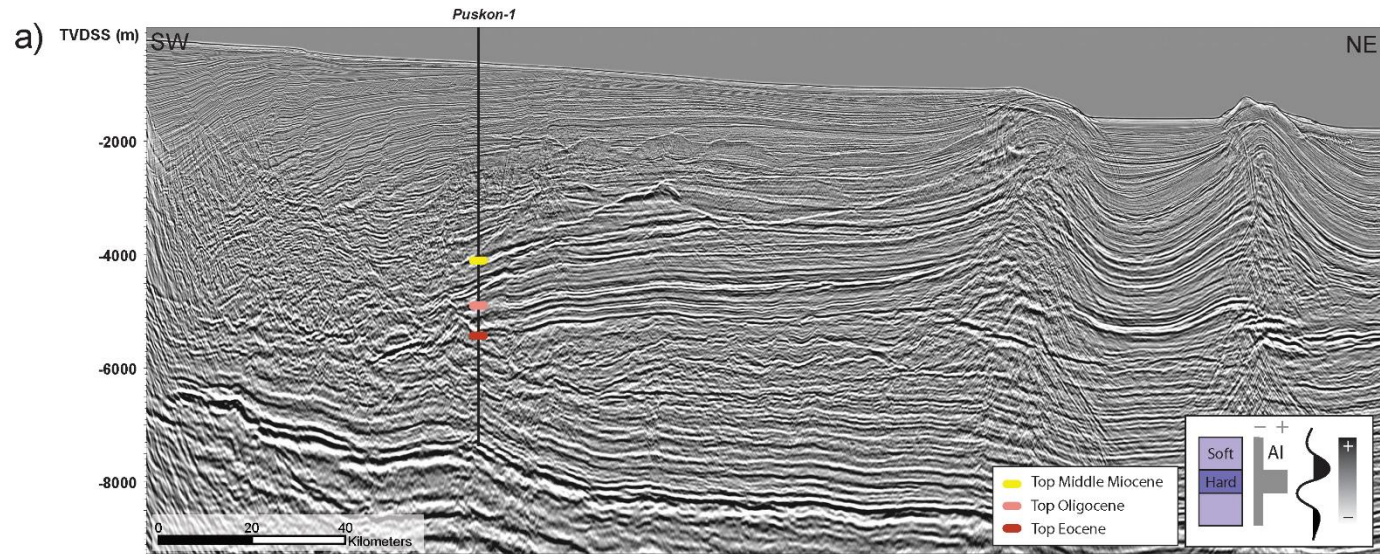


Figure 3.3 a) Stratigraphic column showing the late Eocene to early Miocene interval of interest for this study, with the late Eocene and Oligocene detachments indicated by the thrust symbols. The eustatic sea-level curve is from Haq *et al.*, (1987), the stratigraphic column is modified from Alzaga-Ruiz *et al.*, (2009). **b)** Partial logs from the Puskon-1 well from O'Reilly *et al.*, (2017) show the dominantly, fine-grain lithology of the up-dip section of the Oligocene detachment interval as shown in a).

The seismic survey data were tied to the well top ages (Figure 3.4). The well penetrates approximately 200 m of the up-dip, proximal end of MTD 7, and demonstrates that this interval is: 1) fine-grain dominated in composition, and 2) Oligocene in age; as interpreted by Fick (2016) using well data that was not available to the study. Paleontological data from the Puskon-1 well constrain an Eocene age for depositional units located at the basal detachment level; however, I do not have access to lithological and age information below the base Oligocene. The interpreted ages are consistent with the stratigraphic interpretation of the well by Snedden *et al.*, (2018) along with previous age estimates of the stratigraphic units present in the Mexican Ridges from onshore and shallow-water well data (e.g., Alzaga-Ruiz *et al.*, 2009; Salomón-Mora *et al.*, 2009).

Figure 3.4 a) Uninterpreted, northeast-trending, seismic dip profile intersecting the Puskon-1 well drilled ~55 km from the coast of eastern Mexico to a total depth of 7200 m (locations of this seismic line and Puskon-1 are shown on the map in Figure 2a). The inset schematic illustrates the polarity of the seismic data displayed in **a)**. **b)** Interpreted seismic profile showing age horizons extrapolated from Puskon-1 well. Units located along the basal detachment were interpreted as Eocene, with the up-dip part of the MTD 7 as Oligocene based on the well biostratigraphic ages. TVDSS = total vertical depth subsea.



3.4 Structural and stratigraphic interpretation

3.4.1 Seismic facies classification of MTDs in the southwestern Gulf of Mexico

The majority of MTDs located in the Mexican Ridges structural province display characteristics resembling those of debris flows, with occasional internal slumps (Figure 3.4, Figure 3.5). The MTD units are characterized by their lobate shapes, lateral pinch-out geometries, irregular upper bedding contacts (Figure 3.5), and locally with internal rafted or detached blocks, contorted beds, and shortening structures (Figure 3.5, Figure 3.6). Erosive scouring along the base of the MTD units can be observed in some locations (Figure 3.5 - MTD 7 and MTD 2). Internally, the MTDs are represented by semi-continuous to discontinuous, low-amplitude, semi-transparent, and chaotic seismic reflections characterized as seismic facies 1 (SF-1) in this study (Figure 3.5).

In addition to debris flows, occasional slumping was observed on the flanks of fold structures in the shallow Neogene section of the Mexican Ridges. Seismically recognizable features of MTDs in this setting include; irregular upper bedding contacts, duplex structures, and contorted layers, with both low- and high-amplitude reflections displaying evidence for compressive deformation (Figure 3.5). Discrete slide blocks display high-amplitude, continuous, or semi-continuous internal reflections with a high degree of faulting within the unit (Figure 3.5). This slide block seismic facies is observed within the thin, distal end of MTD 7. Deep-water turbidite fans interbedded with thin debris flows are present throughout the Oligo-Miocene fold-belt strata and are represented by parallel-bedded, continuous and semi-continuous high amplitude reflections (Figure 3.6).

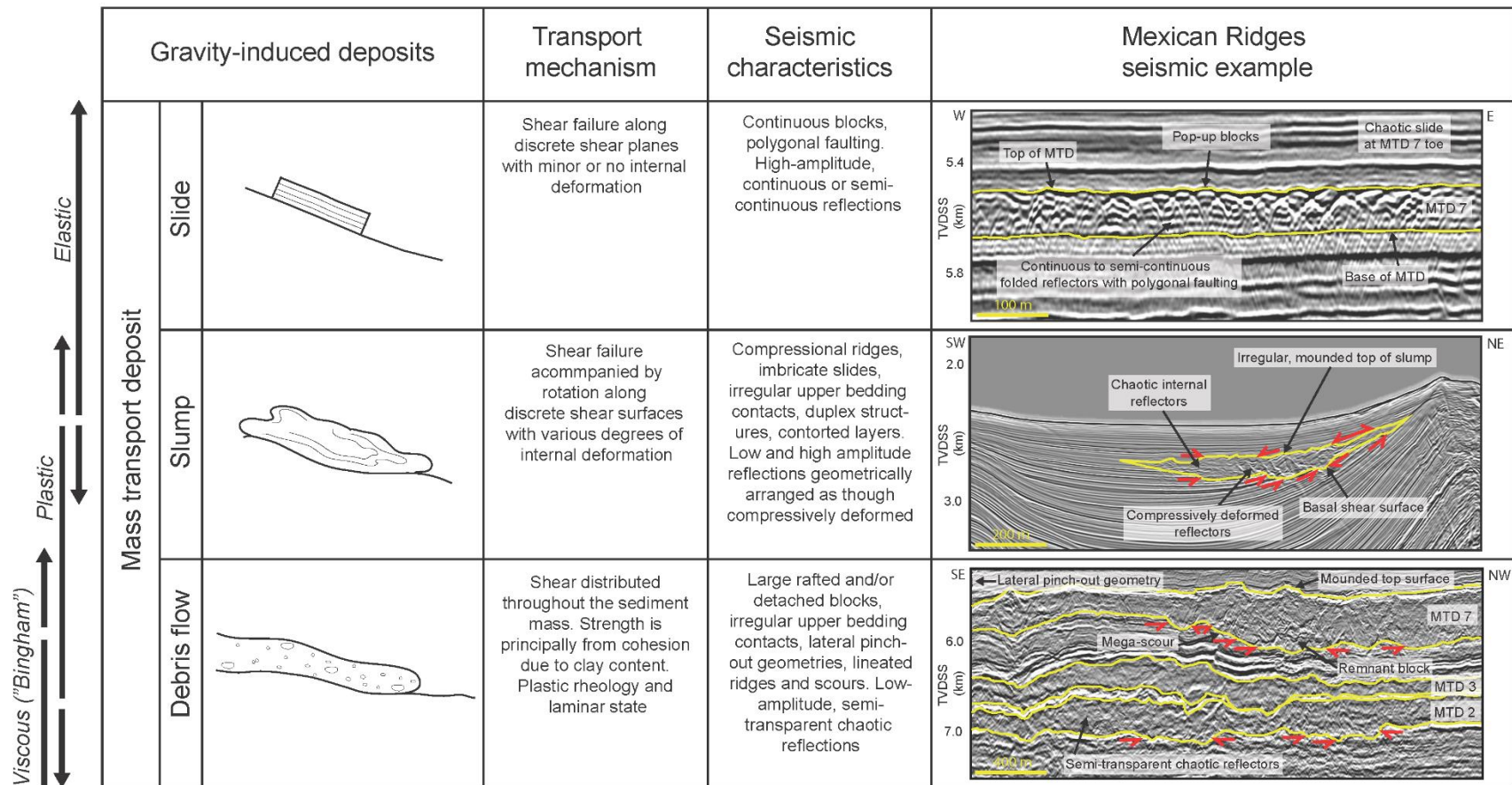


Figure 3.5 Classification of gravity-induced, mass transport deposits compiled from previous authors: Dott (1963); Nardin *et al.*, (1979); Moscardelli *et al.*, (2006); and Moscardelli and Wood (2008); Ogata *et al.*, (2012). All types of slide, slump, and debris flow end-members are present in the Mexican Ridges; however, the majority of Paleogene-age deposits mapped as part of this study are debris flows.

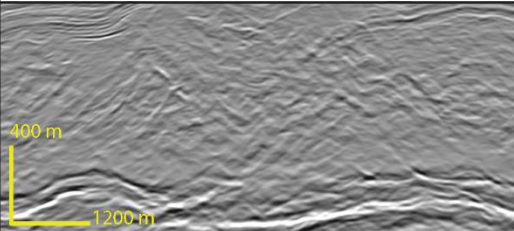
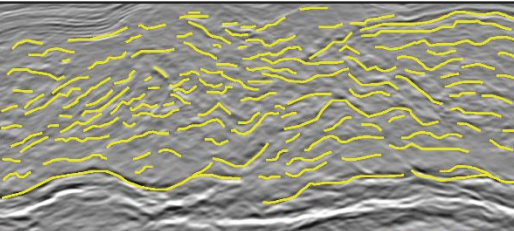
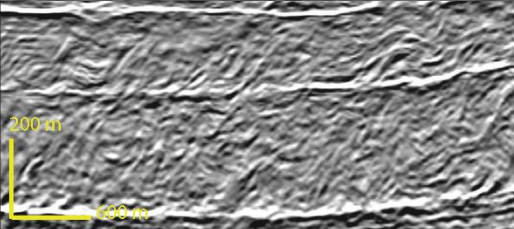
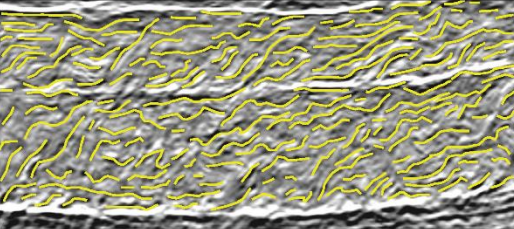
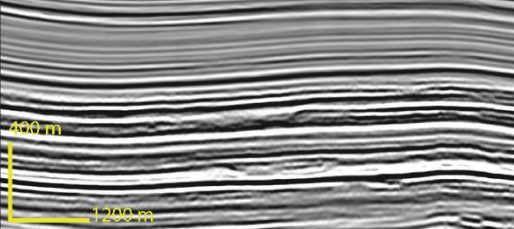
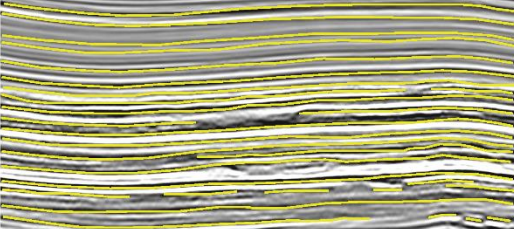
Seismic facies	Seismic example	Fabric interpretation	Characteristics	Interpretation
SF-1 Chaotic, low-amplitude reflection packages			Highly chaotic, semi-continuous to discontinuous, low amplitude, weak reflectors	Dominantly shale and clay-rich MTD deposits containing debris-flow and occasional slumped blocks
SF-2 Imbricate, high-amplitude reflection packages			Imbricate, locally chaotic, semi-continuous to discontinuous reflectors with moderate to high amplitude	Two stacked units showing shortening structures associated with MTD deposition; variable lithology.
SF-3 High-amplitude reflection packages			Thick, parallel, continuous to semi-continuous, high amplitude reflectors	Distal basin floor fans, turbidites. Stacked, sand-rich lobes interbedded with shales

Figure 3.6 Seismic facies classification of gravity-induced depositional sequences within the Mexican Ridges deep-water fold-belt. Three principal seismic facies were identified associated with gravity-induced deposits: 1) Seismic facies 1 (**SF-1**) consists of chaotic, low-amplitude reflectors typical of the shale-rich debris flows; 2) **SF-2** displays imbricated, moderate-amplitude reflectors commonly observed in areas of slumps or debris flows with syn-depositional, compressional deformation; and 3) **SF-3** consists of high amplitude, planar, and continuous reflectors representing sand-rich turbidite fan deposits that provide potential Oligo-Miocene hydrocarbon reservoirs within the Mexican Ridges.

3.4.2 Seismic interpretation of MTDs as detachment units

As a result of regional interpretation of the MTDs extrapolated from the single, well control point at Puskon-1, I define the approximate ages within the detachment zone that is rooted in the thickest and most extensive MTDs. MTDs 1–3 can be confidently interpreted as Eocene-age and are located at the approximate basal detachment level of the Mexican Ridges (Figure 3.7). In the northern area of the Mexican Ridges and east of the Salina del Bravo salt province and Lamprea fold-belt, I map an almost continuous stacked sequence of MTD units of late Paleogene age (Figure 3.7, Figure 3.8). In the southern Mexican Ridges, Eocene, and Oligocene MTDs are thinner and separated by an interval of continuous, parallel reflections in contrast to the MTD stack mapped in the northern area (Figure 3.7, Figure 3.9). MTD 7, interpreted as Oligocene in age, erodes into the older strata by hundreds of meters and displays a maximum thickness of >1400 m. MTD 7 is flanked by smaller, younger units to the north and south (MTDs 8, 9). Units with low seismic amplitude are interpreted as debris flows and slumps and are common throughout the Neogene and Recent sections in the overlying fold-belt. These younger debris flows and slumps are typically much smaller in size than the MTDs mapped in this study and were not mapped on a regional scale. Significant thinning can be observed within the Oligocene – Recent overburden coinciding with the thickest area of MTD 7 across the northern Mexican Ridges. This region that overlies the thickest MTDs exhibits a higher degree of folding and structural deformation in the overlying Mexican Ridges fold-belt as compared to the adjacent areas to the north and south (Figure 3.7).

In the distal, deeper-water area of the Mexican Ridges, individual MTDs are more easily identifiable from their seismic characteristics because of their lesser degree of subsequent

structural deformation (Figure 3.8, Figure 3.9). East of the frontal thrust of the Lamprea fold-belt, detachment folds are gentler, more symmetrical, and associated with minor thrust faults (Figure 3.8). Despite the lesser degree of structural deformation overall, there is still some observable tectonic thickening of the MTD package within the cores of folds. Some thrust faults penetrate the entire MTD package and less commonly the strata that overlie the MTD horizons, although many thrust faults originate from various intervals within the MTD sequence. A majority of thrust faults within the fold-cores terminate once they penetrate the top of the MTD package, but numerous minor thrust faults are present within the overlying strata in the deep-water area east of the deformation front. MTD deposition continues sporadically into the Oligo-Miocene in this area, but following MTD 7, MTD events become progressively smaller in size (Figure 3.8).

Further south in the northern Mexican Ridges, MTD 7 thickens up to ~1000 m despite being east of the Mexican Ridges thrust-front (Figure 3.9). MTD 7 thins distally to the southeast and exhibits truncation of the underlying strata along the base of the MTD 7 unit. Major thrust faults associated with primary folds can be traced downwards from the Miocene section to the Eocene basal detachment. A thrust fault exhibiting a highly variable dip angle is present cutting through MTD 7, and there is also evidence of thrust faults detaching within or along the top of MTD 7 (Figure 3.9). Intensive thrust faulting characterizes the parallel-bedded strata separating MTD 2 and 3 from MTD 7, where many of these thrust faults terminate along the base of MTD 7. Ductile, tectonic thickening is observed within MTD 7, where the unit has been compressed within the cores of folds. Detachment faulting is mainly focused within the overlying pre-

growth section and intervening strata separating the individual Eocene and Oligocene MTD units (Figure 3.9).

Characterization of the proximal areas of MTD units becomes difficult because of the high-degree of gravity-driven contraction and deformation during late Miocene fold-belt formation, especially near to the basal detachment level. In the northern Mexican Ridges, the total thickness of the stacked and deformed MTD package can reach >3.5 km (Figure 3.10). MTD 7 is thickest towards the front of the fold-belt, where there are a high number of asymmetrical, tightly-spaced, and faulted detachment folds, often related to back-thrusting. Thrust faulting is imbricate, and most fold structures involve multiple faults, although the degree of fault deformation from structure to structure can be highly variable. Most major thrust faults detach along the Eocene basal detachment, and some of these thrusts extend to the seafloor, where fault-related folding is visible at the seabed (Figure 3.10).

In the proximal area of the northern Mexican Ridges, numerous smaller, Oligo-Miocene MTDs are present throughout the sequence, as shown in the northwestern part of Figure 3.10. These MTD units thin abruptly in an eastward direction where their thin (seismic reflector scale), distal ends inter-finger with high-amplitude, continuous reflections resembling SF-3 (Figure 3.6). Multiple faults detach from various MTD units within this interval, including a “fishtail fault” structure (Figure 3.10 – observed in the third fold from left). In addition to the tectonic thickening within the MTD units, there is also a significant thickening of the overlying interbedded Oligo-Miocene sequence within the cores of the fold structures (Figure 3.10).

Figure 3.7 a) Uninterpreted, north-trending, 2D seismic strike profile showing the distribution of regionally-extensive Eocene - Oligocene MTDs that provided the stratigraphic control for the basal detachment level. **b)** Interpreted seismic strike profile showing the northern Mexican Ridges area overlies the thickest (>1400 m) area of the structurally-deformed MTD 7. MTD 7 thins southwards (<400km) where thicker parallel-bedded strata separate the individual MTD units. Structural deformation is more intense above the thicker MTD units in the northern Mexican Ridges.

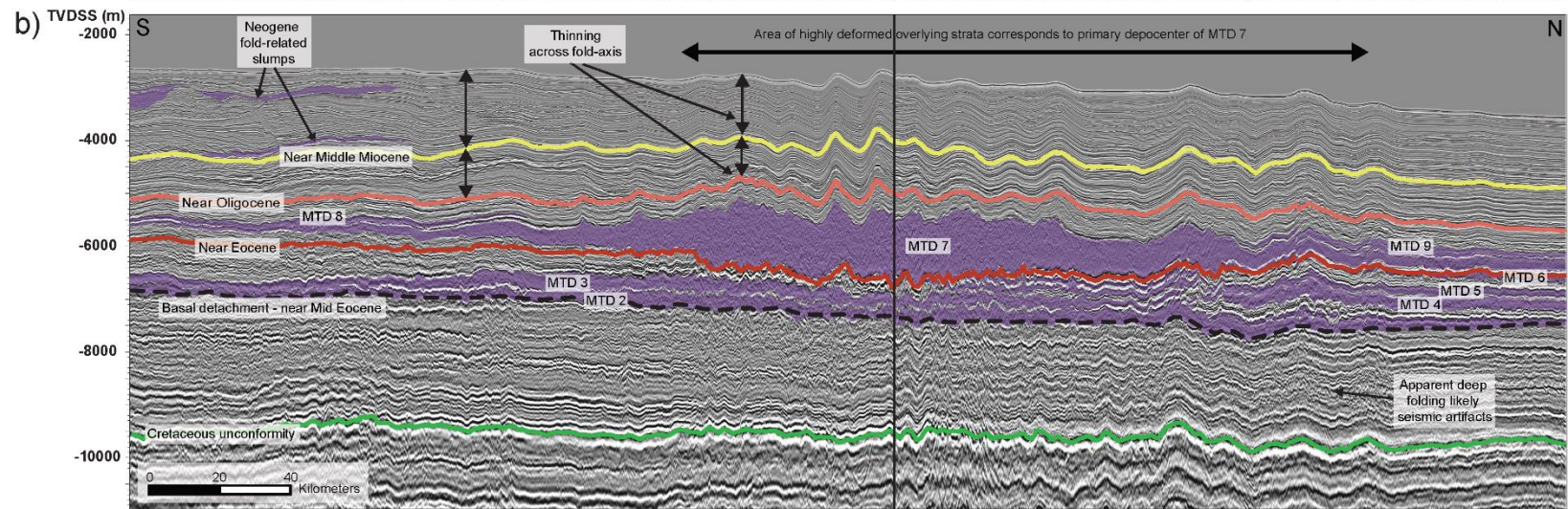
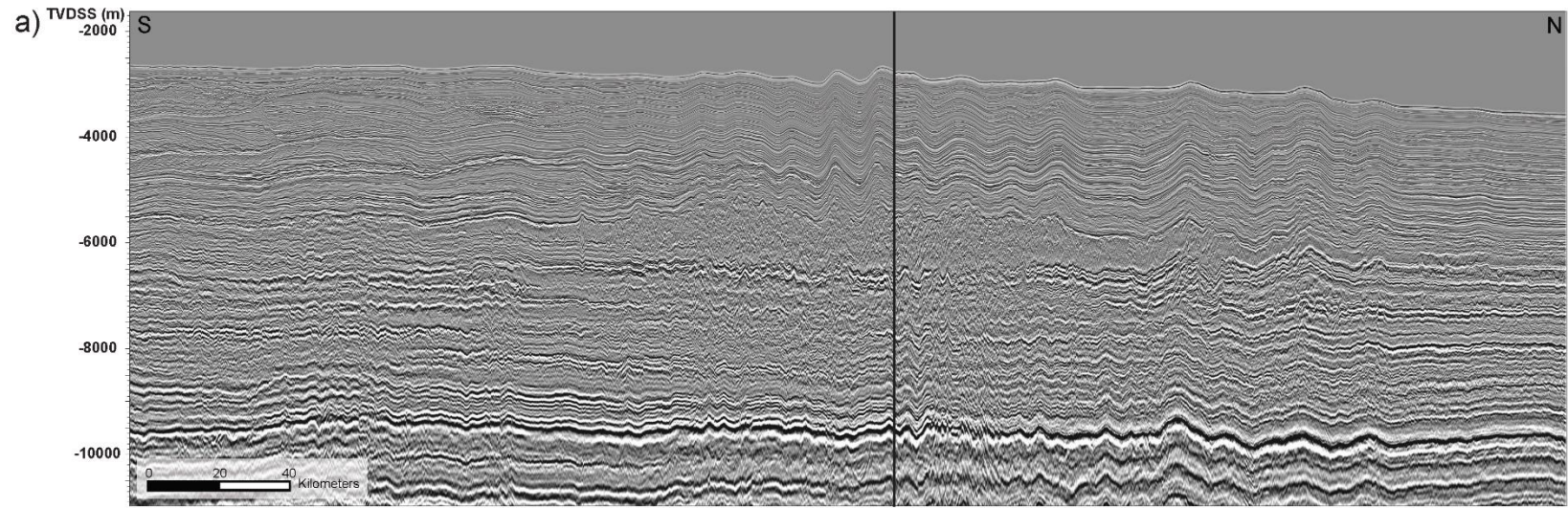


Figure 3.8 **a)** Uninterpreted, northeast-trending seismic dip profile showing the distribution of regionally extensive late Eocene-Oligocene MTDs that form a stacked, 2.5-km-thick package above the basal detachment level. **b)** Interpreted seismic dip profile displaying six stacked MTDs within the late Eocene-Oligocene sequence with minor faults terminating at various intervals within the package. MTDs extend laterally at least 100 km to the west from this area and continue beneath the Salina del Bravo salt canopy.

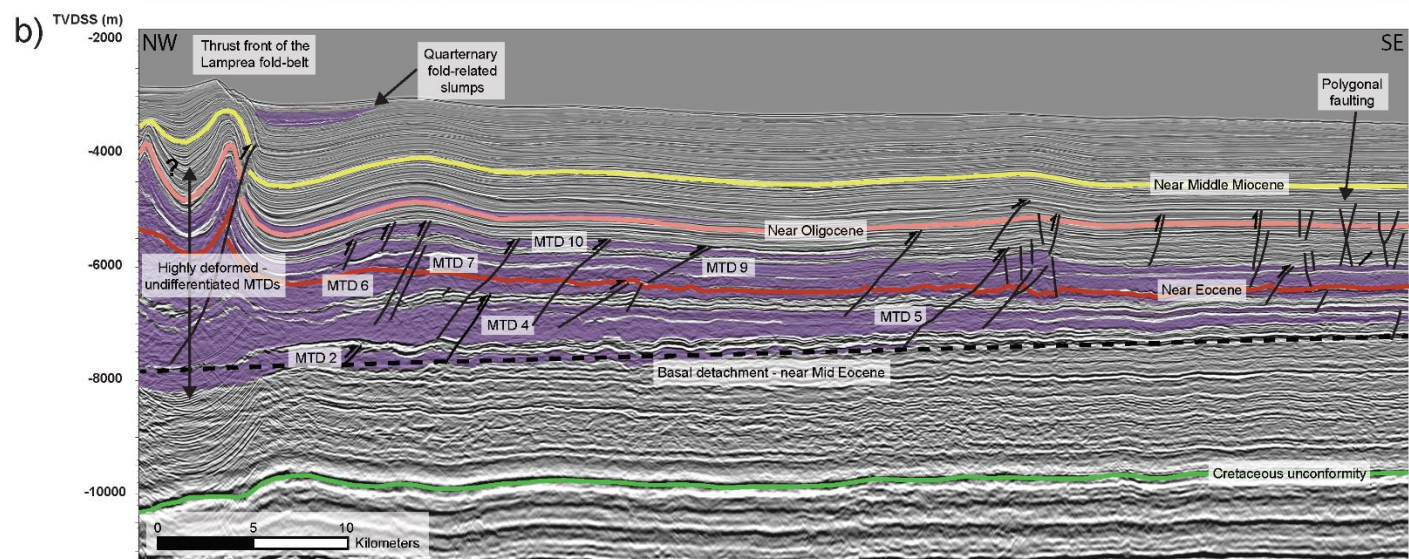
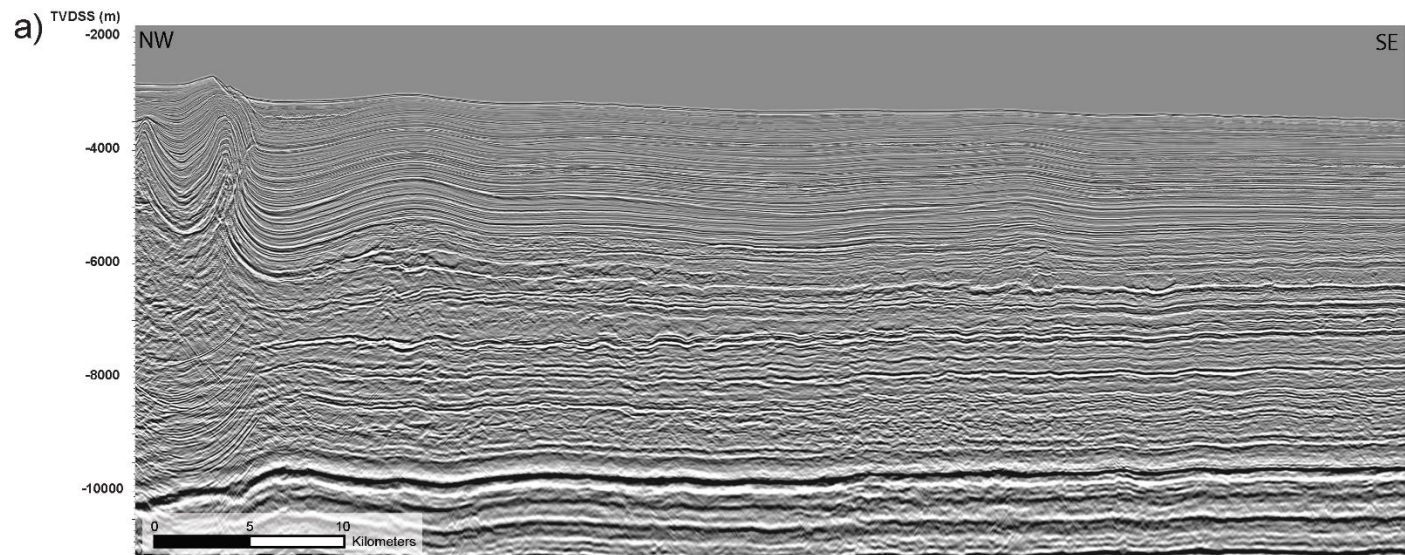
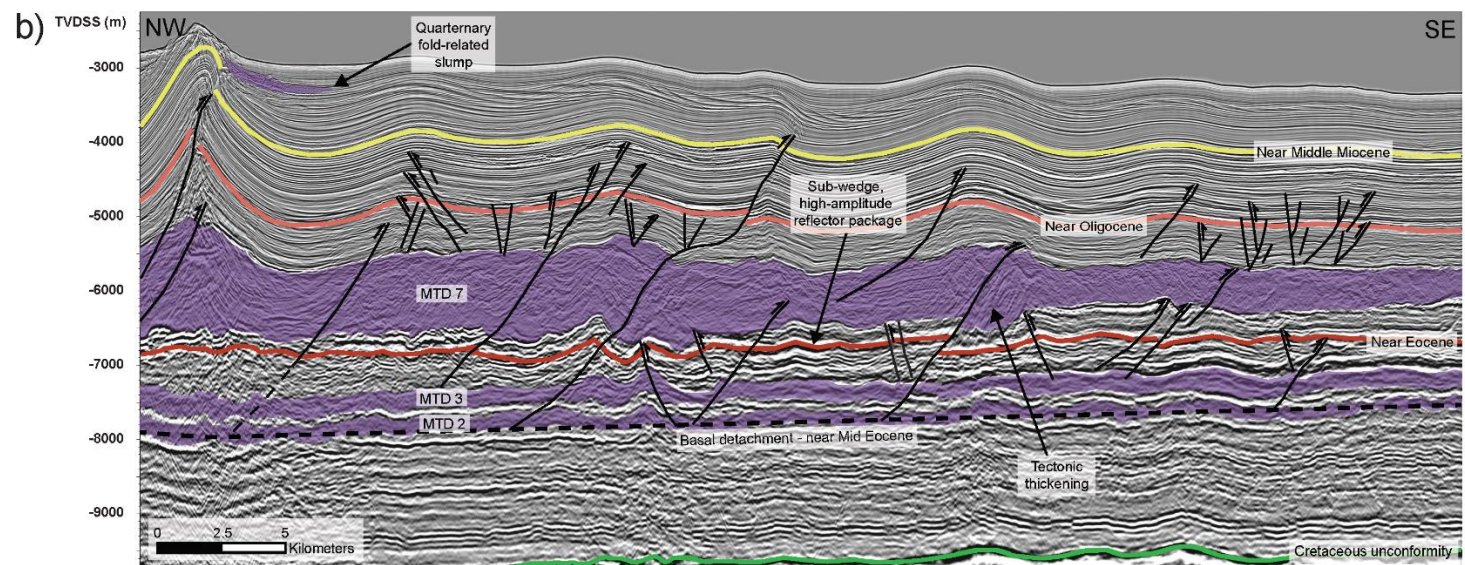
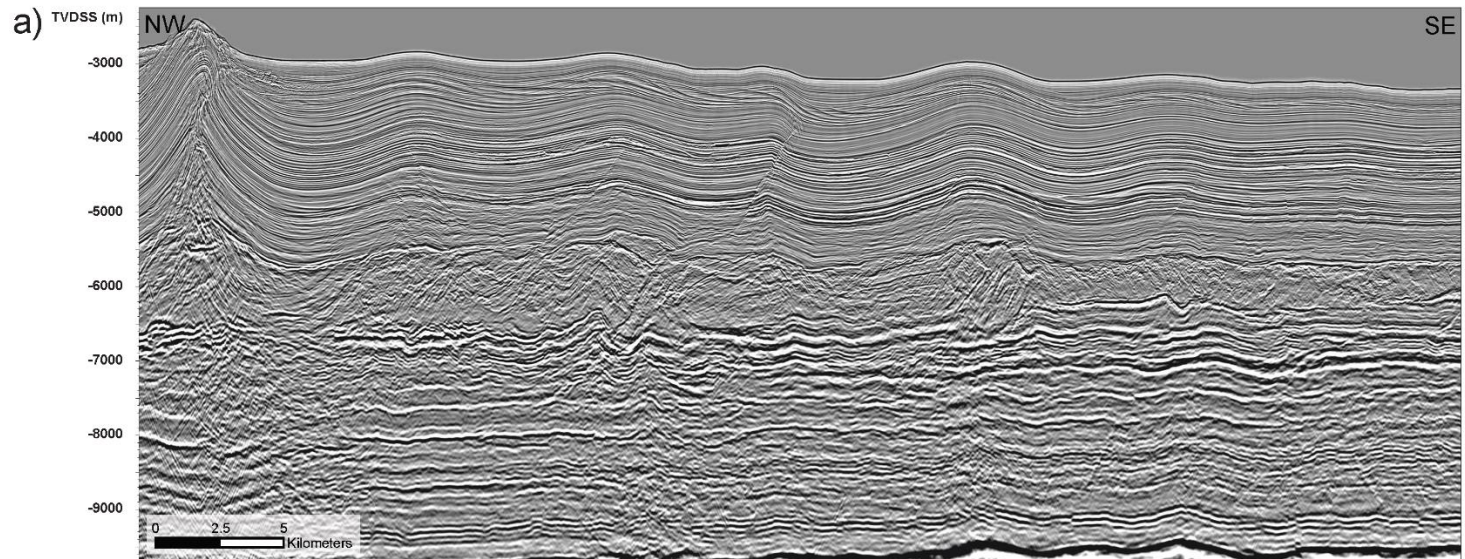


Figure 3.9 a) Uninterpreted, east-trending, seismic dip profile showing the distribution of regionally-extensive Eocene-Oligocene MTDs that are deformed by their proximity above the primary detachment level. b) Interpreted seismic profile showing Eocene (MTD 2, 3) and Oligocene (MTD 7) detachment units in the eastern deep-water area of the Mexican Ridges. Major, thrust faults penetrate most of the section and have propagated to the basal detachment. Smaller thrusts are less laterally extensive and less penetrative. Thrust faults are present in the fold cores overlying MTD 7, with many of these thrusts terminating along the top of this unit and within the underlying, parallel-bedded strata.



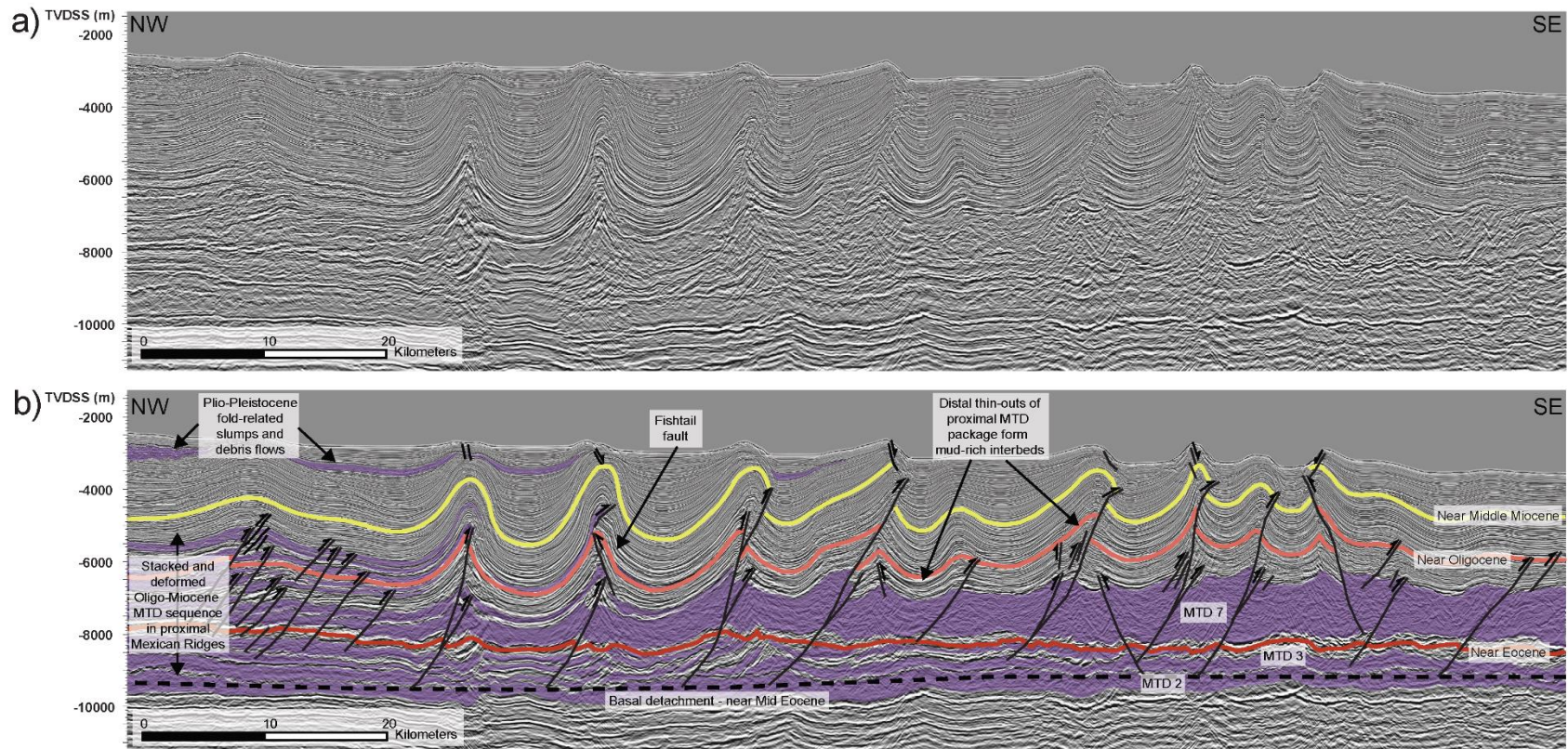


Figure 3.10 a) Uninterpreted, southeast-oriented, seismic dip profile through the thickest (>3000 m) and most intensively structurally-deformed area of MTDs in the northern Mexican Ridges. **b)** Interpreted seismic dip profile illustrating structural thickening of the MTD package and overlying strata. A stacked package of numerous MTDs thins laterally to form fine-grained inter-beds within the strata overlying MTD 7. Thrust faults are imbricated and utilize MTDs as secondary detachments.

3.4.3 Distribution, size, and thickness of Paleogene MTDs

Isochore mapping of selected, regionally correlatable MTD units (MTD 1–12) illustrate significant thickness variations in the MTD units along the length of the Mexican Ridges. The MTD units in Figure 3.11 and 3.12 have been mapped only as far as they are confidently correlatable and distinguishable as individual units. The MTDs commonly become very thin, highly deformed, and amalgamated with other units – particularly in the more structurally complex areas of the Mexican Ridges, and in adjacent locations such as the Lamprea fold-belt and the inner part of the Salina del Bravo salt province; where salt tectonics are the primary control on the structural style (Figure 3.11, 3.12).

The Eocene-age basal detachment unit mapped in the southernmost part of the Mexican Ridges is defined as MTD 1 (Figure 3.11). This Eocene detachment extends across the Catemaco fold-belt and into the Campeche salt province, where it was not mapped as part of this study (Figure 3.1). It is unclear if MTD 1 represents a single unit or multiple stacked and amalgamated units with intensive deformation along the detachment level. MTD 1 thins abruptly to the north, where it is intercalated with MTDs 2 and 3 (Figure 3.11). MTDs 2 and 3, also of Eocene age, are widely distributed and correlateable across the Mexican Ridges, where they exhibit thicknesses of over 600 m and 400 m, respectively. MTD 2 is thickest in the northern Mexican Ridges, while the apparent depocenter of MTD 3 is to the south and east of the Tuxpan Carbonate Platform (Figure 3.11). Towards the northernmost part of the study area, MTD 3 thins significantly and can be traced to the scale of a single seismic reflector (Figure 3.9, Figure 3.11).

Figure 3.11 Summary of isochore maps of selected MTD units mapped in this study. **a)** MTD 1, **b)** MTD 2, **c)** MTD 3, **d)** MTD 4, **e)** MTD 5, **f)** MTD 6. MTDs deposited during the late Eocene are regionally-present over the entire Mexican Ridges, with greater average thicknesses in the northern Mexican Ridges overall.

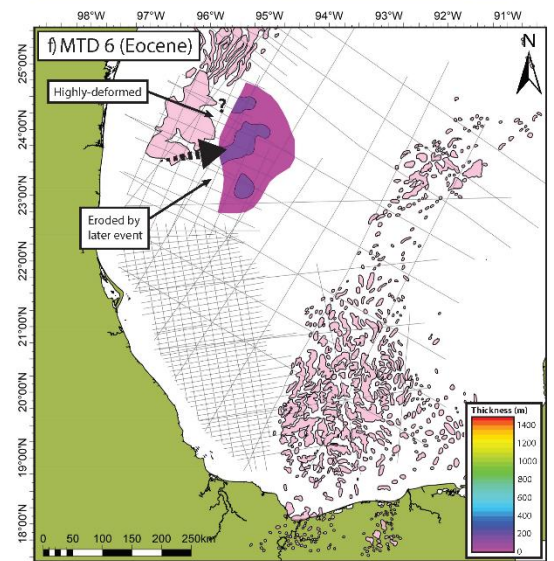
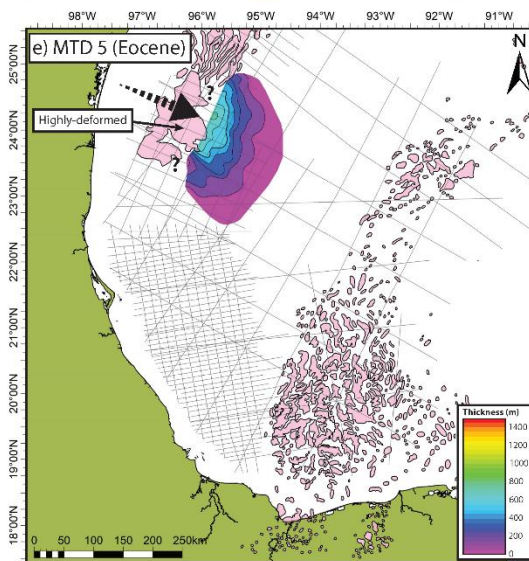
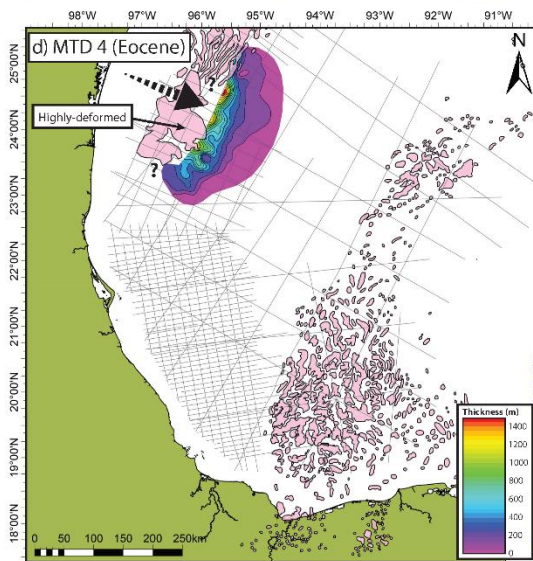
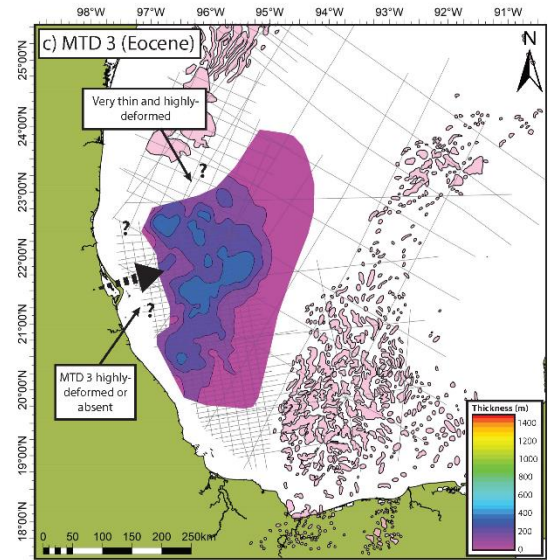
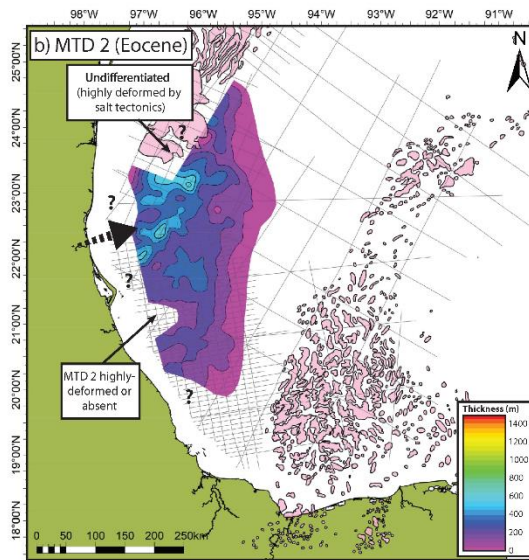
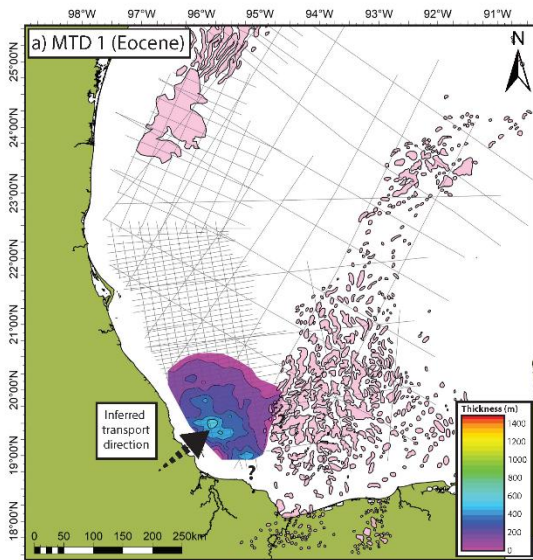
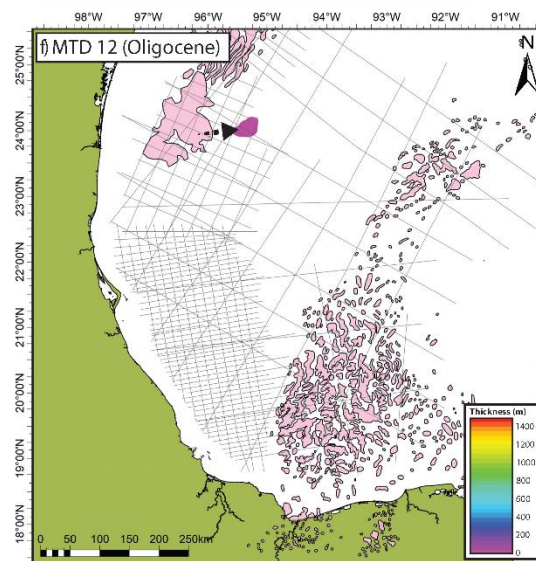
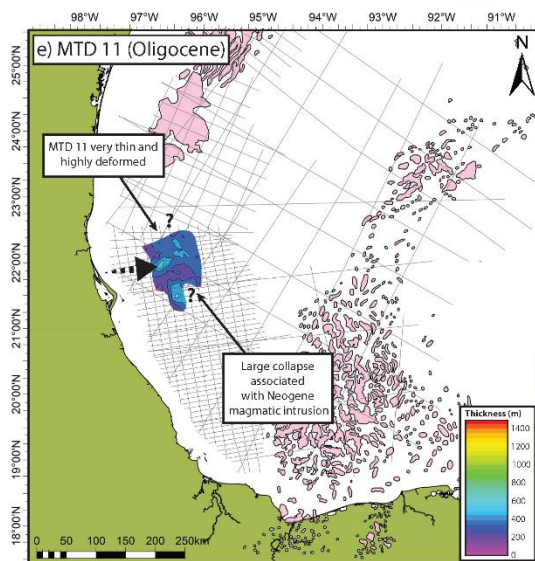
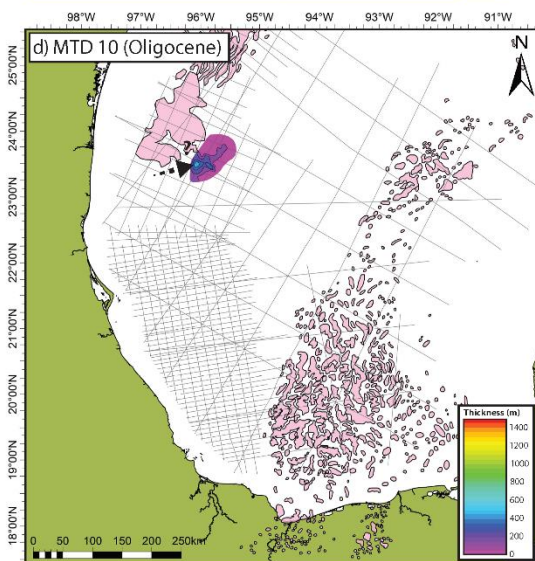
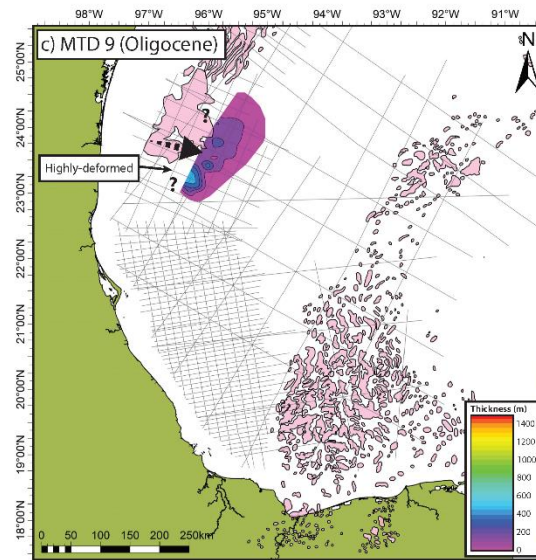
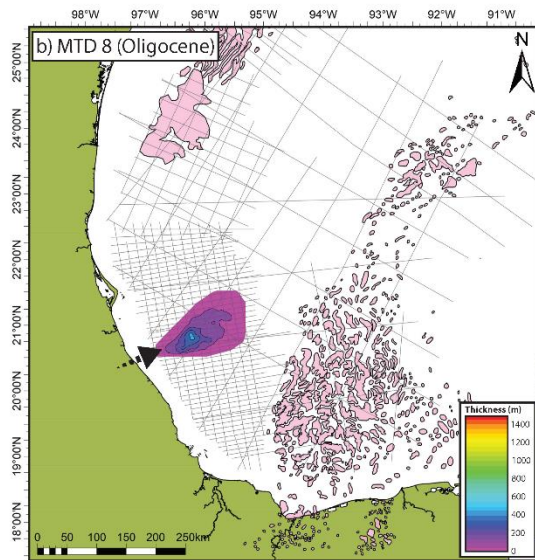
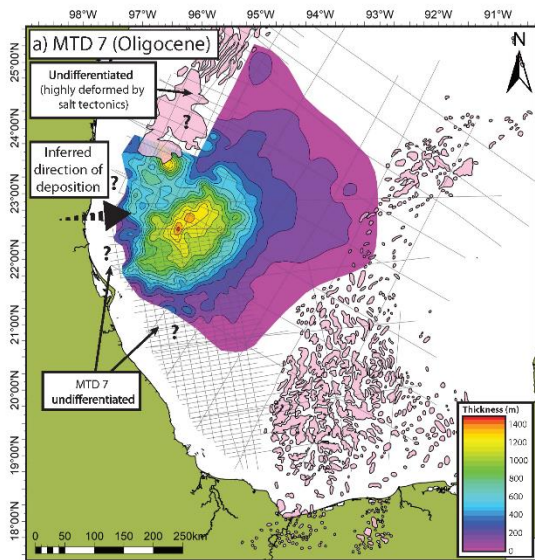


Figure 3.12 Summary of isochore maps of selected MTD units mapped in this study. **a)** MTD 7, **b)** MTD 8, **c)** MTD 9, **d)** MTD 10, **e)** MTD 11, **f)** MTD 12. MTDs deposited during the Oligocene are present predominantly over the northern Mexican Ridges, where thicknesses are greatest, in addition to the areas adjacent to the Salina del Bravo salt province.



In the deep-water Gulf of Mexico east of the Salina del Bravo salt province and Lamprea fold-belt, MTD 4 overlies MTD 2, and reaches thicknesses of >1400 m close to the salt-front (Figure 3.11). Overlying MTD 4, MTD 5 occupies a similar depositional extent and reaches a maximum a thickness of >500 m. Both units thin-out southwards, where they become highly deformed within the Mexican Ridges fold-belt (Figure 3.11). MTD 6 contributes to the stacked sequence in the northernmost part of the study area. MTD 6 attains a maximum thickness of >160 m and is significantly thinner than the preceding MTDs 4 and 5 (Figure 3.11). MTDs 4, 5, and 6 appear to continue westwards beneath the salt canopy and are likely present over significant parts of the Salina del Bravo salt province, where they are heavily deformed, amalgamated, and interact with salt tectonics (Figure 3.11). Although it thins close to seismic reflector scale, MTD 6 appears to be missing towards the southwest across the northern part of the Mexican Ridges due to erosion from the overlying MTD 7 (Figure 3.7, 3.11, 3.12).

Substantially thicker and covering a greater lateral extent than other MTD events in the Mexican Ridges and Salina del Bravo salt province, MTD 7 reaches thicknesses of >1400 m in the northern Mexican Ridges. Although MTD 7 thins significantly to <100 m, the unit can be traced >400 km to the opposing Yucatan margin (Figure 3.12). MTD 7 also thins to <100 m towards the south and is not present over large parts of the southernmost Mexican Ridges (Figure 3.7, 3.12). Similar to MTDs 4–6, MTD 7 also appears to be present across the Salina del Bravo salt province (Figure 3.12).

Following MTD 7, MTD units of Oligocene age become progressively smaller and thinner; however, they are more numerous and primarily concentrated in the northern Mexican Ridges, the Salina del Bravo, and Lamprea fold-belt areas (Figure 3.12). MTD 8 reaches

maximum thicknesses of >400 m and inter-fingers the southern pinch-out of MTD 7 (Figure 3.7, Figure 3.12). MTD 9 is a similar age and located to the north of MTD 7 adjacent to the Salina del Bravo salt province. Although MTD 9 is generally <200 m thick, it extends >400 m beneath some fold axes (Figure 3.12). MTDs 10 and 12 are both located east from the Salina del Bravo salt province in the northern part of the study area, with maximum thicknesses of greater than 450 m and 90 m, respectively. The depocenter of MTD 11 in the northern Mexican Ridges is >300 m thick; however, MTD 11 thins significantly to near seismic reflector scale towards the north where it becomes highly deformed within the fold-belt. Structural disruption of MTD 11 occurs towards the southeastern part of the study area, where a large igneous body intrudes the fold-belt (Pew, 1982), and marks the submarine, eastern terminus of the Miocene-Recent Trans-Mexican volcanic belt (Ferrari *et al.*, 2012) (Figure 3.12).

3.4.4 Structural analysis of MTDs and the overlying Mexican Ridges

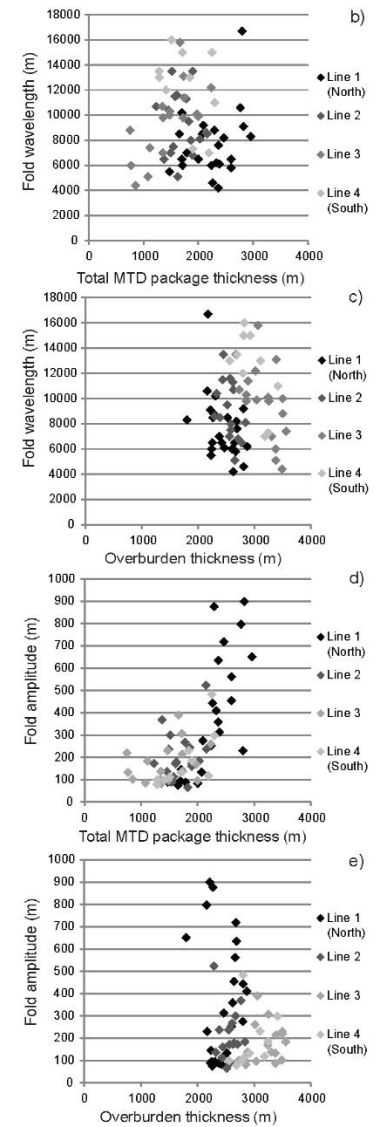
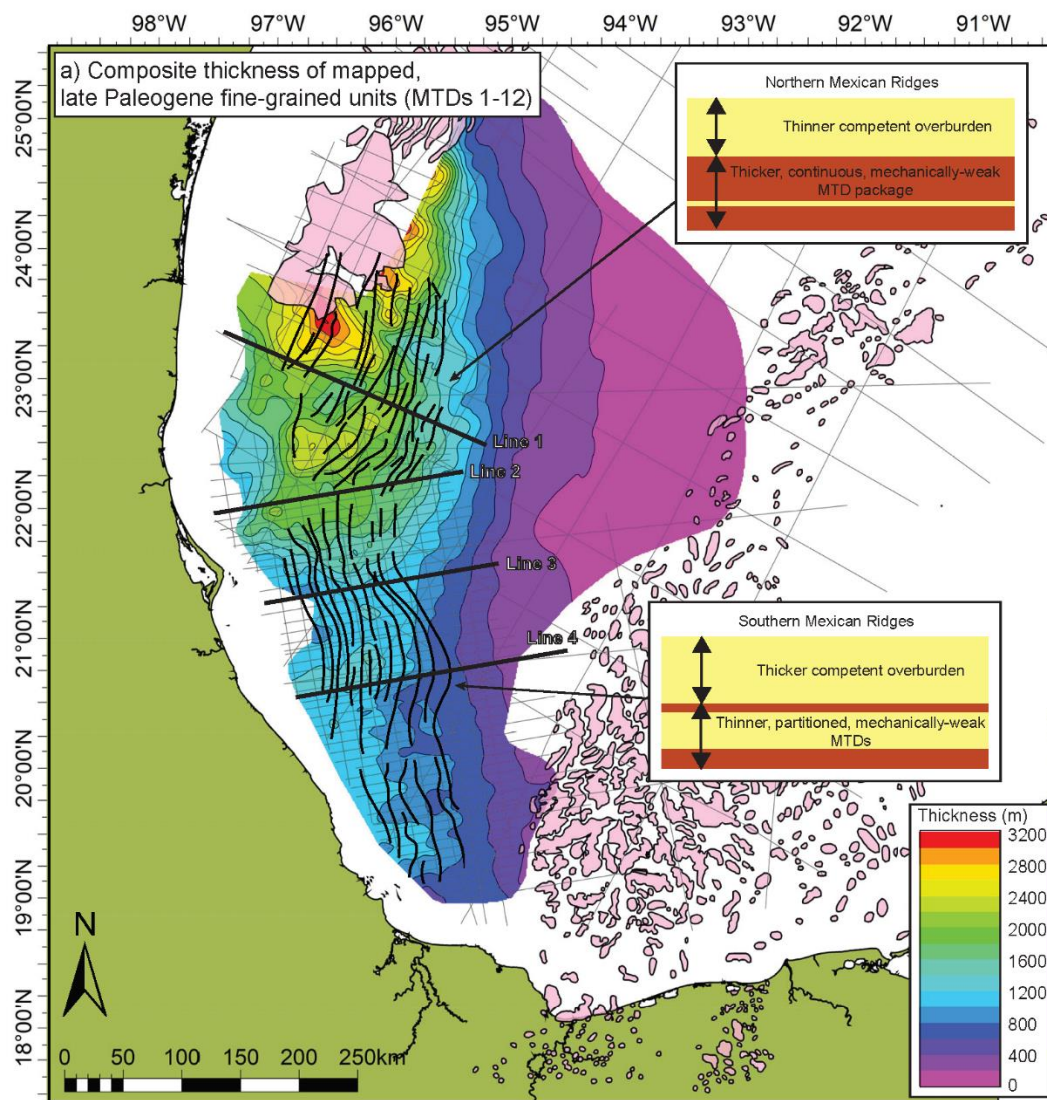
Isochores from each mapped unit (MTDs 1–12) were combined to produce a composite thickness map for the late Paleogene, which is a >3000 m thick and predominantly fine-grained, clastic sequence (Figure 3.13a). The total thickness of the stacked MTD package ranges from a maximum of >3000 m in the Salina del Bravo salt province and northern Mexican Ridges, <2000 m in the southern Mexican Ridges, and <200 m in the abyssal Gulf of Mexico towards the east. The northern Mexican Ridges possesses a mostly continuous sequence of MTD units throughout the late Eocene and part of the Oligocene, with overburden thicknesses <3000 m. In contrast, the southern Mexican Ridges commonly consists of much thinner clay-rich MTD

units that are separated by more competent bedded strata and overlain by a thicker sequence of overburden sediments (up to ~3600 m) (Figure 3.7, Figure 3.13a).

Geometric measurements of fold structures were performed across four representative seismic profiles located from north to south along the length of the Mexican Ridges (Figure 3.13). Data shown in Figure 3.13b–3.13e are based on measurements of two layers: 1) highly-deformed, fine-grained stacked MTD package; and 2) the overlying and more competent section. The MTD interval is measured from the basal detachment to the top of the fine-grained package, and the overburden from the top of the fine-grained package to the seafloor. The MTD layer defined for the southern Mexican Ridges comprises a thicker interbedded section of competent strata separating the MTD units than observed in the northern Mexican Ridges.

Measurements of total MTD thickness versus fold wavelength show that there is a general decrease in fold wavelength with increased MTD package thickness in the northern Mexican Ridges (Figure 3.13b). When plotting overburden thickness versus wavelength, there is also a correlation between shorter fold wavelengths and thinner competent overburden (Figure 3.13c). Trends between total MTD package thickness and fold amplitude show a relationship between thicker underlying MTDs and higher amplitude folds in the northern Mexican Ridges (Figure 3.13d). Measurements of total MTD thickness versus fold amplitude indicate fold amplitude values correspond to a ~1800–3600 m range in overburden thicknesses across the southern and northern Mexican Ridges. However, the largest observed fold amplitudes are only associated with the thickest underlying areas of the MTD package located in the northern Mexican Ridges (Figure 3.13e).

Figure 3.13 **a)** Composite thickness isochore of fine-grained mapped units located near the level of the basal detachment level (MTDs 1-12). Thicknesses range from > 3200 m in the northern Mexican Ridges to < 2500 m in the southern Mexican Ridges. Locations of seismic profiles 1-4 used for thickness and fold geometric measurements are shown on the map. **b)** Measurements of total MTD package thickness compared to fold wavelength. **c)** Measurements of overburden thickness compared to fold wavelength. **d)** Measurements of total MTD package thickness compared to fold amplitude. **e)** Measurements of overburden thickness compared to fold amplitude.



3.4.5 Characterization of DHIs and amplitude anomalies in the Mexican Ridges

Amplitude anomalies observed on the 2D seismic grid and previously published hydrocarbon seep data were compiled for the Mexican Ridges and correlated with its fold and thrust structure (Figure 3.14). Based on these observations, I classify the amplitude anomalies into two categories: 1) evident flat, bright, or dim spots, and 2) less defined, high-amplitude anomalies. Anomalies were identified from the seismic data based on the presence of any higher impedance contrasts (relative to average background reflectivity) that are associated with the mapped fold closures. Observed amplitude anomalies within the Miocene to Recent section typically resemble Class 3, gas-sand AVO characteristics as defined in the classification scheme of Rutherford and Williams (1989). Class 3 sand is low impedance and under-compacted and commonly found at shallow depths elsewhere in the Gulf of Mexico (Rutherford and Williams, 1989). Amplitude anomalies in Class 3 sands display relatively large reflectivities at all offsets (Rutherford and Williams, 1989). It is important to note that the interpreted amplitude anomalies may not necessarily represent hydrocarbon accumulations but also express lithological changes and porosity, which can also be a primary driver for amplitude response (Ware, 2002). Bottom Simulating Reflectors (BSRs), indicating the presence of shallow gas hydrates, were commonly observed across the length of the Mexican Ridges and were also compiled, along with wells with hydrocarbon shows, and nearby discovery fields (Figure 3.14a).

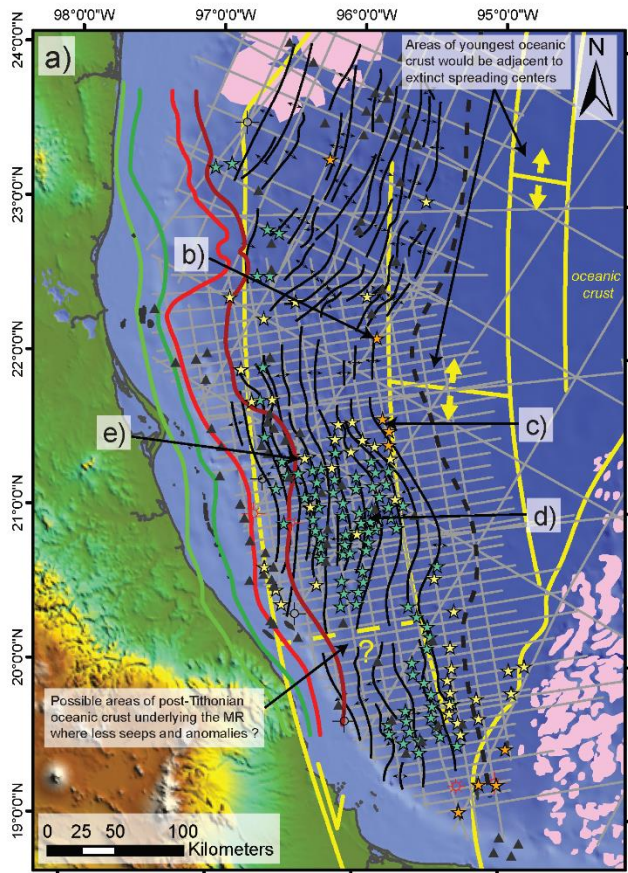
Amplitude anomalies and numerous thermogenic hydrocarbon seeps identified from piston-core data can be observed in both the southern Mexican Ridges and across northern Mexican Ridges, where the finer-grained MTD package is thicker (Holguín-Quiñones *et al.*,

2005, Comisión Nacional de Hidrocarburos, 2015) (Figure 3.14a, 3.14b, 3.14c). Although fewer amplitude anomalies are recorded in the northern Mexican Ridges compared to the southern Mexican Ridges, line spacing of the 2D seismic survey is also less dense across the northern Mexican Ridges. BSRs are most common in the southern Mexican Ridges, particularly in areas east of the Tuxpan Carbonate Platform and in the southernmost region of the fold-belt (Figure 3.14a, 3.14d). Both amplitude anomalies and BSRs closely correlate with anticlinal crests and fold axes, as seen on both seismic data and in map view (Figure 3.14). Shallow high-amplitude anomalies are commonly associated with the BSRs (Figure 3.14d, 3.14e).

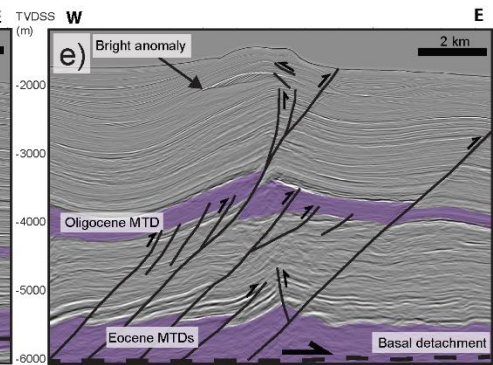
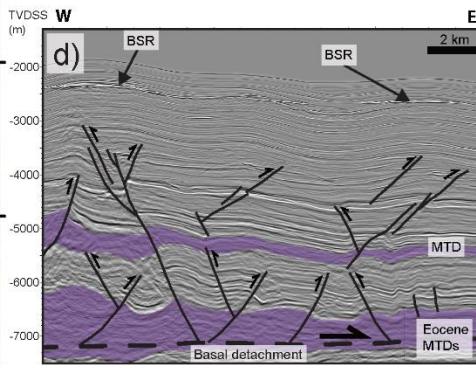
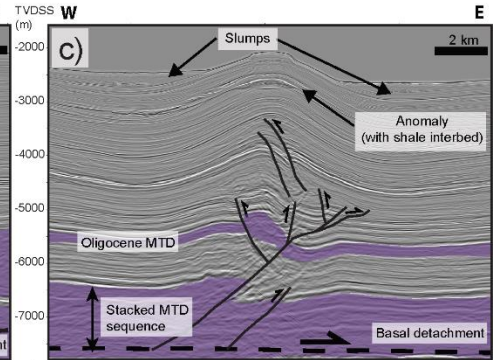
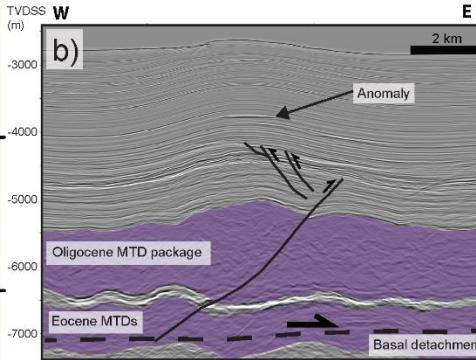
The locations of the continent-ocean boundary, spreading ridge, and fracture zones were interpreted from gravity data by Nguyen and Mann (2016) and have been compared with mapped seismic amplitude anomalies, and hydrocarbon seep data (Comisión Nacional de Hidrocarburos, 2015, Holguín-Quñones *et al.*, 2005, Salomón-Mora, 2013) (Figure 3.14). Areas of post-Tithonian oceanic crust that possess a potential source rock presence risk are predicted to occur in areas of the youngest and least sedimented, late Jurassic, oceanic crust that is adjacent to the short extinct spreading ridges. In the western Gulf of Mexico, these short, east-west-trending spreading ridges show major offsets along oceanic fracture zones (Figure 3.1). Inferred offset locations of youngest oceanic crust, where spreading ridges can be clearly defined, appear to fall outside of the Mexican Ridges area (Figure 3.14). Most of these predicted areas of youngest oceanic crust nearest the spreading ridges with a higher risk for source rock presence fall outside of the Mexican Ridges (Figure 3.14). However, the westernmost, extinct spreading ridge may underlie the southernmost part of the Mexican Ridges, and its location is unclear from gravity data (Román-Ramos *et al.*, 2008; Nguyen and Mann, 2016). Despite this,

the wide distribution of thermogenic seeps linked to the underlying Mesozoic stratigraphy indicates that the entire extent of the Mexican Ridges is likely underlain by Jurassic source rocks (Holguín-Quñones *et al.*, 2005) (Figure 3.14).

Figure 3.14 **a)** Hydrocarbon prospectivity summary map showing mapped amplitude anomalies, hydrocarbon seep data, hydrocarbon fields and select well shows, Jurassic source rock maturity, and locations of seismic examples shown in **b)**, **c)**, **d)** and **e)**. Additional geologic and hydrocarbon data were compiled from previous authors, including Ambrose *et al.*, (2005), Holguin-Quinones *et al.*, (2005); Salomon-Mora (2013); CNH (2015); and Nguyen and Mann (2016). **b)** Seismic example of a tilted amplitude anomaly associated with the crest of a major faulted fold-structure. **c)** Seismic example of a shallow amplitude anomaly disrupted by a shale inter-bed. **d)** Seismic example displaying multiple BSRs and associated amplitude anomalies focused along the crests of anticlines. **e)** Seismic example showing a shallow amplitude anomaly that may be associated with shallow gas hydrates.



- ★ High-amplitude anomaly
- ★ Flat, bright, dim spots
- ★ Bottom simulating reflector (BSR)
- ▲ Hydrocarbon seeps
- ⊛ Gas well
- ⊛ Gas shows or non-commercial
- ⊛ Dry well
- ⊛ Hydrocarbon field
- Shallow salt bodies
- ▭ Extinct COB, transforms, and spreading ridges (Nguyen and Mann, 2015)



- Maturity** (Ambrose et al. 2005)
- Early oil
 - Main oil
 - Main gas
 - Overmature

3.5 Discussion

3.5.1 Characterization of western Gulf of Mexico detachment shales as MTDs

I correlate seismic facies of Paleogene-age Mexican Ridges detachment units with specific types of MTD seismic facies that have been determined from analogous outcrop and well studies (Moscardelli and Wood, 2008; Ogata *et al.*, 2012) (Figure 3.5, 3.6). Based on the observations from seismic mapping, these MTD units form an up to 3500 m stacked sequence of clay-rich debris flows deposited as lobate bodies in a deep-marine setting (Figure 3.7, 3.8, 3.9, 3.10, 3.11, 3.12). The Paleogene MTD sequence was later deformed as a result of the Neogene development of the Quetzalcoatl Extensional System and its resulting down-dip shortening of the Mexican Ridges (Alzaga-Ruiz *et al.*, 2009). Further north, the MTD sequence has been strongly deformed by Oligo-Miocene age salt tectonics in the Salina del Bravo salt province, and outer, shale-cored Lamprea fold-belt (Comisión Nacional de Hidrocarburos, 2015) (Figure 3.2).

Ductile claystone allowed the MTD horizons to accommodate gravitational sliding and contraction along extensive detachment units that underlie the fold-belt. Puskon-1 is the only available lithological control of the MTDs located in their up-dip area, indicating that these MTD units consist dominantly of fine-grained lithologies based on penetration of the Oligocene-age MTD 7 unit (Figure 3.3b). Outcrop studies of basin-wide MTDs in the Northern Apennines (Ogata *et al.*, 2012), and other basinal settings worldwide (Festa *et al.*, 2016), show that a prominent feature of large MTDs is an unsorted, relatively fine-grained matrix, infilling void spaces between clasts of various size, age, and lithology. While MTDs commonly contain sand, MTD lithologies are usually dominated by mud-rich sediments that typically exhibit low

porosity (Shipp *et al.*, 2004). This type of mud-rich, MTD matrix likely represents the predominantly low-amplitude seismic facies characteristic of the MTD horizons (Figure 3.5).

In the Mexican Ridges, the intensity of post-depositional tectonic deformation of the Paleogene MTDs makes it challenging to determine which seismic facies record the original depositional fabric and which seismic facies are a result of post-depositional, structural overprinting (Figure 3.7, 3.10). In other shale detached fold-belts, such as the Niger Delta, over-pressured, muddy intervals that are utilized as detachments are also strongly tectonically disrupted and display similar seismic facies to MTD seismic facies (Wiener *et al.*, 2010) (Figure 3.5, Figure 3.6).

Some of the most compelling evidence that the detachment units in the Mexican Ridges were once debris flows are the erosive bases of the units, as observed in MTD 2 and MTD 7 (Figure 3.5, 3.7, 3.9). In the deep-water eastern area of the Mexican Ridges and Lamprea fold-belts, the detachment units continue to display lobate geometries and seismic characteristics of MTDs despite exhibiting much less structural deformation compared to the proximal fold-belts (Figure 3.8, 3.9, 3.10). The seismic facies of MTD 7 can also be observed hundreds of km east of the Mexican Ridges deformation front on the abyssal plain of the Gulf of Mexico (Figure 3.11). The thin, distal end of MTD 7 in the deep-water area is interpreted to be a compressional toe, where slide blocks and slumping of deep-water pelagic sediments developed in front of the debris flow as a result of its depositional body-force (Figure 3.5).

3.5.2 Mechanisms for controlling MTD deposits in the period following the Laramide orogeny

Based on geometric measurements of area and length, all twelve mapped MTDs group within the upper 15% of global, mass transport deposits sizes as compiled by Moscardelli and Wood (2016) (Figure 3.15). The large-volume MTDs in the study area show they were the result of large-scale, extra-basinal processes, based on the global classification of Moscardelli and Wood (2008). Possible causal mechanisms for the very large sizes of MTDs I describe from the Mexican Ridges include; 1) sea-level fluctuations, 2) gas hydrate dissociation, 3) earthquakes and tectonic activity, 4) high sedimentation rates, and 5) large-scale volcanic activity (Moscardelli and Wood, 2008, 2016).

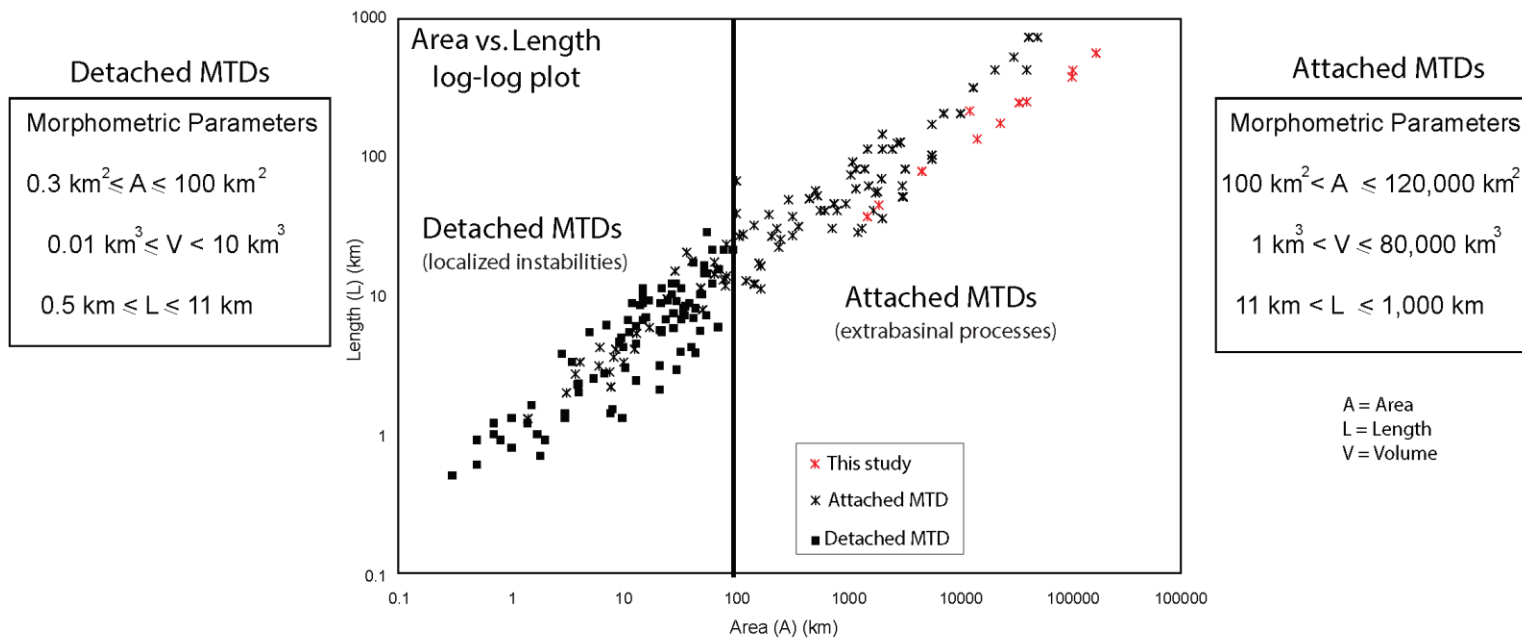


Figure 3.15 Area versus length, log-log plot that compares the sizes of MTDs measured in this study for the Mexican Ridges with MTD measurements from other areas that were compiled by Moscardelli and Wood (2016). The very large sizes of the MTD deposits in the Mexican Ridges indicates an origin resulting from extra-basinal, tectonic events related to the post-Laramide, regional deformation of eastern Mexico.

Post-Laramide deformation and inversion along the pre-existing Sierra Madre Oriental thrust front and its adjacent, foreland area have been dated to between 22 and 40 Ma using low-temperature thermochronology (Gray *et al.*, 2001). This late Eocene to earliest Miocene period of cooling, exhumation, and erosion along the thrust front and foreland basin is roughly age-equivalent to the ages of the mapped MTD events offshore (Figure 3.16). Uplift occurred along the southern Sierra Madre Oriental during the late Eocene and progressed northwards through the Oligocene and earliest Miocene in the region of the Tamaulipas Arch, which is directly adjacent onshore to the northern Mexican Ridges and Salina del Bravo salt province (Gray *et al.*, 2001) (Figure 3.16). This south-to-north pattern of exhumation and erosion along the Laramide orogenic belt is consistent with the pattern of distribution and timing of MTD deposition, as shown in Figure 3.16b and 3.16c. While late Eocene MTDs are widespread across the fold belt (Figure 3.16b), deposition of numerous MTDs in the northern Mexican Ridges and Salina del Bravo salt province occurred during the inversion of the Tamaulipas Arch (Gray *et al.*, 2001) (Figure 3.16c). The increasingly small size and proximal locations of MTDs into the earliest Miocene in the northern Mexican Ridges may reflect the eventual waning of tectonic activity in this area (Figure 3.10).

Inversion of the Laramide foreland basin resulted in high rates of sedimentation into the western Gulf of Mexico, where stratigraphic thicknesses of up to 5–7 km were uplifted and eroded during late Eocene and Oligocene time (Gray *et al.*, 2001). Large scale drainage systems were also located in the Rio Grande area to the north, along with a series of smaller drainage systems that extended further south along the Tampico margin (Galloway *et al.*, 2000, 2011; Galloway, 2005). MTD-related slope failure could have been influenced by distal instabilities

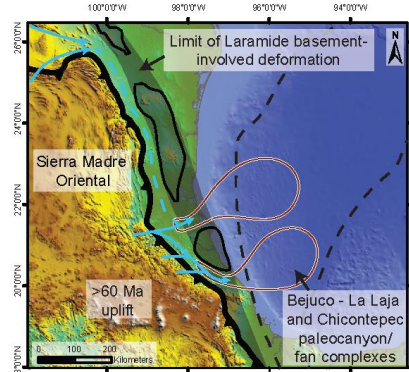
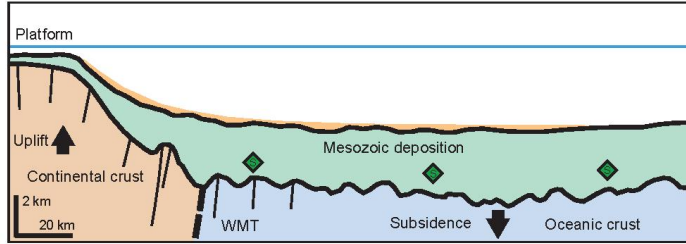
of the Laramide and post-Laramide orogenic belt that led to the observed high rates of nearby sediment outbuilding, particularly in the northern Mexican Ridges and Salina del Bravo salt province. Extensive post-Laramide volcanism across North America would have supplied an influx of a combination of clastic rocks, volcanoclastic rocks, and volcanic ash into the Gulf of Mexico (Galloway *et al.*, 2000; Galloway, 2005). This large influx of clastic rocks combined with volcanic ash may explain the pervasive fine-grained material associated with these late Eocene and Oligocene MTD deposits.

The series of NW-SE trending Mesozoic highs, including the Tamaulipas Arch and Tuxpan Platform (Figure 3.16), were inverted during the Laramide orogeny and post-Laramide tectonic activity that continued to the earliest Miocene and formed the steep shelf-edge along the eastern Gulf of Mexico margin (Gray *et al.*, 2001). The presence of an over-steepened continental margin in this area also reflects the underlying Jurassic-age Western Main Transform, that produced a relatively short transition (over <100 km) from continental crust in eastern Mexico to deeply buried, oceanic crust in the western Gulf of Mexico (Román-Ramos *et al.*, 2008; Nguyen and Mann, 2016) (Figure 3.1, 3.16).

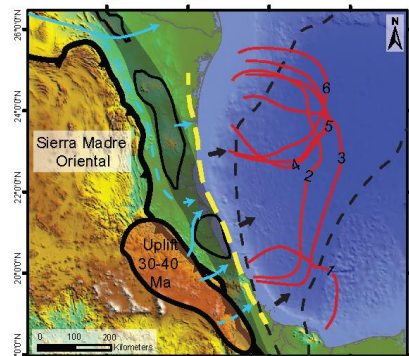
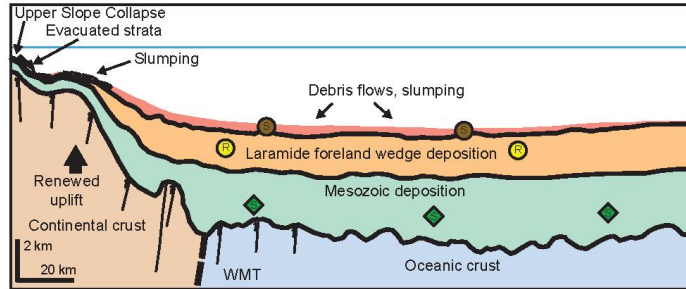
Overall, MTD deposition in the Mexican Ridges resulted from a combination of tectonic activity and high sedimentation rates along a steep, unstable margin, combined with other extra-basinal factors, including sea-level fluctuations, which together, worked to induce shelfal failure. Although not shown on the Haq *et al.*, (1987) sea-level curve (Figure 3.3a), outcrop studies along the US Gulf Coast suggest a significant sea-level fall in the earliest Oligocene related to the initial formation of Antarctic ice (Miller *et al.*, 2008). This sea-level fall could explain the significantly larger size and extent of MTD 7 (Figure 3.12a).

Figure 3.16 Schematic cross-sections and depositional events maps for key periods in the tectonic evolution of the Mexican Ridges. **a)** Laramide orogenic phase from the late Cretaceous and Middle Eocene. **b)** Post-Laramide late Eocene inversion and erosion of the southern Sierra Madre Oriental and coinciding with deposition of MTDs offshore. **c)** Post-Laramide Oligocene inversion and erosion of the northern Sierra Madre Oriental coinciding with deposition of MTDs offshore. **d)** Late Miocene to recent passive-margin gravitational failure and formation of the Mexican Ridges that was closely controlled by deformation of fine-grained Paleogene MTDs. Additional tectonic, structural, and depositional elements compiled from Galloway *et al.*, (2000); Gray *et al.*, (2001); Galloway *et al.*, (2011); Cossey *et al.*, (2016); Yarbuh and Contreras, (2017); Snedden *et al.*, (2018).

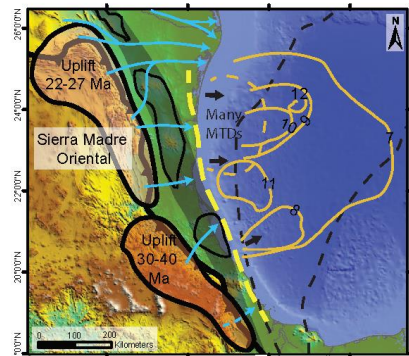
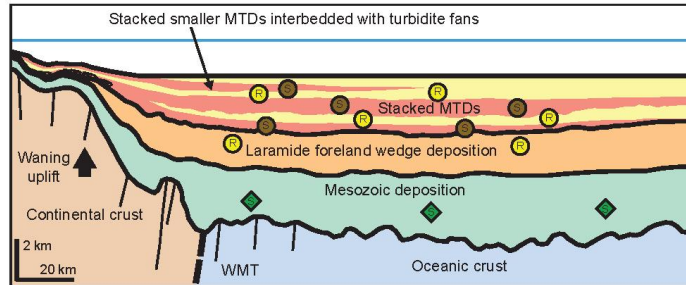
a) Initiation of Laramide orogenic activity (Late Cretaceous)



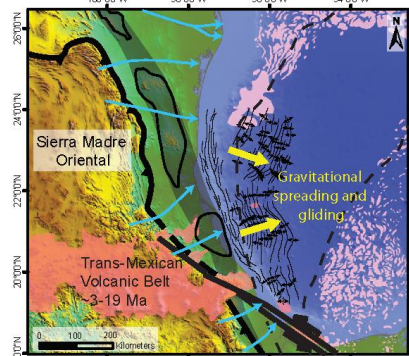
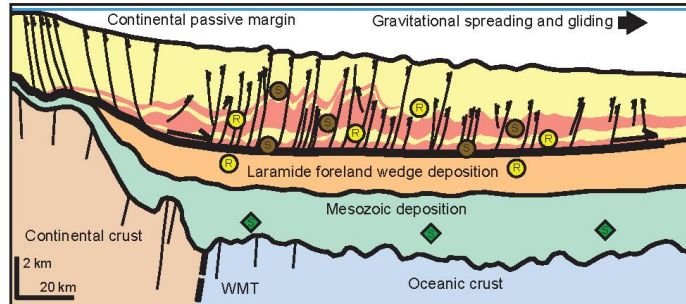
b) Post-Laramide inversion and MTD deposition (Late Eocene)



c) Post-Laramide inversion, pre-gravitational failure (Oligocene - early Miocene)



d) Gravitational failure and passive margin fold-belt (Late Miocene - present day)



- ◆ Source interval
- Structural high
- Paleodrainage
- Late Eocene MTD
- Shallow salt body
- R Reservoir interval
- S Seal interval
- Laramide basement-involved structural trend
- Inferred paleodrainage
- Oligocene MTD
- + Mexican Ridges fold-axis
- Continent - ocean boundary (COB)
- Paleocene - early Eocene canyon-fan complex
- Stacked Oligocene - Miocene MTDs
- Quetzalcoatl Extensional System fault

3.5.3 Control on the structural development of the Mexican Ridges by MTDs

Clay-rich MTD units in the Mexican Ridges display evidence of ductile deformation and distinct tectonic thickening along many anticlinal fold axes (Figure 3.7, 3.8, 3.9). MTD units do not exhibit the high degree of ductile mobility that can be observed in neighboring areas of the US Gulf of Mexico and Campeche salt basin, where Jurassic salt-cored detachments control prominent diapiric structures (Hudec *et al.*, 2013). The Niger Delta fold-belt also displays a higher degree of shale diapirism than observed across much of the Mexican Ridges (Wiener *et al.*, 2010). The lack of significant shale diapirism and associated withdrawal features in the Mexican Ridges indicate a more limited strength contrast between the fine-grained MTDs and their more competent overburden (Mitra, 2002). MTD thickness trends are interpreted to result from a combination of variable and lobate depositional thickness with subsequent tectonic thickening of the mapped units in the Mexican Ridges fold-belt (Figure 3.11, 3.12).

Significant tectonic thickening is also observed within the folded Oligo-Miocene strata that overlie the ductile-deformed MTD horizons that control detachment faulting and suggest this interval may accommodate a substantial proportion of the overall Mexican Ridges contractional deformation. Contractional deformation in the more competent, overlying strata is accommodated mainly by faulting rather than ductile deformation (Figure 3.9, 3.10). However, flexural-flow of fine-grained material from the distal pinch-outs of interbedded Oligo-Miocene MTDs acts as a significant control on contraction in the overlying Oligo-Miocene pre-growth section (Figure 3.10).

Seismic interpretation of fault planes within the Mexican Ridges suggests a widespread, Eocene-age basal detachment located near the base of the stacked MTD package (Figure 3.7, 3.8, 3.9, 3.10). Minor thrust faults appear to detach at various levels within the MTD sequence above the basal detachment and are controlled by lateral thickness changes between individual MTD units (Figure 3.10). The presence of multiple detachments and highly-mobilized shale varies from fold to fold as seen in Figure 3.10. The presence of a “fishtail” fault structure is particularly characteristic of a multiple detachment system, where oppositely-verging faults can be observed splaying off multiple interbedded debris flows within a single fold structure (Harrison and Bally, 1988) (Figure 3.10 – third structure from left).

The inherent mechanical weakness of the late Eocene-Oligocene sequence is not necessarily a result of the MTD formation alone but instead could result from the intrinsic weakness of the initially deposited layers, which were then remobilized and utilized as both MTDs and later as fold-belt detachments. Detachments occur along similar age strata in other areas of the Gulf of Mexico and along discrete horizons of very thin shales (e.g., McDonnell *et al.*, 2009; Comisión Nacional de Hidrocarburos, 2015). These observations suggest that the anomalous mechanical weaknesses of these layers control the amplitude and wavelength of folds in the Mexican Ridges (Figure 3.13).

Salomon-Mora *et al.*, (2011) have previously suggested that the variability in both overburden and detachment thicknesses control variations in structural style across the Mexican Ridges. The measurements of Mexican Ridges fold geometries are consistent with their previous observations (Figure 3.13). Conceptual modeling in the Niger Delta suggests that an area of thicker underlying shale to a thinner overburden would result in a higher degree of

deformation in the overlying strata and partitioned, faster gravitational spreading compared to the area with thinner shale (Wu *et al.*, 2015). Variations in relative shale thicknesses have also suggested a link with over-pressure distribution, which is seen as a primary control on detachment in the Niger Delta (Wiener *et al.*, 2010). The average thickness of the clay-rich MTD package varies significantly across the Mexican Ridges on the order of >1000 m (Figure 3.13a), which may control the distribution of overpressure across the fold-belt. Faster gravitational spreading due to the presence of a broader stacked package of over-pressured, mechanically-weak MTDs in combination with thinner more-competent overburden may be partly responsible for the locally more numerous, closely-spaced, and tighter folds located in the fore-wedge region of the northern Mexican Ridges, that is observed on both seismic lines and in map view (Figure 3.10, 3.13).

While the Niger Delta fold-belt is similarly detached on over-pressured muds, its passive margin fold-belts exhibit a wide variety of fault-bend, fault-propagation, and detachment folds (Corredor *et al.*, 2005). In the Mexican Ridges, however, folds appear to initiate as buckle folds, with continued shortening in the proximal folds becoming accommodated increasingly by imbricate thrusting (Pew, 1982). The less-developed, outermost folds of the Mexican Ridges possess fairly regular wavelengths, have low (<5°) limb-dip angles, and higher length-to-width ratios (Figure 3.8, 3.9). The presence of imbricate, low-angle thrusts in these low-amplitude, distal folds suggests that these thrusts formed during folding. The difficulty of buckling can be attributed to both the low ductility contrast between competent and incompetent units, and the greater relative thickness of competent strata (Pew, 1982). Thinner, more competent overburden strata in comparison to thicker underlying MTD units,

could have allowed folding to occur more easily in the northern Mexican Ridges, despite possessing a lower ductility contrast between the units. As a control of folding in the Mexican Ridges, the weakness of the deformed MTDs and their folded overburden strata are interpreted to act concurrently with the degree of gravitationally stress on the system and total amount of accommodated shortening linked to the Quetzalcoatl Extensional System up-dip. Ancillary factors such as lithological and pore pressure variations are difficult to define with few well penetrations across the fold-belt and cannot be discounted as additional controls on fold development.

This unique character of the Mexican Ridges fold-belt results from a combination of; 1) MTDs forming an anomalously weak shale detachment 2) a thick, layered sequence of over-pressured sediment that can deform ductilely, and 3) apparent absence of significant syn-growth growth patterns across the distal folds, where topographic relief and sedimentation rates at the seafloor are sufficient to balance upwards fold growth. Observation of the dip of the basal detachment and angle of seafloor topography suggests they would form a very low-angled taper wedge (Figure 3.10), which would require a very weak detachment to deform internally (Suppe, 2007).

3.5.4 Implications for hydrocarbon prospectivity

Oceanic spreading in the Gulf of Mexico is thought to have continued into the earliest Cretaceous (Pindell and Kennan, 2009; Nguyen and Mann, 2016), meaning that Jurassic-source rocks may not exist above areas where oceanic crust is younger than Tithonian. A possible area of deeply-buried, young, oceanic crust is inferred east of the Veracruz Basin, where relatively

fewer hydrocarbon seeps and amplitude anomalies are observed (Holguín-Quiñones *et al.*, 2005) (Figure 3.14).

As the Mexican Ridges detaches on Paleogene shales, there is a lack of significant structural deformation below this detachment interval, which reduces the possibility of effective hydrocarbon migration pathways from the lower Mesozoic section (Figure 3.16). The thick, extensive, clay-rich, over-pressured, and largely impermeable MTDs likely form good seal horizons - but may also create barriers for hydrocarbon migration. The presence of lateral equivalents of Paleocene-early Eocene Wilcox sands has been suggested to underlie much of the Mexican Ridges (Snedden *et al.*, 2018). Hydrocarbons migrating from Mesozoic source rocks may encounter this deep carrier system, where present, and migrate laterally up-dip before reaching the detachment zone. Puskon-1 reportedly encountered wet gas shows within these intervals, which could support the existence of Mesozoic source rocks connected to up-dip early Paleogene reservoirs (E&P Magazine, 2012).

Despite the migration risk, the presence of numerous mapped seismic amplitude anomalies in the overlying fold-belt suggests that thrust faults and associated fracturing may provide adequate migration pathways for Mesozoic hydrocarbons to pass through the thick regional seals and underlying carrier beds. In the northern Mexican Ridges, where the MTD package is thicker than the southern Mexican Ridges, amplitude anomalies show a strong correlation with thrust detachment folds (Figure 3.14). Thermogenic hydrocarbons linked to the Mesozoic are confirmed from maps of seafloor seeps that are associated with Mexican Ridges fold-thrust structures at the seafloor. These seeps support the migration of deep hydrocarbons along thrust faults (Holguín-Quiñones *et al.*, 2005; Comisión Nacional de

Hidrocarburos, 2015) (Figure 3.14). The slightly tilted seismic anomaly shown in Figure 3.14b could represent a paleo-oil water contact from residual hydrocarbons, where the structure has been tilted after breaching. Alternatively, the anomaly may indicate a hydrocarbon accumulation within a lower permeability and porosity interval (Ware, 2002) (Figure 3.14b). Another discontinuous amplitude anomaly appears to be truncated by a shale inter-bed (Figure 3.14c).

The presence of numerous BSRs across the Mexican Ridges suggests the presence of a gas-rich system, which correlates well with predicted late Jurassic maturity trends from Ambrose *et al.*, (2009) (Figure 3.14a and 3.14d). Many of the BSRs across the Mexican Ridges can be classified as "clustered" and are analogous to high-saturation BSRs associated with structurally-confined turbidite sequences observed in the Perdido fold-belt further to the north (Portnov *et al.*, 2019) (Figure 3.14d, 3.14e). However, the presence of gas hydrates does not necessarily indicate thermogenic gas (Brooks *et al.*, 1999). Many of the less defined amplitude anomalies may be associated with the shallow gas hydrates, and a significant component of gas found in the Mexican Ridges may originate in the fold-belt as biogenic gas with minor contributions of thermogenic hydrocarbons migrating from deeper sources (Figure 3.14d, 3.14e). The existence of many oil seeps across the Mexican Ridges does not correspond with the high levels of present-day overmaturity observed for their corresponding Mesozoic source intervals (Figure 3.14a). Oil presence could be explained by hydrocarbon fluid re-migration facilitated by the later development of the Mexican Ridges, forming thrust-fault and associated fracture conduits through the MTD package in the period from the late Miocene to present.

3.6 Conclusions

Paleogene-age thrust detachments in the Mexican Ridges and Lamprea fold-belts detach above a >3500 m thick interval of stacked and thrust-deformed MTDs. The MTDs were deposited as large lobes beneath the fold-belts, as well as underlying the salt canopies of the adjacent Salina del Bravo salt province to the north. MTD units control the mechanical stratigraphy, structural style, and tectonic evolution of the overlying Mexican Ridges fold-belt and, consequently, impact its hydrocarbon potential. The main findings of this study are summarized as follows:

1. 12 mapped Paleogene MTDs comprise a stacked, >3500 m thick, stratigraphic interval that form weak, stratigraphic surfaces. These weak surfaces localize the up-dip, normal detachment and the down-dip thrust detachments for the overlying Miocene to Recent, shale-detached Mexican Ridges passive margin fold-belt, and are tectonically deformed across the neighboring salt and shale province of the Salina del Bravo salt province and its peripheral Lamprea fold-belt (Figure 3.7-3.12).

2. MTDs in the Mexican Ridges, Salina del Bravo salt province, and Lamprea fold-belt were deposited as the result of extra-basinal scale processes triggered by post-Laramide tectonic events in eastern Mexico. The MTDs range in maximum composite thickness across 12 individual MTDs from <2000 to >3500 m, can cover areas of >100,000 km², and extend distances of over 500 km from the zone of up-dip, normal faulting in eastern Mexico to the abyssal plain of the Gulf of Mexico (Figure 11, Figure 12). These large MTD volumes place these western Gulf of Mexico MTDs in the top 15% of the largest known gravity-driven

deposits worldwide based on comparison of the results with the global MTD synthesis by Moscardelli and Wood (2016) (Figure 3.15).

3. These MTDs formed as the result of tectonic instability and high rates of clastic deposition adjacent to a steep continental margin. MTDs accompanied post-Laramide (late Eocene-earliest Miocene) exhumation of the Laramide orogenic foreland in eastern Mexico (Figure 3.16). Progressive south-to-north exhumation along the remnant Sierra Madre Oriental thrust front, inferred from low-temperature, thermochronology studies by Gray *et al.*, (2001), correlate with the sequential depositional pattern of MTD units mapped in this study (Figure 3.16b, 3.16c).

4. South-to-north, margin-parallel uplift resulted in the deposition of a significantly thicker, stacked sequence of fine-grain dominated MTDs in the northern Mexican Ridges and Salina del Bravo salt province that was located directly east of the Tamaulipas Arch during the Oligocene (Figure 3.16c). In the northern Mexican Ridges, the thicker MTDs and their thinner overburden provide an important control on the structure of the fold-belt with; 1) shorter fold wavelengths, 2) higher fold amplitudes, and 3) tighter inter-limb angles than observed in the southern Mexican Ridges (Figure 3.13).

5. The broader zone (>200 km) of distributed thrusting of the northern Mexican Ridges is influenced by 1) a thicker (>3500 m) underlying zone of over-pressured, mechanically-weak, fine-grained MTDs; and, 2) a thinner (1800–2900 m) overlying sequence of more mechanically competent overburden (Figure 3.7, 3.13). The Mexican Ridges MTD stratigraphy acts concurrently with and is deformed by up-dip, load-driven gravitational failure along the continental margin.

6. The base of the stacked MTD package forms the primary detachment for the Mexican Ridges, although secondary detachments are locally present across the fold-belt. Many MTD units are variably employed as fault-detachment surfaces (Figure 3.10). The interpretation of pre-existing MTDs utilized as detachment surfaces raises the possibility that other shale-detached fold-belts could be controlled by detachments along extensive and weak MTD horizons.

7. The presence of subsurface, hydrocarbon indicators and thermogenic seafloor seeps associated with break-thrust detachment folds support the existence of an active petroleum system with open, fault-controlled hydrocarbon migration pathways. These fault-controlled pathways focus the migration of hydrocarbons from deep Mesozoic source rocks into shallow overlying Neogene reservoirs (Figure 3.14). Migration pathways are inferred in the northern Mexican Ridges, despite the clay-rich Paleogene MTD sequence being significantly thicker (>3500 m) in the northern Mexican Ridges than the MTDs of the southern Mexican Ridges (<2000 m) (Figure 3.13, Figure 3.14).

8. A task for future work in this study area is improved documentation of Paleogene MTD thickness variability across the deformed zone (Figure 3.11, 3.12, 3.13), understanding the links between deformation and sedimentary response, and cataloging amplitude anomalies in the overlying fold-belts (Figure 3.14). This type of study will help to reduce exploration risk and guide future hydrocarbon prospectivity characterization in these underexplored, deep-water provinces.

CHAPTER 4: CONTROL OF STRUCTURAL DEFORMATION AND SEDIMENTATION BY THE INTERACTION OF SALT AND SHALE TECTONICS ACROSS THE DEEP-WATER LAMPREA FOLD-BELT AND SALINA DEL BRAVO SALT PROVINCE, WESTERN GULF OF MEXICO

4.1 Introduction

The offshore Burgos Basin in the Mexican sector of the on- and offshore, western Gulf of Mexico displays an extensive system of gravitational, sediment load-driven normal faults that are detached along deeply-rooted, autochthonous Jurassic salt bodies and a series of over-pressured Cenozoic shale horizons (Le Roy *et al.*, 2007; CNH, 2015; Hudec *et al.*, 2019). These seaward-dipping, normal detachments connect down-dip into a contractional domain that consists of a deep-water fold and thrust belts. These down-dip fold-belts include a series of allochthonous Jurassic salt bodies known as the Salina del Bravo salt province, and the Lamprea fold-belt; a shallow, Eocene shale-detached thrust and fold-belt located east of the Salina del Bravo salt province (Salomon-Mora 2013; Vazquez-Garcia 2018) (Figure 4.1).

Recent exploration wells have helped to extend the Perdido fold-belt plays from US waters into the Mexican Salina del Bravo salt province. However, most wells to date are located in the northern part of the Mexican margin, and the southernmost extension of the western Gulf of Mexico salt province remains underexplored (CNH, 2015; Smith *et al.* 2019). The southernmost edge of the middle Jurassic salt-cored province is less well defined, where this boundary transitions into Paleogene shale detached compressional systems of the Lamprea and

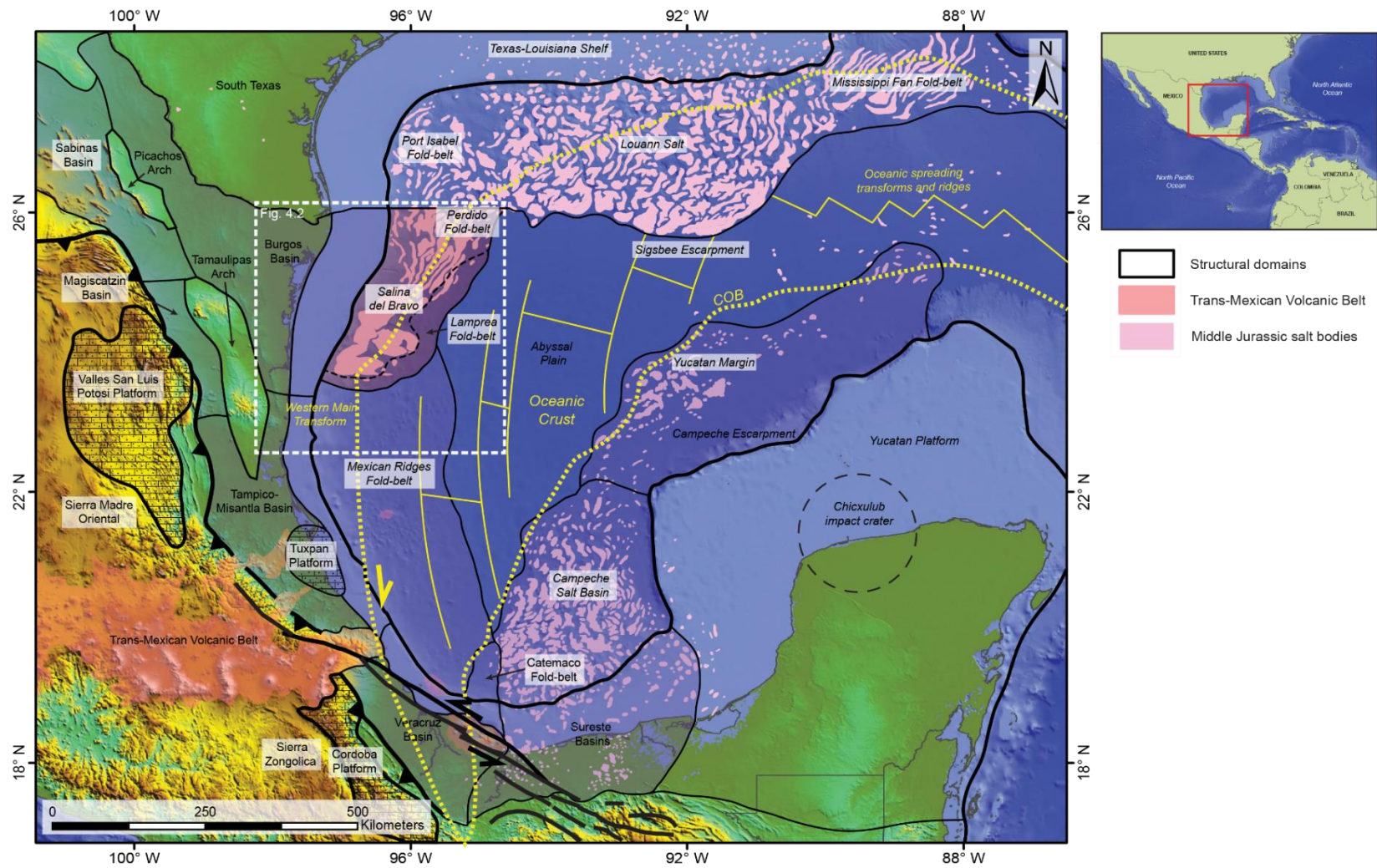
Mexican Ridges fold-belts (Figure 4.1). Deformation is complex and significant differences in structural style are apparent between the northern part of the Salina del Bravo salt province and the south, such as the position of the Perdido fold-belt relative to the overlying salt canopies and the shallow-detached Lamprea fold-belt in the southeast area of the continental margin. This study aims to better characterize the degree of influence that deep, salt-related structures have on the shallow Paleogene shale detached Lamprea fold-belt along the deformation front and how salt and shale tectonics interact along this transition zone. On recent study has suggested the formation of the Lamprea fold-belt is driven mainly by the proximal salt canopy system and influence from deep, autochthonous salt is minimal, which this study aims to test (Billotti *et al.* 2019).

In this study, I use a grid of seismic reflection data covering an area of ~40,000 km² and tied to 3 wells. I analyze the timing of formation, degree of deformation, and controls on sedimentation across the southernmost part of the deep-water Lamprea fold-belt, located adjacent to the southeastern edge of the salt-cored Salina del Bravo salt province (Figure 4.1). I characterize the onset of uplift and the lag time between uplift and the initial onset of deformation for salt versus shale-cored structures using two regional profiles through the Lamprea fold-belt. Pre-growth and syn-growth successions are also characterized across the Lamprea fold-belt. From this analysis, depositional trends can be directly linked to up-dip extensional processes which in turn control the down-dip, gravitationally-detached, compressional system.

The structural analyses of this chapter are based on principles of the excess area and depth to detachment theory, as proposed initially by Epard and Groshong (1993). This theory

allows characterization of the total fault displacement and the amount of layer-parallel strain of the deformed units (Groshong and Eppard 1994). Gonzalez-Mieres and Suppe (2006) and Yarbuh and Contreras (2017) have performed area-depth strain analyses for a series of thrust detachment folds similar to those I will describe from the Lamprea fold-belt. I conduct a similar area-depth analysis for individual detachment folds and for fold-complexes that include multiple imbricate folds and faults and are constrained by a regional base level.

Figure 4.1 Regional map of the western and central Gulf of Mexico, showing the offshore location of the Salina del Bravo salt province and its adjacent and distal Lamprea fold-belt. The transform-dominated, continental margin of western Gulf of Mexico exhibits a steep and narrow continental slope with part of the Salina del Bravo salt canopy and Lamprea fold-belt extruding over Jurassic oceanic crust in the deep-water area. Structural and tectonic elements are modified from Garcia-Palomo *et al.*, (2004); Andreani *et al.*, (2008); Ferrari *et al.*, (2012); CNH (2015); Nguyen and Mann (2016); and Yarbuh and Contreras (2017).



4.2 Geological background

The Gulf of Mexico basin formed as the result of two main phases of Mesozoic opening (Pindell and Kennan 2009; Nguyen and Mann 2016). The first phase, initiating in the Triassic, consisted of northwest-southeast extension and rifting between the North and South American continental plates (Nguyen and Mann 2016). By the earliest Cretaceous, rifting had ended, and the second phase of opening accommodated the counter-clockwise rotation of the Yucatan block away from North America and produced seafloor spreading (e.g., Salvador 1987; Marton and Buffler 1995; Pindell and Kennan 2009; Nguyen and Mann 2016; Lin et al., 2019).

Widespread evaporites were deposited across the GOM basin in the middle Jurassic during the post-rift thermal sag phase around the time of plate separation (Salvador, 1991; Hudec *et al.*, 2013). The subsequent formation of as much as 600 km of oceanic crust separated the salt basin into two parts before seafloor spreading terminated in the earliest Cretaceous (Pindell and Kennan 2009; Nguyen and Mann 2016; Lin et al., 2019; Steier and Mann, 2019). The transform-dominated margin along the western side of the basin resulted in a narrow, steeper continental slope in comparison to the northern and southern salt provinces of the Gulf of Mexico (Figure 4.1) (Hudec *et al.*, 2019). Following the cessation of basin opening, the western margin of the Gulf of Mexico was affected by the late Cretaceous to middle Eocene Laramide orogeny (Feng *et al.*, 1994; Lawton 2008; Gray and Lawton 2011). Ensuing uplift and volcanism during the late Eocene and Oligocene occurred across onshore North America and was associated with widespread Pacific plate subduction (Galloway 2000; Gray *et al.*, 2001; Hudec *et al.*, 2019).

Progressive west-east uplift and erosion of Laramide orogenic belts across onshore Mexico during the Paleocene and Eocene resulted in the deposition of prograding wedges of siliciclastic sediments across the Burgos Basin (Snedden *et al.*, 2018; Hudec *et al.*, 2019). Deep salt-related deformation and extrusion may have begun as early as the Paleocene-Eocene in offshore eastern Mexico (Billotti *et al.*, 2019). However, the western GOM region remained relatively quiescent until the late Eocene-Oligocene, when post-Laramide uplift, tilting, and high-rates of sedimentation destabilized the western margin of the Gulf of Mexico (Hudec *et al.*, 2019). Loading by thick wedges of prograding sediments into the offshore region caused salt in the areas of the Burgos Basin and Kama fold-belt to be evacuated down-dip and facilitated the development of an extensive, deep-rooted extensional fault system along the length of the margin (Salomon-Mora 2013; Hudec *et al.*, 2019). Gravitational and sediment load-driven deformation was transferred and accommodated basinward to a linked down-dip contractional province along both a middle Jurassic salt detachment and a series of late Paleogene shale detachments, (CNH, 2015; Hudec *et al.*, 2019).

Mobilized salt buttressed against a northeast-southwest trending basement high, located along the continental-ocean boundary. This ramping upward and folding deformed the overlying sediments to produce the middle Jurassic salt-cored Perdido fold-belt (Trudgill *et al.*, 1995; Hudec and Norton 2019; Hudec *et al.*, 2019). During this period, salt was also expelled vertically through a series of feeders to develop the extensive shallow salt canopies of the overlying Salina del Bravo salt province along the length of the margin (CNH 2015; Hudec *et al.*, 2019). Although the Perdido fold-belt is exposed ahead of the leading salt canopies in the northeast, the fold-belt trends so that the salt canopies progressively overlie and obscure its

folds towards the southwest of the area (Figure 4.2) (CNH 2015; Hudec *et al.*, 2019, Billotti *et al.*, 2019).

A shallow, Eocene shale-detached contractional system developed in the southern toe-region ahead of the Salina del Bravo salt province and Perdido fold-belt (Salomon-Mora 2013; Billotti *et al.*, 2019). This shale-detached fold-belt has been referred to as the Lamprea fold-belt, which is the equivalent of the Pemex/CNH termed “Peripheral/Periphic fold-belt” (Figure 4.1, 4.2) (Salomon-Mora 2013, CNH 2015, and Vazquez-Garcia 2018). The formation of the Lamprea fold-belt is thought to coincide with a phase of salt deformation during the Miocene (Salomon-Mora 2013; Bilotti *et al.*, 2019; Smith *et al.*, 2019). The Lamprea fold-belt coincides with continued up-dip sediment loading and extensional deformation along the shelf and onshore Mexico, which continues to the present-day (Hudec *et al.*, 2019).

The Lamprea fold-belt detaches on the same over-pressured Eocene shale layers as the Mexican Ridges fold-belt to the south and forms a transitional domain between the exclusively shale-cored Mexican Ridges and the southeastwards-advancing Salina del Bravo salt province (Figure 4.2) (Salomon-Mora 2013; Kenning and Mann 2020). Eocene and Oligocene shales are extensive across the western Gulf of Mexico, and these mechanically weak units may represent what was once a stacked sequence of massive-scale, clay-rich debris flow aprons. These large-scale mass transport deposits (MTDs) would have been deposited as a result of late-to-post Laramide volcanic activity and the tectonic destabilization of eastern Mexico (Kenning and Mann 2020).

4.3 Data and seismic interpretation

4.3.1 Chronostratigraphic interpretation framework

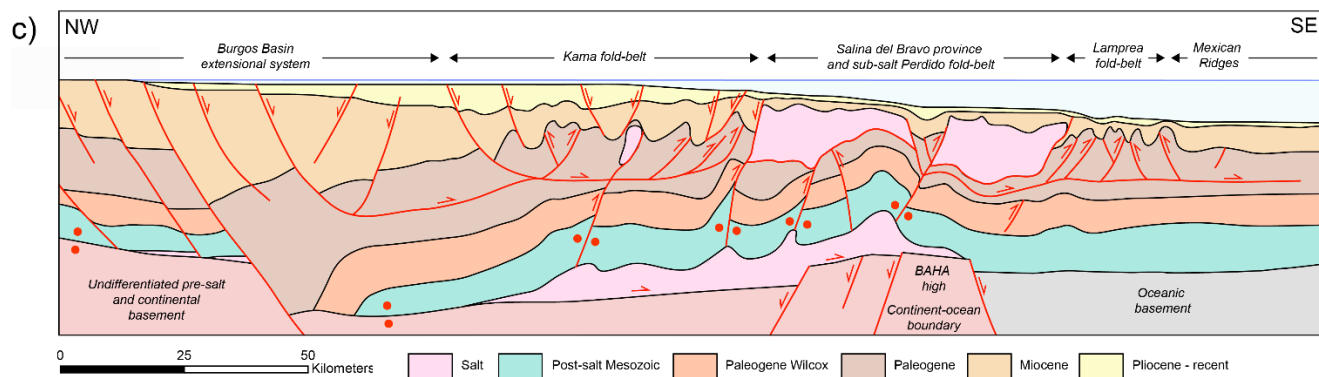
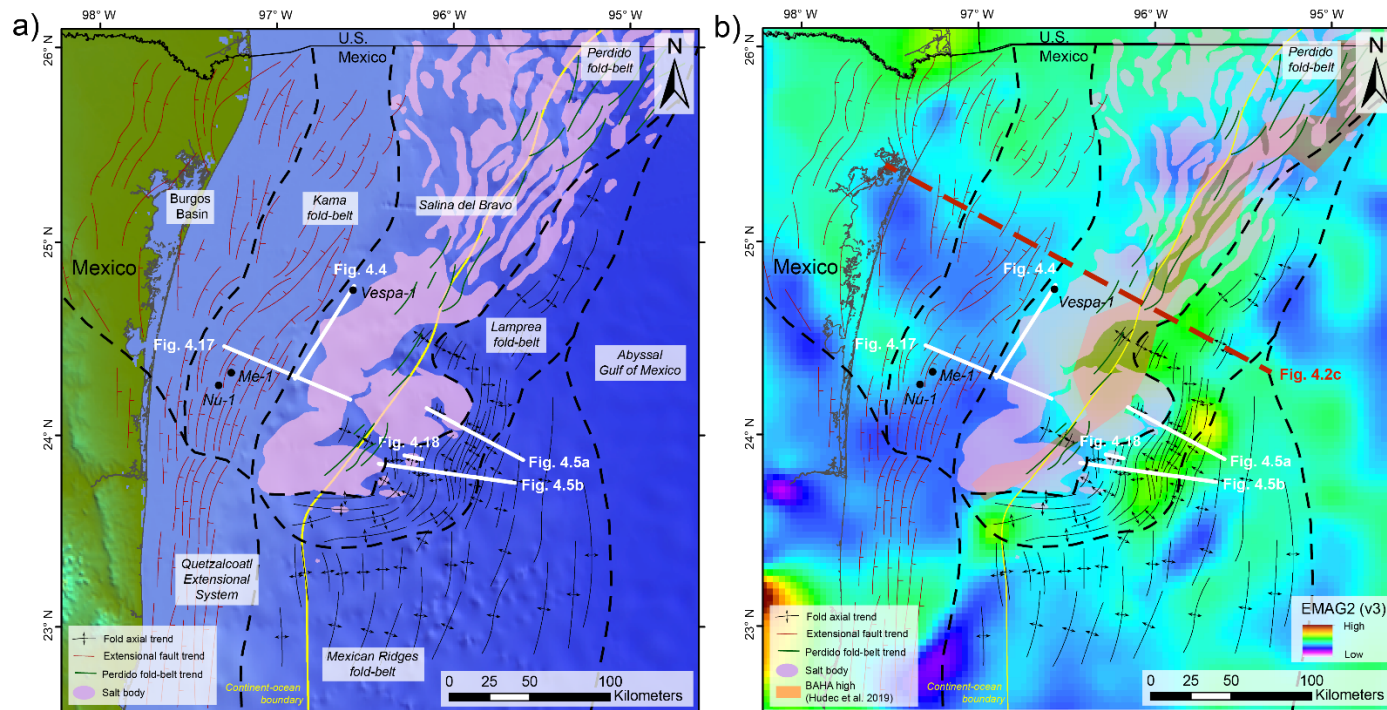
I interpreted a series of regional seismic-reflection profiles covering areas ranging east-west from the deep-water abyssal Gulf of Mexico and across the Lamprea and Mexican Ridges fold-belts, the Salina del Bravo salt province and Kama fold-belt (Figure 4.2). The seismic data were acquired and processed with Kirchhoff depth migration by TGS, forming part of their regional Gulf of Mexico “Gigante” survey. The extent of the available seismic data for this study covers the Paleocene to recent section down to a depth of -9000 m sub-sea.

The underexplored southeastern trend of the Salina del Bravo salt province and Lamprea fold-belt, are the primary focus of this study. There is a distinct lack of deep exploration wells available for precise age control in the area. Due to the scarcity of well penetrations, the study relies partially on seismic age correlations and interpreted profiles from previous authors. Relative ages have been extrapolated across the deep-water Gulf of Mexico from well control in adjacent regions (Figure 4.3) (e.g., Trudgill *et al.*, 1995; Le Roy *et al.*, 2007; CNH 2015; Smith *et al.*, 2019; Kenning and Mann, 2020).

A small number of well penetrations with published data exist along the up-dip Kama fold-belt and Salina del Bravo salt and shale minibasin province (Figure 4.2) (Smith *et al.*, 2019). These wells allow for age constraints on the shallow Miocene-recent section - despite the problems with correlation through the shallow salt canopies into the deep-water area. The primary well used for age constraint was Vespa-1 (O’Reilly *et al.*, 2017), located along the western edge of the Salina del Bravo province and penetrating to the Oligocene (Figure 4.4). Age horizons were defined based on well-seismic tie markers adapted from O’Reilly *et al.*,

(2017). Located in the thick, faulted, sedimentary growth section of the Kama fold-belt, well-seismic schematics of Nu-1 and Me-1 from Salomon-Mora (2013) also provide some age approximation for the area. Both these wells penetrate to the middle Miocene.

Figure 4.2 a) Map of structural elements, seismic figure orientations, shallow salt, and key well locations across the Lamprea fold-belt, Salina del Bravo province, and Kama fold-belt. Up-dip gravitational failure and sediment loading across the Burgos Basin produced an extensive, deep-rooted extensional fault system. Deformation is translated down-dip along Jurassic and Eocene detachment surfaces into a compressional area that extrudes Jurassic salt to form shallow-detached salt canopies and the shale-detached Lamprea fold-belt. Figures 4.5a and 4.5b represent locations of the two seismic profiles that cross a series of anticlines in the deep-water Lamprea fold-belt and used for area-depth strain analysis in this study. **b)** Map of structural elements, seismic figure orientations, and key well locations superimposed on the EMAG2 regional magnetic anomaly map. The position of the BAHA high from Hudec *et al.* (2019) is highlighted. Regional structural elements for a) and b) are modified from Le Roy *et al.*, (2007); CNH (2015); Nguyen and Mann (2015); Yarbuh and Contreras (2017); Vazquez-Garcia (2018); Hudec *et al.* (2019). **c)** Conceptual schematic dip profile across the study area from northwest to southeast. The Lamprea fold-belt, forming the primary focus of this study, represents the contractional deformation front of a margin-wide linked gravitational system. The style of deformation along the margin is controlled by a steep angle of dip combined with the BAHA high acting as a buttress. Schematic based on interpreted sections from CNH (2015).



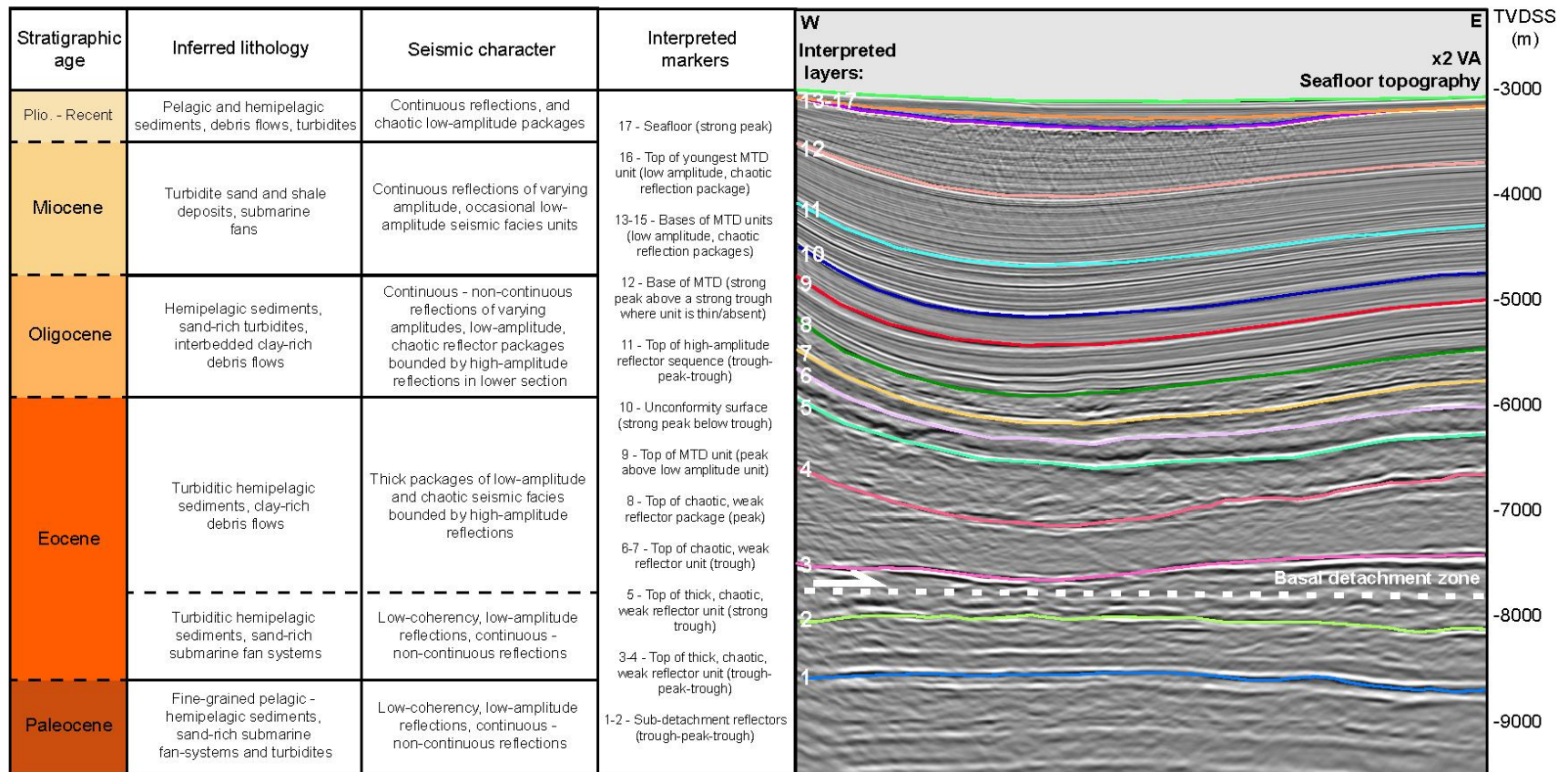


Figure 4.3 Seismic to stratigraphic age correlation for the area of the deep-water Gulf of Mexico that is located directly east of the southern Lamprea and northern Mexican Ridges fold-belts. The white numerals on the left-hand side of the seismic image indicate interpreted horizons used for area-depth strain analysis shown in Figures 4.5a and 4.5b. The basal detachment for the Lamprea fold-belt is inferred from seismic interpretation to be located within layer 3. Age constraints for this undrilled deep-water area were estimated based on up-dip well control and previously interpreted seismic data from Le Roy *et al.*, (2007) and Kenning and Mann (2020).

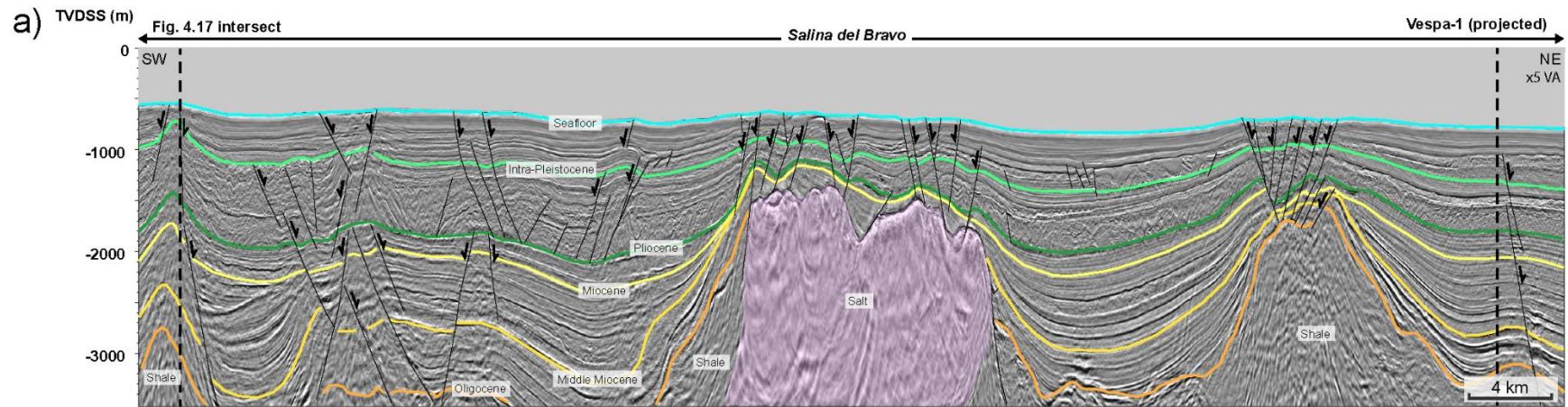


Figure 4.4 Seismic well-tie with the Vespa-1 well that provides age constraints on the Oligocene-Recent strata in the up-dip Salina del Bravo salt province and adjacent Kama fold-belt. Numerous shallow debris flows form correlation markers across parts of the salt canopy and extend across the deep-water Lamprea fold-belt. Age control from the Vespa-1 well was modified from O'Reilly *et al.*, (2017).

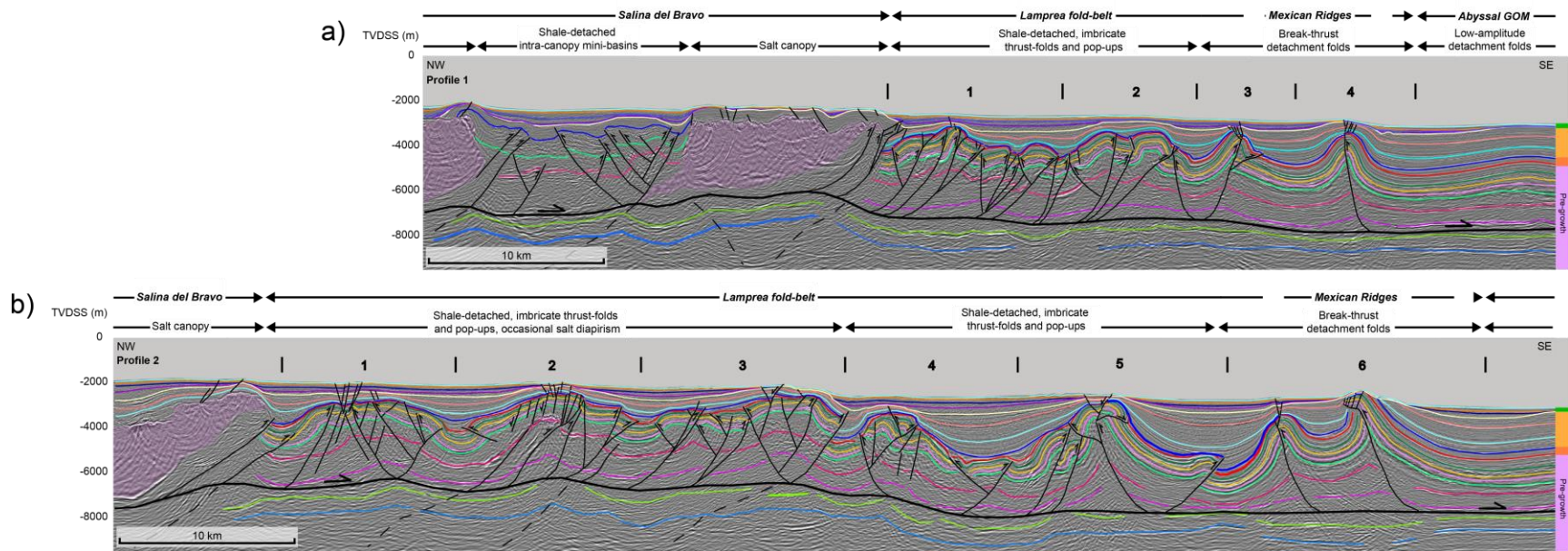


Figure 4.5 a) Seismic profile across the deep-water western Gulf of Mexico in the northern part of the study area. The seismic line is ~40-km long, has a depth penetration of 9 km, and is orientated NW-SE, perpendicular to the strike of the fold structures of the labeled fold belts. The profile covers a narrow section of the Lamprea fold-belt characterized by highly-imbricate folds proximal to the salt canopy front, before transitioning into isolated thrust-detachment folds that are typical of the Mexican Ridges fold-belt to the south. **b)** Seismic profile across the deep-water western Gulf of Mexico in the southern part of the study area. The line is ~80-km long, has a depth penetration of 9 km, and is orientated NW-SE and perpendicular to the strike of the fold structures. The Lamprea fold-belt is significantly wider at this location and is influenced by salt-tectonics in the proximal part of the imbricated fold zone. The structural style of the Lamprea fold-belt transitions into Mexican Ridges detachment folds towards the south-east.

4.3.2 Regional correlation using seismic facies relationships

Horizons representing seismic markers and distinct packages were correlated across the Lamprea fold-belt for their use in area-depth strain analysis (Figure 4.5). These horizons were numbered from base to top. Ages were assigned to them based primarily on the chronostratigraphy from Le Roy *et al.*, (2007), that was adapted from Trudgill *et al.*, (1995) (Figure 4.3). Horizons 1 and 2 are both correlated along semi-continuous, high-amplitude reflectors and represent Paleocene-early Eocene pre-growth strata beneath the Lamprea fold-belt's basal detachment. The basal detachment zone in the deep-water Lamprea is interpreted to be within layer 3 (Figure 4.3, 4.5). Horizons 3-5 are defined by high-amplitude reflectors bounding thick packages of low-amplitude units exhibiting chaotic seismic facies and representing late Eocene detachment shales (Figure 4.3). These low-amplitude packages thin into the Oligocene where they become interbedded by continuous, higher-amplitude reflections used as markers for horizons 6-8, with 8 representing the top of the low amplitude sequence in the distal area (Figure 4.3). Horizon 9 marks the top of a low-amplitude unit interpreted to be a debris flow.

Horizon 10 marks the top of the presumed fold-belt pre-growth sequence in the deep-water area and is characterized by a high-amplitude peak, representing an unconformity across the fold-belt (Figure 4.3, 4.5). Horizons 11 and 12 represent Miocene age markers within the main syn-growth phase. The high-amplitude tops and bases of three shallow, low-amplitude debris flow units that blanket the Lamprea fold-belt within the Pleistocene section below the seafloor represent the remaining interpreted horizons (Figure 4.3).

4.4 Style of folding across the Lamprea fold-belt and deep-water region

4.4.1 Detachment folds

The late Eocene to early Miocene pre-growth sequence of the Lamprea fold-belt and adjacent distal area comprises a wide range of thin-skinned structural styles, with an east-west progression from imbricate thrust-folds and pop-up structures, to thrust-faulted detachment folds and unfaulted detachment folds (Figure 4.5). At least one, unfaulted detachment fold is present in the deep-water area east of the Lamprea fold-belt and can be partially observed along in the westernmost sections of Profiles 1 and 2 (Figure 4.5a and 4.5b). Based on their partial seismic coverage, these folds appear to be typical, low-amplitude, symmetrical structures (Mitra, 2002; Salomon-Mora *et al.*, 2009). These folds detach along the base of a stacked Eocene shale package (Figures 4.3, 4.5). The syn-growth and post-growth succession displays thinning-upwards patterns towards the crests of the folds; however, they do not exhibit clear seismic onlap patterns or truncations (Figure 4.5).

4.4.2 Faulted detachment folds

Folds 3 and 4 along Profile 1 (Figure 4.5a) and fold 6 along Profile 2 (Figure 4.5b) exhibit more asymmetrical geometries with much steeper, highly-rotated limbs and narrow, higher-amplitude fold geometries - compared to the more distal folds described above. The asymmetry of these folds can be attributed to the prominent faults cutting through the cores of the folds, which are predominantly back-thrusts in this area (Figure 4.5). Faulted detachment folds initially form by simple detachment folding and develop thrusts within the deformation

zone as shortening increases and fold limbs lock-up, eventually becoming through-going, connecting with the basal detachment below (Mitra, 2002). These thrust-related detachment folds are of a similar style to those described across the Mexican Ridges fold-belt to the south (Salomon-Mora *et al.*, 2009).

The top of the initial growth phase is defined by an angular unconformity, which truncates the underlying early syn-growth and pre-growth strata, and onto which the syn-growth sequence onlaps both fold limbs across the faulted detachment folds (Figure 4.6b). Some erosion of the underlying strata across the fold crests is possible; however, the break is more likely non-depositional, with similar relationships observed across the nearby Perdido fold-belt to the north (Mount *et al.*, 1990). The geometries of the following Miocene-Pliocene syn- to post-growth succession are also asymmetrical and reflect the underlying pre-growth geometries that suggest a tectonic control on accommodation space and sedimentation.

A third principal syn- to post-growth phase can be observed overlying the primary succession of syn-growth growth strata, where a stacked sequence of debris flows drape the deep-water folds (Figure 4.6). These variably syn- to post-growth MTDs erode and truncate the underlying phase of deposition and display either thinning over the fold crests, or commonly onlap where deformation is recently active in this part of the fold-belt (Figure 4.6b). The thrust-related detachment folds are mature and often display extensional collapse faults at their peaks and continued fold growth up to the level of the seafloor.

4.4.3 Imbricate thrust faults and pop-up structures

Structures 1 and 2 on Profile 1 (Figure 4.5a) and 1, 2, 3, 4, and 5 on Profile 2 (Figure 4.5b) are characterized by groupings of highly imbricate thrust-folds and pop-up structures that are characteristic of the Lamprea fold-belt. The development of pop-up structures is controlled by many factors that include: stratigraphy, rheological contrasts, and thrust-fold propagation rates (Fabbi and Smeraglia 2019). Pop-ups commonly occur in thin-skinned fold-belts characterized by a multi-layered sequence and a weak detachment (Fabbi and Smeraglia 2019). While the structural style of the Lamprea fold-belt differs somewhat from the Mexican Ridges style detachment folds in the eastern area, both areas display similar stratigraphic relationships between their pre-growth and syn- to post-growth successions (Figure 4.6a).

The top of the pre-growth sequence is often capped by a thin phase of initial growth strata and truncated by a growth disconformity, with truncation of the underlying sequence across the entire length of the Lamprea fold-belt that is particularly evident along the crests of protruding folds. The second main syn- to post-growth succession above the unconformity is thinner in the proximal parts of the fold belt, suggesting that these structures may have been uplifted, and a lower accommodation space allowed for more sediment bypass into the deeper water areas. The overlying MTD sequence again erodes a portion of the underlying succession in this area, as evidence by the truncation of the underlying reflectors. The MTD sequence is thicker and better developed in this proximal location and exhibits thinning and less commonly onlap patterns across the underlying fold axes (Figure. 4.6).

4.5 Area-depth strain methodology

Structural geometrical analysis was performed across Profile 1 (Figure 4.5a) and Profile 2 (Figure 4.5b), to mathematically subdivide the stratigraphy as pre-growth versus syn- to post-growth strata. Shortening, layer-parallel strain, and estimates for the depth and angle of the basal detachment are defined across the length of the fold-belt using this analysis. Excess-area depth measurements were performed using the StructureSolver software package for each numbered fold complex along-dip (Figure 4.5a and 4.5b), and each interpreted horizon 1-17 along those profiles (Figure 4.3).

Many previous authors have applied the method to fault-related folds (e.g., Hubert-Ferrari *et al.*, 2005; Gonzalez-Mieres and Suppe 2006; Wiltschko and Groshong 2012; Yarbuh and Contreras 2017; and Carboni *et al.*, 2019). In area-depth strain analysis, the only assumption is a constant area, and the method requires only a few well-imaged marker horizons. The process provides a quick technique to test the feasibility of structural interpretations (Groshong, 2013).

This area-depth strain analysis uses measurements of excess-area (a) of marker horizons versus the depth (h) below a reference level that, in this case, is set at sea-level (Figure 4.7). Measurements can be repeated for multiple horizons. When plotted graphically, the pre-growth strata are expected to yield a linear regression with depth, where an area value of zero represents the basal detachment (Epard and Groshong 1993; Groshong and Epard 1994; Gonzalez-Mieres and Suppe 2006; Groshong 2013). Using this method, I can measure the area-depth displacement (D), linear shortening (L), and layer-parallel strain (S). A statistical parameter (RSq) indicates how well the models fit the data trend so that $RSq = 1$ indicates an exact

relationship between the variability in excess area and depth, and the value of $RSq = 0$ indicates that no relationship exists between excess-area and depth.

Syn-growth and post-growth strata typically thin or onlap onto structural highs, thicken in structural lows and are generally less folded than the underlying pre-growth layers (Figure 4.6a, 4.6b). As the syn- to post-growth strata are less folded, these layers possess progressively less excess-area compared to the underlying pre-growth horizons resulting in a change in slope from the pre-growth linear trend. This change in slope marks the boundary between pre-growth and syn- to post-growth strata, with the syn- to post-growth sequence defined by a decrease in excess-area as depth decreases (Gonzalez-Mieres and Suppe 2006). If there is overlying strata present displaying excess-area values of zero, these layers either represent post-growth deposition once fold growth has ended - or could simply indicate that the rate of sedimentation was higher than the rate of uplift during growth (Figure 4.7).

The distinction between phases of syn-growth and post-growth can be challenging, and the onlap of sediments does not necessarily indicate fold growth. Stratal onlap can instead represent a post-growth basin fill (Mount *et al.*, 1990). Phases of growth within the post-pre-growth sequences are observed to be episodic and highly variable between individual fold structures (Figure. 4.6). Additionally, the end of growth is not simultaneous across the length of the fold-belt. While syn-growth phase I is relatively consistent across the fold-belt, some fold structures display growth relationships throughout various intervals within phase II and III strata. Folds in the most proximal and distal parts of the fold belt typically display the youngest growth close to the seafloor (Figure 4.6a and c). Some folds within the Lamprea fold-belt display draping or horizontal post-growth strata from around the late Miocene to recent with

growth only occurring in the early to middle Miocene (Figure 4.6b). The fold on the right of Figure 4.6b displays intermittent phases of growth strata throughout phase II on its back limb, but mostly draping strata on its forelimb. This observation suggests the larger anticlinal structure that this pop-up forms part of was uplifted as a whole during this later Pliocene growth phase, rather than movement along the individual thrust fault (Figure 4.6b). Despite a complicated end of growth, the excess-area method can still provide us with a confident estimate of the initial onset of growth across phase I.

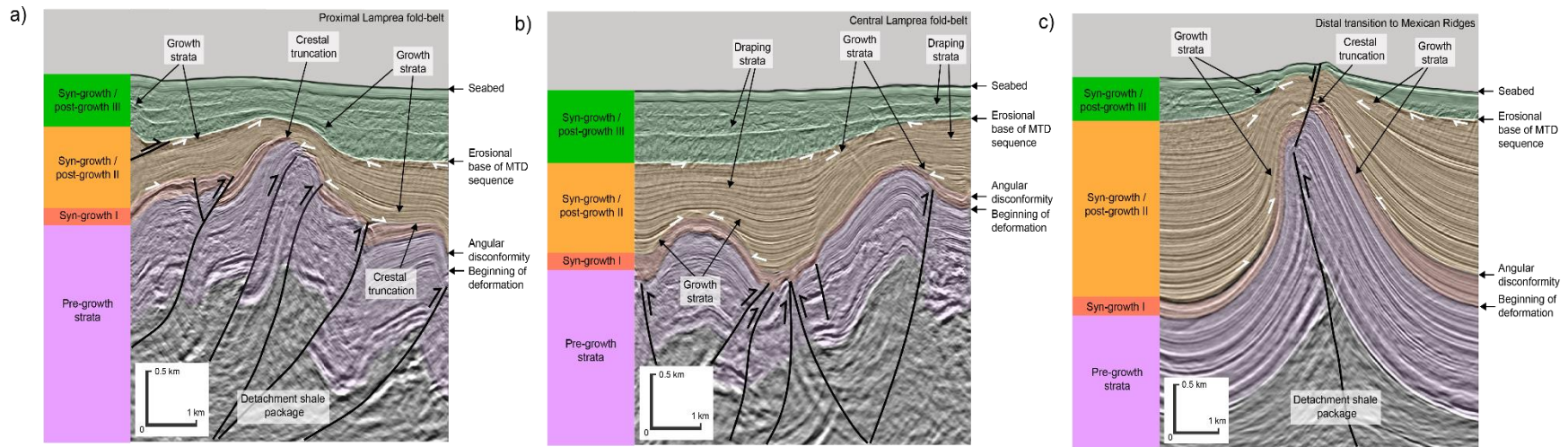


Figure 4.6 Interpreted growth-strata geometries observed from seismic data crossing the Lamprea fold-belt and the Mexican Ridges fold-belt transition. The stratigraphy consists of four primary successions; 1) pre-growth strata of Eocene-Oligocene age deposited before the onset of folding (partially shown in figures), 2) early syn-growth strata of early Miocene age that is often truncated along the crests of folds by an angular disconformity, 3) variably syn-growth to post-growth strata of Miocene-Pliocene age deposited either synchronously with or in-between phases folding, which often display as either thinning or onlapping sets of reflections across the fold crests, and 4) variably syn-growth to post-growth strata of Pleistocene to recent age consisting predominantly of stacked debris flow sequences and unconformable with the previously deposited growth section. **a)** Patterns of onlap and truncation located between the stratigraphic successions in the proximal, imbricate Lamprea fold-belt. **b)** Patterns of onlap and truncation in the central and distal Lamprea fold-belt are broadly similar to the proximal area; however, the episodic timing of fold growth and the end of fold growth can vary across the fold-belt **c)** Similar patterns of onlap and truncation are noted in the distal Mexican Ridges fold-belt transition to the east, and often exhibit growth strata close to the seafloor.

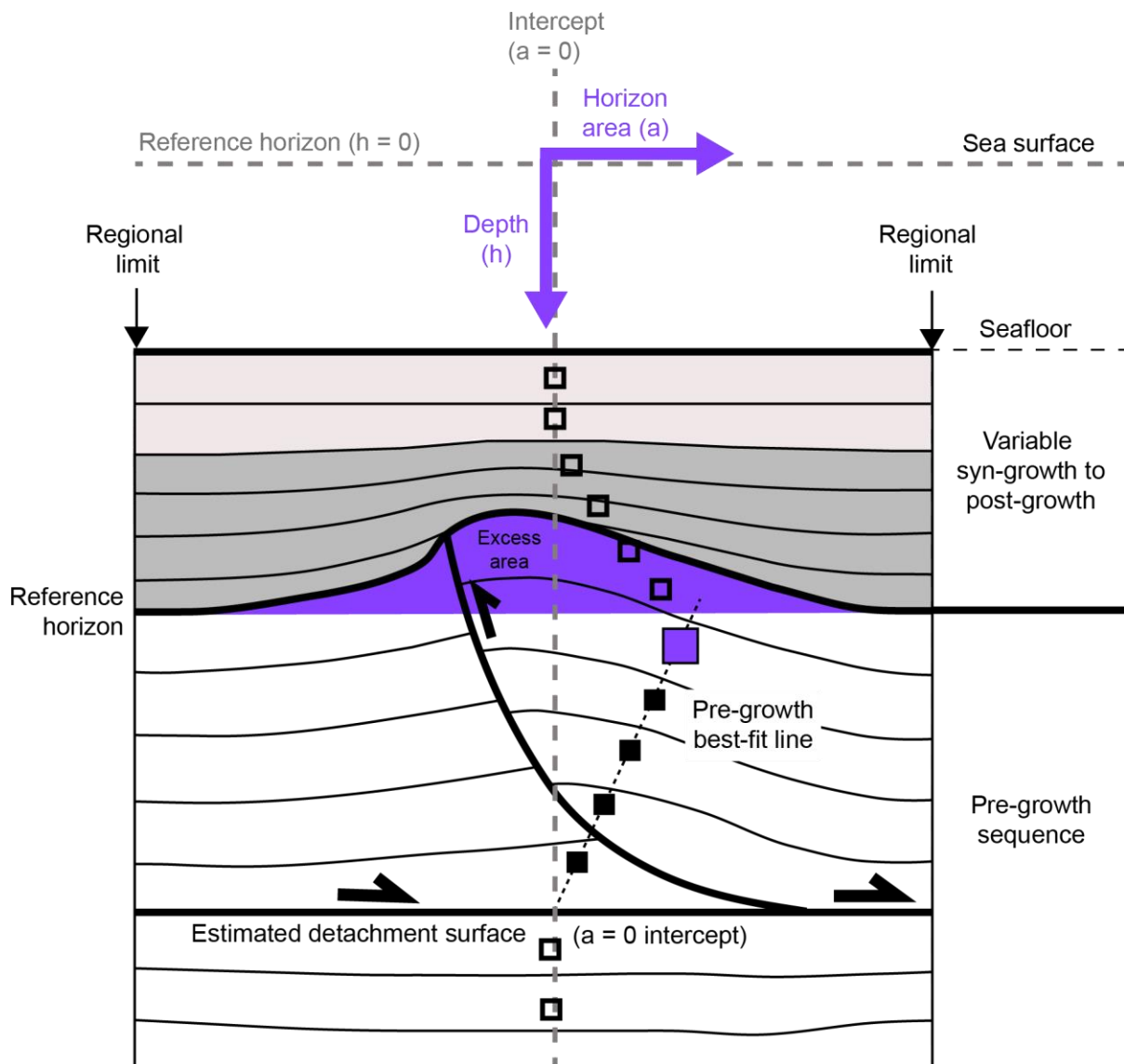


Figure 4.7 Schematic, structural parameters of detachment folds in the framework of an area-depth strain analysis using the depth-to-detachment method. Measurements of the excess area (a) beneath each interpreted horizon of a fold structure are plotted graphically versus depth (h) from a reference horizon, that in this case, is sea-level. Pre-growth strata typically exhibit a linear trend of decreasing area with increasing depth, which allows for an estimation of the basal detachment depth (at $a=0$). Syn- to post-growth strata are expected to exhibit the opposite trend, with progressively decreasing excess area as depth decreases. Overlying units that exhibit zero area either may indicate either post-growth deposition or that the rate of uplift is less than the rate of sedimentation during fold growth.

4.6 Results from Area-depth strain analysis and structural geometric measurements

4.6.1 Structural analysis of pre-growth strata

The results from the area-depth strain analysis are summarized in Figures 4.8-4.14. Overall, the linear data trends of the excess-area display little dispersion and high values of RSq with values between 0.987-1.000 (Figure 4.8, 4.9). Based on the interpretation of the folded pre-growth layers across the fold-belt, I predict a basal detachment that is in the depth range of layer 3 and layer 4 (Figure 4.8, 4.9). Profile 1 (Figure 4.5a) displays a consistent detachment within layer 3 both across the simpler, isolated detachment folds in the distal area, and the grouped imbricate fold complexes (Figure 4.8). Profile 2 (Figure 4.5b) also predicts a relatively consistent detachment depth across the fold-belt in the region of layer 3 and 2 despite more complex structurally geometries of the overlying fold-belt and changes in detachment angle as observed on the seismic (Figure 4.9). Plots of excess-area versus depth show the clear linear regression trend of the pre-growth strata consistently break-down around layers 2 and 3 across both Profile 1 and Profile 2 (Figure 4.10 and 4.11).

Both Profile 1 and Profile 2 indicate higher layer-parallel strain values close to the basal detachment layer with strain values generally decreasing upwards through the pre-growth and syn-growth sequence (Figure 4.8 and 4.9). The narrower Profile 1, towards the north of the study area, exhibits pre-growth layer-parallel strain values of between -0.6% and -22.2%, which are relatively consistent across each of the four folds (Figure 4.8). Profile 2 across the wider part of the fold-belt to the south displays higher layer-parallel strain across the majority of the fold-belt, with calculated values between -2.4% and as high as -38.9% (Figure 4.9). The highest values of layer-parallel strain along Profile 2 are close to the basal detachment level and are

associated with the large, back-thrusted detachment folds east of the propagating contractional system (Figure 4.9f).

Along Profile 1, area-depth displacement remains relatively consistent across the fold structures 1-4, decreasing slightly into the distal Mexican Ridges area for pre-growth layer 8 (Figure 4.12a). Total area-depth displacement for Profile 1 is estimated at 7.35 km for the 31 km section. The layer-parallel strain is highest for fold 2 (Figure 4.12b), which corresponds to the front of the proximal zone of imbricate-faulting of the Lamprea fold-belt (Figure 4.12c). Profile 2 exhibits reasonably uniform area-depth displacement across the proximal part of the Lamprea fold-belt, increasing slightly from fold 1 to fold 3 (Figure 4.13a). Area-depth displacement decreases as the detachment angle changes and deepens where the fold-belt begins to transition into the Mexican Ridges style of folding across fold 4. The area across fold 4 on Profile 2 is laterally equivalent to fold 1 and 2 on Profile 1 and displays similar area-depth displacement. Area-depth displacement increases significantly to between 8-10 km for folds 5 and 6 (Figure 4.13a), which represent large, back-thrusted detachment folds (Figure 4.13c). Total area-depth displacement for Profile 2 is estimated at 35.55 km for the 69 km section. The layer-parallel strain is consistently higher across Profile 2 compared to Profile 1, except for fold 4 (Fig 4.13b). Higher values of layer-parallel strain generally correlate with high values of area-depth displacement (and nominal displacement), as observed across both profiles (Figure 4.12, 4.13). A full range of area-depth strain measurements for each fold structure can be observed in the Appendix section (Table A1.1, A1.2).

Figure 4.8 Area-depth strain analysis of fold structures across Profile 1 located in the map in Figure 4.5a. Estimated detachment depths were consistently estimated within layer 3 with high correlation coefficients (RSq). The values in the format $-D$ ($-N$, $-S\%$) beside each fold complex represent the calculated area-depth displacement (D), nominal displacement (N), and layer-parallel strain (S), respectively. Profile 1 was divided into four sections: **a**) a grouped series of imbricate fold-thrusts, constrained by the regional base level, located ahead of the salt canopy, **b**) a grouped series of pop-ups and imbricate thrust-folds, **c**) an individual detachment fold, and **d**) an individual detachment fold representing the main deformation front.

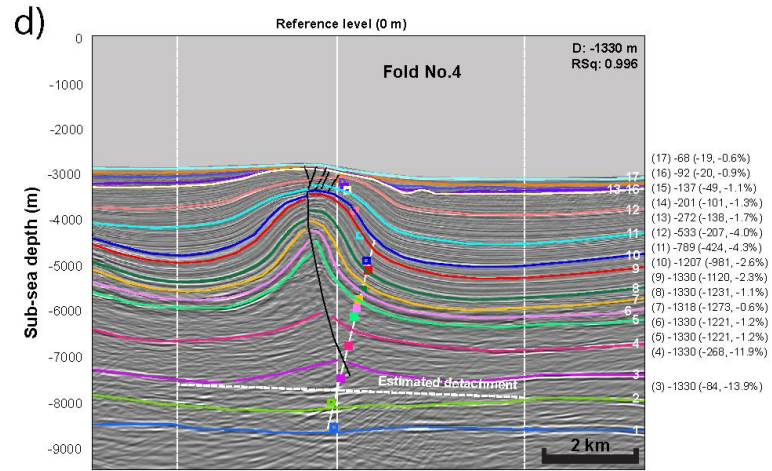
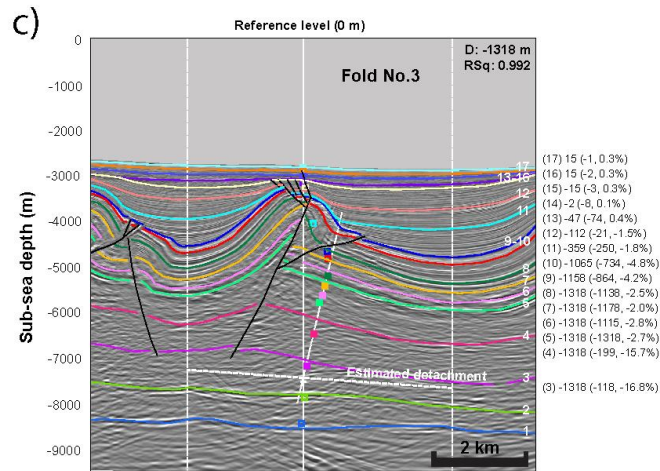
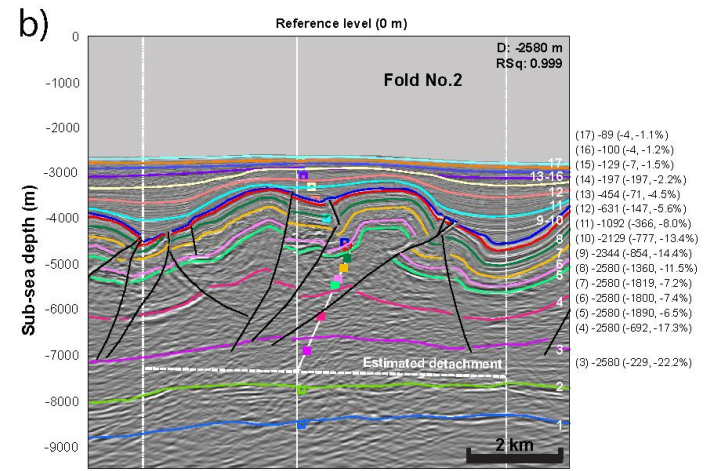
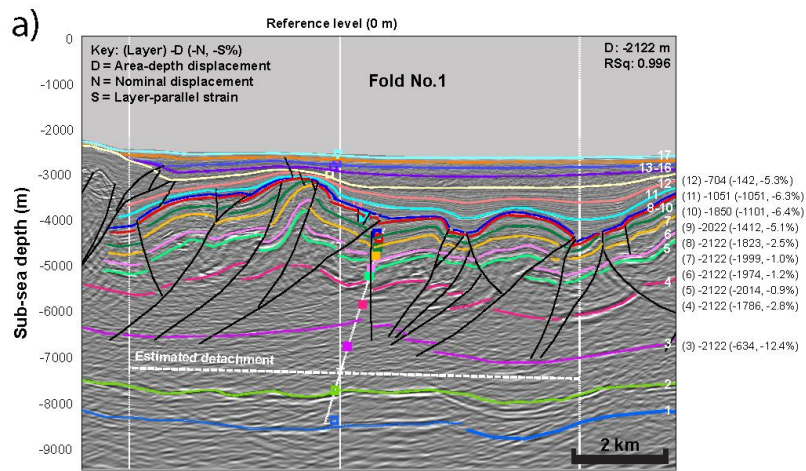
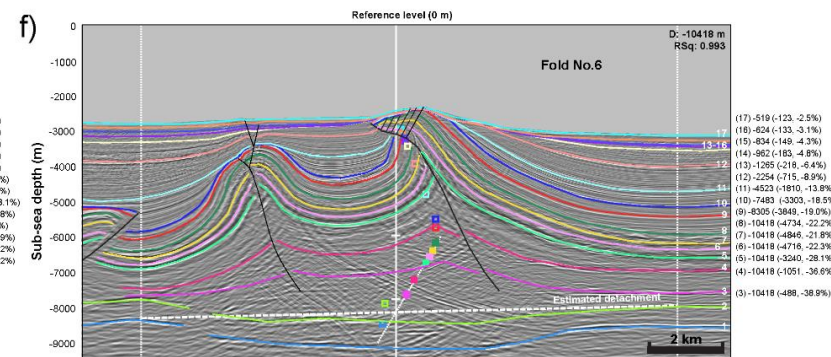
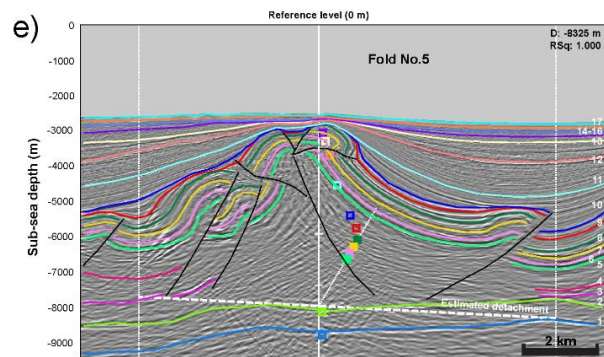
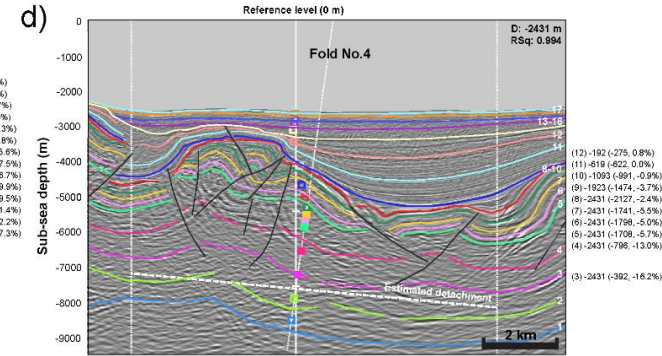
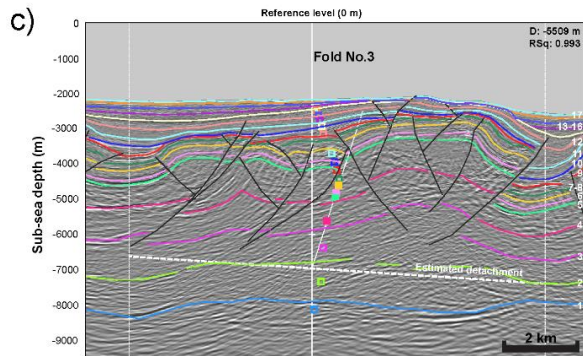
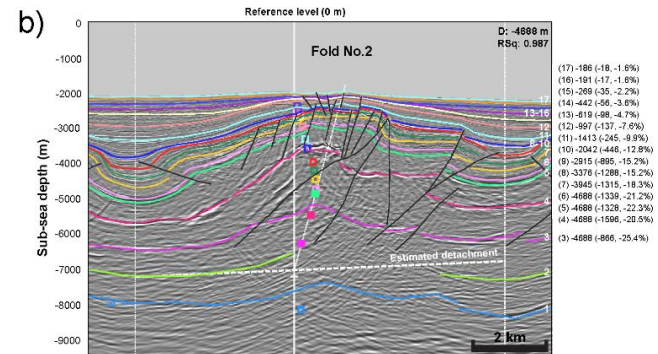
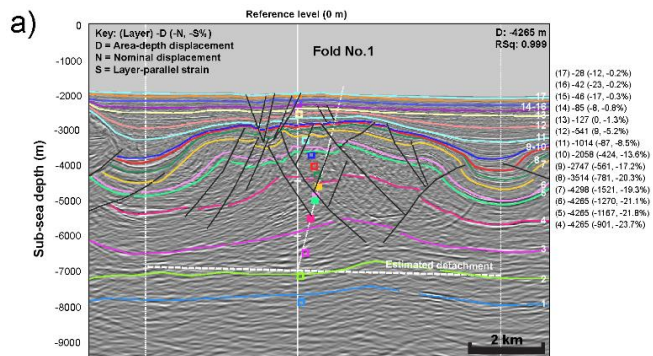


Figure 4.9 Area-depth strain analysis of fold structures across Profile 2 located in the map in Figure 4.5b. Estimated detachment depths were consistently estimated within layer 3 with high correlation coefficients (RSq). The values in the format –D (-N, -S%) beside each fold complex represent the calculated area-depth displacement (D), nominal displacement (N), and layer-parallel strain (S), respectively. Profile 1 was divided into six sections: **a**) a grouped series of imbricate fold-thrusts and pop-ups constrained by the regional base level, **b**) a salt and shale cored fold with numerous faults, **c**) a series of highly-uplifted pop-up structures, **d**) a complex fold structure at the Lamprea to Mexican Ridges transition, **e**) a large fold with multiple associated imbricate thrusts, **f**) a grouping of two detachment folds with limits constrained to the regional base level.



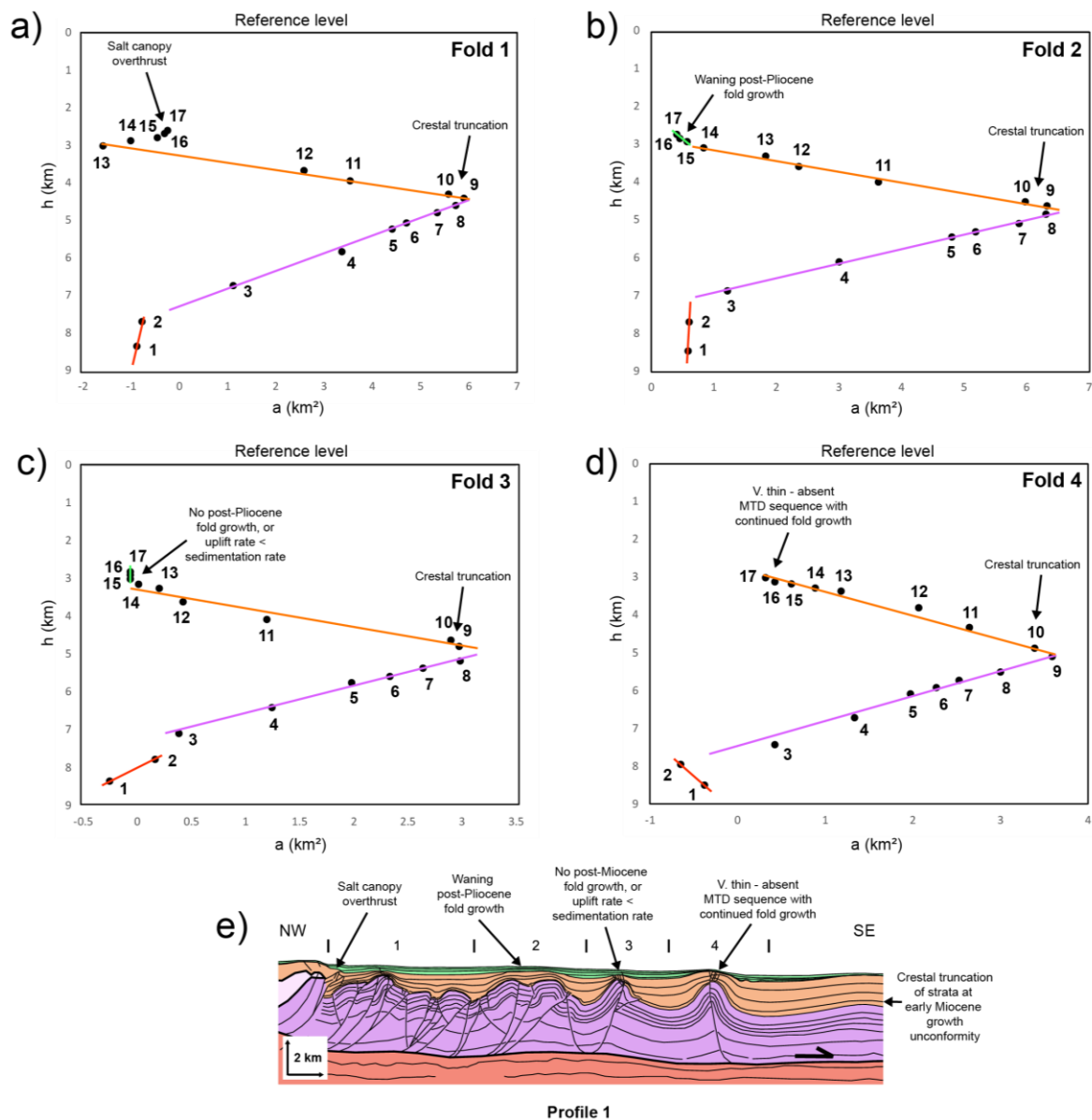
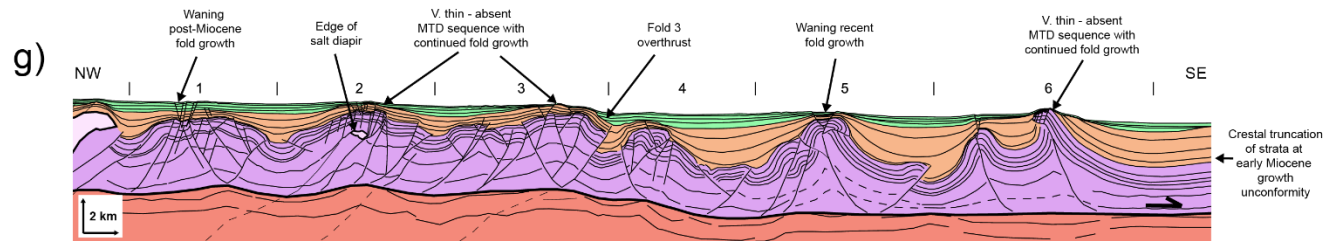
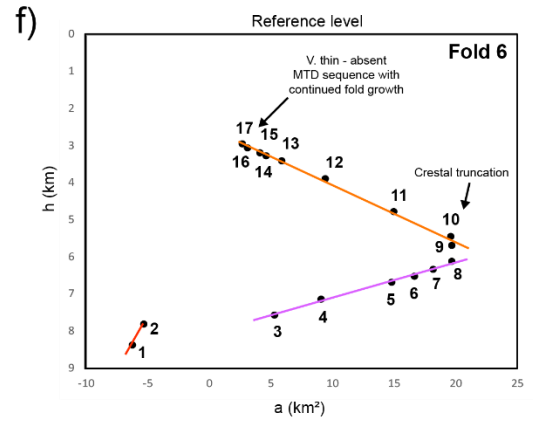
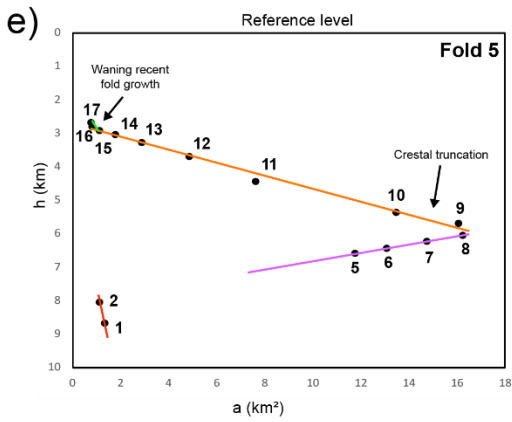
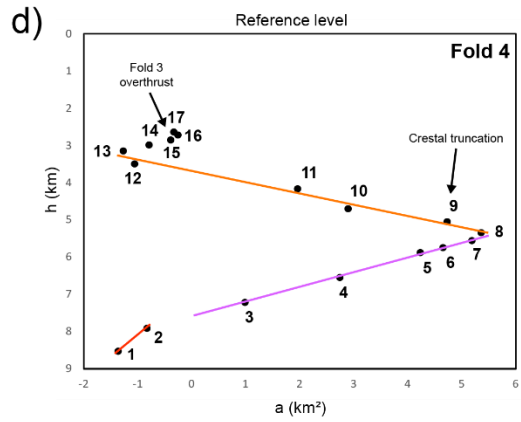
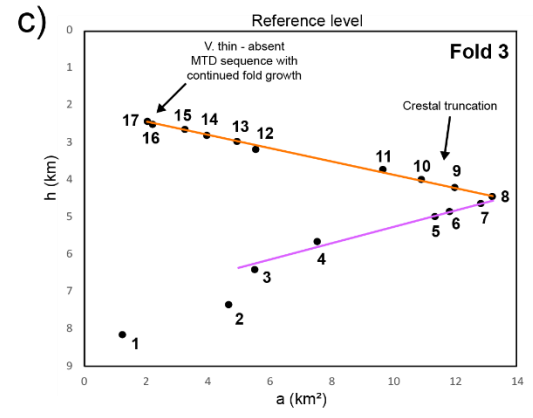
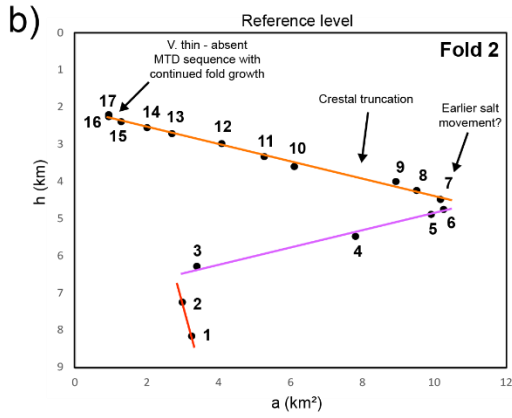
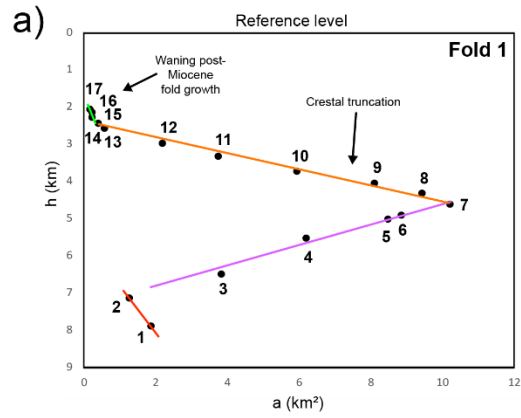


Figure 4.10 Plots of the area of structural relief (a) as a function of depth (h) for folds 1-4 along Profile 1. The slope is obtained by a best-fit line and the break-down of the linear relation marks the onset of folding. For folds 1-4 (**a**), **b**), **c**), and **d**), the onset of growth is observed around layer 9 (Late Oligocene). **e**) Schematic interpretation of Profile 1. It is important to note that both horizon 9 and 10 (Late Oligocene/Early Miocene) exhibit a degree of variable erosion along the crests of the folds, which would reduce the measured area.

Figure 4.11 Plots of the area of structural relief (a) as a function of depth (h) for folds 1-6 along Profile 2. The slope is obtained by a best-fit line, and the break-down of the linear relation marks the onset of folding. For folds 1 and 2 (**a**) and **b**)) the onset of growth is observed around layer 7 (Oligocene), for folds 3 and 4 (**c**) and **d**)) around layer 8, and for folds 5 and 6 (**e**) and **f**)) around layer 9 (Late Oligocene). **g**) Schematic interpretation of Profile 2 that is similar to interpretations of layers 9-10 in Profile 1. Layers 8-10 are interpreted to represent the erosion of fold-crests and may not necessarily represent an earlier onset of fold-growth.



Profile 2

Figure 4.12 Plots of **a)** total calculated area depth displacement and **b)** calculated layer-parallel strain across Profile 1 of the Lamprea fold-belt. Displacement is similar for each fold-complex across this part of the fold belt. Higher layer-parallel strain is associated with fold 2, which represents the front of the Lamprea imbricate-fold zone. **c)** Schematic section based on Profile 1 seismic that displays the measured fold complexes and primary growth packages.

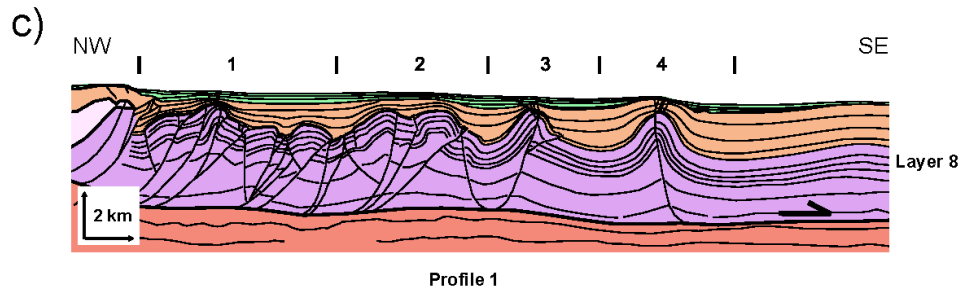
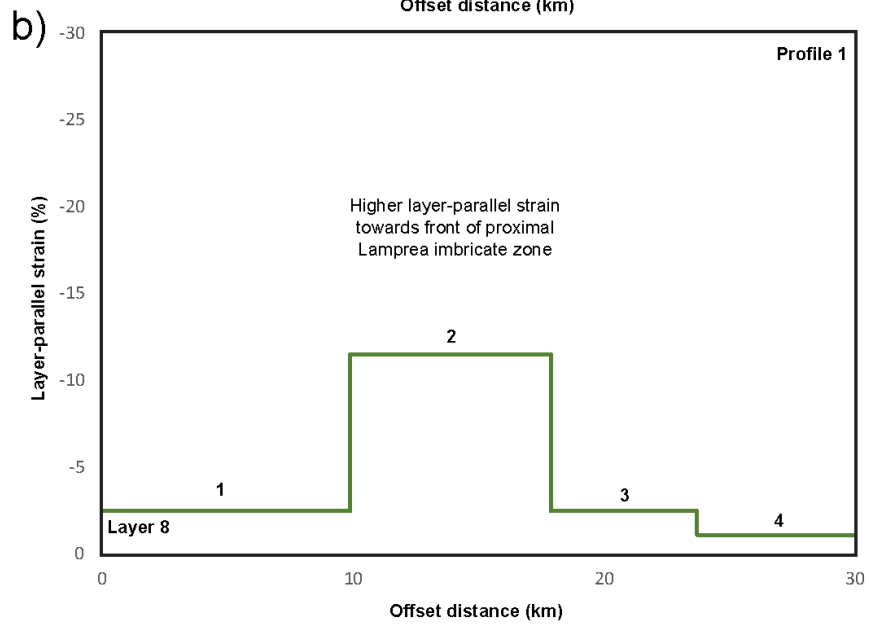
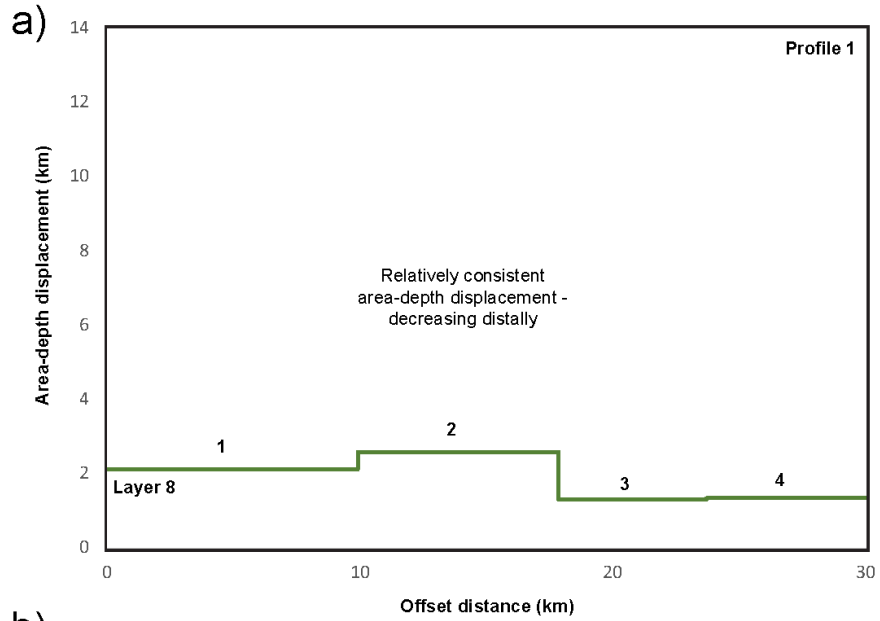
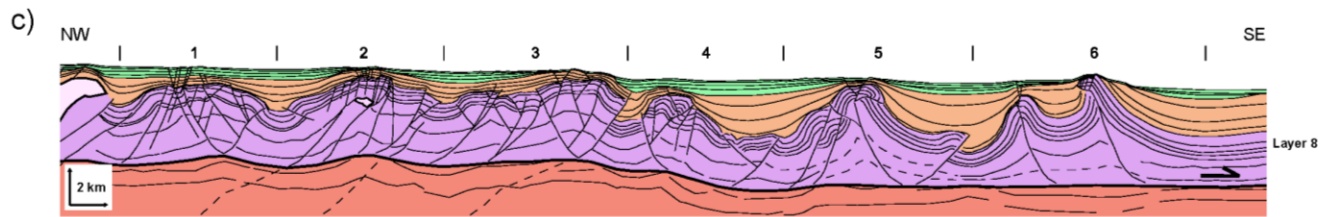
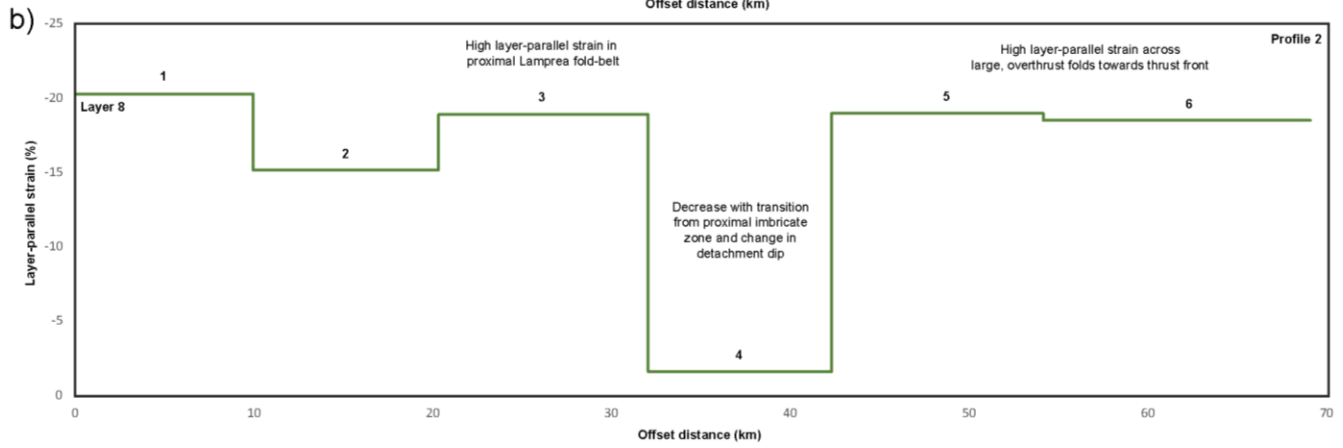
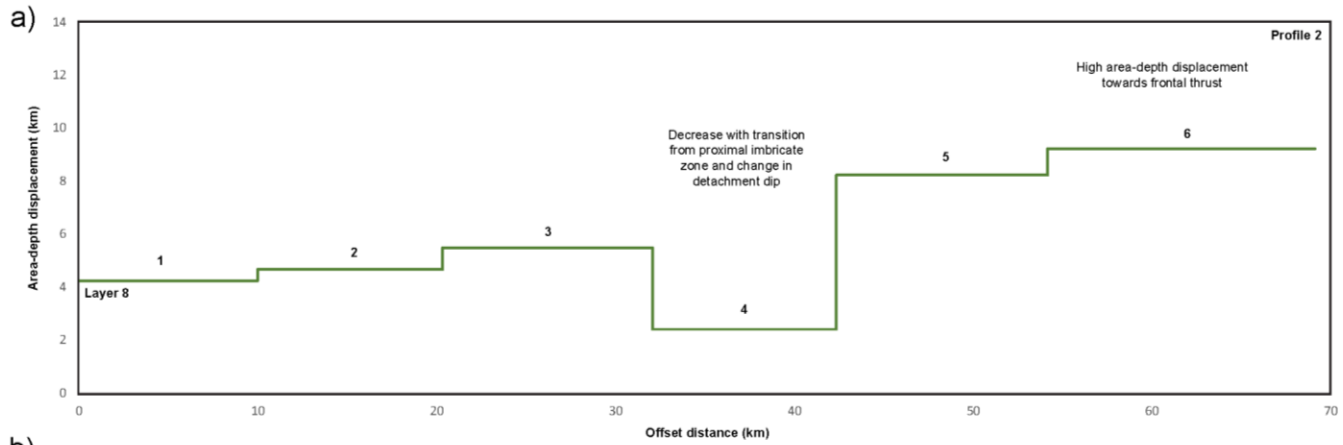


Figure 4.13 Plots of **a)** total calculated area depth displacement and **b)** calculated layer-parallel strain across Profile 2 of the Lamprea fold-belt. Displacement is fairly consistent and increases slightly towards the front of the adjacent Lamprea fold-belt, decreases with a change in detachment angle, then increases across the sizeable outer Mexican Ridges structures in this area that exhibits larger area-depth displacements. The layer-parallel strain of the structures is also consistently high across the profile with the exception of fold 4, which represents a change in detachment angle between the proximal Lamprea fold-belt and the more isolated distal fold structures **c)** Schematic section based on Profile 2 seismic that shows the measured fold complexes and their primary growth packages.



4.6.2 Timing of fold growth onset and associated erosion of pre-growth strata

For Profile 1, the threshold of the positive linear correlation of pre-growth layer measurements, indicating the beginning of fold-growth, occurs between horizon layers 8 and 9 for folds 1, 2 across the proximal Lamprea fold-belt (Figure 4.10a, 4.10b). For fold 3 where the fold-belt begins to transition into the Mexican Ridges-style thrust-related detachment folds (Figure 4.9e), the pre-growth trend similarly breaks-down between layers 9 and 8 (Figure 4.10c). For fold 4 on Profile 1 the relationship breaks down following layer 9 (Figure 4.10d). Reduction in the measured excess area as a result of truncation along the crests of the folds can be observed to varying degrees across the length of Profile 1 (Figure 4.8). Folds 1-2 on Profile 1 exhibit truncation affecting layers 9 and 10 (Figure 4.8a, 4.8b). This truncation, paired with significant crestal collapse with associated normal faulting, is particularly apparent across the axis of fold 3 (Figure 4.8c). Fold 4, located towards the distal end of the section, displays a lesser degree of erosion along its crest, and layer 9 is clearly defined as part of the pre-growth succession in this location (Figure 4.8d).

Fold 1 across Profile 2 displays an earlier break-down of the linear pre-growth trend of area-depth measurements from around layer 7 (Figure 4.11a). Fold 2 containing a small salt diapir and controlled by both salt and shale tectonics, exhibits the earliest break-down of the trend between layers 6 and 7 (Figure 4.11b). Further east along Profile 2, both fold 3 and fold 4 display a linear trend break-down between around layer 8 (Figure 4.11c and 4.11d). As Profile 2 transitions from the proximal Lamprea fold-belt into the distal area defined by Mexican Ridges thrust-related detachment folds (Figure 4.11g), folds 5 and 6 suggest a younger still break-down in the pre-growth trend, occurring between layers 8 and 9 (Figure 4.11e, 4.11f).

Folds 1-3 across the proximal part of the Lamprea fold-belt sit structurally higher compared to folds 4-6 on Profile 2 and folds 1-4 on Profile 1 (Figure 4.10e, 4.10g). This proximal area of Profile 2 defined by folds 1-3 is the lateral equivalent to the area of extensive salt canopies, and minibasins of the Salina del Bravo salt province specified in Profile 1; where more extensive salt canopies have extruded relatively further to the east (Figure 4.5). As such, Fold 3 on Profile 2 corresponds roughly to the position of the front of the leading salt canopy on Profile 1 to the north. Along Profile 2, folds 1-4 exhibit varying degrees of crestal truncation of early syn-growth, and potentially pre-growth strata, affecting layers 8, 9, and 10 (Figure 4.9a, 4.9b, 4.9c, 4.9d). The partially salt-cored fold 2 displays particularly apparent thinning and truncation of layers 8, 9, and 10 with a significant degree of extensional faulting within the pre-growth section overlying the salt-diapir. However, unlike most of the shale-cored folds, fold 2 also displays clear thinning across the fold axis through the Oligocene section, which can be observed for layers 6, 7, and 8 in particular (Figure 4.9b).

Further east along Profile 2, as the Lamprea fold-belt begins to transition into Mexican Ridges style detachment folds, folds 5 and 6 display some erosion of layers 9 and 10 (Figure 4.9e and 4.9f). Folds 5 and 6 in the distal area of Profile 2 are noticeably more massive and asymmetrical compared to their along-strike equivalents of folds 3 and 4 along Profile 1 further north (Figure 4.5). In particular, fold 6 on Profile 2 exhibits significant over-thrusting of the pre-growth succession, resulting in a perceptible increase in seafloor relief and considerable erosion of the pre-growth strata at this location (Figure 4.9f). In Profile 2 clear onlapping seismic growth patterns, as defined in Figure 4.7b, are only apparent across fold 6 following layer 10 (Figure 4.9f). This beginning of observed seismic onlap is the same as that observed

across fold 4 on Profile 1, where crestal truncation is less apparent, and layer 9 is confidently defined as part of the pre-growth succession (Figure 4.9f).

4.6.3 Structural analysis of syn- to post-growth strata

Excess-area versus depth measurements across Profile 1 and 2 folds also display a good linear-fit correlation through the primary growth sequence and is characterized by decreasing measured horizon areas as the fold becomes shallower (Figure 4.9 and 4.10). Three principal syn- to post-growth packages were defined across the Lamprea fold-belt and adjacent deep-water areas, as illustrated in Figure 4.7, with differences in the area-depth trends between phases II and III observed for some of the measured folds (Figure 4.10a, 4.10b, 4.10c, 4.11a, 4.11d, 4.11e).

Fold 1, locally proximally along Profile 1, displays a good trend with little dispersion through the Miocene-Pliocene section. From layer 14 to 17, representing the shallow, Pleistocene MTD growth package, the pattern breaks down and instead displays values of increasing excess-area upwards through the section (Figure 4.10a). At this location, the proximal front of the salt canopy can be observed over-thrusting the synclinal low defining fold 1. The Pleistocene MTD growth package is re-folded and can be seen onlapping the underlying uplifted Miocene and Pliocene section, rendering these measurements inaccurate as a result (Figure 4.8a).

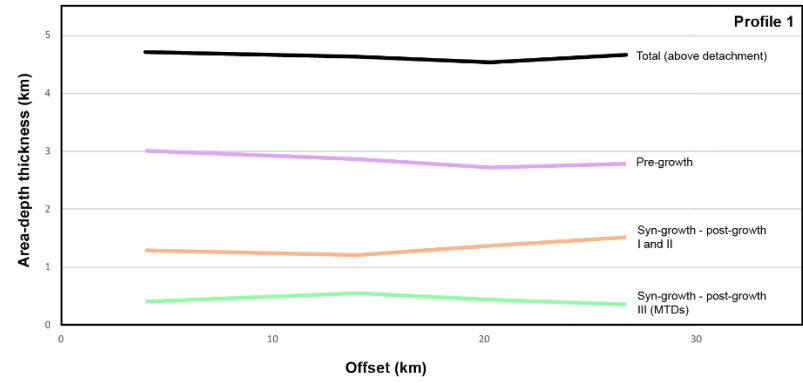
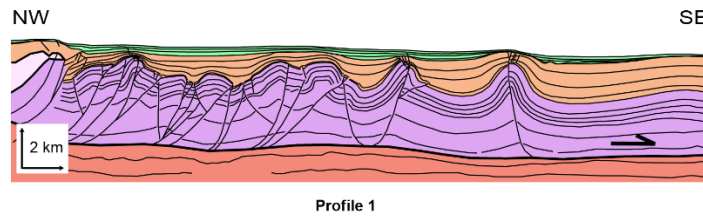
Fold 2 along Profile 1 displays a steepening in the trend of the syn- to post-growth measurements from between layers 14 and 15 up to the seafloor, signaling a decrease in the rate of excess-area loss with depth (Figure 4.10b). Fold 3 also displays a change in the syn- to post-

growth correlation with layers 15 to 17, all exhibiting close to zero excess-area that could be more characteristic of a post-growth rather than a syn-growth area-depth trend (Figure 4.10c). Unlike folds 1-3, the Pleistocene MTD growth sequence is absent to very thin across the fold axis of fold 4 (Figure 4.10e). As a result of this observed thinning and onlap of the MTD sequence, the excess-area versus depth measurements for a consistent trend through what is a mostly complete syn-growth sequence up to the seafloor (Figure 4.10d).

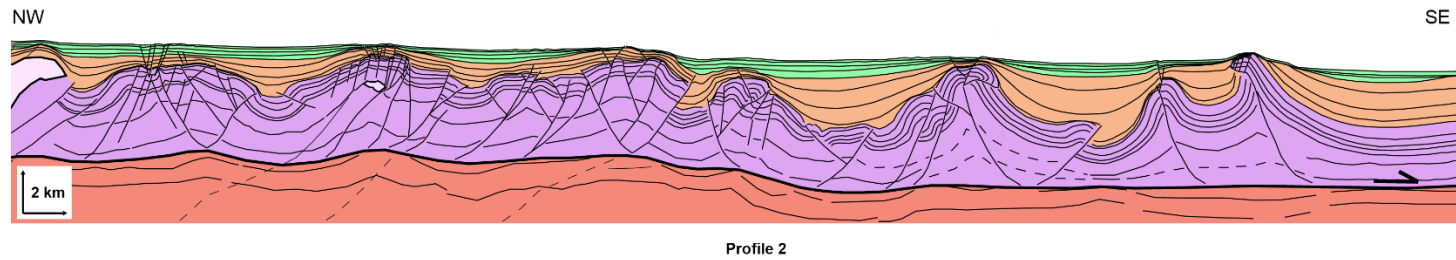
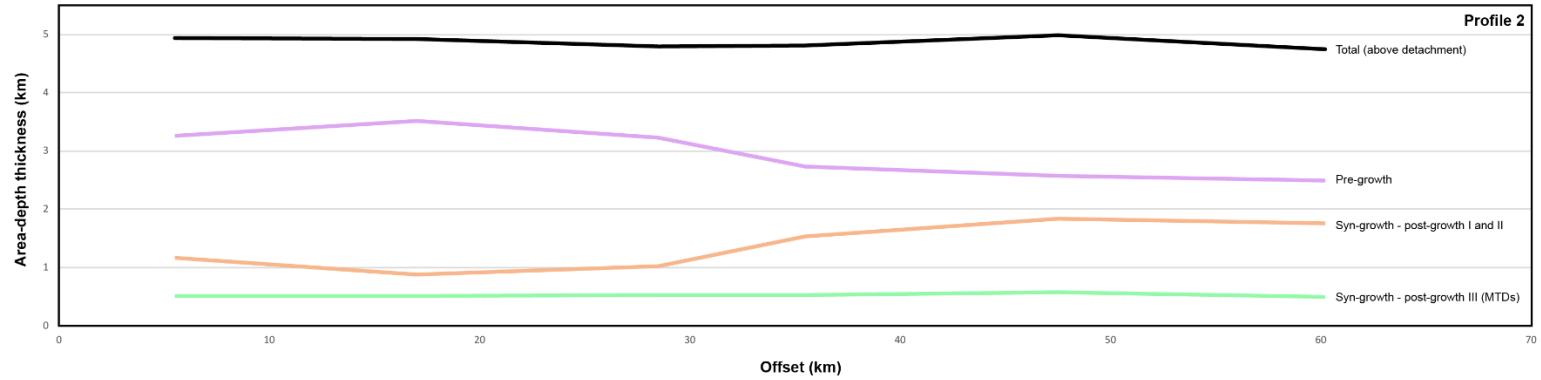
Both folds 1 and 5 along Profile 2 to the south also display a similar change in gradient of the syn-growth trend from around layer 15 and younger (Figure 4.11a and 4.11e), as observed for fold 2 on Profile 1 (Figure 4.10b). A similar issue with measurements of layers 14 to 17 exists for fold 4 on Profile 2 as fold 1 on Profile 1, where significant offset along the frontal thrust of fold 3 has over-thrust the adjacent fold 4 bounding syncline (Figure 4.11d and 4.11g). Folds 2, 3, and 6 along Profile 2 exhibit a consistent, relatively linear trend through the entire growth section up to the seafloor (Figure 4.11b, 4.11c, 4.11f).

Figure 4.14 a) Interpreted schematic depiction of Profile 1 growth sequences and a graph of area-depth calculated thicknesses for each primary sequence along the profile. Pre-growth strata thins slightly towards the front of the fold-belt with a thickening of the total present-day syn-growth sequences. **b)** Interpreted schematic depiction of Profile 2 growth sequences and a graph of area-depth calculated thicknesses for each primary sequence along the profile. Pre-growth strata are thicker more proximally to the west with a thinner overlying present-day syn-growth sequence. Compared to Profile 1, the total sediment thickness is greater despite a slightly thinner pre-growth sequence across the equivalent distal area.

a)



b)



4.6.4 Sediment thickness trends of the principal mapped growth successions

Both Profile 1 and the east half of Profile 2 display similar thicknesses of pre-growth fold-belt strata, which are slightly thinner across Profile 2 by about 200-300 m (Figure 4.14). The fold-belt pre-growth section thickens proximally up to a maximum of about 3.5 km along the western half of Profile 2 (Figure 4.14b). The thickness of the primary Miocene-Pliocene syn- to post-growth phases I and II are up to about 200-300 m higher along the eastern half of Profile 2 as compared to Profile 1 (Figure 4.14). The thicker, structurally-higher pre-growth section across the western half of Profile 2 results in less accommodation space and a significantly thinner corresponding syn- to post-growth succession on the order of as much as 900 m thinner than observed to the east (Figure 4.14b).

The average thickness of the subsequent Pleistocene, MTD-dominated, syn- to post-growth phase is relatively consistent between Profiles 1 and 2 and ranges between about 400-600 m thickness where they thin distally to the west (Figure 4.14). Combined fold-belt sediment thicknesses reach a maximum of close to 5 km, with a total thickness of the deformed wedge averaging around 200-300 m and thicker across the Profile 2 in the southern study area compared to Profile 1 (Figure 4.14).

4.6.5 Characterization of fold-belt structural geometries

Geometric measurements of fold wavelength and amplitude were taken across the length of the fold-belt along both Profile 1 and Profile 2. Measurements were made for each fold-thrust rather than the grouping of structures required for the area-depth strain analysis (Figure 4.14 and 4.15). Measured fold wavelengths across Profile 1 display an overall increase

in both fold wavelength and fold amplitude from west to east with an increased offset distance from the front of the salt canopy (Figure 4.15a and 4.15b). Closely spaced, imbricate thrust-folds and pop-up structures of the Lamprea fold-belt are lower amplitude as individual structures and transition to more massive, but more widely spaced thrust-related detachment folds towards the deformation front in the east (Figure 4.15c).

A similar trend of wider-spaced but higher-amplitude fold structures characterize the easternmost end of Profile 2 to the south, where larger, isolated detachment folds are present (Figure 4.16a, 4.16b, and 4.16c). Directly east along Profile 2, fold wavelengths and amplitudes both become smaller and transition into the Lamprea fold-belt where the folds are similar in magnitude to the westernmost folds in Profile 1 (Figure 4.15a, 4.15b, 4.16a, 4.16b, and 4.16c). The more proximal area in the west of Profile 2 generally comprises lower-amplitude folds, which are usually closely spaced, but with occasional larger wavelength structures (Figure 4.16a and 4.16b). Some of the higher-amplitude, wider-spaced folds include the single salt-cored fold and the significantly uplifted structure corresponding with the front of the proximal fold-belt (Figure 4.16c). Higher-amplitude folds correlate with wider-wavelengths for folds measured across both Profiles 1 and 2 for both the Lamprea fold-belt and Mexican Ridges sub-domains (Figure 4.15 and 4.16).

Figure 4.15 **a)** Graph of individual fold wavelength measurements across the length of Profile 1 that reveals the differences in structural style between the proximal imbricate zone of the Lamprea fold-belt and the more distal and isolated detachment folds, which are typically spaced more widely. **b)** Graph of individual fold amplitude measurements across the length of Profile 1, showing more numerous smaller fold-thrusts in the proximal Lamprea fold-belt and higher-amplitude folds in the distal section. **c)** Interpreted schematic section of Profile 1 showing the primary structural domains with numbering to indicate the folds that were measured.

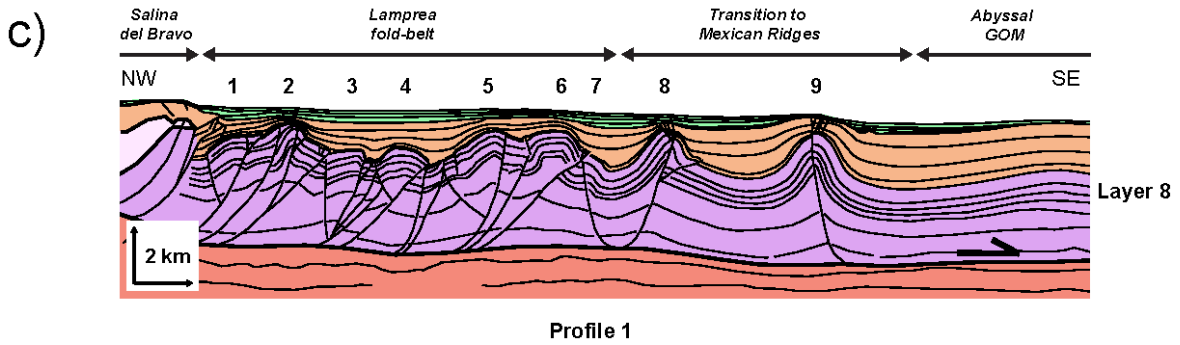
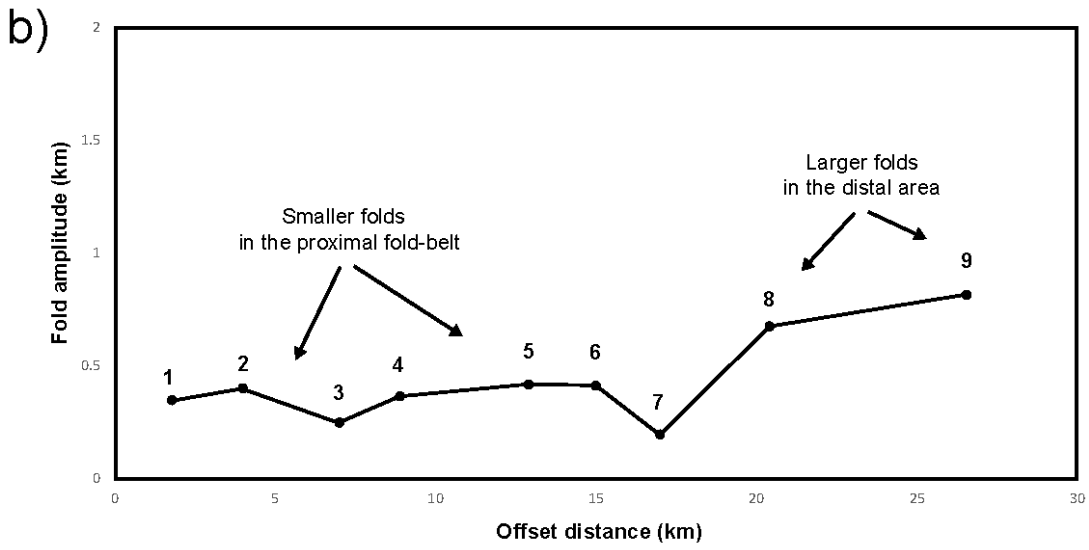
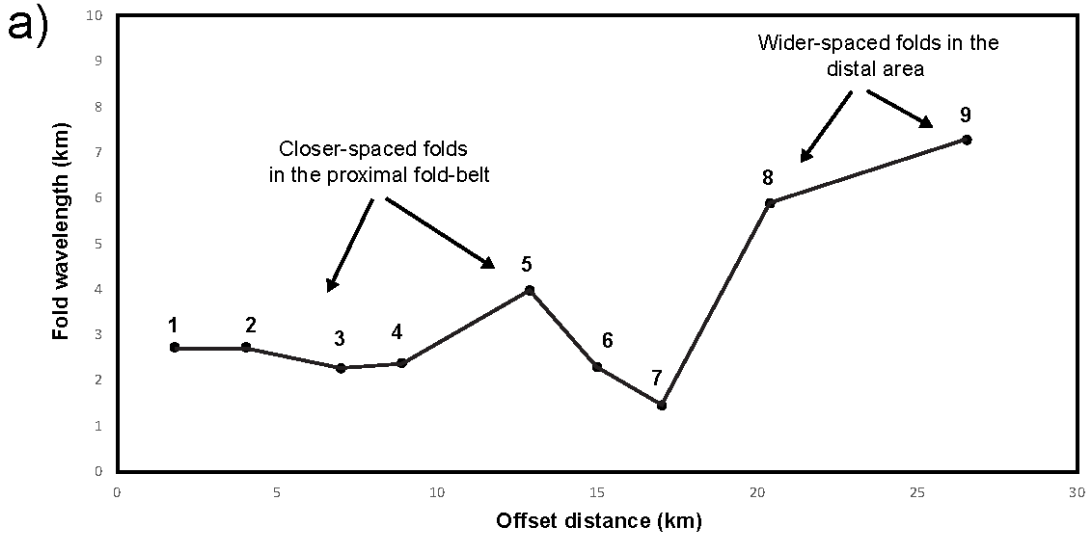
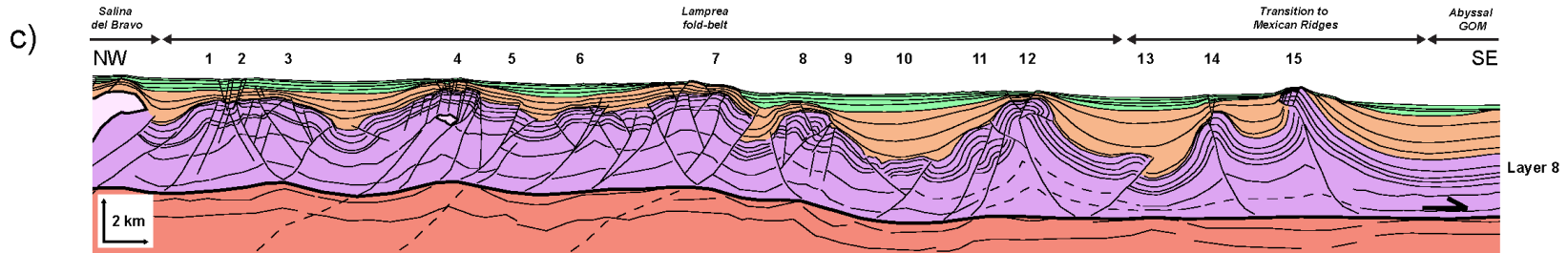
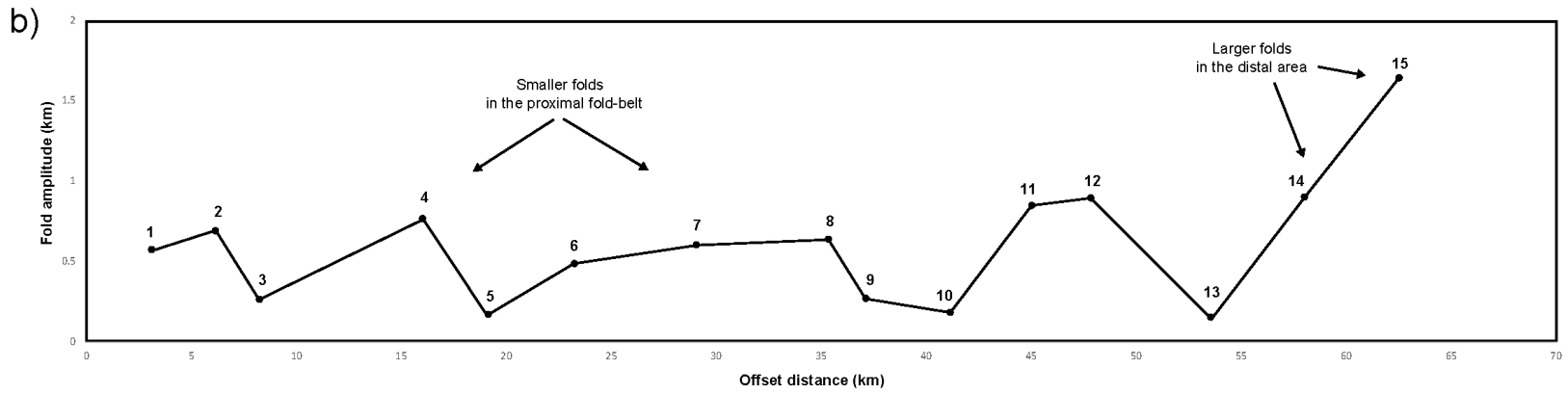
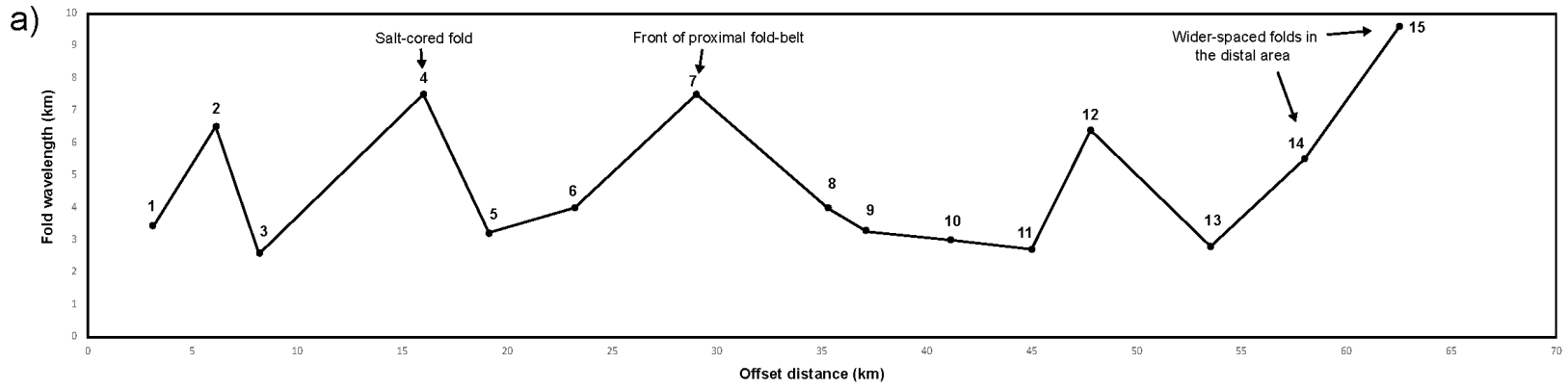


Figure 4.16 **a)** Graph of individual fold wavelength measurements across the length of Profile 2. The proximal area of Lamprea fold-belt in this area consists of both wide and closely spaced thrust-folds. There are more numerous, closely-spaced folds before a transition into the wider-spaced isolated detachment folds of the more distal area. **b)** Graph of individual fold amplitude measurements across the length of Profile 2 that shows higher-amplitude folds in the distal section compared to lower amplitude folds across the proximal Lamprea fold-belt. **c)** Interpreted schematic section of Profile 2 showing the primary structural domains and numbering to indicate the folds that were measured.



4.7 Discussion

4.7.1 Analysis of the growth model and controls on structural deformation

This analysis suggests that there is only one regionally-extensive, detachment surface beneath the Lamprea fold-belt in the vicinity of layer 3 (Figures 4.8-4.11). A single, extensive, detachment surface is indicated by consistent, linear-regression of excess-area versus depth measurements through the entire fold-belt pre-growth strata (Gonzalez-Mieres and Suppe 2006). A single regional detachment across the Lamprea fold-belt that is located at the approximate early Eocene to late Eocene boundary is consistent with the detachment present beneath the Mexican Ridges fold-belt to the south and east (Yarbu and Contreras 2017; Kenning and Mann 2020).

Complex structural deformation and layer thickness changes across the highly thrust-imblicated Lamprea fold-belt increases the uncertainty of calculated area-depth strain values compared to an analysis of individual, geometrically simpler structures such as those that characterize the Mexican Ridges fold-belt (Yarbu and Contreras 2017). Despite the structural complexity, the analysis results in consistent detachment depths across the length of both the Lamprea fold-belt and Mexican Ridges that are reasonably consistent with the seismic observation of the detachment zone (Figures 4.5, 4.8, 4.9).

Fold-belt pre-growth area-depth trends for folds 1, 2, 3, and 4 on Profile 1, and folds 1, 4, and 5 on Profile 2 display excess-area intercepts with sub-detachment measurements (layers 1-2) at relatively near to zero values. However, the remaining folds display detachment depths at clearly non-zero values, which would suggest these latter folds are not area-balanced (Figures 4.8, 4.9). Similar effects have been observed by Yarbu and Contreras (2017) across the

Mexican Ridges fold-belt to the south and could be interpreted as a result of either: 1) diapiric flow of shale into the core of folds; 2) a deeper detachment surface; 3) a velocity pull-up seismic artifact; or 4) the basal detachment is not planar and may be refolded (Yarbu and Contreras, 2017).

Shale flow from beneath synclines is observed across fold 6 on Profile 2 (Figure 4.9f, although shale flow is not observed across the fold-belt (Figure 4.5). Velocity changes through the over-pressured late-Eocene shale package in the Lamprea fold-belt can vary considerably (Vazquez-Garcia 2018), and this factor is likely to negatively impact imaging quality and the observed geometries of seismic reflections beneath the detachment zone. As a result, velocity effects are the most likely explanation for many of the discrepancies in measurements of layers 1 and 2.

The presence of a deeper detachment cannot be completely ruled out, although such a detachment is not regionally present along-strike (CNH, 2015). Any impact from a deeper detachment would only be present towards the proximal area of the Lamprea fold-belt that is closer to deep, autochthonous Jurassic salt. Earlier onset folding and uplift of sub-fold-belt Mesozoic-Eocene strata related to the formation of the Perdido fold-belt is known to have occurred during the Oligocene (Hudec *et al.*, 2019). Deformation of underlying strata as a result of deep salt tectonics could explain excess-area measurements of greater than zero across sub-detachment layers within the proximal area of Profile 2 comprising folds 1-3 (Figure 4.5).

Deep structural effects also explain the structurally-elevated regional detachment surface and changes in the dip of the detachment surface across the proximal part of the fold-belt, as seen on Profile 2 (Figure 4.5). Minor salt bodies are occasionally present within this

area of the Lamprea fold-belt. This salt is likely sourced from deep vertical feeders below the basal Eocene shale detachment (Figure 4.9c, 4.17). However, both the area-depth measurements and seismic observations indicate significant decoupling between the late Eocene to recent, and underlying strata. Any deep structural influence on the development of the shallow-detached Lamprea folds is likely restricted to the proximal fold-belt (folds 1-3 on Profile 2 in Figure 4.5b) and would be of relatively minor magnitude.

4.7.2 Interaction between salt and shale tectonics and their impact on the development of the Lamprea fold-belt

Timing of onset of the structural evolution of the Lamprea fold-belt and adjacent Mexican Ridges style-folds began between the Oligocene and early Miocene across both the length and width of the interpreted sections based on area-depth trends of measured pre-growth strata (Figure 4.10 and 4.11). Although phases of out-of-sequence thrust movement is expected due to the presence of numerous back-thrusts and observed differences in episodes of seismic growth relationships throughout the succession, area-depth measurements appear to indicate a general basinward younging of the onset of folding along both Profiles 1 and 2 (Figure 4.10 and 4.11). Profile 1 ranges from the onset of the growth trend from layer 8-9 to layer 9 in the distal area (Figure 4.10). The proximal region of Profile 2, equivalent to the vast salt canopy on Profile 1, displays earlier onset from layer 6-7, to layer 9 in the distal area (Figure 4.11).

Truncation of the top of the early phase I syn-growth, and pre-growth sequences are marked by an early Miocene unconformity (represented by layer 10) and are variable across the fold-belt (Figure 4.8, 4.9) (Vazquez-Garcia, 2018). Truncation may be responsible for reducing

measured excess fold-areas that results in pre-growth layers plotting as if they were syn-growth; however, erosion appears to be minimal and exposed pre-growth strata at fold crests likely experienced non-deposition during this phase of development (Figure 4.6, 4.7, 4.8, 4.9). The thin, initial early Miocene growth phase displays progressive truncation of its deposited layers away from the fold crest along its back limb. This process is a result of the progressive rotation and steepening of the underlying pre-growth strata onto which it was deposited as these folds formed (Mount *et al.*, 1990). The early Miocene angular unconformity capping the early syn-rift phase I is regionally present across the fold-belt, and seismic onlap patterns marking phase II syn-growth and post-growth basin fill are typically not observed until this horizon with only observed thinning towards the fold crests in phase I (Figure 4.6). Basinward-younging of the pre-growth to syn-growth transition, as indicated by excess-area measurements, could instead represent an increase in the degree of proximal truncation of pre-growth beds along the fold-belt. However, despite this, the interpretation of earlier onset of deformation towards the west of the Lamprea fold-belt appears more likely given the relatively low degree of erosion. Structural restorations by Salomon-Mora (2013) also suggest an earlier onset of deformation for the area of the Lamprea ahead of the southern lobe of the salt canopy (location of Profile 2), compared to the northern area (Profile 1), which would be consistent with my findings.

Evidence for earlier onset of a degree of deformation closer to the salt-front can be more plausibly established for folds 1 and 2 on Profile 2 - where some thinning can be observed across layers 9 and 8 (Figures 4.9a and 4.9b). Both seismic onlap patterns and thinning of units across the fold-axes are present within the Oligocene section of a fold containing an isolated diapir within the Lamprea fold-belt (Figure 4.17). These relationships suggest that salt-involved

structures began developing earlier across the fold-belt and before the onset of widespread shale-tectonics (Figure 4.18). Salt was likely extruded from the deep section along vertical feeders and was emplaced within the mechanically weak Eocene shale layers prior to the initiation of widespread shale tectonics. As a result, the Lamprea fold-belt represents several phases of deformation from the late Oligocene through to the present day that is related to both the initial salt diapirism and subsequent, episodic, phases of development of the salt canopies.

The interpreted Oligocene timing for the beginning of salt movement in the Lamprea fold-belt is consistent with the onset of major load-driven extensional deformation up-dip, which activated basinward salt movement and its extrusion in the Salina del Bravo salt province and also formed the Perdido fold-belt during this period (Figure 4.18) (Hudec *et al.*, 2019). However, the prominent early Miocene unconformity is interpreted to mark the top of the onset of substantial shale-tectonics and widespread structural development of the Lamprea fold-belt, with primary fold growth occurring in the Miocene based on the seismic observations and area-depth measurements (Figures 4.10, 4.11, 4.14).

A Miocene-age formation of the Lamprea fold-belt is coincident with a focus of sedimentation, development of mobile-shale structures, and detachment surfaces west of the salt canopy in the Kama fold-belt area of the offshore Burgos basin (Hudec *et al.*, 2019). Consequently, the formation of the shale-detached Lamprea fold-belt was controlled by the resulting Miocene reactivation and extrusion of the proximal Salina del Bravo salt canopy and linked to ongoing depocenters immediately up-dip (Figure 4.18) (Bilotti *et al.*, 2019; Smith *et al.*, 2019). My area-depth measurements and estimated depth of basal detachment suggest that

the shallow Lamprea fold system is largely decoupled from the deeper autochthonous Jurassic salt detachment and support this salt extrusion hypothesis by these previous workers.

Salt is typically more mobile compared to shale and features a continuous process of deformation until evacuated. In contrast, shale mobility requires significant over-pressure to become mobile, and deformation occurs more episodically (Morley and Guerin 1996). Episodes of fold-belt growth sometimes separated by periods of inactivity that are often highly variable between individual shale-detach folds may partly represent this process (Figure 4.6). Transfer of contractional force from a highly-mobile, primarily salt-controlled detachment system in the Salina del Bravo province to a more resistant shale-controlled system can explain the degree of close-spaced, highly-imbricate thrusting and disposition to back-thrusting across the Lamprea fold-belt as the result of higher basal friction along the basal detachment. The occurrence of mud volcanoes and shale diapirism increases with proximity to the Jurassic salt province across the western Gulf of Mexico (Salomon-Mora 2013).

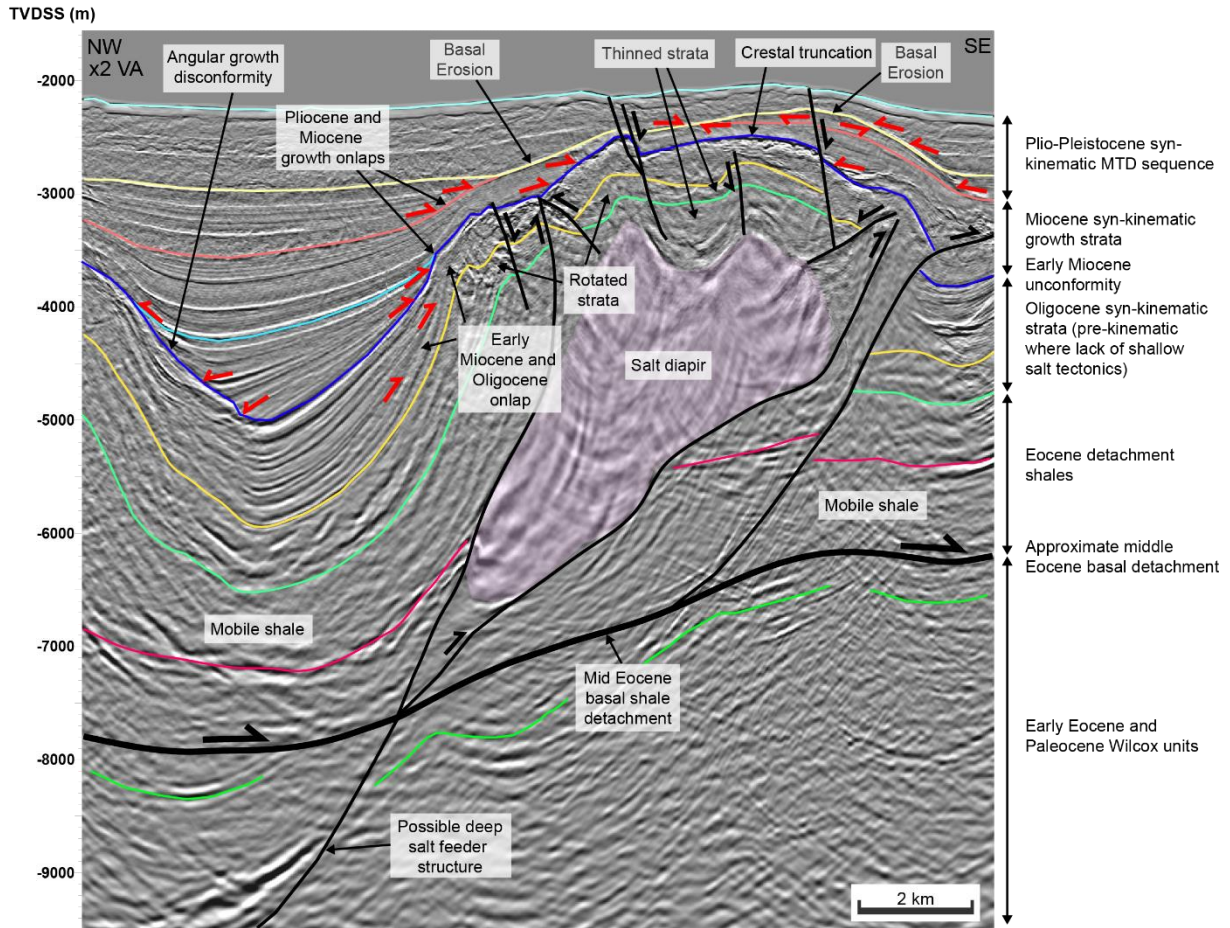


Figure 4.17 Interpreted seismic section oriented NW-SE through an isolated salt diapir in the Lamprea fold-belt. The salt diapir is emplaced within the Eocene shale-layers and has been extruded either along the Eocene shale detachment from the main proximal salt canopy or alternatively and more likely from a deep and underlying salt feeder structure. Erosion along the crest of folds is consistent with that observed across the Lamprea fold-belt (layer 10 – Early Miocene), and is interpreted as the regional onset of fold-belt growth. Onlap patterns within the Oligocene strata not observed across exclusively shale-cored folds and support the interpretation for earlier development of the salt-controlled structures across the Lamprea fold-belt (and Salina del Bravo salt province) in post-early Oligocene time.

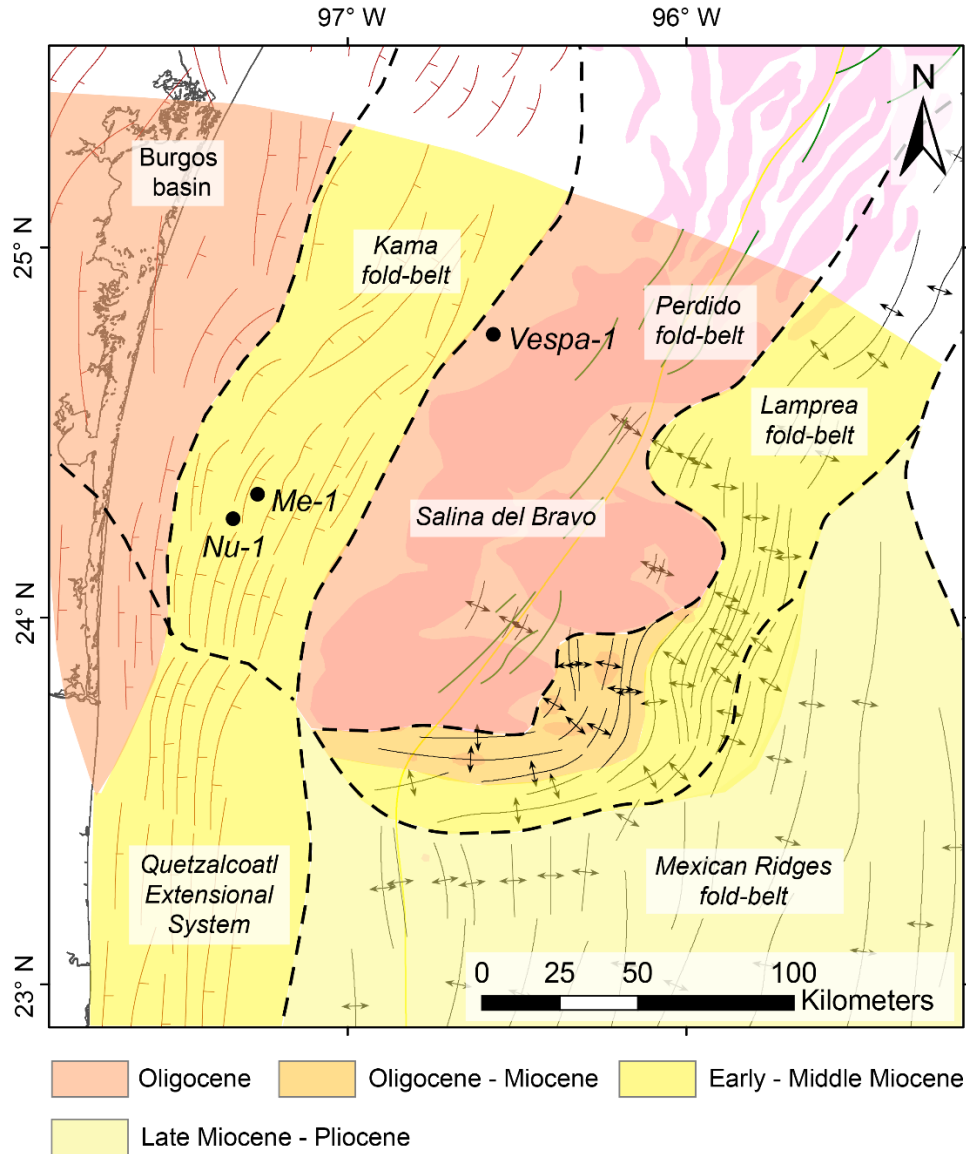


Figure 4.18 Map displaying the interpreted ages for the prime onset of deformation for each of the structural sub-provinces within the immediate study area of the western Gulf of Mexico. In the extensional domain, major growth deposition began in the offshore Burgos basin by the Oligocene coinciding with formation of the Perdido fold-belt down-dip. Formation of the Paleogene shale-detached Lamprea fold-belt occurred as a result of a phase a salt canopy extrusion related to continued basinward sedimentation and formation of the shallow shale-detached Kama fold-belt, behind the salt canopy to the west. Most of the Paleogene shale-detached Mexican Ridges fold-belt formed later and is unrelated to salt tectonics, driven primarily by up-dip, gravity-driven loading and extensional collapse along the Quetzalcoatl shelf-edge. Regional structural elements are modified from Le Roy *et al.*, (2007); CNH (2015); Nguyen and Mann (2015); Yarbuh and Contreras (2017); Vazquez-Garcia (2018); Hudec *et al.* (2019).

4.7.3 Mechanisms for mass transport deposit development across the deep-water syn- to post-growth succession

Laterally-correlateable Pleistocene MTDs are present across the entire length of the Lamprea fold-belt. The majority of these debris-flow units are unlikely to have been deposited due to instabilities resulting from contractional fold growth across the fold-belt (Figure 4.5). Instead, these debris flows can be correlated across the Salina del Bravo salt province to the west, whereas in some locations where they also blanket the top of the salt canopy (Figure 4.19). Formation of Pliocene to recent debris flows can be linked to the extensive extensional fault system in the Kama fold-belt area and offshore Burgos basin up-dip where they likely originated as a result of tectonic instabilities and movement along regional fault planes. Up-dip zones of sediment evacuation are associated with zones of faulting and collapse in the up-dip growth wedge where truncation of reflectors represents a series of erosional escarpments (Figure 4.19). Extensional faulting becomes progressively younger seaward, from Miocene near the coast to presently active structures near the shelf-slope break (Hudec *et al.*, 2019). Numerous debris flows present in the Pliocene to recent section may be the result of a renewed phase of structural deformation and instability associated with high rates of deposition and sediment loading that especially deform the Kama fold-belt area.

Lamprea and Mexican Ridges fold axes with thin or absent Pleistocene MTD units overlying them are interpreted to have continued active growth during MTD deposition and up to the present. The observed steepening of area-depth measurements through the MTD layers across some measured folds indicate structures that exhibited lower rates of tectonic uplift than

the rate of sedimentation (Figures 4.10b, 4.11a, 4.11e) - or had effectively ended their growth phase following the Miocene (Figure 4.10c).

4.7.4 Oligocene play concept and hydrocarbon potential of the southeastern

Lamprea fold-belt trend

The structural style and timing of fold-belt formation constrained by the structural analysis provide important implications for hydrocarbon prospectivity for the study area of the southeastern Lamprea fold-belt. Hydrocarbon exploration to date has mostly been focused along the Perdido fold-belt and Salina del Bravo salt province to the north. As a result, the southeastern Lamprea remains largely unexplored (Figure 4.20). Lamprea discoveries have been made in Oligocene turbidite fan reservoirs in several wells, including Melaoetus-1, which targeted a similar style fold structure along the northern part of the Lamprea fold-belt (Smith *et al.*, 2019) (Figure 4.20).

One of the main risks for the Lamprea fold-belt is hydrocarbon migration. Expelled hydrocarbons would be required to migrate from deep late Jurassic source rocks, through a thick, presumably impermeable, late Eocene layered-shale sequence in order to reach Oligocene age reservoirs in the overlying fold-belt (Figure 4.20b). The presence of sufficient fault conduits in the underlying section is required to transport hydrocarbons up to and past the basal shale detachment interval, forming complex migration pathways and timing. The presence of such salt-controlled structures becomes riskier to the east with increasing distance from the salt front. Jurassic source rocks in the southeastern area are currently predicted to be in the gas-window, and they would have likely have reached thermal maturity before the proposed early Miocene

formation of the Lamprea fold-belt (Figure 4.20a) (Smith *et al.*, 2019). The presence of salt is also likely to depress the thermal regime of the underlying sedimentary section and could result in less thermally mature source rocks with more favorable timing of hydrocarbon expulsion in parts of the Salina del Bravo salt province (Davison and Cunha, 2017; Smith *et al.*, 2019). Understanding the relative timing between hydrocarbon charge and Lamprea trap formation, and how the timing of thermal maturity changes between salt and shale dominated locations, is a challenge for understanding this area.

Despite these challenges, there are numerous observed oil seeps associated with Lamprea, and Mexican Ridges folds in the study area (Figure 4.20a) (Salomon-Mora 2013; CNH 2015). The presence of oil seeps indicates that oil was expelled and trapped beneath Eocene shales before being re-migrated along shallow fault conduits corresponding to the early Miocene formation of the overlying Lamprea fold-belt. The presence of oil and gas seeps in the Lamprea, and Salina del Bravo minibasins support the feasibility that migration can be focused from deep sources into overlying Oligocene traps despite the uncertainties (Figure 4.20).

Figure 4.19 a) Seismic age interpretation of the up-dip Kama fold-belt and Salina del Bravo salt province. Numerous shallow debris flows form correlation markers across parts of the salt canopy and into the deep-water area. Numerous large debris flows of mostly Pleistocene age originate from the up-dip extensional fault zone, blanket parts of the salt canopy, and correlate with interpreted marker horizons within the stacked shallow debris flow package present across the shale-core minibasins and distal Lamprea fold-belt. **b)** Detailed interpretation of the Kama fold-belt faulted section. Many of the debris flow units can be traced up-dip into zones of erosion, collapse, and slumping that are associated with extensive normal faulting in the thick growth strata.

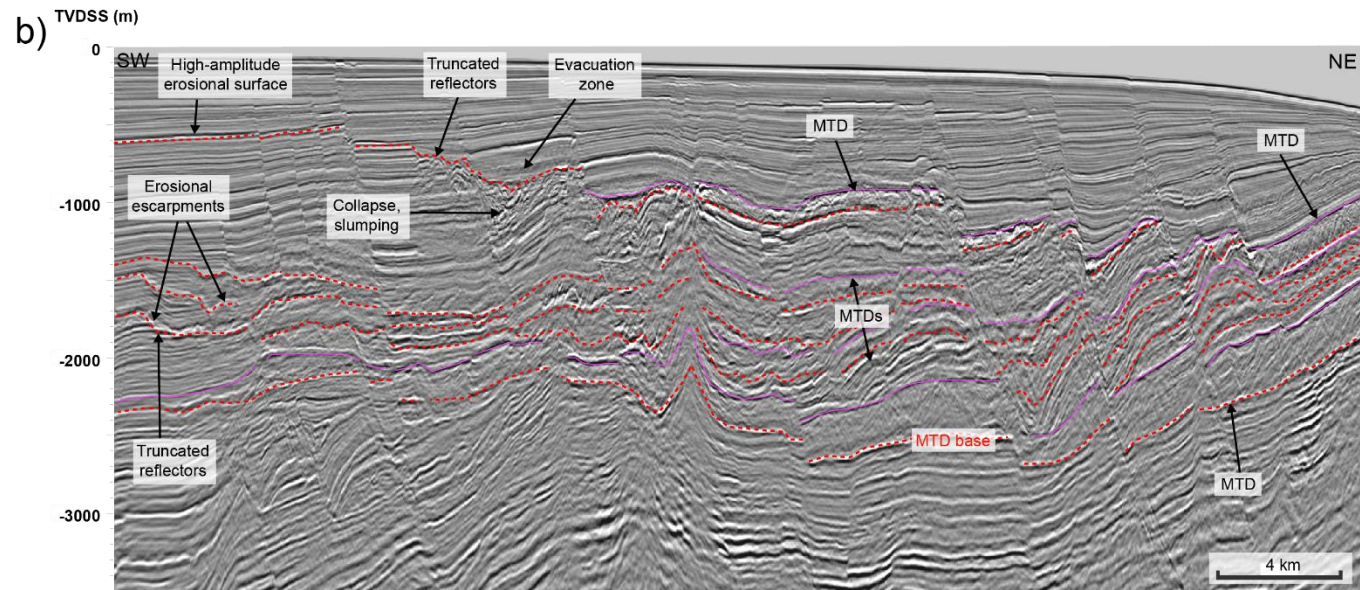
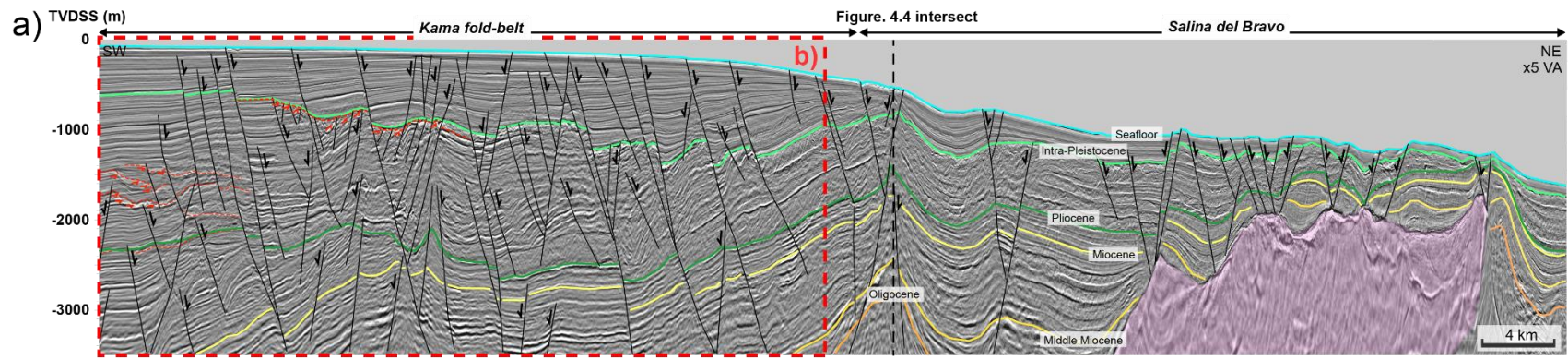
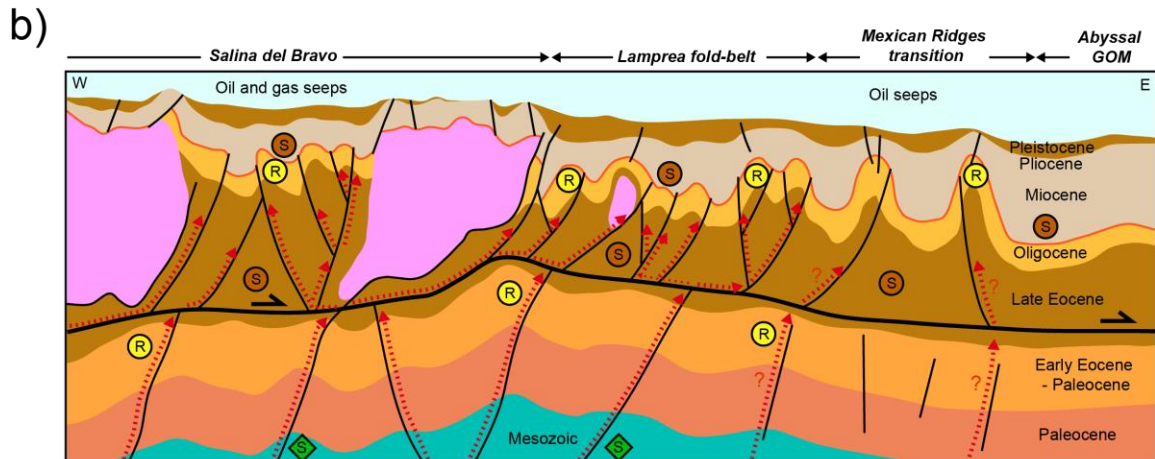
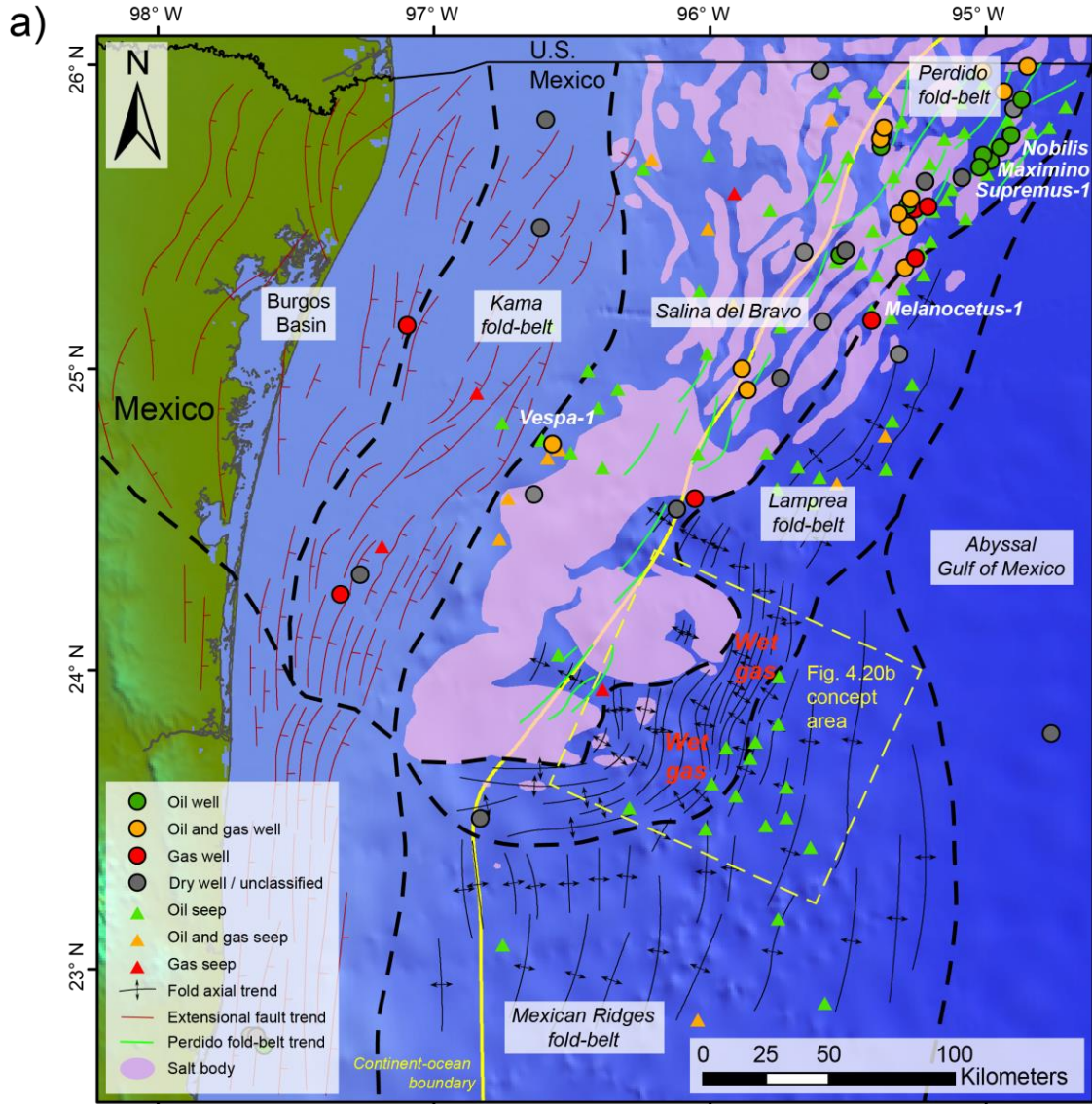


Figure 4.20 a) Map summarizing the SE Lamprea fold-belt trend, which was the focus of this study, in relation to compiled well results and hydrocarbon seep data. Wells that encountered hydrocarbons in the Oligocene section are highlighted along the length of the Perdido and Lamprea fold-belts to the north and are associated with numerous oil slicks that extend into the underexplored SE Lamprea trend. **b)** Schematic summary section integrating the results of this study with information on petroleum systems. Oligocene reservoirs above the thick shale detachment of the Lamprea fold-belt would require complex migration routes that are charged by underlying Mesozoic source rocks. The most obvious potential migration routes follow deep salt-related structures. The influence of these inferred migration routes decrease to the east across the fold-belt and increases migration risk - despite the presence of numerous oil seeps in the distal area. Regional structural elements for a) are modified from Le Roy *et al.*, (2007); CNH (2015); Nguyen and Mann (2015); Yarbuh and Contreras (2017); Vazquez-Garcia (2018); Hudec *et al.* (2019). Well data is modified from CNH (2019) and seep locations from CNH (2015).



4.8 Conclusions

1. Excess-area versus depth measurements of thrust detachment folds constrains the reconstruction of early Miocene to recent deformational across the deep-water Lamprea fold-belt and adjacent Mexican Ridges along the southeastern edge of the Salina del Bravo salt province. Calculated depth-to-detachment estimates support the presence of a single, regional, basal detachment surface located at the approximate early Eocene to late Eocene boundary. This detachment is structurally higher in the proximal Lamprea fold-belt and typically exhibits along-profile changes in the angle of dip.

2. Area-depth measurements across the Lamprea fold-belt suggest a mostly early Miocene age of onset of deformation and initiation of shale tectonics with primary fold-belt growth occurring during the Miocene. Results suggest shallow fold-belt formation was driven primarily by a Miocene phase of reactivation and extrusion of the proximal Salina del Bravo salt canopies. The effect of deep, underlying autochthonous salt tectonics has a negligible impact on this southernmost part of the Lamprea fold-belt.

3. The Lamprea fold-belt is characterized by highly-imbricate faulting and pop-up structures before the fold-belt transitions to individually higher-amplitude, and larger-wavelength thrust-related detachment folds in the area south and east into the Mexican Ridges.

4. The Lamprea fold-belt in the southern part of the study area is significantly wider (69 km) compared to its 40 km width 31 km to the north. The southern part of the study area exhibits; 1) an earlier onset of deformation (Oligocene-early Miocene); 2) a higher degree of truncation of the early syn- to pre-growth succession; 3) a thicker syn- to post-growth sequence; 4) larger, high-amplitude fold structures exhibiting more considerable amounts of area-depth

displacement and layer-parallel strain; and 4) an increased interaction with salt tectonics in the most proximal part of the fold-belt.

5. Isolated Jurassic salt diapirs are present across the proximal Lamprea fold-belt, where these diapirs were extruded from deep, underlying vertical feeder systems into the overlying, mechanically-weak Eocene shale sequence. Folds cored by both salt and mobile shale display earlier onset of growth and coincide with the onset of significant Oligocene salt-related tectonic activity across entire the Salina del Bravo salt province, prior to initiation of widespread shale tectonics across the Lamprea fold-belt in the Miocene.

6. Three principal, syn- to post-growth successions characterize the Lamprea fold-belt; 1) a thin, mostly early Miocene-age initial growth phase displaying thinning towards, and truncation away from fold crests, 2) a thick, mostly Miocene-age variably syn- to post-growth phase; and 3) an overlying shallow Pleistocene stacked sequence of MTDs close to the seafloor that for most part exhibits lower growth rates, and erodes the underlying section. This regionally extensive, Pleistocene to recent MTD sequence developed as a result of erosion, slumping, and tectonic instability associated with a phase of basinward-younging extensional faulting, sediment loading, and shale diapir collapse in the Kama fold-belt area directly west of the Salina del Bravo salt province.

7. Hydrocarbon plays exist within folded Oligocene turbidite fan reservoirs within the Lamprea fold-belt. However, relatively recent Miocene-age deformation of the Lamprea fold-belt reflects a complex timing history and series of migration routes. Deep underlying, Jurassic salt-related structures are required to facilitate the migration of hydrocarbons from deep, Mesozoic source rock intervals, through the shale-rich Eocene detachment zone, and into

overlying fold-belt structures. Hydrocarbon migration, therefore, becomes progressively higher risk with increasing distance from the Salina del Bravo deformation front to the east.

8. Although the timing of onset and the causal mechanisms for deformation across the Lamprea fold-belt have been characterized in this study, our observations suggest that the timing of fold-growth is highly complex. Multiple phases of growth can vary considerably between individual folds along-profile, and the end of growth is inconsistent across the fold-belt. Further work, such as full restorations, are required to more closely constrain these specific episodes of fold growth, distinguish them from intervening periods of lack of growth, and examine how these may vary across different areas of the fold-belt.

CHAPTER 5: SUMMARY AND CONCLUSIONS OF THIS DISSERTATION

5.1 Tectonic controls on the geological development of the Mexican Gulf of Mexico

The three studies within this dissertation each propose new insights into the regional tectonic controls on structural and stratigraphic development of the Mexican sector of the Gulf of Mexico basin. Each study provides a focus and evaluation of different sections of the Mesozoic-Cenozoic stratigraphy across the region. My analysis has characterized key differences in passive-margin fold-belt formation between the three sub-areas, controlled primarily by their unique tectonic histories and is summarized here.

Chapter 2: Regional mapping of the deep-water Yucatan margin revealed differences in sedimentation patterns through time, which impact the burial history and maturity of potential source rock horizons across the area. The Yucatan margin is a conjugate to offshore Florida, rather than the Salina del Bravo salt province, and this results in a much broader, unrestricted, salt-involved gravitational system and much less salt deposited. The Yucatan margin is in contrast to the narrow, steep continental margin found along offshore eastern Mexico, which is bounded at its basinward edge by a topographic basement feature known as the BAHA high (Hudec and Norton 2019). The location of the Yucatan study area means that influence from the Laramide orogeny that affected onshore Mexico and the western Gulf of Mexico is minimal compared to the other two study areas. As a result, the Yucatan margin has been tectonically quiescent since the Mesozoic.

Chapter 3: The Mexican Ridges province is unique in that a large part of the fold-belt developed above a substrate of late Jurassic oceanic crust rather than a thinned continental margin. As such, there is a lack of middle Jurassic salt across the area, and the fold-belt is controlled primarily by detachment along late Paleogene shale layers and associated with up-dip gravitational collapse along the continental shelf-edge. Mapping of regional detachment shales indicated that significant differences in thickness and distribution along-strike, act as a control on the structural development of the overlying fold-belt. The eastern continental margin of Mexico exhibits a greater influence from the Laramide orogeny, and the late Paleogene detachment shales were interpreted to be a stacked series of debris flow aprons with deposition linked to significant, nearby post-Laramide tectonic activity.

Chapter 4: The Salina del Bravo salt province in the western Gulf of Mexico forms the southernmost limit of the northern half of the Gulf of Mexico continental crust and post-rift salt basin before transitioning into the Lamprea fold-belt and Mexican Ridges. The structural architecture of the region is controlled primarily by its narrow and steep continental margin in this part of the Gulf of Mexico combined with the existence of the BAHA basement high forming a buttress along the continent-ocean boundary. Due to proximity to post-Laramide tectonic activity, the area possesses thick late Paleogene shales as observed across the Mexican Ridges, in addition to middle Jurassic salt. The structural analysis demonstrated that the proximal shallow salt tectonics act as the main driver for associated shale tectonics along the Lamprea fold-belt deformation front.

5.2 Regional impacts on petroleum system risk and hydrocarbon prospectivity

The geological and geophysical analyses conducted provide additional insight into the hydrocarbon prospectivity and critical risk factors for future exploration for each of the three highly-frontier study areas. Variation in the tectonic evolution and related passive-margin fold-belt development as a control on hydrocarbon prospectivity has been individually assessed for each project study area in the preceding chapters and is summarized here (Figure 5.1). Figure 5.1 characterizes the regional petroleum system risk across the most underexplored provinces of the Mexican sector of the Gulf of Mexico, based on the findings compiled by this study. Assigned risk values are qualitative and relative; as the three study areas are highly underexplored until future drilling tests specific play areas, they are all at present high-risk overall by definition.

The deep-water Yucatan margin study has demonstrated that there is a high probability for an active late Mesozoic petroleum system operating in the diapir and minibasin province along the outer marginal rift. Hydrocarbon slick data confirmed by the thermal modeling suggests the area is a low risk for oil and gas maturity. This area is also more proximal to sand-rich turbidite fan systems that prograde northwards via the Veracruz trough along the western edge of the Campeche salt basin (Figure. 5.1). Petroleum system risk increases up-dip to the southeast as shallower burial results in lower predicted source rock thermal maturity, and long-distance lateral migration is increasingly required to charge potential traps (Figure 5.1).

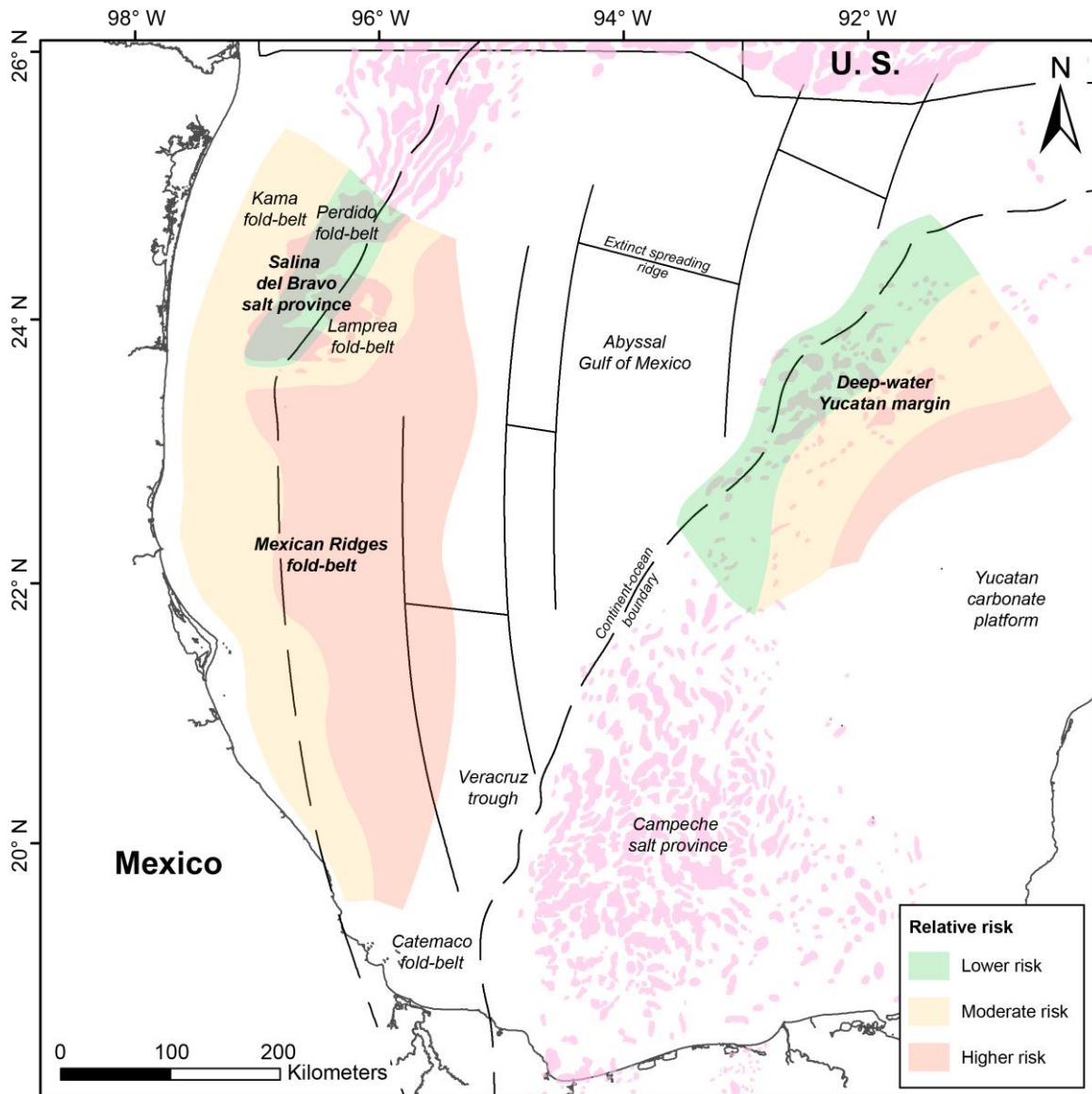


Figure 5.1 Regional map of the Mexican sector of the Gulf of Mexico showing assessed petroleum system risk. Characterized risk is purely qualitative and based on evaluations made during the course of this study. Risk is relative between the areas within the study as currently all three provinces are significantly underexplored, and therefore remain high-risk regions for hydrocarbon exploration overall. Continent-ocean boundary and spreading ridges from Nguyen and Mann (2015).

Potential Norphlet-equivalent aeolian reservoirs in the extensional salt-roller province are indicated to be present; however, Oxfordian source rock presence is not confirmed. There are no deep exploration wells to date in the region, and as such, the area as a whole remains high-risk unless potential future play-opening discoveries can be confirmed. The multiple thermal maturity scenarios developed in this study have helped to characterize this critical but to date little characterized risk factor. The region holds promising future potential for hydrocarbon exploration, and therefore developing these concepts is crucial for an area with limited data such as this.

The southernmost part of the Salina del Bravo salt province, including the associated, shallow-detached Lamprea and Kama fold-belts, and the underlying Perdido fold-belt have been demonstrated to possess future potential hydrocarbon prospectivity. Many discoveries in Paleogene reservoirs have been encountered in Perdido and Lamprea fold-belt structures to the north, and these plays could continue along-strike further south along the margin. Despite the presence of shallow detachments along thick impermeable shale sequences in the late Paleogene, the additional presence of underlying middle Jurassic salt and associated faulting allow for potential hydrocarbon migration routes from deep Mesozoic source rocks into shallow reservoir intervals. Petroleum system risk increases to the east over the oceanic crust as the distance from the salt front and associated deep structural migration pathways becomes farther (Figure. 5.1).

The deep, folded Perdido fold-belt and overlying salt canopies mini-basins of the Salina del Bravo salt province provide large structural traps, and more likely more favorable present-day source rock maturities compared to the more deeply-buried and salt-poor areas of

the Lamprea and Kama fold-belts (Figure. 5.1). However, one of the main risks across the region as a whole remains these complicated hydrocarbon migration routes and differences in timing between source rock generation and migration with structural development of trapping structures. Detailed mapping of the deformation front along the Lamprea fold-belt in this study has resulted in the characterization of the timing of phases of fold-belt formation. The interaction between salt and shale tectonics was also analyzed, and as discussed, is a crucial factor in assessing the petroleum system architecture of the area.

Generally, the Mexican Ridges is likely to be the highest risk area for exploration out of the three study areas (Figure 5.1). As the fold-belt overlies mostly oceanic crust, it does not possess middle Jurassic salt and therefore lacks significant deep structural expression beneath its Paleogene MTD shale detachment. The timing of Tithonian source rock deposition relative to oceanic crust formation also means substantial areas of the petroleum system are effectively unproven to date. Petroleum system risk improves in the more proximal regions of the fold-belt overlying thinned continental crust and where present-day source rock maturity is more favorable. If hydrocarbons generated in the deep-water migrate up-dip via Paleogene carriers or beneath impermeable detachment shales, they are more likely to be trapped in structures along the edge of the continental shelf. As part of this study, mapping the thickness distributions of the late Paleogene detachment MTDs across the fold-belt is crucial to characterize the critical petroleum systems risk resulting from the presence of these thick impermeable units. Despite these challenges, there are numerous documented oil and gas seeps across the fold-belt, and numerous amplitude anomalies associated with detachment folds were identified in this study and suggested there is some promising hydrocarbon

potential for the region. However, the presence of oil seeps above areas of post-mature Tithonian source rocks and relatively recent late Miocene timing of fold-belt formation suggests a complex migration history and likely indicates the re-migration of hydrocarbons. Although the Mexican Ridges was demonstrated as a gas-rich system, it is unclear how much of this may be biogenic rather than thermogenic hydrocarbons.

Overall, the frontier regions of the Mexican sector of the Gulf of Mexico basin exhibit promising potential for future hydrocarbon prospectivity and should be a region where future exploration efforts are focused. This study has highlighted the importance of sub-regional tectonics as a control on many different aspects of the margin architecture, and the subsequent impact on petroleum prospectivity. As further exploration wells are drilled and more data collected over time, our understanding of these regions and specific plays within them will continue to improve, as well as our characterization of the petroleum systems risk.

BIBLIOGRAPHY

Alzaga-Ruiz, H., Granjeon, D., Lopez, M., Seranne, M., Roure, F., 2009. Gravitational collapse and Neogene sediment transfer across the western margin of the Gulf of Mexico: Insights from numerical models. *Tectonophysics*, 470, 21-41.

Ambrose, W. A., Fouad, K., Sakurai, S., Jennette, D. C., Brown Jr., L. F., Guevara, E. H., Dunlap, D. B., Wawrzyniec, T. F., Talukdar, S. C., Garcia, M. A., Romano, U. H., Ruiz, H. R., Hernandez, R. C., Vega, J. A., and Zamora, E. M., 2009. Neogene tectonic, stratigraphic, and play framework of the southern Laguna Madre–Tuxpan continental shelf, Gulf of Mexico. In: C. Bartolini, and J. R. Roman Ramos, eds., *Petroleum systems in the southern Gulf of Mexico: AAPG Memoir 90*, 477–502.

Andreani, L., Rangin, C., Martínez-Reyes, J., Le Roy, C., Aranda-García, M., Le Pichon, X., Peterson-Rodriguez, R., 2008. The Neogene Veracruz fault: evidences for left-lateral slip along the southern Mexico block. *Bull. Soc. géol. Fr.*, 197 (2), 195-208.

Bentley Sr., S. J., Blum, M. D., Maloney, J., Pond, L., Paulsell, R., 2016. The Mississippi River source-to-sink system: perspectives on tectonic, climatic, and anthropogenic influences, Miocene to Anthropocene. In: *Source-to-Sink Systems: Sediment & Solute Transfer on the Earth Surface*, eds: Welsh, J. P., Wiberg, P., Aalto, R., *Earth-Science Reviews*, 153, 139-174.

Bilotti, F., Roberts, M., Liu, J., Brennan, P., Smith, S. A., 2019. Structural evolution of the Perdido fold-belt, Mexico. *GeoGulf Transactions*, 69, 455.

Brooks, J. M., Bryant, W. R., Bernard, B. B., Cameron, N. R., 1999. The nature of gas hydrates on the Nigerian continental slope. *Annals of the New York Academy of Sciences*, Third International Conference of Gas Hydrates, Park City, Utah, July 18-22, 1999.

Cantú-Chapa, A. 2001. Mexico as the western margin of Pangea based on biogeographic evidence from the Permian to the Lower Jurassic, in C. Bartolini, R. T. Buffler, and A. Cantú-Chapa, eds., *The western Gulf of Mexico Basin: Tectonics, sedimentary basins, and petroleum systems: AAPG Memoir 75*, 1-27.

Cantu-Chapa, A. 2009. Upper Jurassic stratigraphy (Oxfordian and Kimmeridgian) in petroleum wells of Campeche Shelf, Gulf of Mexico, in C. Bartolini and J. R. Roman Ramos, eds., *Petroleum systems in the southern Gulf of Mexico: AAPG Memoir 90*, 79 – 91.

Carboni, F., Back, S., Barchi, M. R., 2019. Application of the ADS method to predict a “hidden” basal detachment: NW Borneo fold-and-thrust belt. *Journal of Structural Geology*, 118, 210–223.

Christeson, G. L., Van Avendonk, H. J. A., Norton, I. O., Snedden, J. W., Eddy, D. R., Karner, G. D., Johnson, C. A., 2014. Deep crustal structure in the eastern Gulf of Mexico, *Journal of Geophysical Research-Solid Earth*, 119 (2), 6782-6801.

Clark, J, Ochos, J., Stockli, D., Fildani, A., Gerber, T., Covault, J., Guzman, J., Vinnels, J., Marshall, J., (2019), Provenance and Morphology of Extensive Oligocene-Miocene Deep-Water Fan Systems Sourced from Chiapas-Veracruz and Sierra Madre Oriental, Gulf of Mexico. 2019 AAPG Annual Conference and Exhibition, San Antonio, Texas.

Comisión Nacional de Hidrocarburos, 2015. Perdido fold belt, subsalt belt, Mexican Ridges, petroleum geological synthesis. Accessed 18 September, 2017:

<https://rondasmexico.gob.mx/wp-content/uploads/2016/01/ATLASAGUASPROFUNDASNORTEVERSIONINGLES06012016OK.pdf>

Comisión Nacional de Hidrocarburos, 2015. Saline Basin, petroleum geological synthesis.

Accessed 25 January 2019: <https://rondasmexico.gob.mx/media/1557/geological-atlas-cs.pdf>

Comisión Nacional de Hidrocarburos, 2017. Round 2.4 Bid Round. Accessed September 29,

2018: <https://rondasmexico.gob.mx/eng/rounds/round-2/cnh-r02-1042017/monitoring-and-transparency/>

Corredor, F., Shaw, J. H., Bilotti, F., 2005. Structural styles in the deep-water fold and thrust belts of the Niger Delta. AAPG Bulletin, v. 89, No. 6, 753-780.

Cossey, S. P. J, Van Nieuwenhuise, D., Davis, J., Rosenfeld, J. H., and Pindell, J. 2016. Compelling evidence from eastern Mexico for a Late Paleocene/Early Eocene isolation, drawdown, and refill of the Gulf of Mexico. Interpretation, 4 (1), SC63-SC80.

Cunha, T. A., Lawrence, S., Garner, L., Farrimond, P., Weston, J., 2018. Heat-flow and source rock maturity modeling in the distal domain of the western African margin. AAPG Search and Discovery Article #30584.

Davison, I., Alsop, G. I., Evans, N. G., Safaricz, M., 2000. Overburden deformation patterns and mechanisms of salt diapir penetration in the Central Graben, North Sea. Marine and Petroleum Geology, 17, 601-618.

Davison, I., Cunha, T. A., 2017. Allochthonous salt sheet growth: Thermal implications for source rock maturation in the deep-water Burgos Basin and Perdido Fold Belt, Mexico. Interpretation, 5 (1), T11-T21.

Dott, R. H., 1963. Dynamics of subaqueous gravity depositional processes. AAPG Bulletin, 47 (1), 104-128.

E&P Magazine, 2012. Pemex confirms wet gas in deep-water exploration well. Accessed October 22, 2018: <https://www.epmag.com/pemex-confirms-wet-gas-deep-water-exploration-well-672246>

Eddy, D. R., Van Avendonk, H. J. A., Christeson, G. L., Norton, I. O., Karner, G. D., Johnson, C. A., Snedden, J. W., 2014. Deep crustal structure of the northeastern Gulf of Mexico: Implications for rift evolution and seafloor spreading. *Journal of Geophysical Research-Solid Earth*, 119 (9), 6802-6822.

Epard, J.L., Groshong Jr., R.H., 1993. Excess area and depth to detachment. *AAPG Bulletin*, 77, 1291–1302.

Feng, J., Buffler, R. T., Kominz, M. A., 1994. Laramide orogenic influence on late Mesozoic-Cenozoic subsidence history, western deep Gulf of Mexico basin. *Geology*, 22, 359-362.

Ferrari, L., Orozco-Esquivel, T., Manea, V., Manea, M., 2012. The dynamic history of the Trans-Mexican Volcanic Belt and the Mexico subduction zone. *Tectonophysics*, 522-523, 122-149.

Festa, A., Ogata, K., Pini, G. A., Dilek, Y., Alonso, J. L., 2016. Origin and significance of olistostromes in the evolution of orogenic belts: A global synthesis. *Gondwana Research*, 39, 180-203.

Fick, A., 2016. Seismic Characterization of an Oligocene, Ductile, Sedimentary Wedge Underlying the Mexican Ridges Fold-thrust belt, Western Gulf of Mexico. Unpublished capstone thesis: University of Houston, Houston, United States, 35 p.

Fredericks, B. C., Blum, M. D., Snedden, J. W., Fillon, R. H. 2020. Early Mesozoic synrift Eagle Mills Formation and coeval siliciclastic sources, sinks, and sediment routing, northern Gulf of Mexico basin, GSA Bulletin.

Galloway, W. E., 2008. Depositional Evolution of the Gulf of Mexico Sedimentary Basin. *Sedimentary Basins of the World*, 5, 505-549.

Galloway, W. E., 2005. Gulf of Mexico depositional record of Cenozoic North American drainage basin evolution. In: M. D. Blum, S. B. Marriott, and S. F. LeClair, eds., *Fluvial Sedimentology VII: Ghent, Belgium, International Association of Sedimentologists Special Publication*, 35, 409-423.

Galloway, W. E., Ganey-Curry, P. E., Li, X., Buffler, R. T., 2000. Cenozoic depositional history of the Gulf of Mexico basin. *AAPG Bulletin*, 84 (11), 1743-1774.

Galloway, W. E., Whiteaker, T. L., Ganey-Curry, P., 2011. History of Cenozoic North American drainage basin evolution, sediment yield, and accumulation in the Gulf of Mexico basin. *Geosphere*, 7 (4), 938-973.

Garcia-Palomo, A., Macias, J. L., Espindola, J. M., 2004. Strike-slip faults and K-alkaline volcanism at El Chichon volcano, southeastern Mexico. *Journal of Volcanology and Geothermal Research*, 136 (3-4), 247-268.

Godo, T., 2017. The Appomattox field: Norphlet Aeolian sand dune reservoirs in the deep-water Gulf of Mexico. In: R. K. Merrill and C. A. Sternbach, eds., *Giant fields of the decade 2000–2010: AAPG Memoir 113*, 29–54.

Goldhammer, R. K., Johnson, C. A., 2001. Middle Jurassic–Upper Cretaceous paleogeographic evolution and sequence-stratigraphic framework of the northwest Gulf of Mexico Rim. In: C. Bartolini, R. T. Buffler, A. Cantú -Chapa, eds., *The western Gulf of Mexico Basin: Tectonics, sedimentary basins, and petroleum systems: AAPG Memoir 75*, 45-81.

Gomez, E., Doe, M., Villarroel, S., Noell, K., Ysaccis, R., Kornpihl, D., El-Toukhy, M., Forrest, G., 2018. Recent Yucatan Seismic Survey Revealing a New Frontier Exploration in the Gulf of Mexico. *AAPG Search and Discovery Article #30582*.

Gonzalez-Mieres, R., Suppe, J., 2006. Relief and shortening in detachment folds. *Journal of Structural Geology*, 28, 1785-1807.

Grajales-Nishimura, J. M., G. Murillo-Muneton, C. Rosales-Dominguez, E. Cedillo-Pardo, and J. Garcia-Hernandez, 2003. Heterogeneity of Lithoclast Composition in the Deep-water Carbonate Breccias of the K/T Boundary Sedimentary Succession, Southeastern Mexico and Offshore Campeche. In: C. Bartolini, R. T. Buffler, and J. Blickwede, eds., *The Circum-Gulf of Mexico and the Caribbean: Hydrocarbon habitats, basin formation, and plate tectonics: AAPG Memoir 79*, 312–329.

Gray, G. G., Lawton, T. F., 2011. New constraints on timing of Hidalgoan (Laramide) deformation in the Parras and La Popa basins, NE Mexico. *Boletín de la Sociedad Geológica Mexicana*, 63 (2), 333-343.

Gray, G. G., R. J. Pottorf, D. A. Yurewicz, K. I. Mahon, D. R. Pevear, and R. J. Chuchla, 2001. Thermal and chronological record of syn- to post-Laramide burial and exhumation, Sierra Madre Oriental, Mexico. In: C. Bartolini, R. T. Buffler, and A. Cantú-Chapa, eds., *The western Gulf of Mexico Basin: Tectonics, sedimentary basins, and petroleum systems: AAPG Memoir 75*, 159-181.

Groshong Jr., R.H., Epard, J.-L., 1994. The role of strain in area-constant detachment folding. *Journal of Structural Geology*, 16, 613–618.

Guzman-Vega, M. A., Mello, M. R., 1999. Origin of Oil in the Sureste Basin, Mexico. AAPG Bulletin, 83 (7), 1068-1095.

Hantschel, T., Kauerauf, A. I. 2009. Fundamentals of Basin and Petroleum Systems Modeling, Springer, 1-404.

Harrison, J. C., Bally, A. W., 1988. Cross-sections of the Parry islands fold belt on Melville Island, Canadian Arctic islands: Implications for the timing and growth history of some thin-skinned decollement systems. Bulletin of Canadian Petroleum Geology, 36 (3), 311-332.

Haq, B. U., Hardenbol, J., Vail, P. R., 1987. Chronology of fluctuating sea level since the Triassic. Science, 235 (4793), 1156-1167.

Holguín-Quñones, N., Brooks, J. M., Román-Ramos, J. R., Bernard, B. B., Lara-Rodríguez, J., Zumberge, J. E., Medrano-Morales, L., Rosenfeld, J., De Faragó Botella, M., Maldonado-Villalón, R., Martínez-Pontvianne, G., 2005. Estudio regional de manifestaciones superficiales de aceite y gas en el sur del golfo de México, su origen e implicaciones exploratorias. Boletín de la Asociación Mexicana de Geólogos Petroleros.

Hood, K. C., L. M. Wenger, O. P. Gross, and S. C. Harrison, 2002. Hydrocarbon systems analysis of the northern Gulf of Mexico: Delineation of hydrocarbon migration pathways

using seeps and seismic imaging. In: Surface exploration case histories: Applications of geochemistry, magnetics, and remote sensing, D. Schumacher and L. A. LeSchack, eds., AAPG Studies in Geology No. 48 and SEG Geophysical References Series No. 11, 25–40.

Hubert-Ferrari, A., Suppe, J., Gonzalez-Mieres, R., and Wang, X., 2007. Mechanisms of active folding of the landscape (southern Tian Shan, China). *Journal of Geophysical Research*, 112 (B3).

Hudec, M., Norton, I. O., 2019. Upper Jurassic structure and evolution of the Yucatan and Campeche subbasins, southern Gulf of Mexico. *AAPG Bulletin*, 103 (5), 1133-1151.

Hudec, M. R., Dooley, T., Peel, F. J., Soto, J., 2019. Controls on the evolution of passive-margin salt basins: Structure and evolution of the Salina del Bravo region, northeastern Mexico. *GSA Bulletin* (2019).

Hudec, M. R., and Norton, I. O., 2019. Upper Jurassic structure and evolution of the Yucatan and Campeche subbasins, southern Gulf of Mexico. *AAPG Bulletin*, 103 (5), 1133-1151.

Hudec, M., Norton, I. O., Jackson, M. P. A., Peel, F. J., 2013. Jurassic evolution of the Gulf of Mexico salt basin. *AAPG Bulletin*, 97 (10), 1683-1710.

Jacques, J. M., and Clegg, H., 2002. Late Jurassic Source Rock Distribution and Quality in the Gulf of Mexico: Inferences from Plate Tectonic Modeling. *Gulf Coast Association of Geological Societies Transactions*, 52, 429-440.

Katz, B. J., 1984. Source quality and richness of deep sea drilling project site 535 sediments, southeastern Gulf of Mexico. http://deepseadrilling.org/77/volume/dsdp77_11.pdf

Kenning, J. J., and Mann, P., 2020. Control of structural style by large, Paleogene, mass transport deposits in the Mexican Ridges fold-belt and Salina del Bravo, western Gulf of Mexico. *Marine and Petroleum Geology*, 115.

Kennicut, M. C., McDonald, T. J., Comet, P. A., Denoux, G. J., Brooks, J. M., 1992. The origins of petroleum in the northern Gulf of Mexico. *Geochimica et Cosmochimica Acta*, 56 (3), 1259-1280.

Lawton, T. F., 2008. Laramide sedimentary basins. In: K. J. Hsü, ed., *Sedimentary basins of the world*, 5, 429-450.

Le Roy, C., Rangin, C., Le Pichon, X., Thi Ngoc, H. N., Andreani, L., Aranda-Garcia, M., 2007. Neogene crustal shear zone along the western Gulf of Mexico margin and its implications for gravity sliding processes. Evidences from 2D and 3D multichannel seismic data. *Bull. Soc. géol. Fr.*, 178 (2), 175-185.

Lin, P., Bird, D. E., Mann, P., 2019. Crustal structure of an extinct, late Jurassic-to-earliest Cretaceous spreading center and its adjacent oceanic crust in the eastern Gulf of Mexico. *Marine Geophysical Research*, 40 (3), 395-418.

Magoon, L.B., Hudson, T.L. and Cook, H.E., 2001. Pimienta–Tamabra (!) – A giant supercharged petroleum system in the southern Gulf of Mexico, Onshore and Offshore Mexico. In: Bartolini, C., Buffler, R.T. and Cantu´ -Chapa (Eds.) *The western Gulf of Mexico Basin: Tectonics, sedimentary basins, and petroleum systems*. AAPG Memoir No. 75, 83–125.

Mann, P., Padilla y Sanchez, R., Nguyen, L., Lankford-Bravo, D., 2016. Geologic and geophysical evidence for a Pacific origin for seawater filling the Callovian Gulf of Mexico evaporite basin. AAPG Annual Convention and Exhibition, Calgary, 19-22nd June 2016.

Marton, G. L., Buffler, R. T., 1999. Jurassic-Early Cretaceous tectono-paleogeographic evolution of the southeastern Gulf of Mexico basin. *Sedimentary Basins of the World*, 4, 63-91.

Marton, G., Buffler, R. T., 1995. Jurassic Reconstruction of the Gulf of Mexico Basin. *International Geology Review*, 36 (6), 545-586.

McDonnell, A., Hudec, M. R., Jackson, M. P. A., 2009. Distinguishing salt welds from shale detachments on the inner Texas shelf, western Gulf of Mexico. *Basin Research*, 21, 47-59.

Mello, U. T., Karner, G. D., Anderson, R. N., 1995. Role of salt in restraining the maturation of subsalt source rocks. *Marine and Petroleum Geology*, 12 (7), 697-716.

Miller, K. G., Browning, J. V., Aubry, M., Wade, B. S., Katz, M. E., Kulpecz, A. A., Wright, J. D., 2008. Eocene-Oligocene global climate and sea-level changes: St. Stephens Quarry, Alabama. *GSA Bulletin*, 120 (1-2), 34-53.

Mitra, S., 2002. Structural models of faulted detachment folds. *AAPG Bulletin*, 86 (9), 1673-1694.

Morley, C. K., and Guerin, G., 1996. Comparison of gravity deformation styles and behavior associated with mobile shales and salt. *Tectonics*, 15 (6), 1154-1170.

Moscardelli, L., Wood, L., 2008. New classification system for mass transport complexes in offshore Trinidad. *Basin Research*, 20, 73-98.

Moscardelli, L., Wood, L., 2016. Morphometry of mass-transport deposits as a predictive tool. *GSA Bulletin*, 128 (1-2), 47-80.

Moscardelli, L., Wood, L., Mann, P., 2006. Mass-transport complexes and associated processes in the offshore area of Trinidad and Venezuela. *AAPG Bulletin*, 90 (7), 1059-1088.

Mount, V. S., Suppe, J., Hook, S. C., 1990. A Forward Modeling Strategy for Balancing Cross Sections. *AAPG Bulletin*, 74 (5), 521-531.

Naehr, T. H., Birgel, D., Bohrmann, G., MacDonald, I. R., Kasten, S., 2009. Biogeochemical controls on authigenic carbonate formation at the Chapopote “asphalt volcano”, Bay of Campeche. *Chemical Geology*, 266, 390-402.

Nagihara, S., Jones, K. O. 2005. Geothermal heat flow in the northeast margin of the Gulf of Mexico, *AAPG Bulletin*, 89 (6), 821-831.

Nagihara, S., Sclater, J. G., Phillips, J. D., Behrens, E. W., Lewis, T., Lawver, L. A., Nakamura, Y., Garcia-Abdeslem, J., Maxwell, A. E., 1996. Heat flow in the western abyssal plain of the Gulf of Mexico: Implications for thermal evolution of the old oceanic lithosphere. *Journal of Geophysical Research-Solid Earth*, 101 (B2), 2895-2913.

Nardin, T. R., Hein, F. J., Gorsline, D. S., Edwards, B. D., 1979. A review of mass movement processes, sediment and acoustic characteristics, and contrasts in slope and base-of-slope systems versus canyon-fan-basin floor systems. *SEPM Special Publication*, volume 27, eds: Doyle, L. J., Pilkey, O. H., 61-73.

Nguyen, L. C., and Mann, P., 2016. Gravity and magnetic constraints on the Jurassic opening of the oceanic Gulf of Mexico and the location and tectonic history of the Western Main transform fault along the eastern continental margin of Mexico. *Interpretation*, 4 (1), 2324-8866.

Ogata, K., Mutti, E., Pini, G. A., Tinterri, R., 2012. Mass transport-related stratal disruption within sedimentary mélanges: Examples from the northern Apennines (Italy) and south-central Pyrenees (Spain). *Tectonophysics*, 568-569, 185-199.

O'Reilly C., Keay, J., Birch-Hawkins, A., Bate, D., Halliday, J., 2017. Regional Play Types in the Mexican Offshore. *GeoExPro*, Vol. 14, No. 4.

O'Reilly, C., Birch-Hawkins, A., Dirkx, R., Winter, F., Cooke, R., 2017. Seismic facies analysis of the western Gulf of Mexico and implications for play types. *Gulf Coast Association of Geological Societies Transactions*, 67, 471-475.

Ortuño, A. S., E. Soriano M., C. Romero M., J. Rosales R., E. Bahena R., S. Hernandez G., and A. Cardenas, 2009. Two-dimensional and three-dimensional numerical simulation of petroleum systems approaching the deep-water Gulf of Mexico (Kayab Area, Campeche Sound, Mexico): Definition of thermally mature and prospective areas. In: C. Bartolini and J.

R. Roman Ramos, eds., Petroleum systems in the southern Gulf of Mexico: AAPG Memoir 90, 117–136.

Patton, J. W., Choquette, P. W., Guannel, G. K., Kaltenback, A. J., Moore, A., 1984. Organic geochemistry and sedimentology of lower to mid-Cretaceous deep-sea carbonates, sites 535 and 540, leg 77, http://deepseadrilling.org/77/volume/dsdp77_10.pdf

Paull, C. K., Caress, D. W., Gwiazda, R., Urrutia-fucugauchi, J., Rebolledo-vieyra, M., Lundsén, E., Anderson, K., Sumner, E. J., 2014. Cretaceous-Paleogene boundary exposed: Campeche Escarpment, Gulf of Mexico. *Marine Geology*, 357, 392-400.

Pew, E., 1982. Seismic structural analysis of deformation in the southern Mexican Ridges. Unpublished master's thesis: The University of Texas at Austin, Austin, United States, 114 p.

Pilcher, R. S., Murphy, R. T., McDonough Ciosek, J., 2014. Jurassic raft tectonics in the northeastern Gulf of Mexico. *Interpretation*, 2 (4), 2324-8866.

Pindell, J. 1985. Alleghenian reconstruction and subsequent evolution of the Gulf of Mexico, Bahamas, and Proto-Caribbean, *Tectonics*, 4 (1), 1-39.

Pindell, J. 2010. History of tectonic modeling and implications for depositional architecture in the Gulf of Mexico: Where we should go from here, Gulf Coast Association of Geological Societies Transactions, 60, 917-929.

Pindell, J., and Dewey, J., F. 1982. Permo-Triassic reconstruction of western Pangea and the evolution of the Gulf of Mexico/Caribbean region. Tectonics, 1 (2), 179-211.

Pindell, J., Graham, R., Horn, B. W., 2018. Role of outer marginal collapse on salt deposition in the eastern Gulf of Mexico, Campos and Santos basins. Geological Society, London, Special Publications, 476, 6 March 2018.

Pindell, J. L. and Kennan, L. 2009. Tectonic Evolution of the Gulf of Mexico, Caribbean and Northern South America in the Mantle Reference Frame: An Update. In: James, K., Antonieta-Lorente, M. and Pindell, J., Eds., The Geology and Evolution of the Region between North and South America, Geological Society of London, London, 227-242.

Pindell, J., Radovich, B., Horn, B. W. 2011. A New Perspective on Rifting. GeoExPro, 8 (6), 38-40.

Pindell, J., Graham, R., Horn, B. 2014. Rapid outer marginal collapse at the rift to drift transition of passive margin evolution, with a Gulf of Mexico case study. Basin Research, 26, 1-25.

Pindell, J., Miranda, E. C., Ceron, A., Hernandez, L. 2016. Aeromagnetic Map Constrains Jurassic-Early Cretaceous Synrift, Break Up, and Rotational Seafloor Spreading History in the Gulf Mexico. In: Lowrie, C., and Snedden, J., et al., eds., Mesozoic of the Gulf Rim and Beyond: New Progress in Science and Exploration of the Gulf of Mexico Basin, Perkins-Rosen Research Conference, GCSSEPM Transactions, Houston, 2016, 123-153.

Pindell, J., Weber, B., Hale-Erich, W., Cossey, S., Bitter, M., Molina Garza, R., Graham, R., and Erlich, R.N. 2020. Strontium isotope dating of evaporites and the breakup of the Gulf of Mexico and Proto-Caribbean Seaway, In Martens, U., and Molina Garza, R.S., eds., Southern and Central Mexico: Basement Framework, Tectonic Evolution, and Provenance of Mesozoic-Cenozoic Basins: Geological Society of America Special Paper 546.

Priestley, K., McKenzie, D., Ho, T. 2018. A Lithosphere-Asthenosphere Boundary – a Global Model Derived from Multimode Surface-Wave Tomography and Petrology, in Yuan, H., Romanowicz, B., eds. Lithospheric Discontinuities, AGU, 111-123.

Pulham, A. J., Salel, J., Peel, F., J., Nicholson, T., Rives, T., Wu, J., Delph, B., Requejo, R. 2019. The Age of the Louann Salt; Insights from Historic Isotopic Analyses in Salt Stocks from the Onshore Interior Salt Basins of the Northern Gulf of Mexico, Salt Tectonics, Associated Processes, and Exploration Potential: Revisited: 1989-2019, 37th Annual GCSSEPM Perkins-Rosen Research Conference, December 3-6, 2019, Houston, Texas.

Ricoy-Paramo, V. 2005. 3D seismic characterisation of the Cantarell Field, Campeche Basin, Mexico. Unpublished Doctoral Thesis, Cardiff University, United Kingdom, 424 p.

Rodriguez, A. B., 2011. Regional Structure, Stratigraphy, and Hydrocarbon Potential of the Mexican Sector of the Gulf of Mexico. Unpublished Master of Science thesis, University of Texas at Austin (2011), 177.

Román-Ramos, J. R., Cruz-Mercado, M. A., Salomón-Mora, L. E., Rosas-Lara, C., C., 2008. Continent-oceanic boundary deep structure in a shear margin: Western main transform, offshore Veracruz, Southern Gulf of Mexico. In: C. Bartolini and J. R. Román-Ramos, eds., Petroleum systems in the southern Gulf of Mexico: AAPG Memoir, 90, 409-420.

Rowan, M. G., Peel, F. J., Vendeville, B. C., 2004. Gravity-driven fold belts on passive margins. In: K. R. McClay, ed., Thrust tectonics and hydrocarbon systems: AAPG Memoir, 82, 157-182.

Rowan, M. G., 2018. The South Atlantic and Gulf of Mexico salt basins: crustal thinning, subsidence and accommodation salt and presalt strata, Geological Society, London, Special publications, 476.

Rueda-Gaxiola, J., 2009. The palynostratigraphy of red-bed and salt units of the Mexican petroleum sub-basins of the Gulf of Mexico. In: C. Bartolini and J. R. Roman Ramos, eds., *Petroleum systems in the southern Gulf of Mexico: AAPG Memoir 90*, 137–154.

Rutherford, S. R., Williams, R. H., 1989. Amplitude-versus-offset variations in gas sands. *Geophysics*, 54, 6, 680-688.

Sandwell, D. T., Müller, R. D., Smith, W. H. F., Garcia, E. and Francis, R. 2014. New global marine gravity model from Cryo-Sat-2 and Jason-1 reveals buried tectonic structure. *Science*, 346, 6205, 65-67.

Salomon-Mora, L. E., 2013. Structure and Tectonics of the Salt and Shale Provinces, Western Gulf of Mexico. Unpublished doctoral dissertation: University of Aberdeen, 476 p.

Salomón-Mora, L. E., Aranda-García, M., Román-Ramos, J. R., 2009. Contractional growth faulting in the Mexican Ridges, Gulf of Mexico. In: C. Bartolini and J. R. Román-Ramos, eds., *Petroleum systems in the southern Gulf of Mexico: AAPG Memoir 90*, 93-115.

Salomon-Mora, L. E., Cruz-Mercado, M., Alsop, I., Archer, S., 2011. Tectonics, structure, and hydrocarbon potential of the Mexican Ridges fold belt, western Gulf of Mexico. *Gulf Coast Association of Geological Societies Transactions*, 61, 403-419.

Salvador, A., 1987. Late Triassic-Jurassic Paleogeography and Origin of the Gulf of Mexico Basin. AAPG Bulletin, 71 (4), 419-451.

Salvador, A., 1991. Origin and development of the Gulf of Mexico basin. In: The Gulf of Mexico Basin.

Sanford, J. C., Snedden, J. W., Gulick, S. P. S., 2016. The Cretaceous-Paleogene boundary deposit in the Gulf of Mexico: Large-scale oceanic basin response to the Chicxulub impact. Journal of Geophysical Research, 121, 3, 1240-1261.

Santamaria-Orozco, D. M., 2000. Organic Geochemistry of Tithonian Source Rock and Associated Oils from the Sonda de Campeche, Mexico. Unpublished PhD dissertation, University of Aachen, Germany, 190.

Saunders, M., Geiger, L., Rodriguez, K., Hargreaves, P., 2016. The Delineation of Pre-Salt License Blocks in the Deep Offshore Campeche-Yucatan Basin. AAPG Search and Discovery Article #10867.

Sawyer, D. S., Buffler, R. T., Pilger, R. H., Jr., 1991. The crust under the Gulf of Mexico basin. In: Salvador, A., ed., The Gulf of Mexico Basin: Boulder, Colorado, Geological Society of America, The Geology of North America, v. J.

Shipp, C. R., Nott, J. A., Newlin, J. A., 2004. Physical characteristics and impact of mass transport complexes on deep-water jetted conductors and suction anchor piles. Offshore Technology Conference, 3-6 May, Houston, Texas.

Smith, S. A., Bilotti, F., Holmes, C., Liu, J., 2019. The Oligocene play of the Perdido fold belt trend, deep-water Mexico. *GeoGulf Transactions*, v. 69, p. 279-301.

Snedden, J. W., Galloway, W. E., Whiteaker T. L., Ganey-Curry, P. E., 2012. Eastward shift of deep-water fan axes during the Miocene in the Gulf of Mexico: possible causes and models. *GCAGS Journal*, 1, 131-144.

Snedden, J. W., Norton, I. O., Christeson, G. L., Sanford, J. C., 2014. Interaction of deep-water deposition and a mid-ocean spreading center, eastern Gulf of Mexico basin, USA. *Gulf Coast Association of Geological Societies Transactions*, 64, 371-383.

Snedden, J. W., Tinker, L. D., Virdell, J., 2018. Southern Gulf of Mexico Wilcox source to sink: Investigating and predicting Paleogene Wilcox Reservoirs in eastern Mexico deep-water areas. *AAPG Bulletin*, 102 (10), 2045-2074.

Stabler, C., Gonzalez, R. 2020. Pre-Salt Lacustrine Petroleum System, Onshore Mexico. *AAPG Search and Discovery Article #30655*

Steier, A., 2018. Jurassic-Cretaceous Stratigraphic and Structural Evolution of the Northern Yucatan Margin, Gulf of Mexico Basin. Unpublished master's thesis: University of Houston, Houston, Texas. 76 p.

Steier, A., Mann, P., 2019. Late Mesozoic gravity sliding and Oxfordian hydrocarbon reservoir potential of the northern Yucatan margin. *Marine and Petroleum Geology*, 103, 681-701.

Suppe, J., 2007, Absolute fault and crustal strength from wedge tapers, *The Geological Society of America*, v. 35, no. 12, 1127-1130.

Trudgill, B. D., Rowan, M. G., Fiduk, J. C., Weimer, P., Gale, P. E., Korn, B. E., Phair, R. L., Gafford, W. T., Roberts, G. R., Dobbs, S. W., 1999. The Perdido Fold Belt, Northwestern Deep Gulf of Mexico, Part 1: Structural Geometry, Evolution and Regional Implications. *AAPG Bulletin*, 83 (1), 88-113.

Turcotte, D., and G. Schubert, 2002. *Geodynamics* (2nd ed.): Cambridge University Press. 848 p.

Vazquez-Garcia, O., 2018. Tectonic synthesis of the deep-water Lamprea thrust and fold belt, offshore Burgos Basin, western Gulf of Mexico. Unpublished master's thesis: Colorado School of Mines, 148 p.

Vilà, M., Fernández M., Jiménez-Munt, I., 2010. Radiogenic heat production variability of some common lithological groups and its significance to lithospheric thermal modeling. *Tectonophysics*, 490, 152–164.

Waples, D. W., Pacheco, J., Vera, A., 2004. A method for correcting log-derived temperatures in deep wells, calibrated in the Gulf of Mexico. *Petroleum Geoscience*, 10 (3), 239-245.

Ware, P., 2002. Potential Problems in Interpreting Amplitude Anomalies. AAPG Search and Discovery Article #40053.

Watkins, J.S., and R.T. Buffler, 1996. Gulf of Mexico deep-water frontier exploration potential. In: O. Jones, and R.L. Freed, eds., *Structural framework of the northern Gulf of Mexico*: Trans. Gulf Coast Assoc. Geol. Soc., 79-92.

Weimer, P., Bouroullec, Adson, J., Cossey, S. P. J., 2017. An overview of the petroleum systems of the northern deep-water Gulf of Mexico. *AAPG Bulletin*, 101 (7), 941-993.

Wiener, R. W., Mann, M. G., Angelich, M. T., Molyneux, J. B., 2010. Mobile shale in the Niger Delta: characteristics, structure, and evolution. In: L. Wood, ed., *Shale tectonics*: AAPG Memoir 93, 145-161.

Wiltschko, D.V. & Groshong, R.H., 2012. The Chamberlin 1910 balanced section: Context, contribution, and critical reassessment. *Journal of Structural Geology*, 41, 7–23.

Wu, J. E., McClay, K., Frankowicz, E., 2015. Niger Delta gravity-driven deformation above the relict Chain and Charcot oceanic fracture zones, Gulf of Guinea: Insights from analog models. *Marine and Petroleum Geology*, 65, 43-62.

Yallup, C., 2019. The Pre-salt of Southern Mexico: Is There Potential for Oil? *Exploration Insights*, May 2019 Issue, Halliburton.

Yarbu, I., Contreras, J., 2017. The interplay between deformation, erosion and sedimentation in the deep-water Mexican Ridges foldbelt, western Gulf of Mexico basin. *Basin Research*, 29, 446-464.

Yarbu, I., González, A., Spelz-Madero, R. M., Negrete-Aranda, R., Contreras, J., 2018. Development of detachment folds in the Mexican Ridges foldbelt, western Gulf of Mexico basin. *Tectonics*, 37, 2013-2028.

APPENDIX

Table A1.1 Area-depth strain measurements for folds along Profile 1 (Figure 4.9)

Fold 1

Horizon	Area (m)	Area (km)	Depth (m)	Depth (km)	Area-Depth Displacement (D)	Section Length (SL)	Restored Bed Length (RBL=SL-D)	Deformed Bed Length (DBL)	Nominal Displacement (SL-DBL)	Layer-Parallel Strain ((DBL-RBL)/(RBL))
17	-253702	-0.253702	2593	2.593	54	9908	9855	9913	-5	0.6
16	-315269	-0.315269	2679	2.679	68	9908	9841	9918	-9	0.8
15	-464118	-0.464118	2784	2.784	102	9909	9806	9939	-31	1.4
14	-1019597	-1.019597	2869	2.869	229	9913	9683	9973	-61	3
13	-1586350	-1.58635	3003	3.003	368	9924	9556	10114	-191	5.8
12	2577368	2.577368	3659	3.659	-704	9907	10612	10049	-142	-5.3
11	3542108	3.542108	3947	3.947	-1051	9908	10959	10274	-366	-6.2
10	5586021	5.586021	4297	4.297	-1849	9912	11761	10937	-1025	-7
9	5906294	5.906294	4398	4.398	-2023	9911	11934	11329	-1418	-5.1
8	5724402	5.724402	4608	4.608	-2118	9908	12026	11731	-1824	-2.5
7	5351179	5.351179	4783	4.783	-2118	9907	12026	11907	-2000	-1
6	4711877	4.711877	5058	5.058	-2118	9908	12027	11883	-1975	-1.2
5	4419317	4.419317	5232	5.232	-2118	9908	12026	11922	-2014	-0.9
4	3358283	3.358283	5834	5.834	-2118	9917	12036	11704	-1786	-2.8
3	1106899	1.106899	6745	6.745	-2118	9919	12038	10553	-634	-12.3
2	-782256	-0.782256	7700	7.7		9909		10048	-139	
1	-889449	-0.889449	8341	8.341		9908		9935	-27	

Fold 2

Horizon	Area (m)	Area (km)	Depth (m)	Depth (km)	Area-Depth Displacement (D)	Section Length (SL)	Restored Bed Length (RBL=SL-D)	Deformed Bed Length (DBL)	Nominal Displacement (SL-DBL)	Layer-Parallel Strain ((DBL-RBL)/(RBL))
17	406086	0.406086	2715	2.715	-89	7989	8078	7993	-4	-1.1
16	446617	0.446617	2807	2.807	-100	7989	8089	7993	-4	-1.2
15	562947	0.562947	2910	2.91	-129	7989	8117	7995	-7	-1.5
14	831493	0.831493	3062	3.062	-197	7988	8185	8004	-15	-2.2
13	1822497	1.822497	3270	3.27	-454	7988	8442	8059	-71	-4.5
12	2345390	2.34539	3565	3.565	-631	7989	8620	8136	-147	-5.6
11	3631328	3.631328	3958	3.958	-1092	7989	9081	8355	-366	-8
10	5976200	5.9762	4477	4.477	-2129	7988	10118	8766	-777	-13.4
9	6320790	6.32079	4586	4.586	-2344	7989	10333	8843	-854	-14.4
8	6304135	6.304135	4820	4.82	-2580	7994	10573	9354	-1360	-11.5
7	5866216	5.866216	5053	5.053	-2580	7998	10578	9817	-1819	-7.2
6	5183580	5.18358	5288	5.288	-2580	7993	10573	9792	-1800	-7.4
5	4801952	4.801952	5423	5.423	-2580	7993	10573	9883	-1890	-6.5
4	2999253	2.999253	6081	6.081	-2580	7989	10568	8681	-692	-17.9
3	1212551	1.212551	6832	6.832	-2580	7993	10573	8222	-229	-22.2
2	603270	0.60327	7671	7.671		7993		8038	-45	
1	588891	0.588891	8422	8.422		7999		8034	-35	

Table A1.1 (continued) Area-depth strain measurements for folds along Profile 1 (Figure 4.9)

Fold 3

Horizon	Area (m)	Area (km)	Depth (m)	Depth (km)	Area-Depth Displacement (D)	Section Length (SL)	Restored Bed Length (RBL=SL-D)	Deformed Bed Length (DBL)	Nominal Displacement (SL-DBL)	Layer-Parallel Strain ((DBL-RBL)/(RBL))
17	-66241	-0.066241	2817	2.817	15	5800	5785	5801	-1	0.3
16	-66476	-0.066476	2903	2.903	15	5800	5785	5802	-2	0.3
15	-67061	-0.067061	2993	2.993	15	5800	5784	5803	-3	0.3
14	8905	0.008905	3133	3.133	-2	5800	5802	5807	-8	0.1
13	195637	0.195637	3251	3.251	-48	5799	5847	5873	-74	0.4
12	419768	0.419768	3603	3.603	-112	5802	5914	5824	-21	-1.5
11	1193482	1.193482	4062	4.062	-359	5803	6162	6053	-250	-1.8
10	2895872	2.895872	4630	4.63	-1065	5804	6869	6538	-734	-4.8
9	2971882	2.971882	4783	4.783	-1158	5805	6963	6669	-864	-4.2
8	2981223	2.981223	5155	5.155	-1318	5808	7126	6947	-1138	-2.5
7	2637784	2.637784	5369	5.369	-1318	5806	7124	6984	-1178	-2
6	2330691	2.330691	5574	5.574	-1318	5808	7126	6923	-1115	-2.8
5	1976693	1.976693	5732	5.732	-1318	5807	7125	6929	-1122	-2.7
4	1240949	1.240949	6408	6.408	-1318	5814	7132	6014	-199	-15.7
3	377290	0.37729	7097	7.097	-1318	5838	7156	5956	-118	-16.8
2	161978	0.161978	7774	7.774		5814		5823	-9	
1	-261527	-0.261527	8337	8.337		5802		5821	-19	

Fold 4

Horizon	Area (m)	Area(km)	Depth (m)	Depth(km)	Area-Depth Displacement (D)	Section Length (SL)	Restored Bed Length (RBL=SL-D)	Deformed Bed Length (DBL)	Nominal Displacement (SL-DBL)	Layer-Parallel Strain ((DBL-RBL)/(RBL))
17	318485	0.318485	2989	2.989	-68	7627	7695	7646	-19	-0.6
16	421880	0.42188	3090	3.09	-92	7628	7720	7648	-20	-0.9
15	615410	0.61541	3166	3.166	-137	7628	7765	7677	-49	-1.1
14	884658	0.884658	3266	3.266	-201	7625	7827	7726	-101	-1.3
13	1174776	1.174776	3341	3.341	-272	7625	7897	7763	-138	-1.7
12	2067164	2.067164	3787	3.787	-534	7625	8159	7832	-207	-4
11	2646541	2.646541	4316	4.316	-792	7632	8423	8056	-424	-4.4
10	3386227	3.386227	4859	4.859	-1210	7626	8836	8607	-981	-2.6
9	3588739	3.588739	5073	5.073	-1337	7630	8967	8744	-1113	-2.5
8	2992976	2.992976	5491	5.491	-1337	7631	8967	8865	-1234	-1.1
7	2524778	2.524778	5696	5.696	-1337	7632	8969	8898	-1265	-0.8
6	2266339	2.266339	5888	5.888	-1337	7633	8969	8907	-1274	-0.7
5	1974604	1.974604	6067	6.067	-1337	7634	8970	8854	-1221	-1.3
4	1327942	1.327942	6697	6.697	-1337	7626	8962	7893	-268	-11.9
3	426354	0.426354	7399	7.399	-1337	7624	8960	7707	-84	-14
2	-654026	-0.654026	7926	7.926		7624		7639	-15	
1	-381737	-0.381737	8459	8.459		7624		7638	-15	

Table A1.2 Area-depth strain measurements for folds along Profile 2 (Figure 4.10)

Fold 1

Horizon	Area (m)	Area (km)	Depth (m)	Depth (km)	Area-Depth Displacement (D)	Section Length (SL)	Restored Bed Length (RBL=SL-D)	Deformed Bed Length (DBL)	Nominal Displacement (SL-DBL)	Layer-Parallel Strain ((DBL-RBL)/(RBL))
17	136739	0.136739	2054	2.054	-28	9947	9975	9959	-12	-0.2
16	202859	0.202859	2131	2.131	-42	9947	9989	9970	-23	-0.2
15	216493	0.216493	2263	2.263	-46	9947	9993	9964	-17	-0.3
14	386505	0.386505	2432	2.432	-85	9947	10032	9955	-8	-0.8
13	561172	0.561172	2570	2.57	-127	9947	10074	9947	0	-1.3
12	2172882	2.172882	2960	2.96	-541	9946	10487	9938	9	-5.2
11	3715727	3.715727	3316	3.316	-1014	9947	10961	10034	-87	-8.5
10	5924704	5.924704	3731	3.731	-1823	9947	11771	10313	-365	-12.5
9	8074459	8.074459	4041	4.041	-2747	9949	12696	10510	-561	-17.2
8	9415928	9.415928	4300	4.3	-3514	9949	13463	10730	-781	-20.3
7	10187015	10.187015	4598	4.598	-4265	9948	14213	11469	-1521	-19.3
6	8829069	8.829069	4893	4.893	-4255	9933	14187	11203	-1270	-21
5	8445994	8.445994	5003	5.003	-4255	9933	14187	11100	-1167	-21.8
4	6184627	6.184627	5528	5.528	-4255	9934	14189	10835	-901	-23.6
3	3808555	3.808555	6473	6.473		9930		10253	-323	
2	1245354	1.245354	7132	7.132		9930		10022	-92	
1	1862282	1.862282	7879	7.879		9931		9992	-61	

Fold 2

Horizon	Area (m)	Area (km)	Depth (m)	Depth (km)	Area-Depth Displacement (D)	Section Length (SL)	Restored Bed Length (RBL=SL-D)	Deformed Bed Length (DBL)	Nominal Displacement (SL-DBL)	Layer-Parallel Strain ((DBL-RBL)/(RBL))
17	902209	0.902209	2176	2.176	-186	10383	10569	10400	-18	-1.6
16	913729	0.913729	2242	2.242	-191	10383	10574	10399	-17	-1.6
15	1250412	1.250412	2370	2.37	-269	10382	10651	10418	-35	-2.2
14	1986625	1.986625	2524	2.524	-442	10382	10824	10439	-56	-3.6
13	2680668	2.680668	2688	2.688	-619	10383	11001	10480	-98	-4.7
12	4045974	4.045974	2962	2.962	-997	10382	11379	10519	-137	-7.6
11	5231655	5.231655	3319	3.319	-1413	10382	11795	10627	-245	-9.9
10	6090175	6.090175	3576	3.576	-1767	10383	12151	10780	-397	-11.3
9	8897497	8.897497	3970	3.97	-2915	10388	13304	11283	-895	-15.2
8	9481707	9.481707	4213	4.213	-3376	10389	13765	11678	-1288	-15.2
7	10145961	10.145961	4450	4.45	-3945	10393	14339	11708	-1315	-18.3
6	10241926	10.241926	4740	4.74	-4489	10397	14885	11736	-1339	-21.2
5	9888780	9.88878	4860	4.86	-4688	10396	15084	11724	-1328	-22.3
4	7788049	7.788049	5453	5.453	-4688	10392	15081	11988	-1596	-20.5
3	3377475	3.377475	6263	6.263	-4688	10388	15077	11254	-866	-25.4
2	2951486	2.951486	7234	7.234		10383		10606	-223	
1	3230403	3.230403	8147	8.147		10389		10741	-352	

Table A1.2 (continued) Area-depth strain measurements for folds along Profile 2 (Figure 4.10)

Fold 3

Horizon	Area (m)	Area(km)	Depth (m)	Depth(km)	Area-Depth Displacement (D)	Section Length (SL)	Restored Bed Length (RBL=SL-D)	Deformed Bed Length (DBL)	Nominal Displacement (SL-DBL)	Layer-Parallel Strain ((DBL-RBL)/(RBL))
17	2018481	2.018481	2412	2.412	-433	11698	12131	11724	-25	-3.4
16	2216860	2.21686	2491	2.491	-484	11699	12183	11766	-67	-3.4
15	3231143	3.231143	2638	2.638	-729	11700	12429	11737	-36	-5.6
14	3960435	3.960435	2777	2.777	-922	11700	12622	11817	-118	-6.4
13	4939860	4.93986	2943	2.943	-1196	11698	12895	11859	-161	-8
12	5544198	5.544198	3166	3.166	-1419	11698	13117	11865	-167	-9.5
11	9634425	9.634425	3699	3.699	-2857	11723	14579	12389	-666	-15
10	10886257	10.886257	3965	3.965	-3503	11731	15234	12674	-943	-16.8
9	11967212	11.967212	4186	4.186	-4147	11719	15865	13342	-1623	-15.9
8	13169279	13.169279	4429	4.429	-4982	11721	16704	13543	-1821	-18.9
7	12794074	12.794074	4610	4.61	-5251	11720	16971	13871	-2151	-18.3
6	11800126	11.800126	4821	4.821	-5251	11714	16956	13530	-1816	-20.2
5	11313153	11.313153	4962	4.962	-5251	11715	16967	13409	-1693	-21
4	7528029	7.528029	5624	5.624	-5251	11720	16971	14043	-2323	-17.3
3	5506529	5.506529	6387	6.387		11712		13586	-1874	
2	4651313	4.651313	7334	7.334		11693		11902	-209	
1	1228188	1.228188	8127	8.127		11700		11841	-141	

Fold 4

Horizon	Area	Depth	Area-Depth Displacement (D)	Section Length (SL)	Restored Bed Length (RBL=SL-D)	Deformed Bed Length (DBL)	Nominal Displacement (SL-DBL)	Layer-Parallel Strain ((DBL-RBL)/(RBL))		
17	-335533	-0.335533	2595	2.595	67	10254	10187	10264	-9	0.7
16	-259958	-0.259958	2680	2.68	53	10254	10201	10268	-14	0.7
15	-391784	-0.391784	2822	2.822	82	10254	10172	10263	-8	0.9
14	-806291	-0.806291	2954	2.954	173	10254	10081	10269	-15	1.9
13	-1282970	-1.28297	3129	3.129	286	10257	9971	10379	-123	4.1
12	-1060261	-1.060261	3457	3.457	255	10257	10002	10609	-352	6.1
11	1948084	1.948084	4148	4.148	-562	10254	10816	10882	-628	0.6
10	2878212	2.878212	4672	4.672	-979	10265	11243	11271	-1006	0.2
9	4723612	4.723612	5025	5.025	-1825	10284	12109	11768	-1484	-2.8
8	5343589	5.343589	5317	5.317	-2327	10288	12615	12418	-2130	-1.6
7	5181022	5.181022	5525	5.525	-2456	10295	12751	12039	-1744	-5.6
6	4634545	4.634545	5714	5.714	-2456	10298	12754	12097	-1799	-5.2
5	4223668	4.223668	5862	5.862	-2456	10299	12754	12007	-1708	-5.9
4	2733941	2.733941	6537	6.537	-2456	10301	12757	11098	-797	-13
3	971766	0.971766	7203	7.203	-2456	10303	12759	10696	-393	-16.2
2	-838687	-0.838687	7886	7.886		10306		10597	-292	
1	-1368527	-1.368527	8518	8.518		10178		10385	-207	

Table A1.2 (continued) Area-depth strain measurements for folds along Profile 2 (Figure 4.10)

Fold 5

Horizon	Area (m)	Area (km)	Depth (m)	Depth (km)	Area-Depth Displacement (D)	Section Length (SL)	Restored Bed Length (RBL=SL-D)	Deformed Bed Length (DBL)	Nominal Displacement (SL-DBL)	Layer-Parallel Strain ((DBL-RBL)/(RBL))
17	736471	0.736471	2679	2.679	-138	11864	12003	11903	-39	-0.8
16	780488	0.780488	2778	2.778	-149	11864	12014	11878	-14	-1.1
15	1111574	1.111574	2896	2.896	-218	11864	12082	11890	-26	-1.6
14	1742631	1.742631	3037	3.037	-351	11864	12215	11911	-48	-2.5
13	2830874	2.830874	3265	3.265	-598	11863	12460	11951	-88	-4.1
12	4822498	4.822498	3686	3.686	-1118	11865	12983	12101	-235	-6.8
11	7507035	7.507035	4490	4.49	-2139	11883	14022	12651	-767	-9.8
10	13428637	13.428637	5348	5.348	-5063	11894	16958	13896	-2002	-18.1
9	16022163	16.022163	5694	5.694	-6947	11879	18826	14543	-2664	-22.8
8	16221810	16.22181	6027	6.027	-8235	11880	20115	16302	-4422	-19
7	14687866	14.687866	6221	6.221	-8235	11880	20115	16909	-5029	-15.9
6	13049639	13.049639	6417	6.417	-8235	11878	20113	17260	-5382	-14.2
5	11711818	11.711818	6575	6.575	-8235	11876	20111	17259	-5284	-14.2
4										
3										
2	1083610	1.08361	8032	8.032		11880		11935	-54	
1	1314406	1.314406	8667	8.667		11885		11945	-59	

Fold 6

Horizon	Area (m)	Area (km)	Depth (m)	Depth (km)	Area-Depth Displacement (D)	Section Length (SL)	Restored Bed Length (RBL=SL-D)	Deformed Bed Length (DBL)	Nominal Displacement (SL-DBL)	Layer-Parallel Strain ((DBL-RBL)/(RBL))
17	2654759	2.654759	2943	2.943	-519	15137	15656	15260	-123	-2.5
16	3114121	3.114121	3064	3.064	-624	15138	15762	15272	-133	-3.1
15	4060796	4.060796	3192	3.192	-834	15139	15973	15288	-149	-4.3
14	4605800	4.6058	3270	3.27	-962	15137	16098	15319	-183	-4.8
13	5878250	5.87825	3412	3.412	-1265	15136	16401	15354	-218	-6.4
12	9389120	9.38912	3893	3.893	-2254	15135	17389	15849	-715	-8.9
11	14917849	14.917849	4760	4.76	-4523	15135	19658	16945	-1810	-13.8
10	19550169	19.550169	5446	5.446	-7483	15149	22633	18453	-3303	-18.5
9	19685264	19.685264	5688	5.688	-8305	15147	23452	18996	-3849	-19
8	19643037	19.643037	6110	6.11	-10418	15141	25559	19874	-4734	-22.2
7	18147085	18.147085	6338	6.338	-10418	15140	25558	19986	-4846	-21.8
6	16645988	16.645988	6506	6.506	-10418	15140	25558	19856	-4716	-22.3
5	14766561	14.766561	6681	6.681	-10418	15137	25555	18386	-3249	-28.1
4	9020662	9.020662	7145	7.145	-10418	15142	25560	16193	-1051	-36.6
3	5248334	5.248334	7556	7.556	-10418	15134	25552	15622	-488	-38.9
2	-5318672	-5.318672	7804	7.804		15165		15252	-87	
1	-6288074	-6.288074	8379	8.379		15165		15301	-136	